UNIVERSIDAD COMPLUTENSE DE MADRID
FACULTAD DE CIENCIAS BIOLÓGICAS

TESIS DOCTORAL

Alcohol y dieta occidental: un nuevo modelo fisiológico para el estudio del eje intestino-hígado en la progresión de la enfermedad hepática crónica

An exprimental dual model to examine the rol of gut-liver axis in the progression of chronic liver disease

MEMORIA PARA OPTAR AL GRADO DE DOCTOR

PRESENTADA POR

Raquel Benedé Ubieto

Directora

Yulia Nevzorova

Madrid

UNIVERSIDAD COMPLUTENSE DE MADRID

FACULTAD DE CIENCIAS BIOLÓGICAS

TESIS DOCTORAL

ALCOHOL Y DIETA OCCIDENTAL: UN NUEVO MODELO FISIOLÓGICO PARA EL ESTUDIO DEL EJE INTESTINO-HÍGADO EN LA PROGRESIÓN DE LA ENFERMEDAD HEPÁTICA CRÓNICA

AN EXPERIMENTAL DUAL MODEL TO EXAMINE THE ROLE OF GUT-LIVER AXIS IN THE PROGRESSION OF CHRONIC LIVER DISEASE

MEMORIA PARA OPTAR AL GRADO DE DOCTORA

PRESENTADA POR

RAQUEL BENEDÉ UBIETO

DIRECTORA

YULIA NEVZOROVA

UNIIVERSIDAD COMPLUTENSE DE MADRID

FACULTAD DE CIENCIAS BIOLÓGICAS

PROGRAMA DE DOCTORADO EN BIOQUÍMICA, BIOLOGÍA MOLECULAR Y BIOMEDICINA

TESIS DOCTORAL

ALCOHOL Y DIETA OCCIDENTAL: UN NUEVO MODELO FISIOLÓGICO PARA EL ESTUDIO DEL EJE INTESTINO-HÍGADO EN LA PROGRESIÓN DE LA ENFERMEDAD HEPÁTICA CRÓNICA

AN EXPERIMENTAL DUAL MODEL TO EXAMINE THE ROLE OF GUT-LIVER AXIS IN THE PROGRESSION OF CHRONIC LIVER DISEASE

MEMORIA PARA OPTAR AL GRADO DE DOCTORA

PRESENTADA POR

RAQUEL BENEDÉ UBIETO

DIRECTORA

YULIA NEVZOROVA

The best view comes after the hardest climbs.

Anonymous

Acknowledgements

Acknowledgements

No sé cuántas veces me había imaginado escribir por fin estas líneas. Aunque la verdad es que, llegado el momento, cuesta arrancar y encontrar las palabras adecuadas, tanto, como costó empezar a escribir cada uno de los apartados que la componen. El síndrome del folio en blanco supongo… Aunque admito que he procrastinado este momento por miedo a olvidarme a alguien, ya que han sido muchos los que han aportado su granito de arena a este trabajo, los que han tirado fuerte de mi durante estos años y me han ayudado a levantarme o a hacerme menos dura cualquier caída. A aquellos que han celebrado éxitos conmigo, que me han completado como persona y llenado un poquito más como científica, gracias.

First of all, I would like to thank the **Dra. Yulia Nevzorova** for giving me the opportunity in 2018 to join her lab. I was not sure if science life was for me but during these 6 years, we have built a successful, helpful, and hardworking team that made all effort worth it. It is important to highlight her compromise and kind attention. No matter what time it was, she was always willing to discuss experiments and closely share her experiences to encourage me in every step I took. I am thankful for all the congresses, publications, and knowledge you shared with me.

No podría continuar, sin agradecer al **Dr. Francisco Javier Cubero** toda su ayuda, y su apoyo durante estos años. Espero que nunca pierdas la pasión por todo lo que haces, ciencia, deporte, idiomas y un poquito de *afterwork*. Gracias por haberme hecho partícipe en tus proyectos y por enseñarme en muchos aspectos como funciona el mundillo de la ciencia.

Gracias a los **miembros del Departamento de Inmunología de la Facultad de Medicina**, por acogerme desde el principio y generar un ambiente de trabajo muy fructífero. Por confirmarme que el peor marrón que me pudo tocar fue gestionar los residuos biosanitarios.

I really need to thank all the valuable scientifics that work in **MedKlinik III Department** in the RWTH Uniklinik Aachen and **Max**. For all the support during my stay in Aachen and for making things easier and taking care of me.

Y… creo que estoy tardando demasiado en nombrar a mi querido ***LOVELY LIVER LAB***, con los que he compartido muchos momentos y hemos logrado complementarnos los unos a los otros funcionando como un engranaje digno de los mejores relojes suizos.

First, I would like to thank also to our **Chinese lovely liver lab**, the ones who left, **Feifei**, **Marker**, **Hui**, **Fengjie** and **Kang**, from whose I learned a lot and guided me at the beginning of this adventure; and for the ones that are still here, **HangHang** and **Bao**, for sharing beautiful moments with us and all your Chinese traditions that I must admit I love.

A **Nuria** por todos los momentos, risas y teorías locas que trataban de explicar lo inexplicable. Te echamos de menos.

A **Alex**, por sacarme una sonrisa cuando más harta estaba, incluso cuando estaba harta de ti y tu movimiento nervioso con la pierna. Por llevar a cabo la misión más importante y complicada durante estos años: evitar que me enfadara.

A **Héctor**, por no haberla liado demasiado los primeros meses que estuviste en el lab, y ayudarme a ejercitar mi ~~nula~~ poca paciencia. La verdad es que has sido el mejor pupilo que he tenido. Espero que hayas y sigas aprendiendo mucho de nosotros y que sigas creciente tanto como estos primeros meses. Te espera un largo camino, pero seguro que valdrá la pena.

A la ya Dra. Lamas-Paz, **araña**. No pude tener mejor acogida cuando puse un pie en el lab. Por las largas tardes en el laboratorio hasta más allá de la hora de cenar, tratando de salvar una liada (sin éxito generalmente).

A la recién estrenada Dra. Morán, **Laula**. Por quitar importancia a cosas que realmente no la tenían, pero yo no veía. Por el cariño y todas las risas compartidas durante este tiempo. No pude tener mejor suerte de que fueras mi compañera en nuestros inicios.

A mi compi y ya doctora **Olga**. Hemos formado un muy buen equipo durante estos años que no habría cambiado por nada. Gracias por tu orden, por ser calma y siempre tratar de buscar una solución con la mente fría y el corazón contento.

A la mejor lab mánager que he conocido (y la única), a mi consejera, mi compañera de poyata, pero sobre todo a una gran amiga con la que he compartido mucho en muy poco… **Marina**, no sabría cómo agradecerte todo.

A **Carlos**, por tu cercanía, tu implicación desde el primer día que llegaste, tus consejos, tu sinceridad y tus ganas de ayudarnos. Por enseñarnos a apreciar y buscar la calidad en todo lo que hacemos y hagamos en un futuro.

A la **ciencia** en general. Por alimentar mi curiosidad y mis ganas de saber. Por hacerme disfrutar de ella, como de uno de esos libros que no puedes soltar hasta llegar al final. Por ser esperanza para todos, aunque realmente solo te conozcamos y valoremos unos pocos.

Al **atletismo**, mi vía de escape. Por todos los valores que me has enseñado y todos los momentos que he vivido. Aunque quizá no todos hayan sido buenos, puedo aseguraros que siempre he aprendido algo. Por el poder terapéutico, por estúpido que parezca, que tiene el anillo de 6 calles de tartán.

Sin duda, lo mejor no sólo han sido todos los éxitos en la pista, sino lo que me ha regalado fuera de ella: Mis entrenadores, y compañeros de entrenamiento y amigos, sin los cuales probablemente ponerme en unos tacos de salida, y entrenar tantas horas a la semana, habría dejado de tener sentido hace mucho tiempo. A **Sandra**, que, desde el principio, cuando llegué a Madrid me acogió y me hizo sentir como en casa. A **Naza**, por encontrar siempre las palabras y apoyarme, tanto dentro como fuera de la pista. Al campeón en hacerme reír siempre, **Soto**, aunque tus consejos financieros sobre las criptomonedas (por ahora), no han mejorado en absoluto mi economía como estudiante predoctoral.

A **Pablo**, mi compi de aventuras, viajes, entrenamientos, competiciones, cafecitos al sol, cenas veganas, y risas. Por estar siempre ahí para mí, y porque lo estés muchos años más.

Al resto de la **Chupipandi**, sólo vosotros hacéis que este deporte siga siendo chupi, no me faltéis nunca.

A **Mimi,** que me enseñó a escucharme, a comprenderme y a quererme un poquito más. Gracias por recordarme el verdadero sentido de todo, y por ayudarme a encontrar aquel sendero por el que sí quería caminar (y correr).

A **Álvaro**, mi compañero de vida. Contigo sobran las palabras. Gracias por quererme y aguantar tanto mis malas caras como mis momentos de locura y felicidad extrema en un intervalo de menos de 30 segundos. Te mentiría si te

prometiera que esto iba a cambiar, pero te gustan las montañas rusas, y este será un viaje irrepetible.

Y sonará tópico, pero he dejado para el final a lo más importante, mi **familia**. Siempre seréis casa para mí. Gracias a vosotros soy quien soy hoy. Jamás habría llegado hasta aquí sin vuestro apoyo incondicional.

A uno de mis pilares fundamentales, mi **madre**. Ella sí que ha aguantado viento y marea. Gracias por recordarme que soy fuerte y no dejar que me rindiera nunca. Por las largas conversaciones por teléfono de todos los días donde yo te contaba cosas de experimentos que probablemente ni entendías, pero me escuchabas atentamente para tranquilizarme después. No importa cuantas horas estuviéramos hablando, te quedabas con todas aquellas palabras tan extrañas para poder preguntarme al día siguiente como había ido. Y sí, al final me salió el *vesterbló* de ZO-1.

A mi **padre**, mi otro pilar esencial, por aguantar estoicamente llamadas a cualquier hora y esperar a que mamá te contara luego cómo me había ido el día. Por ser el mejor técnico por videollamada para arreglar cualquier cosa. Por hacerme desconectar cuando volvía a Jaca, esos días esquiando y enseñarme a valorar la montaña y cada rincón del Pirineo.

A mi **hermano**, mi tercer pilar. Por tener siempre preparado un calificativo poco amable para hacerme rabiar y así demostrar que en el fondo me tienes cariño. Te robé las tijeras rojas de cuando éramos niños, y probablemente algo más, pero gracias por aguantarme como hermana pequeña y cuidarme.

Y sin el cuarto pilar, mi vida no se tendría en pie. Gracias a los que ya se fueron, a mis **abuelos**, en los que pienso cada día y espero que se sientan orgullosos y me sigan acompañando allá donde estén. Gracias por una infancia tan feliz, y enseñarme qué es lo verdaderamente importante.

No podría sentirme más afortunada de que **todos** forméis parte de mi vida y hayáis estado presentes en esta aventura. Espero que estéis listos para la siguiente.

Table of contents

Table of Contents

Resumen / Abstract

1. RESUMEN / ABSTRACT

1.1. RESUMEN

Introducción y objetivos

Alrededor de 844 millones de personas en todo el mundo sufren de enfermedad hepática crónica, provocando aproximadamente 2 millones de muertes al año. Actualmente, el consumo de alcohol junto con la obesidad y el sobrepeso, son las principales causas de enfermedad hepática crónica en los países occidentales. La presencia de ambos agentes causales en el mismo individuo es altamente plausible y se conoce como enfermedad hepática de etiología dual, alcohólica y no alcohólica (*BASH*), por sus siglas en inglés.

El papel central del hígado en el metabolismo del alcohol y los lípidos lo convierte en uno de los órganos más afectados en BASH. Recientes estudios han demostrado que la enfermedad hepática crónica es principalmente sistémica, induciendo fallos en el tejido adiposo blanco, resistencia a la insulina, cambios en la permeabilidad intestinal y disbiosis. Además, se ha descrito recientemente que el eje intestino-hígado es un contribuyente clave en la fisiopatología de las enfermedades hepáticas crónicas. BASH es un área inexplorada en el campo de la hepatología, sin embargo, ha cobrado gran importancia debido al creciente número de pacientes afectados.

Por tanto, el objetivo principal de nuestro estudio ha sido desarrollar un modelo experimental múrido que reproduzca los efectos sinérgicos del alcohol y la dieta occidental imitando la fisiopatología de la enfermedad humana. Además, buscamos caracterizar la relevancia de la interacción entre el hígado, el intestino y la microbiota para definir posibles dianas terapéuticas.

Métodos

En nuestros experimentos, ratones C57Bl/6J Wt de 10 semanas de edad fueron tratados con una dieta DUAL compuesta por dieta occidental y un 10% de alcohol en agua de bebida conteniendo un 6.75% de D-glucosa durante 10, 23 y 52 semanas. El tratamiento con sólo dieta occidental, o un 10% de alcohol en el agua de bebida o dieta y agua normal, fueron utilizados como controles.

1. El hígado fue caracterizado histológicamente en términos de esteatosis, inflamación, fibrosis y carcinoma hepatocelular. Además, se definieron las vías metabólicas, inflamatorias y fibróticas en el tejido hepático mediante estudios metabolómicos, proteómicos y transcriptómicos.

2. La fisiología intestinal, la barrera intestinal y la permeabilidad fueron estudiadas. Además, se realizó el análisis de la composición de la microbiota mediante secuenciación del ARNr 16s. Dicha composición fue comparada con una cohorte de pacientes con enfermedad hepática crónica de etiología dual.

3. Se utilizó el tratamiento con dieta DUAL de 10 semanas para la depleción de la microbiota utilizando una combinación de antibióticos que se administró: a) en el agua de bebida durante las últimas 4 semanas de tratamiento; b) mediante la administración por sonda oral durante los últimos 10 días de la dieta DUAL.

4. Se realizaron modulaciones terapéuticas de la microbiota a través de a) la aplicación de probióticos VSL#3 (mezcla de bacterias liofilizadas a alta concentración) o b) el trasplante de microbiota de ratones donantes sanos a ratones enfermos (alimentados con dieta DUAL) durante las 4 últimas semanas de tratamiento. El impacto sobre el hígado y el intestino de ambos procedimientos fue evaluado.

5. La capacidad terapéutica de los cambios dietéticos en la regresión de la esteatohepatitis y la fibrosis inducida por la dieta DUAL en ratones alimentados con la misma durante 10 y 23 semanas, seguido de su sustitución por una dieta con agua y comida normal durante 21 días, fue estudiada.

Resultados

Los ratones alimentados con dieta DUAL aumentaron rápidamente su peso corporal. Simultáneamente desarrollaron hiperglucemia e hipercolesterolemia en estado de ayuno, daño hepático significativo, esteatosis junto con cambio de morfología de los hepatocitos (*ballooning*), inflamación e infiltración de células inmunes en el parénquima hepático y fibrosis tras 23 semanas de dieta DUAL. Tras 52 semanas presentaban cirrosis y el desarrollo de micronódulos en la superficie hepática.

La dieta DUAL indujo cambios macroscópicos y microscópicos en colon. Además, provocó inflamación, y extenso daño en el intestino que afectó

enormemente a la integridad de las barreras intestinales, induciendo así un aumento de la permeabilidad intestinal. Asimismo, se identificó una profunda disbiosis intestinal en los ratones del grupo DUAL perfectamente comparable a la observada en pacientes con enfermedad hepática crónica de etiología dual.

A continuación, se procedió al uso de antibióticos para la depleción de la microbiota. Como consecuencia, se observó una mejora de la permeabilidad intestinal, así como del fenotipo hepático y una reducción de la endotoxemia. Por tanto, demostramos que el daño hepático inducido por la dieta DUAL estaba principalmente mediado por la microbiota intestinal.

b) El trasplante de microbiota de un donante sano indujo una mejora leve en la fisiología hepática e intestinal sólo frente a los daños causados por la alimentación a corto plazo con dieta DUAL de 10 semanas. Los daños causados por la alimentación a largo plazo resultaron prácticamente irreversibles haciendo uso del trasplante de microbiota.

El remplazo de la dieta DUAL por dieta y agua estándar fue la mejor opción terapéutica para la enfermedad hepática crónica temprana inducida por la alimentación DUAL a corto plazo. Sin embargo, la sustitución de la dieta DUAL solo indujo una pequeña mejora de la esteatohepatitis y la fibrosis hepática cuando se aplicó sobre el tratamiento con dieta DUAL a largo plazo.

Conclusión

El modelo múrido DUAL reprodujo con éxito el daño hepático, incorporando los principales factores de riesgo presentes en la condición humana, como el consumo de alcohol, la obesidad y el síndrome metabólico, incluyendo estadios más avanzados, como la fibrosis, cirrosis y cáncer hepático.

El acusado daño sobre el colon, la inflamación, el deterioro de la barrera intestinal, el aumento de la permeabilidad y la disbiosis encontrada en los ratones DUAL es muestra de la activación del eje intestino-hígado y revela el papel de la microbiota en el desarrollo de la enfermedad. Las intervenciones terapéuticas tempranas basadas en su modulación podrían ser beneficiosas para detener el desarrollo de la enfermedad hepática crónica de etiología dual.

En conjunto, el nuevo modelo DUAL puede considerarse una herramienta útil, ya que imita los principales aspectos de la enfermedad hepática crónica a nivel

sistémico, pudiendo contribuir así al desarrollo de nuevas dianas terapéuticas y tratamientos que resultan más que necesarios.

1.2. ABSTRACT

Introduction and aims

Around 844 million people worldwide suffer from chronic liver disease (CLD) resulting in approximately 2 million deaths per year. Nowadays, alcohol and overweight/obesity are the leading causes of CLD in Western countries. Due to the high prevalence, the presence of both conditions in the same individual is highly plausible and known as "both alcoholic and non-alcoholic steatohepatitis" (BASH).

The central role of the liver in alcohol and lipid metabolism sets it as one of the most damaged organs in BASH. However, recent evidence showed that CLDs are mainly systemic and induce white adipose tissue (WAT) failure, insulin resistance (IR), changes in gut permeability and intestinal microbiome dysbiosis. Moreover, gut-liver axis has been recently described as one key contributor in CLD pathophysiology. Despite this, BASH remains an area not well explored, and it has a great importance given the increasing number of patients affected.

Therefore, the main aim of our study was to develop an innovative experimental mouse model which resembles the compound effects of alcohol and western diet (WD) and closely mimics human pathogenesis. In addition, we aimed to characterize the relevance of the liver-gut-microbiome crosstalk in order to define potential therapeutic circuits.

Methods

For our experiments we fed 10-week-old C57Bl/6J Wt mice with DUAL diet that was composed by WD and 10% of alcohol in sweetened (6.75% D-glucose) drinking water for 10, 23 and 52 weeks. Single feedings with WD, 10% alcohol or chow diet/normal water were used as controls.

1. Liver histology in terms of steatosis, inflammation, fibrosis, and HCC was characterized. Moreover, metabolic, inflammatory, and fibrotic pathways in liver were further defined by metabolome, proteomic and transcriptomic studies.

2. Gut physiology, intestinal barrier and permeability were studied; 16s rRNA microbiome profiling performed and compared to a cohort of BASH patients.

3. Short-term feeding (10 weeks) was used for antibiotic-induced microbiota-depletion (AIMD) using a cocktail of antibiotics which was administered: a) in the drinking water during the last 4 weeks of feeding; or b) by oral gavage during the last 10 days of DUAL diet.

4. Therapeutic modulations of microbiome were performed by a) application of VSL#3 probiotics (high-concentrated mixture containing freeze-dried bacteria), or b) Fecal microbiome transplantation (FMT) from healthy donor mice, performed the last 4 weeks of short- and long-term feeding period.

The safety, tolerability, and impact of both methods on liver and gut phenotypes were determined.

5. The therapeutic impact of dietary changes on the regression of DUAL- induced steatohepatitis and fibrosis was performed in mice fed with DUAL diet for short (10 weeks) and long (23 weeks) period followed by the replacement with chow diet and normal water.

Results

DUAL fed mice rapidly increased their body weight during the treatment period. Simultaneously to obesity, animals developed basal hyperglycemia and hypercholesterolemia, significant liver damage, micro- and macrovesicular steatosis with hepatocytes ballooning, inflammation, and immune cell infiltration into the hepatic parenchyma. Already after 23 weeks of feeding, DUAL diet fed mice exhibited advanced accumulation of collagen in portal and bridging areas. 52-week DUAL feeding induced cirrhosis and the development of single or multiple micronodules on the liver surface.

DUAL feeding induced prominent macroscopical and microscopical changes in the colon. Moreover, DUAL feeding induced significant colonic inflammation and intensive intestinal cell death was not compensated by proliferation, and as a result the gut barriers were prominently affected and permeability was increased. Importantly, the intestinal dysbiosis induced by DUAL diet was highly comparable to those identified in BASH patients.

Next, we performed antibiotic-induced microbiota-depletion (AIMD) and confirmed that antibiotic cocktail improved permeability, reduced endotoxemia and attenuated the hepatic phenotype in DUAL mice. Thus, we proved that the

phenomenon of DUAL induced liver damage was primarily mediated by gut microbiota.

The microbiome modulation showed that a) The use of probiotics in short-term DUAL feeding did not exert any remarkable benefit in terms of obesity, hepatic steatosis, inflammation or liver fibrosis. Analogously, no notable improvements were detected in the intestine of DUAL mice. b) FMT from healthy donors induced mild improvement in liver and gut physiology, but only in short-term DUAL feeding.

DUAL diet withdrawal was the best therapeutic option for early CLD induced by short-term feeding of 10 weeks. Nevertheless, after the long-term DUAL feeding, the diet replacement only resulted in a slight improvement of steatohepatitis and fibrosis in the liver.

Conclusion

Overall, DUAL preclinical murine model successfully induced liver damage by incorporating key risk factors present in the human condition such as alcohol consumption, obesity, and metabolic syndrome (MS). It naturally mimics the progression of human pathology, including advanced liver fibrosis, cirrhosis and end-stage tumorigenesis.

Strong colonic damage, inflammation, impairment of barriers, increased gut permeability and intestinal dysbiosis in DUAL mice point to the activation of gut-liver axis and thus reproduce systemic pathophysiology of CLD. Microbiota plays the principal role for the activation of the gut-liver axis and for induction of DUAL-phenotype. Gut-based early therapeutic interventions could be beneficial to halt development of BASH.

Altogether, the innovative DUAL model can be a valuable toolbox, as it mimics the main features of human CLD, thereby contributing to the development of very much needed therapeutic targets.

Abbreviations

2. ABBREVIATIONS

4-HNE	4-Hydroxinonenal
ABX	Antibiotics
ACC	Acetyl-CoA carboxylase
ADH	Alcohol dehydrogenase
AIMD	Antibiotic-induced microbiota-depletion
ALD	Alcohol-related Liver disease
ALDH2	Aldehyde dehydrogenase 2
ALT	Alanine aminotransferase
AMP	Adenosine monophosphate
AMPK	AMP-activated kinase
AP	Alkaline phosphatase
ApoB100	Apoprotein B100
ASH	Alcoholic steatohepatitis
AST	Aspartate aminotransferase
ATP	Adenosine triphosphate
BA	Bile acid
BASH	Both alcoholic and non-alcoholic steatohepatitis
BMI	Body mass index
BSEP	Bile salt export pump
CA	Cholic acid
CC3	Cleaved caspase 3
CDCA	Chenodeoxycholic acid

CLD	Chronic liver disease
CPT-1	Carnitine palmitoyltransferase-1
CPT-2	Carnitine palmitoyltransferase-2
DAMPs	Damage-associated molecular patterns
DC	Dendritic cell
DEN	Diethylnitrosamine
DG	Diacylglycerides
DNL	*De novo* lipogenesis
ECM	Extracellular matrix
ER	Endoplasmic reticulum
EtOH	Ethanol
FASN	Fatty acid synthase
FATP	Fatty acid transport protein
FC	Free cholesterol
FFA	Free fatty acid
FMT	Faecal microbiota transplantation
FXR	Farnesoid X receptor
GALT	Gut-associated lymphoid tissue
GCA	Glycocholic acid
GPAT	Glycerophosphate acyltransferase
GPLs	Glycerophospholipids
GTT	Glucose tolerance test
GVB	Gut vascular barrier
H&E	Hematoxylin and eosin

HCC	Hepatocellular carcinoma
HSCs	Hepatic stellate cells
IBD	Inflammatory bowel disease
ICAM-1	Intercellular adhesion molecule-1
IEC	Intestinal epithelial cell
IF	Immunofluorescence
IGF-1	Insulin-like growth-factor-1
IHC	Immunohistochemistry
IL	Interleukin
INF	Interferon
IP	Intraperitoneal
IR	Insulin resistance
ITT	Insulin tolerance test
JAMs	Junctional adhesion molecules
KCs	Kupffer cells
LDH	Lactate dehydrogenase
LPS	Lipopolysaccharide
LSECs	Liver sinusoidal endothelial cells
MAMPs	Microorganism-associated molecular patterns
MCP-1	Monocyte chemoattractant protein-1
MLC	Myosin regulatory light chain
MMPs	Metalloproteinases
MNL	Mesenteric lymph nodes
MS	Metabolic syndrome

MUC2	Mucin-2
MUFA	Monounsaturated fatty acid
NAFLD	Non-alcoholic fatty liver disease
NASH	Non-alcoholic steatohepatitis
NEFA	Non-esterified fatty acids
NF-κB	Nuclear factor kappa B
NK	Natural killer
NKT	Natural killer T
NLR	NOD-like receptor
ORO	Oil red O
OTU	Operational taxonomic units
PAMPs	Pathogen-associated molecular patterns
PC	Phosphatidylcholine
PCA	Principal component analysis
PCNA	Proliferating cell nuclear antigen
PDGF	Platelet-derived growth factor
PE	Phosphatidylethanolamine
PEMT	Phosphatidylethanolamine N-methyltransferase
PFA	Paraformaldehyde
PGN	Peptidoglycan
PP	Peyer’s patches
PPAR γ	Peroxisome proliferator-activated receptor γ
PRRs	Pattern recognition receptors
PUFA	Polyunsaturated fatty acid

PV-1	Plasmalemma vesicle-associated protein-1
ROS	Reactive oxygen species
RT-qPCR	Quantitative real-time polymerase chain reaction
SCD-1	Stearoyl-Coenzyme A desaturase 1
SCFA	Short chain fatty acid
SFAs	Saturated fatty acids
SID	Selective intestinal Decontamination
SILT	Solitary intestinal lymphoid tissue
SR	Sirius red
SREBP	Sterol regulatory element binding protein
T2DM	Type 2 diabetes mellitus
TBS	Total bile salt
TCA	Tricarboxylic acid cycle
TCR	T-cell receptor
TEM	Transmission electron microscopy
TG	Triglycerides
TGF-β1	Transforming growth factor-β1
TGR5	G protein-coupled receptor
TJs	Tight junction
TLCA	Taurolithocholic acid
TLR	Toll-like receptor
TNFR1	Tumor necrosis factor receptor 1
TNF-α	Tumor necrosis factor-α
TUNEL	Terminal deoxynucleotidyl transferase dUTP Nick end labeling

VCAM-1	Vascular cell adhesion molecule-1
VLDL	Very low-density lipoproteins
WAT	White adipose tissue
WB	Western blot
WD	Western diet
ZO	Zona occludens

Introduction

3. INTRODUCTION

3.1. ANATOMY AND PHYSIOLOGY OF THE LIVER

The liver is the largest gland and organ in the body that performs multiple functions. In human adults it weighs 1.5 kg which comprises approximately 2.5% of the overall body weight (1, 2), whereas in mice it ranges from 3-5% (3). It is located beneath the right and partially left parts of the diaphragm and is surrounded by a fibrous layer named Glisson's capsule. The liver consists of four lobes – two major lobes which are the right and the left lobes, and two smaller ones called the caudate and the quadrate (1).

It is characterized as having a dual blood supply: the intestinal and central circulation. The vena porta brings oxygen-poor blood containing nutrients, toxins, and microorganisms from the gastrointestinal tract and spleen to the liver. The oxygenated blood from the central circulation is carried to the liver by the hepatic artery (4).

These two blood supplies irrigate the portal triad area of the liver and pass through the hepatic sinusoids, which serve as a filtration system, to reach the central vein, allowing the optimal exchange of necessary molecules for liver metabolism (5). The hepatic vein drains blood from the central vein and carries it to the inferior vena cava.

The bile, a product of liver metabolism, flows across the biliary system to the hepatic duct and can be stored in the gallbladder. Blood and bile fluxes circulate in opposite directions in the liver (6) **(Fig. 1).**

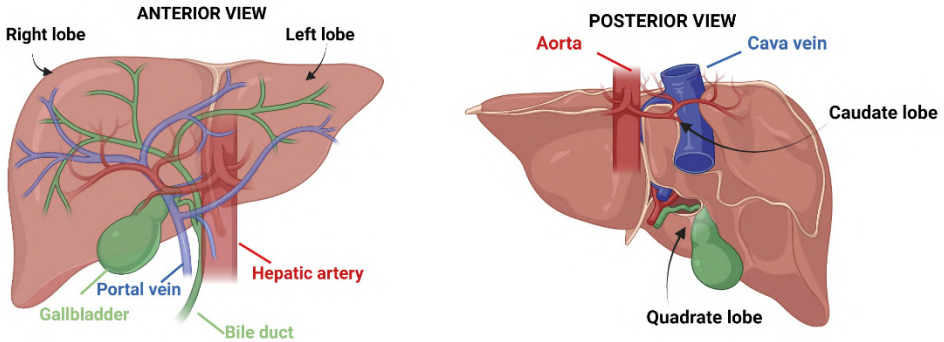

Fig. 1. Liver anterior and posterior view. Anatomically the liver has 4 major lobes. The right and left visible from the anterior view and quadrate and caudate lobe distinguished from the posterior view. Blood and bile flow are represented. Figure created with BioRender.com.

3.2. LIVER FUNCTIONS

Liver functions are crucial for the survival of humans and mammals. The liver is one of the master contributors in maintaining glucose homeostasis. It stores glucose in the form of carbohydrates (glycogen). When basal glucose levels are compromised, through glycogenolysis and gluconeogenesis, it can release glucose to the bloodstream. In addition, the excess of carbohydrates is converted into fatty acids by the liver. Besides, the oxidation of fatty acids is one of the regulators of energy (7).

Liver has an exocrine function (bile production that is stored in the gallbladder and released for digestion of fats and fat-soluble vitamins) and endocrine function (it secretes hormones such as Insulin-Like Growth-Factor-1 (IGF-1)) (7).

One of the most important metabolic functions of the liver is its detoxifying capacity. It can metabolize, neutralize, and eliminate alcohol, drugs, xenobiotics and chemicals (7).

Moreover, the liver controls other physiological processes such as the metabolism of proteins (plasma proteins, hormones, carrier proteins, clotting factors and fibrinolysis), regulation of blood clotting and blood flow, storage of vitamins and minerals, etc. (7).

3.3. THE IMPORTANCE OF LIVER STRUCTURE IN MAINTAINING LIVER FUNCTIONS

Microscopically the liver is highly organized. The acinus is the functional and structural unit of the liver. The hepatic lobule forms the acinus, which is a polyhedral hexagonal structure surrounded by conjunctive tissue, sinusoids and biliary. The central vein is located in the middle of the lobule, and the portal vein, hepatic artery and biliary tracts are placed at the vertices, integrating the portal triad (8) **(Fig. 2).**

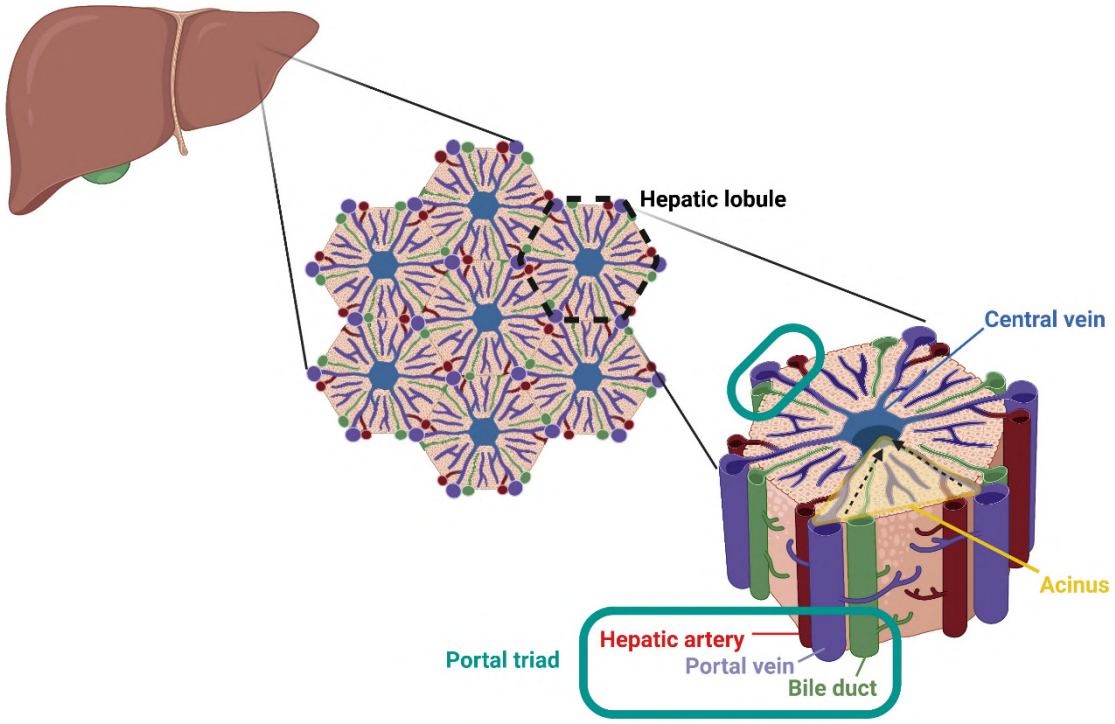

Fig. 2. Microscopical organization of the liver. Hepatic lobule and centripetal disposition of acinus is highlighted. Central vein and portal triad composed by the hepatic artery, the portal vein and the bile duct are represented. Figure created with BioRender.com.

Blood flow in each acinus is centripetal, from the portal triad toward the central vein, and the acinus is divided into three areas according to the Rappaport model (9). The hepatocytes are the primary cell type found in the liver and are responsible for metabolic functions. The location of hepatocytes in the lobule determines their metabolic function. Periportal hepatocytes have a higher level of activity in terms of catabolism, oxidation, and detoxification due to their exposure to high concentrations of nutrients, oxygen, and toxins; meanwhile, hepatocytes close to central area accomplish anabolic functions (10) **(Fig. 3).**

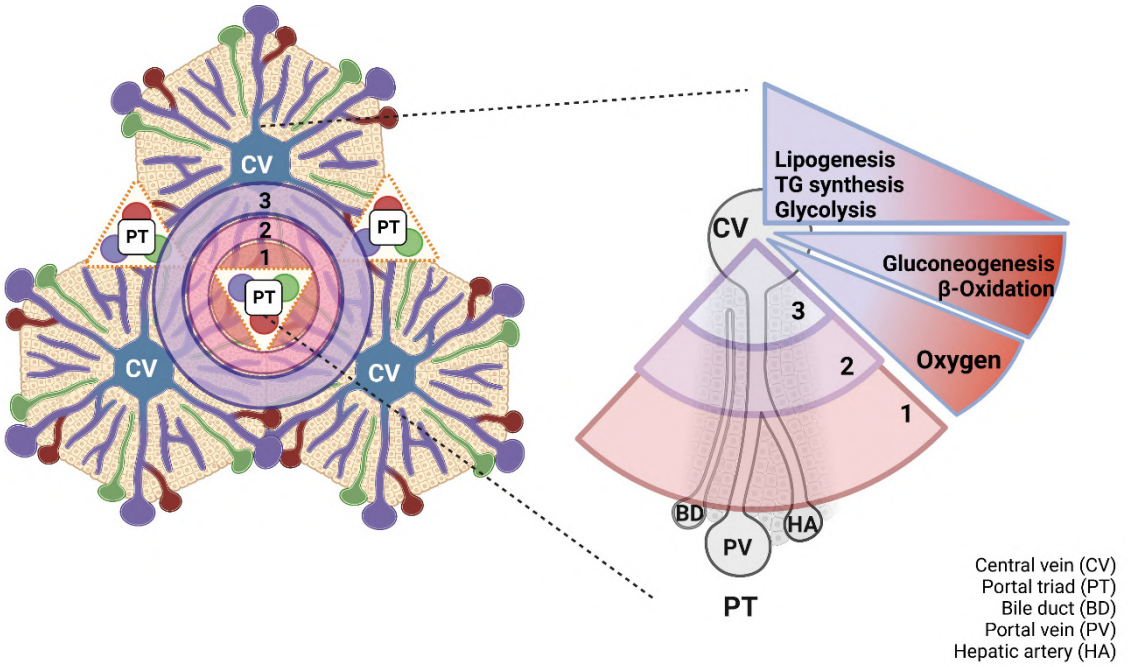

Fig. 3. Centripetal blood flow in each acinus. Blood goes from portal triad to central vein. Acinus is divided in three areas according to the oxygen concentration. Near the portal triad, oxygen concentration is higher, and hepatocytes are specialized in catabolic and oxidative functions, whereas the central vein area is specialized in anabolic activities (Rappaport model). Bile flows in the opposite direction, towards the bile duct. Kietzmann T. Metabolic zonation of the liver: The oxygen gradient revisted. Redox Biol. 2017. (11): 622-630. https://doi.org/10.1016/j.redox.2017.01.012) Figure created with BioRender.com.

3.4. CELLS IN THE LIVER

The liver can be characterized not only by functional heterogeneity, but also by cellular heterogeneity **(Fig. 4)**. Most of the liver mass (80%) is comprised of hepatocytes, which are parenchymal cells. Hepatocytes are radially disposed in the liver lobule separated from the bloodstream by a layer of endothelial cells. This structure creates an open space known as Space of Disse.

Moreover, in the liver we find cholangiocytes, epithelial cells that form the intrahepatic and extrahepatic bile ducts.

The remaining 20% of cells are non-parenchymal cells, including (8):

- Endothelial sinusoidal cells (LSECs): They surround the sinusoidal space and have pores in their cytoplasm that allow blood to flow around the hepatocytes (11).

- Kupffer cells (KCs): Macrophages that belong to the mononuclear phagocytic system. KCs are attached to the endothelium and extend processes into Disse's space. They are activated in response to pathogenic substances or liver cell injury. When activated, they produce pro-inflammatory cytokines and reactive oxygen species (ROS) that, in turn, can activate hepatic stellate cells (HSCs) and remodel the extracellular matrix (ECM) (12).
- HSCs are located in the Space of Disse. They mainly store lipids and vitamin A. Under physiological healthy conditions they maintain a non-proliferative, quiescent phenotype. However, after liver damage, HSCs transdifferentiate into myofibroblasts, becoming star-shaped cells which proliferate and exert chemotactic properties. Diet, alcohol and toxic compounds lead to the activation of KCs, which release cytokines and chemokines that directly affect HSCs triggering the fibrogenic process (13).
- Liver oval cells are small cells found in the biliary ductules (canals of Hering) which are considered to be bipotential progenitor cells in adult livers and are capable of generating hepatocytes and bile duct cells after severe liver damage (14).

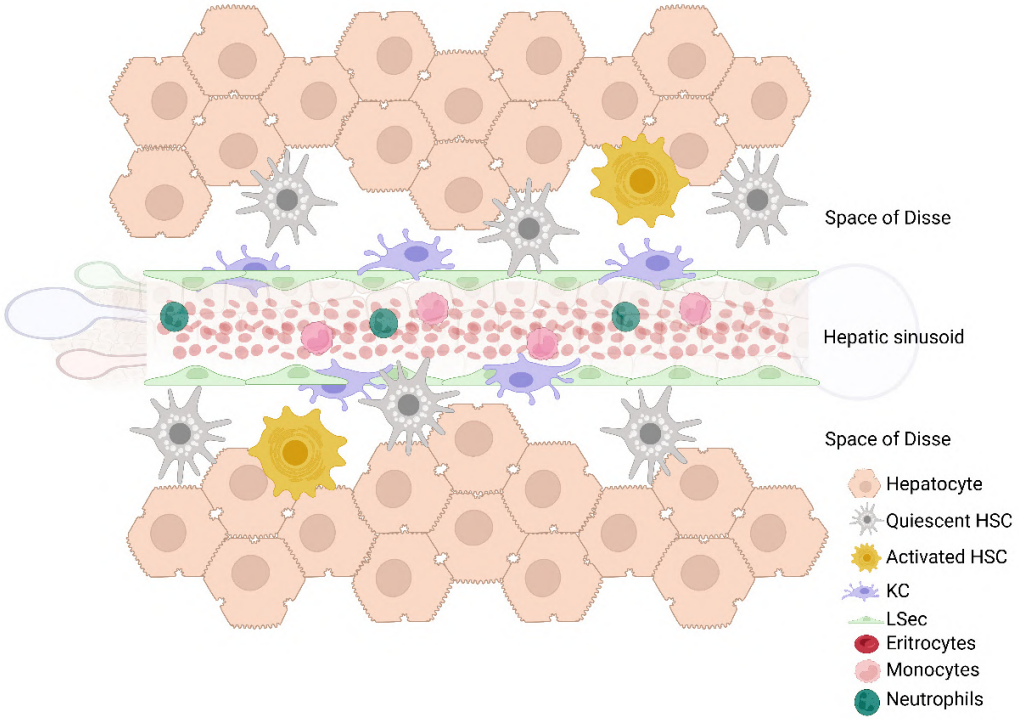

Fig. 4. Cells in the liver. Types and location. Figure created with BioRender.com.

3.5. LIPID METABOLISM IN THE LIVER

The liver plays a crucial role in lipid metabolism. The metabolic pathways involved in lipid metabolism are interconnected and regulated in a cross-dependent manner (15) **(Fig. 5)**.

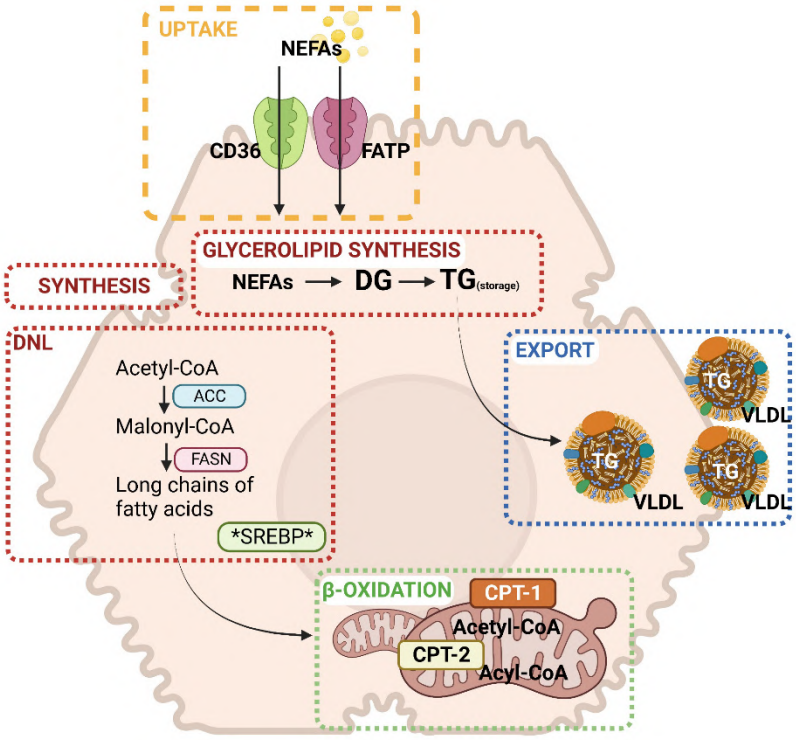

Fig. 5. Lipid metabolism in the liver. Main uptake, synthesis, oxidative and export pathways are highlighted. Uptake: NEFA are captured from the bloodstream through CD36 and the Fatty Acid Transport Protein (FATP). Synthesis: NEFA can be esterified or added combined to glycerol to form glycerolipids. Lysophosphatidate is formed by the enzyme GPAT, DG by the lysophosphatidate acyltransferase, and TG through the diacylglycerol acyltransferase. TG can be stored in the liver or exported to other organs. Hepatic *de novo* lipogenesis (DNL) is activated under high energy fuel conditions. AcetylCoA is the precursor of MalonylCoA, process carried by the enzyme acetyl-CoA carboxylase (ACC). Then, long chains of fatty acids are formed and FASN and SREBP take part in the process. Oxidation is activated under low energy fuel conditions. Long chain fatty acids are oxidized in the mitochondria by CPT-1 and CPT-2. AcetylCoA formed by CPT-1 activity can be oxidized in the TCA cycle. The liver can export lipids to other tissues through VLDL formation. Figure created with BioRender.com.

3.5.1. Fatty acid uptake

Non-esterified fatty acids (NEFAs) can arise from the hydrolysis of complex lipids by lipases or the hydrolysis of fatty acid-CoA by thioesterases. NEFA from the blood enter liver cells via the fatty acid transport protein (FATP) or the fatty acid

translocase (CD36) or simply diffusion. NEFA uptake is proportional to the bloodstream fat concentration (15).

Within the hepatocytes, the destiny of these fatty acids can be towards the synthesis of more complex fatty acids such as diacylglycerides (DG) or triglycerides (TG) or towards oxidative processes. TGs are the main form of lipid storage in the liver from DG. Meanwhile, DG not only act as precursor of TG, but also of other lipid compounds such as phosphatidylcholine (PC) and phosphatidylethanolamine (PE), but also can act as a signaling molecule that has been described to lead to lipotoxicity and to play a role in insulin resistance (IR) (16, 17).

3.5.2. De novo synthesis of fatty acids

Hepatic *de novo* lipogenesis (DNL) is the biochemical process of synthesizing fatty acids from acetyl-CoA subunits coming from different metabolic pathways in the liver (18). DNL plays a significant role in regulating energy levels. The production of lipids is closely regulated by both hormonal and nutritional factors. In general, diets high in carbohydrates encourage DNL, whereas fasting or consuming high amounts of fats, inhibits it. Insulin levels and tissue's insulin sensitivity are critical factors that influence this process (15).

In humans and rodents, the liver, and the white adipose tissue (WAT) are the two major tissues involved in fat synthesis. Under high energy condition or post-prandial signals (insulin induced by dietary carbohydrates) signals, DNL is activated in the liver. Very low amounts of TG are stored in the liver. Most of them are exported to other tissues (including the WAT) through very low-density lipoproteins (VLDL) providing not only an energy source but also components for membrane building. Meanwhile, fatty acid synthesis in WAT generates a long-term energy reservoir (15, 19).

Fatty acid synthesis can be summarized by the addition of carbons to a primer chain composed by Acetyl-CoA which is subsequently extended to malonyl-CoA by the acetyl-CoA carboxylase (ACC), the limiting step in this pathway, and finally derives to long chains of fatty acids (20).

The rate of fatty acid synthesis is strongly linked to the activity of the fatty acid synthase (FASN), which is a multifunctional enzyme responsible for facilitating the entire process of palmitate synthesis (21).

The regulation of lipogenic gene expression by insulin and fatty acids is mainly mediated by transcription factors, such as sterol regulatory element binding proteins (SREBPs) (22).

3.5.3. Glycerolipid synthesis

Most NEFA in mammalians can be esterified into phospholipids and incorporated into membranes or lipoprotein capsules. When NEFA levels are overloaded, they are combined with glycerol to form glycerolipids. In this process, Acyl-CoA chains are transferred one after the other to glycerol-3-phosphate to form lysophosphatidate, DG and TG. The enzymes that regulate these steps are the glycerophosphate acyltransferase (GPAT), lysophosphatidate acyltransferase and diacylglycerol acyltransferase (23).

Hence, TGs act as a storage pool in a context of excess of energy, high adenosine triphosphate (ATP). In this context, SREBP-1c and the Peroxisome proliferator-activated receptor γ (PPARϒ) overexpression, among other transcription and nuclear factors, enhances the activity of FASN and GPAT.

In contrast, when energy fuel is low (low ATP – high adenosine monophosphate (AMP)), (AMP)-activated kinase (AMPK) increases the acyl-CoA flux into the pathway of β-oxidation mainly controlled by the enzyme carnitine palmitoyltransferase-1 (CPT-1) while simultaneously inhibits GPAT activity and TG synthesis (15).

3.5.4. Fatty acid oxidation

Non-esterified acyl-CoA may be oxidized, either in the mitochondria or peroxisomes. Mitochondrial oxidation may be either complete or incomplete.

3.5.4.1. Intramitochondrial oxidation

β-Oxidation pathways result in the formation of acetyl-CoA. During this process electrons are transferred in last place to the electron transport chain to drive ATP synthesis. The acetyl-CoA can be oxidized completely to carbon dioxide in the tricarboxylic acid cycle (TCA) (15).

The enzyme CPT-1 plays a crucial role in β-oxidation, thus, it regulates the entry of 14C or longer fatty acids into the mitochondria. This enzyme is integrated in the outer mitochondrial membrane and its function is to convert fatty acids to acyl-carnitine molecules that can be transported across the mitochondrial membrane. Once inside the mitochondrial matrix, the acyl-carnitine molecules are reconverted to acyl-CoA by Carnitine palmitoyltransferase-2 (CPT-2).

The activity of CPT-1 is inhibited by Malonyl-CoA, the first product of fatty acid *de novo* synthesis (23, 24).

3.5.4.2. Peroxisomal and microsomal oxidation

While short, medium, and long chain fatty acids are oxidized by mitochondrial β-oxidation, very long chain fatty acids metabolism is performed by peroxisomes.

The initial step is dehydrogenation plus an oxidative reaction catalyzed by acyl-CoA oxidase, leading to the production of H_2O_2 instead of reduced NAD^+. Additionally, peroxisomes lack an electron transport chain, resulting in lower ATP production compared to mitochondrial β-oxidation. However, this pathway copes in a context of high fatty acid content (15, 25).

Moreover, very long chain fatty acids can also be metabolized by the cytochrome P450 CYP4A ω-oxidation system to dicarboxylic acids. These acids cannot be readily metabolized by mitochondria but are the preferred substrate for the peroxisomal β-oxidation pathway. The induction of this system would be an adaptive response by the hepatocyte to maintain cellular lipid homeostasis (15, 25).

3.5.4.3. Ketogenesis

When there is an increase in the uptake of fatty acids, the liver often produces significant amounts of acetoacetate and β-hydroxybutyrate, known as ketone bodies. This process is called ketogenesis, and it is intensified during times of increased NEFA uptake, when low insulin levels activate CPT-1, allowing for the extensive uptake of fatty acids into mitochondria (15).

3.5.5. TG export (VLDL synthesis and secretion)

TG can be exported from the liver to other tissues by VLDL. They are mainly composed of apoprotein B100 (ApoB100) that is generated in the endoplasmic

reticulum (ER) in the hepatocytes and controls VLDL product. Lipid components are also added to the VLDL by the microsomal triacylglycerol transfer protein (23).

3.6. NON-ALCOHOLIC FATTY LIVER DISEASE (NAFLD)

NAFLD refers to the accumulation of fat in the liver that occurs in the absence of significant alcohol consumption. The dietary habits (high consumption of refined sugars and carbohydrates and high-fat food content) as well as genetics, and digestive disorders, play a fundamental role. Some of the risk factors for NAFLD include overweight or obesity, type 2 diabetes mellitus (T2DM) or insulin resistance (IR), and dyslipidemia, which are traits associated with metabolic syndrome (MS) (26).

The pathogenesis of obesity related to NAFLD begins when an excess of lipids and energy is stored in the liver. Hepatic steatosis in NAFLD is triggered by excessive TG synthesis in hepatocytes, from substrate lipids coming from diet, WAT and DNL (27). Massive lipid accumulation in the liver leads to an imbalance of lipid metabolism inducing ER stress, mitochondrial dysfunction and, ultimately, cell death that subsequently causes chronic inflammation and extended liver damage.

3.7. ALCOHOLIC RELATED LIVER DISEASE

Similarly, chronic alcohol consumption is one of the leading causes of chronic liver disease (CLD). Alcohol-related liver disease (ALD) is a major cause of alcohol related morbidity and mortality through cirrhosis, liver cancer and acute and chronic liver failure. The liver is considered the most affected organ in cases of ALD due to its crucial role in alcohol metabolism (28, 29).

3.8. ALCOHOL METABOLISM IN THE LIVER

The liver is responsible for eliminating around 90% of alcohol from the body, with only a small percentage being removed by the kidneys and lungs. This is because the liver has a high concentration of enzymes that are involved in breaking down alcohol.

Alcohol dehydrogenase (ADH) is the primary enzyme responsible for converting ethanol into a toxic by-product, the acetaldehyde. NAD+ is used as a cofactor during this reaction, altering redox cell balance (30).

Cytochrome P450 isozymes, including CYP2E1, 1A2 and 3A4, are found mainly in microsomes and are also involved in alcohol metabolism. Although CYP2E1 can bind more ethanol than ADH, its catalytic efficiency is slower (31).

Acetaldehyde is a toxic intermediate metabolite from ethanol, and it can lead to a variety of toxic, pharmacological, and behavioral responses. It is subsequently converted into acetate by aldehyde dehydrogenase (ALDH2) in the mitochondria and can be transported in the blood to be used as an energy source of peripheral tissues (31, 32). Although acetaldehyde is a short-life compound, its damage relies in the inducement of mitochondrial dysfunction that, in turn, compromises acetaldehyde metabolism, leading to a vicious cycle. Damage interferes with the structure and function of proteins and enzymes in the body, leading to metabolic dysfunction in the liver.

Alcohol has direct effects on fatty acid uptake, contributing to WAT lipolysis and can increase the supply of intestine-derived fatty acids from chylomicrons (33).

Moreover, among other effects, alcohol metabolism produces high levels of NADH. The decreased redox potential of the cell induces an inhibition in the lipid oxidation, contributing to fat accumulation in the liver (33).

Additionally, alcohol exposure modulates many of the lipid regulatory factors and lipogenic enzymes, and, in doing so, augments hepatic TG accumulation. In terms of export, it has been described that alcohol is able to impair VLDL assembly and secretion (34).

Altogether, alcohol metabolism would trigger steatosis, which involves the buildup of fat in the liver. This condition is observed in around 90% of alcoholics and has been described as one of the first signs of ALD. However, prolonged alcohol abstinence reverses hepatic steatosis (35).

Lipid accumulation in the liver would induce oxidative stress and liver damage, leading to a more extreme inflammatory stage known as alcoholic steatohepatitis (ASH). Steatohepatitis is a more severe stage and increases the risk of cardiovascular complications, cancer and liver-related mortality (36) **(Fig. 6).**

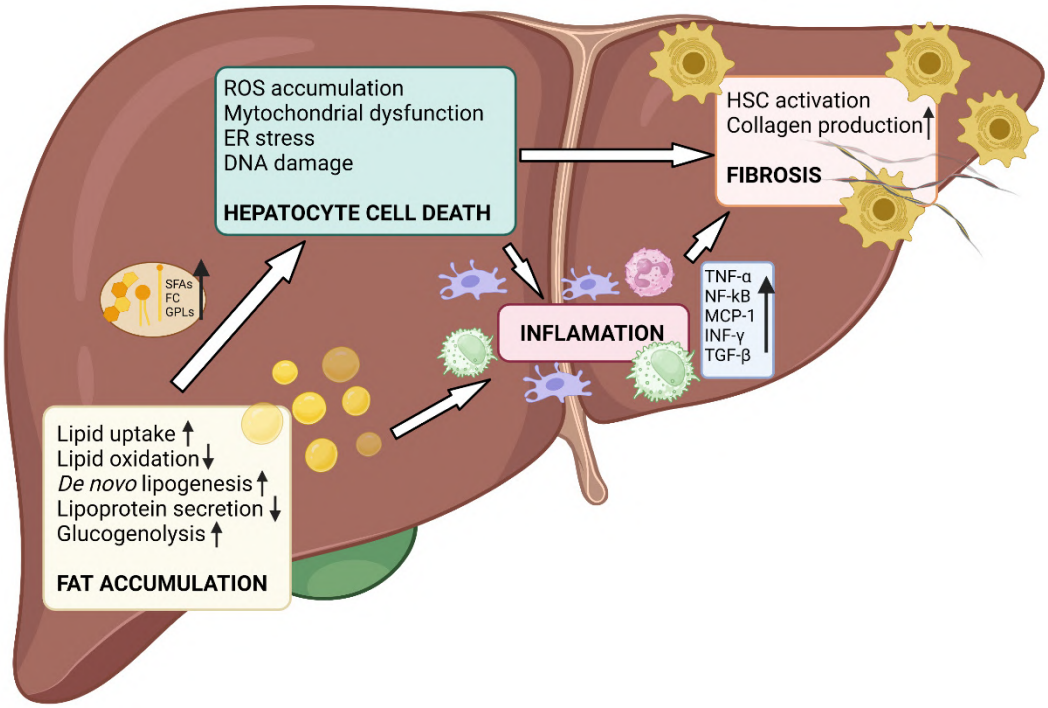

Fig. 6. CLD pathogenesis of NAFLD and ALD. Fat accumulation is triggered by an imbalanced lipid metabolism inducing hepatocyte cell death and inflammation. Prolonged damage and chronic inflammation lead to HSC activation and fibrosis. Figure created with BioRender.com

3.9. FURTHER STAGES OF ALD AND NAFLD

The excessive buildup of fat in the liver is the cause and consequence of lipid metabolism disruption, described by an imbalance between lipolysis, lipid uptake, lipogenesis, lipid oxidation and export. Although not all lipids are toxic, some of them, such as saturated fatty acids (SFAs), free cholesterol (FC), glycerophospholipids (GPLs) and sphingolipids, cause cellular injury and promote cell death (37). ER stress and mitochondrial dysfunction induced by massive lipid accumulation are key factors in the development of lipotoxicity and cell death (38).

Subsequently, the activation of hepatic cell death can activate a proinflammatory response driven by Tumor Necrosis Factor Receptor 1 (TNFR1) signaling that results in transcription of a wide spectrum of genes involved in the inflammatory response, such as proinflammatory cytokines, via transcription factor nuclear factor kappa B (NF-κB) (39).

Liver inflammation in ASH and Non-alcoholic Steatohepatitis (NASH) is orchestrated by multiple intricate mechanisms and its complex nature is not fully understood. Healthy livers encompass many types of immune cells such as resident macrophages (KCs), natural killer (NK) cells and natural killer T (NKT) cells. Chronic activation of innate immune system is fundamental in the development of steatohepatitis. Scientific evidence suggests that KCs, infiltrating macrophages and monocytes play a fundamental role in the development of the disease, leading to more severe stages. Secreted chemokines, such as monocyte chemoattractant protein-1 (MCP-1), apart from contributing to hepatocyte cell death, recruit neutrophils and cells of monocyte/macrophage lineage to the liver, boosting liver inflammation. Moreover, NKT cells have been described to accumulate with the progression of the disease. Besides, adaptive immunity has been described to be activated in NAFLD. In most studies, it results in a reduction in the number of intrahepatic CD4- but not CD8- T cells, as well as an increase in the production of interferon (INF)-γ, interleukin (IL)-17 and ROS in intrahepatic T cells (40).

Activated KCs, infiltrating macrophages/monocytes, injured hepatocytes and T-cells release chemokines and cytokines such as platelet-derived growth factor (PDGF) and transforming growth factor-β1 (TGF-β1), among others, thereby activating HSCs and changing their phenotype into myofibroblast-like cells, consisting in an essential step in the development of hepatic fibrosis (41, 42).

Active HSCs are the responsible of ECM deposition (43). ECM accumulation damages the liver's natural architecture and disrupts cellular homeostasis, leading to liver dysfunction. Persistent injury leads to further activation of HSCs, resulting in excessive production and accumulation of ECM. Immune cells such as macrophages are attracted to the injury site and further activate HSCs, playing a key role in regulating fibrosis progression through the production of profibrogenic cytokines and metalloproteinases (MMPs) (44).

As liver fibrosis progresses to cirrhosis, portal hypertension, and hepatic failure, the composition of the ECM changes, affecting the functions of the surrounding cells, including immune cells and HSCs, leading to phenotypic and functional switches. The pathological features of CLD, including fibrosis, inflammation, oxidative stress, and hepatocyte regeneration, create a favorable environment to tumor growth and the development of hepatocellular carcinoma (HCC) (45) **(Fig. 7).**

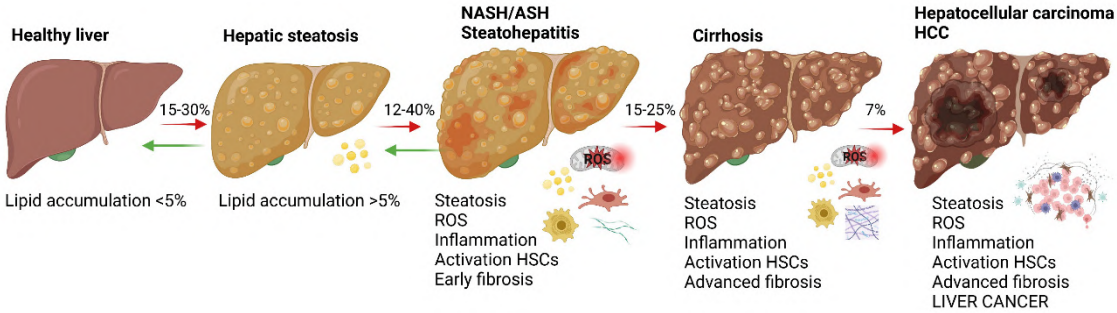

Fig. 7. NAFLD and ALD disease progression. Classical stages of NAFLD and ALD development are simple steatosis, non-alcoholic steatohepatitis (NASH) or alcoholic steatohepatitis (ASH), cirrhosis, and HCC. First stages of the disease are reversible and represented by a green arrow, while advanced stages are not. Figure created with BioRender.com.

3.10. BOTH ALCOHOLIC AND NON-ALCOHOLIC STEATOHEPATITIS (BASH)

Nowadays, in most parts of the world, lifestyle frequently involves the combination of a western diet (WD) (high-fat, high-sugar, high-refined carbohydrate diet) plus alcohol consumption together with a sedentary lifestyle. Recent clinical studies have demonstrated a significant causal connection between alcohol intake and the development of liver disease in patients with NASH.

However, only 30% of heavy drinkers develop further stages of CLD, which would indicate the interaction of other risk factors like the gender, some drugs use, the alcohol type, etc. Additionally, obesity and NAFLD have been identified as important risk factors in the development of advanced stages of ALD (46, 47). Moreover, alcohol consumption also constitutes a risk factor in more severe NASH forms (47).

Therefore, due to the overlapping of habits, patients currently report dual features of ALD and NAFLD, which we are going to name both alcoholic and non-alcoholic steatohepatitis (BASH) **(Fig. 8).**

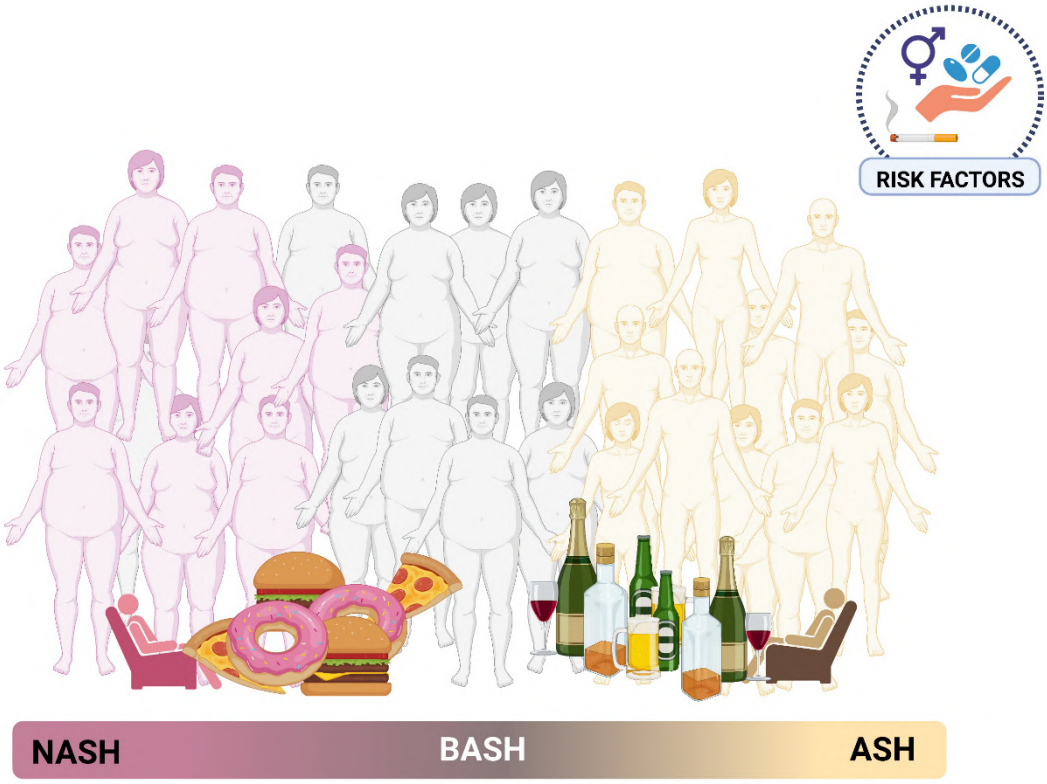

Fig. 8. BASH concept. Current overlapping of dietary habits, sedentary lifestyle, and alcohol consumption lead to **B**oth of **Al**coholic and non-alcoholic **S**teato**H**epatitis (BASH). Figure created with BioRender.com.

3.11. GUT-LIVER AXIS: SECOND OR MAIN ROLE IN CLD DEVELOPMENT?

These days it is known that ALD and NAFLD are systemic diseases that not only affect the liver.

Obesity involves WAT dysfunction and dyslipidemia, leading to the abnormal ectopic accumulation of lipids in non-storage organs such as the liver, muscles, and even the brain (48).

The significant involvement of the liver in lipid and alcohol metabolism would explain their potential to induce hepatic injury. However, it is well known that alcohol is primarily absorbed in the stomach and small intestine before reaching the liver (49) and, similarly, fat is also absorbed in the gut (50). Thus, both alcohol

and excessive fat consumption can lead to gastrointestinal symptoms, inflammation, and imbalance of gut bacteria, inducing gut damage, which definitely will affect the liver, since both organs are connected in different ways (49, 51).

The intimate connection and the strict mutual cooperation between gut and liver realizes a functional entity called “gut-liver axis”. This connection involves reciprocal interactions at cellular and molecular level between the gut, its microbiota, and the liver, which are influenced by various factors such as diet, genetics, and the environment. Under normal physiological conditions, the portal vein facilitates the transport of nutrients, bacterial compounds, and their metabolites from the gut lumen to the liver, which contributes to maintaining homeostasis (52, 53) **(Fig. 9).**

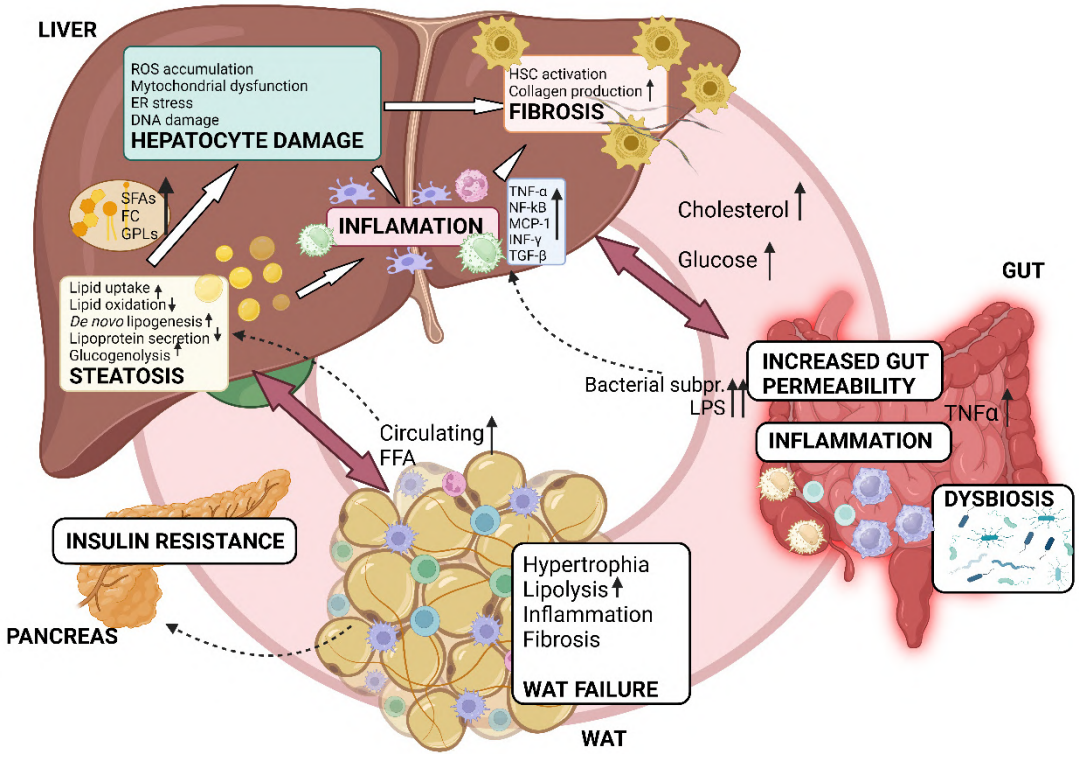

Fig. 9. Pathophysiology of CLD: the systemic hypothesis or systemic pathogenesis. WAT dysfunction plays an important role in the development of IR and in hepatic lipid accumulation. Connection between gut and liver plays a pivotal role in the development of CLD: diet and alcohol directly influence on the gut, increase intestinal permeability and induce dysbiosis. Figure created with BioRender.com.

3.12. GUT ANATOMY AND PHYSIOLOGY

The gut is one of the most extensive mucosal surfaces in the human body and serves as a barrier that safeguards against pathogenic microorganisms and toxic substances. It also plays a vital role in nutrient and water absorption from ingested food.

The gut can be anatomically divided into the small intestine, where we can find the duodenum, jejunum and ileum, and the large intestine formed by the colon and rectum (54). In the small intestine, the epithelium is organized in finger-like protrusions known as villi, whereas the colon lacks villi and displays a flatter surface. Epithelial cells are continuously renewed from invaginations known as the crypts of Lieberkühn, where multipotent stem cells give rise to the different cell types of the intestinal epithelium closely connected to the gut barrier, which include columnar absorptive cells or enterocytes, mucous secreting goblet cells, enteroendocrine cells and Paneth cells (54, 55, 56) **(Fig. 10).**

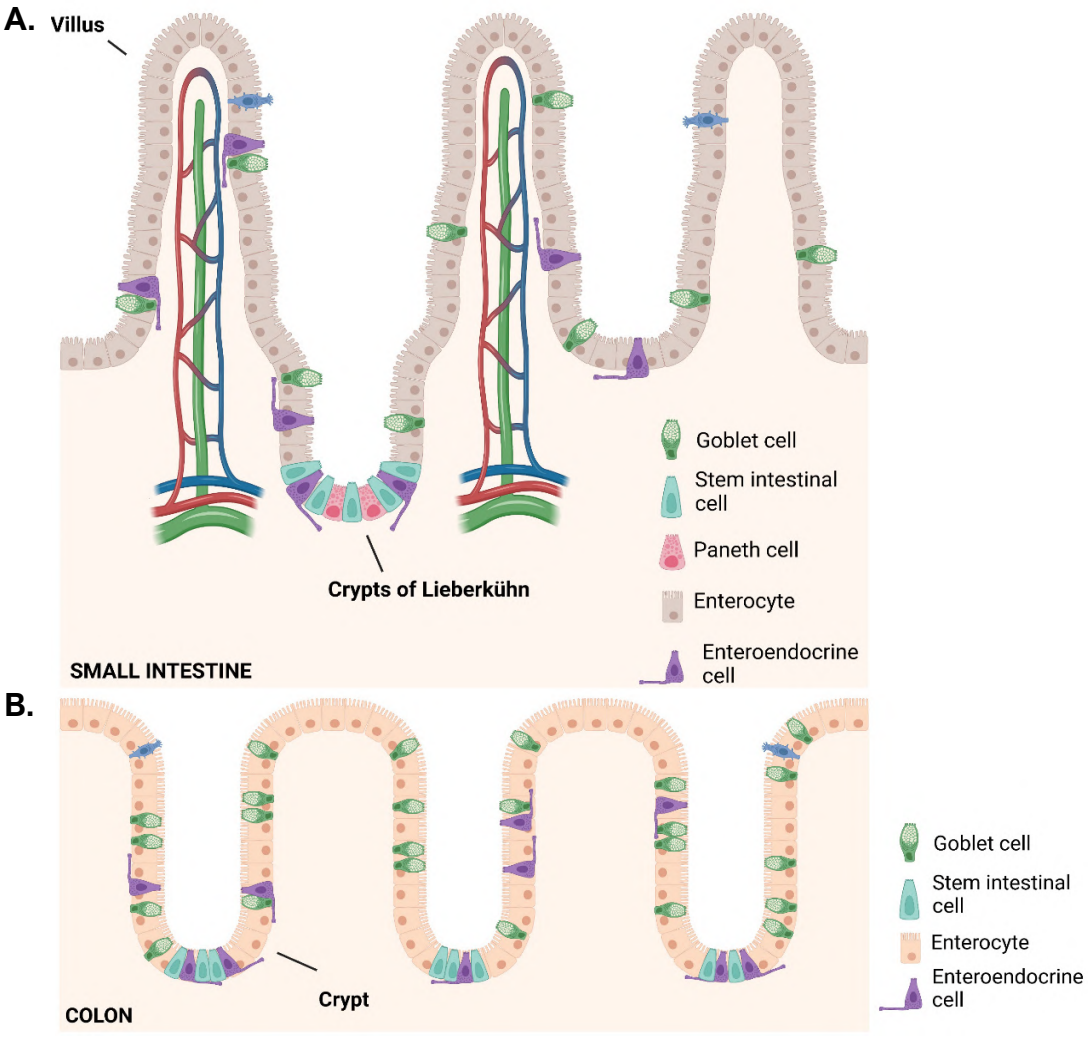

Fig. 10. A. Epithelium organization of the small intestine. Graphical representation of villi, crypts, and different type of intestinal cells. **B.** Colon epithelium. Graphical representation of crypts and different type of colonic cells. Figure created with BioRender.com.

The gut and liver are anatomically linked through portal circulation, which is the physical connection of the gut-liver axis. However, the presence of the intestinal barrier restricts the extent to which the intestine and liver are connected (54).

3.13. GUT BARRIER

The gut barrier is comprised of three major lines of defense: 1. the mechanical barrier, 2. the immune barrier, and 3. the biological barrier. These barriers can interact in between to maintain gut homeostasis (57).

3.13.1. The mechanical barrier

The mechanical barrier is made of the mucus layer, intestinal epithelial cells (IECs), tight junctions between the cells, and mucosal lamina propria **(Fig. 11)**.

3.13.1.1. The mucus layer

The mucosal surface of the gastrointestinal tract is covered in mucus, a substance composed mainly of water (>98%) and proteins such as mucin-2 (MUC2) and MUCA5C in the stomach, which are produced by goblet cells (58).

The stomach and colon have double layer of mucus, while the small intestine has only a single layer (59). The main function of the mucus layer is to shield the intestinal cells from external agents and to facilitate nutrient absorption (58) **(Fig. 11A)**.

3.13.1.2. Epithelial cells

The intestinal barrier is composed of five different types of cells: enterocytes, goblet cells, enteroendocrine cells, Paneth cells, and microfold cells. These cells are replenished by a group of stem cells located in the intestinal crypts (57).

The gut epithelium is not permeable to hydrophilic solutes, which means that molecules and nutrients can only pass through it via specific transporters. There are two primary pathways for transport: the transcellular route, which includes aqueous pores, active carrier-mediated absorption for nutrients and endocytosis,

and the paracellular route, which allows ions and hydrophilic molecules to pass through (60) **(Fig. 11B)**.

3.13.1.3. Tight Junctions (TJs) barrier

The paracellular pathway is controlled by a group of proteins known as junctional complexes that include tight junctions (TJs), adherent junctions, desmosomes, and gap junctions. TJs are composed of three groups of transmembrane proteins (claudin family, the Marvel domain-containing proteins and immunoglobulin superfamily), which interact with the cytoskeletal actomyosin ring (61).

Claudins interact with the zonula occludens (ZO) family of scaffolding proteins via their cytoplasmic region (62), which, in turn, are essential for TJ assembly. Besides claudins, membrane proteins like TJ-associated MARVEL domain-containing proteins (TAMPs: occludin, tricellulin, MarvelD3) and junctional adhesion molecules (JAMs) within the immunoglobulin superfamily localize to TJs (63).

To maintain the homeostasis, TJs facilitate the passage of substances through two pathways: the "pore" pathway, which is very selective, and the "leak" pathway, which is not as selective. As a result, TJs provide a mechanical boundary between the luminal space and other components of the intestinal barrier (64) **(Fig. 11C)**.

3.13.1.4. The gut vascular barrier

The gut vascular barrier (GVB) represents the inner layer of defense in the multilayered intestinal barrier system that finely regulates the translocation of substances from the intestinal lumen to the systemic circulation. The GVB is composed mainly of gut endothelial cells, which are linked by adherent junctions, TJs, catenin and cadherin proteins, and play a vital role in regulating the permeability of blood vessels. These cells are fenestrated. The small pores are delimited by a fenestrae diaphragm regulated by plasmalemma vesicle-associated protein-1 (PV-1), which is essential for maintaining endothelial homeostasis and permeability (65).

In addition to their role in regulating vascular permeability, endothelial cells also play a role in mucosal immunology, expressing Toll-like receptors (TLRs) and adhesion molecules such as E-selectin, vascular cell adhesion molecule-1 (VCAM-1), and intercellular adhesion molecule-1 (ICAM-1). They form a layer with

pericytes and enteric glial cells underneath the intestinal epithelium called the GVB. Enteric glial cells help to maintain the integrity of the intestinal barrier by communicating with enteric neurons and releasing soluble factors such as S-nitroso glutathione, which controls paracellular permeability by increasing TJ protein expression (65, 66) **(Fig. 11D)**.

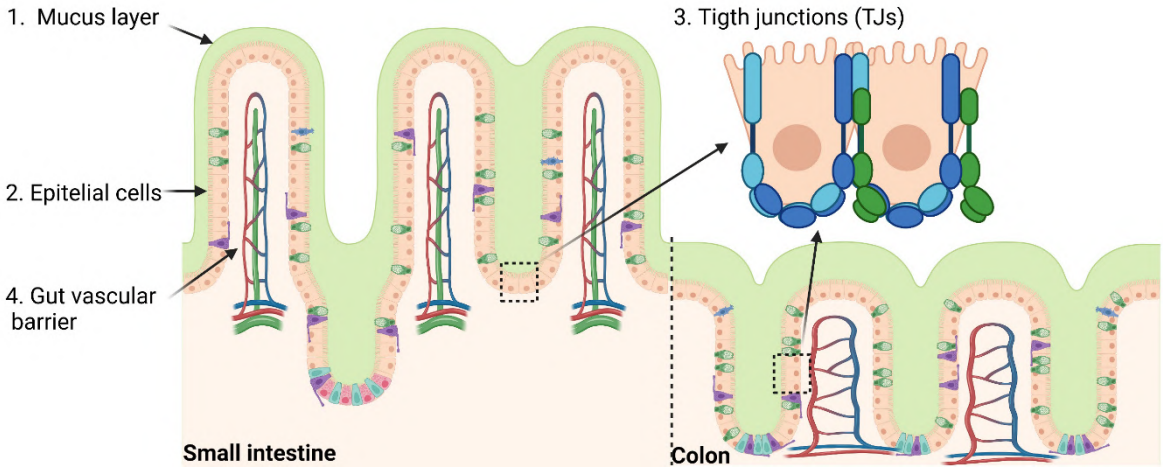

Fig. 11. Gut mechanical barrier components. **A.** Mucus layer is the outer mechanical barrier composed by mucus. **B.** Epithelial cells: enterocytes, goblet cells, enteroendocrine cells, Paneth cells and microfold cells. **C.** Tight junctions (TJs) are composed of proteins that control the paracellular pathway, as well as adherent junctions, desmosomes, and gap junctions. **D.** Gut vascular barrier (GVB) constitutes the inner layer of defence, and it is composed by endothelial cells linked by TJs among others and different proteins that play a fundamental role regulating blood vessel permeability. Figure created with BioRender.com.

3.13.2. The immune barrier

The mucosal surface of the gut is protected by a range of immune cells, including IECs, intraepithelial lymphocytes, and Paneth cells (more abundant in the small intestine) (67).

Gut cells and Paneth cells are the first line of defense against pathogens secreting cytokines and antimicrobial products such as defensins (67).

Microfold cells are specialized epithelial cells that participate in inflammatory responses by capturing antigens in the luminal surface of the intestinal mucosa and transporting them to Peyer's patches (PP) through transcytosis for antigen presentation. These cells mainly recognize bacteria-derived molecules, through TLRs and NOD-like receptors (NLRs), which activate defense mechanisms

through the secretion of cytokines and chemokines that signal to the underlying immune cells (68).

PP are the sites of induction of IgA positive plasma cells in response to pathogens and immune cell signaling. In this line, we can also highlight the presence of intestinal M cells, which contribute to the mucosal immunological surveillance and induction IgA-secreting plasma (67).

Additionally, innate and adaptive immunity agents are present in the lamina propria and gut-associated lymphoid tissue (GALT). These structures are called in the small intestine, Peyer's patches and are large clusters of lymphoid tissue, while in colon they are denominated as isolated lymphoid follicles (69) **(Fig. 12).**

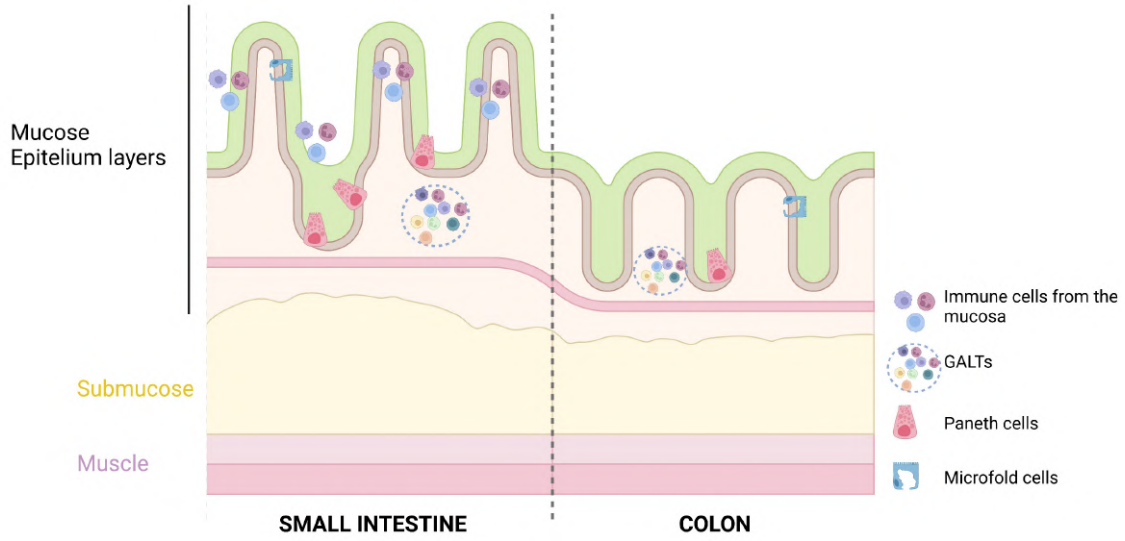

Fig. 12. Immune barrier. Immune cells are mainly located in the gut mucose and include macrophages, lymphocytes, Paneth cells (more abundant in the small intestine) and microfold cells. Moreover, the gut-associated lymphoid tissue (GALT) is located in the lamina propria and can be classified into Peyer's Patches (PP) or isolated lymphoid follicles. Figure created with BioRender.com.

3.13.3. The microbial barrier

The microbial gut barrier is the third component of the gut barrier. The intestinal microbiota consists of highly diverse communities of prokaryotic and eukaryotic microorganisms as well as viruses. After birth, the gut becomes colonized with comparably few different microorganisms and the ecosystem is relatively unstable. Thereafter, diversity of the microbiota increases and eventually results in the formation of a complex microbial ecosystem (70).

Human adult microbiota is composed of 100 trillion microorganisms that include commensal bacteria, pro- and anti-inflammatory, pathogenic and non-pathogenic bacteria, fungi, and viruses that maintain gut homeostasis (71, 72). The intestinal microbiota increases in density from the small intestine to the colon, where it reaches approximately 10 trillion cells per gram of colonic content (70).

Gut microbiome is a complex and dynamic community that keeps a symbiotic relationship with the host. During the life of an individual, the microbiome changes in percentage and population. Under healthy and physiological conditions, it maintains host immune homeostasis (73, 74, 75). It provides efficient protection from infection by enteric pathogens ("colonization resistance"), stimulates maturation of the immune system and facilitates the conversion of non-digestible complex carbohydrates (76, 77).

Some phyla are usually present in the gut microbiome: *Firmicutes, Bacteroidetes, Proteobacteria, Verrycomicobia, Actinobacteria* and *Fusobacteria (78)*. Most often the microbiome takes part in metabolic processes including the fermentation of polysaccharides and the regulation of bile acid (BA) production. Besides, they contribute to the choline metabolism and the process of energy harvest, providing protection against pathogens or even stimulating the endogenous ethanol production (79, 80, 81).

Hence, the excessive proliferation of some bacterial species, or the loss of some commensal bacteria, as well as variations in the total number of bacteria, is named dysbiosis, and it is frequently associated to disruption of host metabolism and to the pathogenesis of several proinflammatory diseases (82, 83, 84).

3.14. GUT BARRIER MICROBIOME CROSSTALK

The interactions among microbiome and mechanical and immunological components that constitute the gut barrier are essential for intestinal and systemic homeostasis.

3.14.1.Microbiota and mechanical gut barrier interactions

Mucus metabolism is influenced by several factors, being one of them the microbiota that can affect the structure and function of the outer mucus layer. It

has been described that germ-free animals have thinner mucus layer and fewer goblet cells (85). Meanwhile, some bacterial subproducts such as lipopolysaccharide (LPS) and peptidoglycan can stimulate mucus secretion; some resident bacteria, like *Akkermansia mucinphila,* can break down mucus to obtain energy for themselves and other commensal bacteria in a balanced way (86, 87). This process is more active when the diet is low in fiber, as fiber serves as an energy source for the microbiota (88). Additionally, immune cells play a role in regulating mucus metabolism through the secretion of cytokines (89).

One of the primary roles of gut microbiota is to obtain nutrients for the intestinal cells and break down undigested dietary products, such as fiber and protein (77). Specifically, by anaerobically fermenting complex carbohydrates that have not been digested, the gut microbiota can create short-chain fatty acids (SCFAs) like butyric, propionic, and acetic acid. These SCFAs serve as an energy source for IECs and have regulatory functions. They can influence cell proliferation and reduce cytokine production by neutrophils and macrophages, leading to an immunotolerogenic phenotype (90). Moreover, SCFAs can enhance the production of the mucus layer by modifying the transcription of mucin genes in goblet cells, and can also encourage the reassembly of TJs, thereby strengthening the intestinal epithelial barrier (91, 92).

3.14.2.Microbiota and immune system interaction

The gut microbiota also contributes to the development of the host's immune system by producing metabolites, microorganism-associated molecular patterns (MAMPs), including pathogen-associated molecular patterns (PAMPs), and antigens (93). Bacterial translocation refers to the process by which pathogens or their products move from the intestinal lumen to the mesenteric lymph nodes (MNL) (94). LPS, which is present in Gram-negative bacteria membrane, is one example of a MAMP recognized by receptors on cells from the innate immune system, including TLRs. These receptors are pattern recognition receptors (PRRs) that are typically found on the surface of immune and intestinal cells as transmembrane proteins, and are capable of identifying bacterial, viral, or parasitic ligands (95). When activated by pathogens or commensal bacteria, TLRs

can trigger an immune response through the induction of the NF-κB, a group of transcription factors involved in the production of inflammatory cytokines. This symbiotic interaction between commensal bacteria and the host immune system plays a protective role in maintaining intestinal homeostasis (96, 97).

3.15. GUT-LIVER AND LIVER GUT-CROSSTALK

The concept of “gut-liver axis” had initially been proposed to describe the presence of antibodies directed against intestinal microorganisms and food antigens in the circulation of patients with liver cirrhosis (98), the common end stage of CLD.

Both gut and liver diseases are frequently associated with a perturbed regulation of gut-liver communication and persistent alterations of the intestinal microbiota, a situation also referred to as dysbiosis. This fact, together with the disruption of mechanical gut barrier, altered immune homeostasis and imbalanced bile salts pool, triggers enhanced gut permeability “leaky gut” and systemic inflammation.

Alterations of the structure and functions of the gut microbiota have major effects on the gut and liver. In fact, studies show that the microbiota has an ethiopathogenic role in gut and liver diseases and that, in turn, gut and liver disease alter the enteric microbiota composition (99, 100).

Yet, the clinical relevance of the gut-liver axis is not limited to aspects concerning microbiota and bacterial dissemination. Gut- and liver- derived mediators including cytokines, hormones, bile salts and other factors, directly link the function of both organs.

Moreover, liver disease disrupts gut homeostasis and leads to changes in gut microbiota composition and intestinal permeability, which correlates with the severity of liver dysfunction. Portal hypertension causes alterations in intestinal barrier function, allowing normally restricted substances to enter the bloodstream. The translocation of bacterial products or fragments triggers the immune system activation and inflammation. This process not only exacerbates liver dysfunction but also initiates a series of reactions throughout the body, leading to a systemic inflammatory condition characteristic of advanced liver cirrhosis (53).

3.15.1.Metabolic crosstalk between gut and liver

Gut-liver communication is not unilateral from gut to liver. Inversely, bile salts and other products of hepatocytes and cholangiocytes, as well as immune mediators, reach the intestine via the bile and blood stream. These liver products regulate nutrient uptake, metabolism, bacterial overgrowth, and barrier function in the gut (101).

BA synthesis is the primary pathway of cholesterol catabolism. Bile is made of various substances, including cholesterol, phospholipids, and bile salts.

Most of the total BA synthesis and the limiting step for the classical BA synthesis pathway is performed by the Cholesterol 7α-hydroxylase, encoded by the gene *Cyp7a1.* To a lesser extent, the enzyme sterol 27-hydroxylase (*Cyp27a1*) is the main responsible for the alternative synthesis pathway of bile salts.

The most abundant BAs in humans include the primary bile salts, cholic acid (CA) and chenodeoxycholic acid (CDCA). Before BAs are transported out of the hepatocytes, most of them are conjugated to taurine or glycine.

Once the BA biosynthesis in hepatocytes is completed, BAs are excreted into the bile canaliculi through the canalicular bile-salt export pump (BSEP). Under normal conditions, bile is stored in the gallbladder and released into the intestinal lumen upon feeding, ensuring the digestion and absorption of ingested lipids (102, 103). Moreover, bile salts remanent in the ileum can be changed by the microbiota to create secondary bile salts, deoxycholic acid (DCA) and lithocholic acid (LCA). Later, they are reclaimed in the terminal ileum and effluxed to the enterohepatic circulation (102).

These secondary bile salts are then absorbed in the ileum by the apical Na^+-dependent bile-salt transporter (ASBT, SLC10A2), effluxed by OST-α/β to the enterohepatic circulation transported back to the liver, where they are mainly internalized by the Na^+-taurocholate cotransporting polypeptide (NTCP), located in the basolateral membrane of the hepatocytes (104). This process is known as the entero-hepatic cycle (102).

Following the initial passage through the liver, BAs that have not been eliminated (less than 10%) undergo filtration by the renal glomerulus and are subsequently reabsorbed by epithelial cells found in the proximal convoluted tubules of the

kidney. This coordinated action of transport systems works to minimize the excretion of BAs in feces and urine. While healthy individuals typically have negligible amounts of BAs in their urine, their presence becomes readily detectable in cases of cholestasis (105).

Within the intestines, bile salts help to break dietary lipids by emulsifying them, making them more accessible to digestive enzymes and nutrients. Bile salts also have the ability to directly prevent the growth of many bacteria in the gut and limit the colonization of others. Certain bacterial species can also modify the bile salt composition by converting primary bile salts into secondary ones (103).

Bile salts not only help with digestion, but they also have hormonal effects by activating certain receptors in the intestine such as the farnesoid X receptor (FXR), vitamin D receptor, and G protein-coupled receptor (TGR5). When these receptors are activated, they work against the production of inflammatory cytokines. This signal is then sent to the liver through the portal vein, which helps to regulate the production and secretion of BAs. Therefore, bile salts, their receptors, and the molecules that regulate their signaling play an important role in the communication between the gut and the liver (103) **(Fig. 13).**

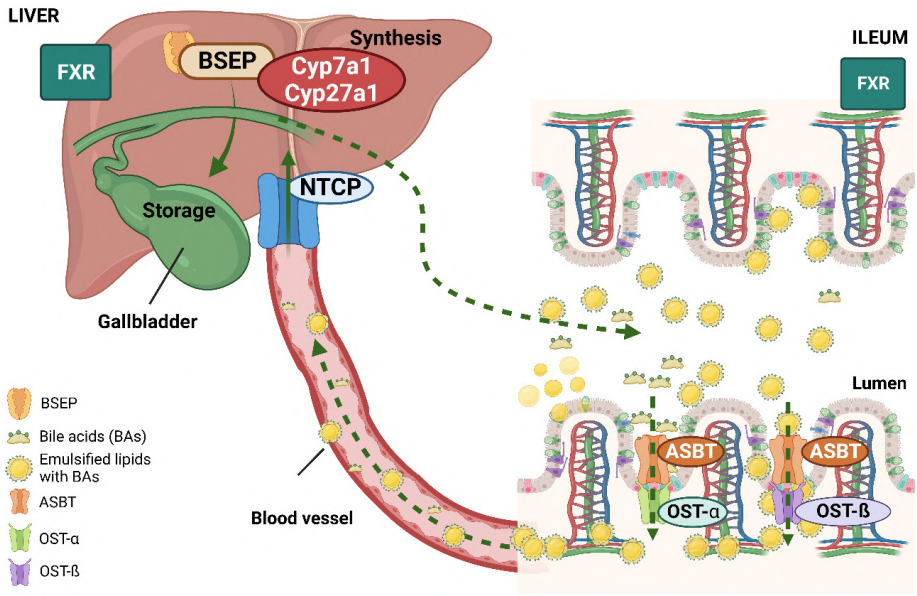

Fig. 13. Enterohepatic bile acid cycle. Bile synthesis is performed in the liver by Cyp7a1 and Cyp27a1 enzymes. When synthesis is completed, BA are released in the bile canaliculi through the bile salt export pump (BSEP) and stored in the gallbladder. In the ileum, bile salts are absorbed by ASBT and efluxed by OST-α/β to the circulation. Back to the liver they are uptaken by NTCP, a transporter located in the basolateral membrane of the hepatocytes. Image created with BioRender.com.

3.15.2. Immunological crosstalk between the gut and the liver

Gut and liver also present interconnected immune circuits in both organs. Both are unique sites for priming and shaping innate and adaptive immune responses and share a similar supply of microbiota, food-derived antigens, and immune stimuli (55).

The gut lamina propria harbors dense populations of immune cells, as well as the liver has its own resident population of immune cells mainly constituted by KCs. It has been described the shared expression of immune molecules that coordinate immune communication in gut and liver, where immune cell functions in the gut and liver are shaped by respective organ-specific microenvironments (106, 107).

3.15.3. Microbiome crosstalk to the liver

Gut microbiome is a particularly important mediator of the gut-liver axis (108). Microbiome serves as the primary mechanism of interaction with the liver via TLRs. Animals possess 13 TLRs, whereas humans have only 10. The presence of multiple widely expressed TLRs allows for the recognition of various pathogens, triggering the appropriate immune response by the innate immune system. PAMPs consist of microbial molecular structures like LPS from Gram-negative bacteria, lipoteichoic acid and peptidoglycan (PGN) from Gram-positive bacteria, lipoglycans, lipopeptides, and lipomannans from mycobacteria, zymosan from yeast, as well as DNA from viruses and bacteria. Damage-associated molecular patterns (DAMPs) include components of the extracellular matrix and plasma membrane, nuclear and cytosolic proteins, and elements from damaged organelles (109).

Each TLR possesses the ability to recognize specific molecular patterns. TLR1, TLR2, TLR4, TLR5, and TLR6 bind to molecules associated with bacterial membranes such as LPS, lipoprotein, and PGN. On the other hand, TLR3, TLR7, TLR8, and TLR9 detect viral, bacterial, or endogenous nucleic acids. TLR4, in conjunction with TLR2, can identify antigens from bacteria, fungi, parasites, viruses, and DAMPs. LPS, which is a constituent of the cell wall in gram-negative

bacteria and interacts with TLR4, is one of the extensively studied mediators of host-microbe interactions (109) **(Fig. 14)**.

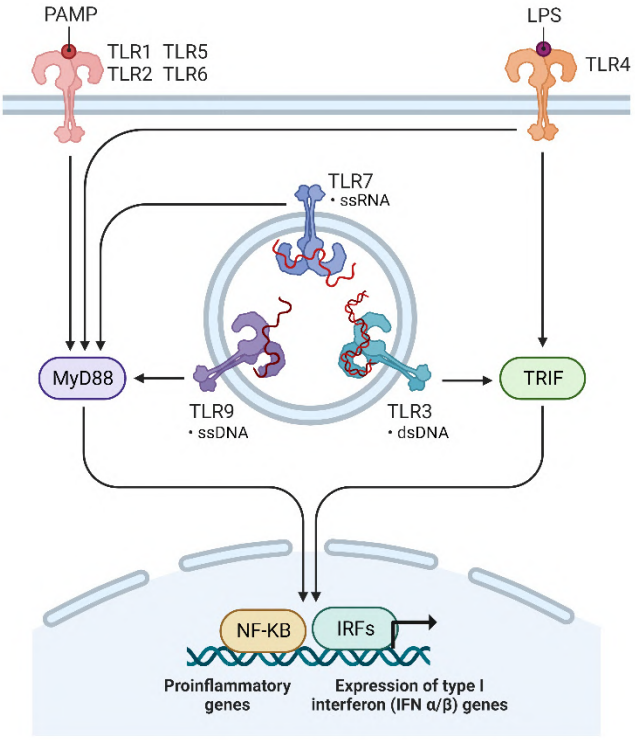

Fig. 14. TLR types. TLR1, 2, 4, 5, and 6 bind to molecules associated with bacterial membranes. Concretely, TLR4, one of the most studied TLRs, binds to the LPS from the Gram-Negative bacteria cell wall. TLR3, 7, 8 and 9 recognize viral, bacterial, or endogenous nucleic acids. Immune response initiation is mediated by TLR activation. Figure from BioRender.com.

In a healthy liver, TLR expression is low at the mRNA level, and TLR-signaling pathways remain inactive. However, under pathological conditions where TLR tolerance against endogenous ligands is compromised, the TLR-mediated immune response induces the expression of proinflammatory/anti-inflammatory cytokines and interferons. The liver consists of various cell populations with immune competence, which can respond to TLR signals (hepatocytes primarily express TLR2; KCs express TLR2, TLR3, TLR4, and TLR9; HSCs express TLR2, TLR4, and TLR9, etc.), highlighting the complexity of immune responses involved in liver-associated inflammatory or immune pathologies (109).

Intestinal bacterial overgrowth is common in patients with liver disease and LPS-mediated signals have been suggested to contribute to disease initiation and progression, as well as to complications of liver diseases (110, 111, 112). In fact, mice deficient TLR4-signaling, which are unable to transmit LPS-mediated signals, are protected in experimental models of NASH and HCC (113, 114).

Moreover, bacterial action goes further, and some microbe-derived activities can exert complex biological effects. Microbial generation of endogenous ethanol and

the degradation of choline have been proposed to enhance TG storage, thereby contributing to liver dysfunction (115).

Specific changes in the gut microbiota associated with different pathologies, frequently referred to as dysbiosis, have been implicated on the initiation and progression of ALD and NAFLD (116, 117, 118).

3.16. HEALTH AND ECONOMIC BURDEN OF CHRONIC LIVER DISEASE: ALD AND NAFLD

ALD is a major driver of global liver related morbidity and mortality. There are 2.4 billion annual drinkers, and the lifetime prevalence of any alcohol use disorder is 5.1-8.6%. Combined, alcohol-associated cirrhosis and liver cancer account for 1% of all deaths worldwide with this burden expected to increase (119).

Meanwhile, the global prevalence of NAFLD is currently estimated to be nearly 25% and is growing rapidly, fueled by increasing rates of obesity and T2DM. (120).

Besides the clinical outcomes related to ALD and NAFLD, liver diseases are associated with significant impairments to health-related quality of life and large economic burdens (121).

In the United States, over 64 million people are projected to have NAFLD, with annual direct medical costs about $103 billion. In Europe, Germany, France, Italy, and the UK together, there are 52 million people with NAFLD with an annual cost of about €35 billion. The burden is significantly higher when societal costs are included (122). In Spain, it is estimated that NAFLD affects at least the 25.8% population aged between 15 and 85 years. The risk of developing more advanced stages of NAFLD increases for patients older than 45 years. Moreover, it is estimated that health costs associated to the disease in Spain range between €53 and €69 million (123).

Costs related to ALD are increasing due to increasing outpatient care together with the prevalence of the studied comorbidities. Similarly to NAFLD, costs for treatment for patients are also growing; they are thought to take approximately

1% of the gross national product from high-income and middle-income countries (121).

3.17. CLINICAL MANAGEMENT OF CLD (NAFLD/ALD)

Despite extensive research on understanding the pathophysiology of ALD/NAFLD, there are still no targeted therapies available. The treatment for ALD remains as it was 50 years ago: abstinence, nutritional support, and corticosteroids. As for NAFLD, the treatment modality is mainly directed toward weight loss and co-morbidity management (124).

3.17.1. Dietary intervention for CLD management

Epidemiological research has demonstrated the link between eating habits and liver disease. It is now widely acknowledged that diet plays a crucial role in the development of CLD and is also a fundamental aspect of its management. Recent investigations have suggested that a diet high in sugar, saturated fats, and cholesterol contributes to the progression and emergence of NAFLD. Conversely, a diet abundant in fruits, protein, polyunsaturated fats, and vegetables is associated with a reduced risk of NAFLD (125). Some studies proposing dietary interventions advocate a regimen in which carbohydrates primarily come from cereals, fruits, and vegetables, protein accounts for approximately 12% of the total daily energy intake, and fat is minimized and derived from vegetables. Besides, these interventions emphasize the avoidance of alcohol and smoking. Changing dietary habits highlight the significant role of diet in the treatment of liver disease (125, 126).

3.17.2. Changing sedentary lifestyle for CLD management

It has been previously discussed that CLD worsens in the presence of obesity and MS features. Additionally, individuals diagnosed with both conditions face a high risk of developing cardiovascular diseases, such as myocardial infarction and stroke. Considering the elevated susceptibility of these patients to severe liver damage and cardiovascular issues, prioritizing weight loss and lifestyle changes

becomes crucial in their overall care (127). Several studies indicate that physical exercise can directly benefit the liver and indirectly affect it through non-hepatic pathways (128, 129). Physical activity, including structured exercises, offers advantages that go beyond weight loss and serves as a fundamental treatment for patients with NAFLD. Both aerobic and resistance training have proven effective in reducing hepatic steatosis and mitigating the cardiovascular risk associated with NAFLD (128, 129).

However, it is difficult to address patients to new lifestyle interventions of diet and physical exercise, due to habits can even go beyond clinical recommendations.

3.17.3. Pharmacotherapy and clinical management of CLD

In recent years, some drugs have been proposed and studied for NAFLD management such as FXR modulators that tend to improve glucose tolerance and homeostasis, insulin sensitivity and lipid metabolism (130, 131).

3.17.4. Microbiome modulation in the management of CLD?

Close connection between the gut and the liver (gut-liver axis) and dysbiosis as one of highlighted features in CLD, sheds light on another putative therapy for the management of the disease: the restorage of intestinal microbial diversity.

Preclinical and clinical studies suggest that the microbiome could be used as a novel target to alleviate the pathophysiology of NAFLD using probiotics or Fecal Microbiota Transplantation (FMT). However, these studies present some limitations (132, 133, 134).

3.17.4.1. Prebiotics, probiotics and symbiotics

Probiotics are a group of beneficial microorganisms that actively colonize the human gut and reproductive system, aiming to improve the imbalanced microbiota of the host. Studies have shown that supplementing with probiotics can decrease the presence of pathogenic bacteria by absorbing endotoxins, enhance the balance of microecology, and reduce the production and entry of harmful substances into the liver. As a result, probiotics play a preventive and alleviating role in the pathological process of NAFLD (135, 136).

On the other hand, prebiotics are indigestible food ingredients that can effectively improve host health by selectively stimulating the growth and activity of specific bacterial colonies. They work by influencing the activity of probiotics and have a positive impact on the human body (137).

When probiotics and prebiotics are combined, they are named symbiotics and their collective effects are mutually beneficial (137).

3.17.4.2. Fecal Microbiota Transplantation (FMT)

At present, FMT is a clinically established and highly effective treatment for recurrent *Clostridioides difficile* infection (138). This procedure involves introducing a solution containing fecal matter from a healthy donor into the recipient's intestinal tract (138). Researchers have also suggested exploring the potential of FMT in treating other gastrointestinal diseases such as inflammatory bowel disease (IBD) (139). In recent small-scale clinical trials, FMT has demonstrated safety and potential effectiveness in enhancing outcomes for individuals with advanced liver disease. However, there are still several unresolved questions that need to be addressed before FMT can be widely implemented in clinical practice (138).

3.18. CLINICAL MANAGEMENT OF ADVANCED STAGES OF CLD

Most individuals with NAFLD do not experience noticeable symptoms during the early stages before cirrhosis develops. They often go to medical attention when liver function tests or imaging studies are conducted for unrelated reasons, revealing abnormalities. Unfortunately, a delayed diagnosis of the disease can result in patients progressing irreversibly to advanced stages of CLD, which significantly complicates their treatment options (140). Bitterly, it looks like the only treatment option for patients with end-stages of CLD such as extensive cirrhosis or HCC is the liver transplant (141, 142) that it is usually controversial due to the comorbidities associated with end stage CLD and obesity features in the case of NAFLD and the economic impact that implies (143).

Open questions

4. OPEN QUESTIONS

The lifestyle in the prosperous parts of the world often includes the overlapping of WD (high fat and high sugar diet) with alcohol intake. Current clinical studies showed a strong causative link between both dietary habits and the onset of CLD. However, the mechanisms by which WD and alcohol together trigger liver damage still remain unclear. In general, BASH is a grey area in the hepatology field with a huge unmet need for preclinical and clinical studies, and many urgent questions that require to be answered.

- Up to today, no **animal model has encompassed all pathological characteristics of human CLD** (144). A novel experimental physiological mouse model that reproduces systemic and intrahepatic features would be helpful to understand BASH pathophysiology.

- Is BASH a **systemic disease?** The liver has a central role in alcohol and fat metabolism. However, other organs are also involved in the pathological process. WAT failure is a critical condition in obese people that can induce IR. Both are considered as serious risk factors for the development of CLD.

- What is the role of **gut-liver axis** in BASH? Alcohol and WD both can directly affect the gut, increasing damage, gut permeability and induce intestinal dysbiosis. Gut and liver crosstalk can be considered as one of the main contributors to CLD development.

- **Microbiome** has been described to be a second entity in the human body, with strong ability to modify metabolism and modulate immunity (145). What is the role of the microbiome in the development of CLD dual etiology?

- Up to date, **no clinical treatment** has been approved for NAFLD/ALD. Abstinence and intervention of dietary habits and sedentary lifestyle are recommended for people with CLD. **Can targeting intestinal microbiota modulation be used as a possible therapeutic approach in BASH?**

Objectives

5. OBJECTIVES

We followed **three overarching general aims** in the current project:

1. **Establish a novel experimental mouse model of CLD dual etiology, which simultaneously combines chronic alcohol administration and WD intake (DUAL model) and has the following characteristics:**
    - Physiological.
    - Mimics the main extra- and intrahepatic features of CLD as it occurs in humans.
    - Progresses to advanced stages of CLD: fibrosis, cirrhosis, and HCC.
    - Simple, reproducible and has a low mortality rate.

2. **Analyze the relevance of the gut-liver crosstalk and define molecular mediators and functional circuits in the context of the novel DUAL model.**
    - 2.1. Perform comprehensive phenotyping and molecular analysis of gut after DUAL feeding.
    - 2.2. Define and confirm the role of intestinal microbiota as a potential key modulator.

3. **Test therapeutic interventions that can ameliorate the effects induced by DUAL diet on liver and gut physiology.**
    - 3.1. Reveal therapeutic benefits/limitations of the intestinal microbiome modulation as novel therapeutic strategy.
    - 3.2. Compare the putative beneficial effect of dietary intervention with microbiome modulation after short- and long-term DUAL diet.

Materials & Methods

6. MATERIALS AND METHODS

6.1. MATERIALS

6.1.1. Chemicals

Reagent	Manufacturer
20% D-Glucose solution	Braun, Frankfurt, Germany
25% Glutaraldehyde aqueous	Thermo Fisher Scientific, MA, USA
30% acrylamide/bis solution	Bio-Rad, CA, USA
4X Laemmli buffer	Bio-Rad, CA, USA
Acetic acid (glacial) 100% (CH_3COOH)	AppliChem, Darmstadt, Germany
Acetone (C_3H_6O)	AppliChem. Darmstadt, Germany
AEBSF hydrochloride	Thermo Fisher Scientific, MA, USA
Ammonium persulfate (APS, $(NH_4)_2S_2O_8$)	Bio-Rad, CA, USA
Bodipy® 500/510 C1, C12 fatty acids (2 µg/g body weight, molecular probes #D3823	Thermo Fisher, MA, USA
Bovine serum albumin, lyophilized powder, ≥96% (BSA)	Sigma-Aldrich, MO, USA
Calcium chloride ($CaCl_2$)	Sigma-Aldrich, MO, USA
$Ca^{2+}Mg^{2+}$-Free PBS	Sigma-Aldrich, MO, USA
Chloroform ($CHCl_3$)	AppliChem, Darmstadt, Germany
Complete mini	Roche, Basel, Switzerland
D(+)-glucose ($C_6H_{12}O_6$)	Sigma-Aldrich, MO, USA
Dako faramount aqueous mounting medium	Dako, Agilent, Glostrup, Denmark
Diethylnitrosamine (DEN)	Sigma-Aldrich, MO, USA
Direct red 80 (Sirius red)	Sigma-Aldrich, MO, USA

Di-sodium hydrogen phosphate 7-hydrate for analysis ($Na_2HPO_4 \cdot 7H_2O$)	AppliChem, Darmstadt, Germany
DMEM (Dulbecco's Modified Eagle Medium)	Thermo Fisher Scientific, MA, USA
Dimethyl sulfoxide (DMSO, $(CH_3)_2SO$)	Sigma-Aldrich, MO, USA
Dithiothreitol (DTT) ($C_4H_{10}O_2S_2$)	Thermo Fisher Scientific, MA, USA
Dodecyl sulphate sodium salt (SDS) for analysis, ($C_{12}H_{25}NaO_4S$)	AppliChem, Darmstadt, Germany
ECL prime western blotting detection reagents	GE Healthcare, Amersham, UK
Eosin Y ($C_{20}H_6Br_4Na_2O_5$)	Sigma-Aldrich, MO, USA
Ethanol absolute for analysis (CH_3CH_2OH)	AppliChem, Darmstadt, Germany
Ethylenediamine-tetra acetic acid (EDTA, $(HO_2CHH_2)_2NCH_2CH_2N(CH_2CO_2H)_2$)	Sigma-Aldrich, MO, USA
EDTA (0.5M; pH 8.0 sterile)	Thermo Fisher Scientific, MA, USA
Fetal bovine serum (FBS)	Thermo Fisher Scientific, MA, USA
FITC Dextran 4 kDa	TdB Labs AB, Uppsala, Sweden
Formaldehyde solution 4% (CH_2O)	AppliChem, Darmstadt, Germany
Goat serum	Thermo Fisher Scientific, MA, USA
Hydrochloric acid technical grade 37% (HCl)	AppliChem, Darmstadt, Germany
Hydrogen peroxide 30% (H_2O_2)	AppliChem, Darmstadt, Germany
ImmPACT DAB HRP Substrate	Vector Laboratories, Petersburg, UK
Insulin	Sigma-Aldrich, MO, USA
Isoflurane ($C_3H_2ClF_5O$)	Solvet, Segovia, Spain
Isopropanol (C_3H_8O)	AppliChem, Darmstadt, Germany
Mayer's hematoxylin ($C_{16}H_{14}O_6 \cdot 12H_2O$)	AppliChem, Darmstadt, Germany

Methanol (MetOH) BioChemica (CH_3OH)	AppliChem, Darmstadt, Germany
Normal horse serum blocking solution, 2.5%	Vector Laboratories, Petersburg, UK
Non-fat dried milk powder	AppliChem, Darmstadt, Germany
Nonidet P-40 (NP40)	AppliChem, Darmstadt, Germany
Novex sharp protein standard	Thermo Fisher Scientific, MA, USA
Oil red O	Sigma-Aldrich, MO, USA
Osmium Tetroxide	Sigma-Aldrich, MO, USA
Paraplast Plus Embedding Medium	Leica, Wetzlar, Germany
PhosSTOP™	Roche, Basel, Switzerland
Picric acid saturated aqueous solution ($C_6H_3N_3O_7 \cdot H_2O$)	Sigma-Aldrich, MO, USA
Precision plus protein standards	Bio-Rad, CA, USA
Ponceau S solution	Sigma-Aldrich, MO, USA
Potassium chloride> 99.0% (KCl)	Merck, Darmstadt, Germany
Restore western blot stripping buffer 500 mL	Thermo Fisher Scientific, MA, USA
Roti®-Histokitt	Carl Roth, Karlsruhe, Germany
Sodium bicarbonate ($NaHCO_3$)	Sigma-Aldrich, MO, USA
Sodium citrate ($Na_3C_6H_5O_7$)	AppliChem, Darmstadt, Germany
Sodium chloride for molecular biology (NaCl)	AppliChem, Darmstadt, Germany
Sodium dihydrogen phosphate monohydrate ($NaH_2PO_4 \cdot H_2O$)	AppliChem, Darmstadt, Germany
Sodium fluoride (NaF)	Sigma-Aldrich, MO, USA
Sodium hydroxide (NaOH)	AppliChem, Darmstadt, Germany
Spurr embedding resine	Electron Microscopy Sciences, Hatfield, UK
Tetramethylethylenediamine (TEMED)	Bio-Rad, CA, USA

Tissue-Tek® O.C.T.™ compound	Sakura Finetek Europe (SPE), Alphen aan den Rijn, The Netherlands
Tris/glycine buffer 10x	Bio-Rad, CA, USA
Tri-sodium citrate 2-hydrate ($HOC(COONa)(CH_2COONa)_2 \cdot 2H_2O$)	AppliChem, Darmstadt, Germany
Tris ($C_4H_{11}NO_3$)	AppliChem, Darmstadt, Germany
Triton X-100	AppliChem, Darmstadt, Germany
Trizol reagent	Thermo Fisher Scientific, MA, USA
Tween-20	Sigma-Aldrich, MO, USA
Vectashield mounting medium with DAPI	Vector Laboratories, Petersburg, UK
Water for molecular biology · H_2O	AppliChem, Darmstadt, Germany
Xylene (C_6H_{10})	Carl Roth, Karlsruhe, Germany

6.1.2. Standard kits and enzymes

Kit/Assay	Manufacturer	Reference
Biocal calibrator (Triglycerides)	Gernon RAL Técnica para el laboratorio, S.A., Barcelona, Spain	GN90125
ECL™ prime western blotting detection reagents Amersham	Thermo Fisher Scientific, MA, USA	RPN2232
High-capacity cDNA reverse transcription kit	Thermo Fisher Scientific, MA, USA	4374966
In situ cell death detection kit, fluorescein	Roche, Basel, Switzerland	11684795910
Live/Dead fixable aqua	Thermo Fisher, MA, USA	L34957
LPS ELISA Kit	Antibodies, Aachen, Germany	ABIN6574100

Mouse Albumin ELISA kit (E99-134)	Bethyl laboratories, MA, USA	E99-134
Pierce BCA protein assay kit (Reagent A: contains sodium carbonate, sodium bicarbonate, Pierce BCA detection reagent in 0.1 N sodium hydroxide. Reagent B: bright blue clear solution free of particulate matter)	Thermo Fisher Scientific, MA, USA	23227
RBC Lysis buffer	Thermo Fisher, MA, USA	00-4333-57
Total bile acids assay kit	Diazyme Laboratories, Inc., CA, USA	DZ042A

Enzyme	Manufacturer
BLOXALL® endogenous blocking solution, peroxidase, and alkaline phosphatase	Vector Laboratories, Petersburg, UK
Collagenase IV	Thermo Fisher, MA, USA
DNAse	Thermo Fisher, MA, USA
SYBR GreenER™ qPCR super mix	Thermo Fisher Scientific, MA, USA

6.1.3. Standard buffer and media

Phosphate-Buffer Saline (PBS)	
10x PBS	**Volume/Quantity**
NaCl	78.80 g
KCl	3.50 g
Na_2HPO_4	26.80 g
NaH_2PO_4	2.76 g

Distilled H_2O (dH_2O)	1 L

1x PBS	**Volume**
10x PBS	100 mL
dH_2O	1 L

Bile – Hall's bilirubin stain reagents	
10% Ferric Chloride	**Volume/Quantity**
Ferric chloride	0.5 g
dH_2O	5 mL
Van Gieson's solution	**Volume/Quantity**
1% Acid fuchsin	1 ml
Picric acid, saturated	45 ml
Fouchet's reagent	**Volume/Quantity**
Trichloracetic acid	12.5 g
dH_2O	50 ml
10% ferric chloride (after mixing)	5 ml

Sirius Red stain reagents	
Picro-Sirius red (SR) solution	**Volume/Quantity**
Direct Red 80	0.25 g
Picric acid saturated aqueous solution*	250 mL

*Picric acid is an explosive product in contact with the oxygen

Acidified water	**Volume**
Acetic acid	1.5 mL
dH_2O	300 mL

Methanol-Carnoy (*Metacarn* fixation solution for gut)	
Reagent	**Volume/Quantity**
Methanol	120 mL (60%)
Glacial acetic acid	20 mL (10%)
Chloroform	60 mL (30%)

*Add all the reagents in this order, otherwise *metacarn* solution would be white.

Oil Red O (ORO) stain reagents	
Oil red O (ORO) stock solution	**Volume/Quantity**
ORO powder	0.5 g
Isopropanol	100 mL
Oil red O (ORO) working solution	**Volume**
ORO stock solution	48 mL
dH_2O	32 mL

* ORO stock solution should be prepared in advanced and perfectly mixed during 2 h warming it at 65ºC. Working solution should be filtered four times with Whatman paper to avoid solid particles. Both solutions must be kept in dark.

Hepatic triglycerides homogenization buffer		
Triglycerides (TG) buffer	**Volume/Quantity**	**pH Value**
EDTA	70 mg	pH 7.5
Tris-HCl	22 mg	
Sucrose	4.27 g	
dH_2O	50 ml	

Nuclei permeabilization buffer. TUNEL staining		
150 mM Na-citrate solution	**Volume/Quantity**	**pH Value**
150 mM Na-citrate	8.8 g	pH 6.0
Triton-X-100	0.2 mL	
1x PBS	200 mL	

Antigen demasking buffer. Immunohistochemistry (IHC) staining		
10 mM Na-citrate solution	**Volume/Quantity**	**pH Value**
10 mM Na-citrate	1.76 g	pH 6.0
Tween 20x	0.3 mL	
1x PBS	600 mL	

FACS Buffer		
Reagent	**Volume/Quantity**	**Final concentration**
FBS	15 ml	3%
EDTA	2 ml	2 mM
Sodium azide	1 ml	0.2%
CMF PBS	482 ml	

Digestion Buffer for FACS		
Reagent	**Volume/Quantity**	**Final concentration**
Collagenase (75 mg/ml)	150 µl	0.75 mg/ml
DNAse (5mg/ml)	150 µl	0.05 mg/ml
DMEM	15 ml	

RIPA Buffer		
RIPA	**Volume/Quantity**	**Final concentration**
SDS 10%	1.0 mL	0.1 %
Sodium deoxycholate	0.5 g	0.5 %
NP40	0.5 mL	0.5 %
NaCl 5M	3.0 mL	150 mM
Tris-HCl 1 M, pH = 7,8	5.0 mL	50 mM

EDTA	2.0 mL	250 mM
dH_2O	100.0 mL	

RIPA Complete	**Volume/Quantity**
PhosSTOP	1 tablet
Complete Mini	1 tablet
DTT	20 µL
AEBSF hydrochloride (100 mM)	100 µL
RIPA buffer	10 mL

* RIPA buffer should be kept at 4ºC. Complete RIPA buffer should be kept at -20ºC.

Western Blot Buffers	
1x SDS-RUNNING buffer	**Volume/Quantity**
Tris/glycine buffer	100 mL
10% SDS	10 mL
dH_2O	1 L
1x TRANSFER buffer	**Volume**
Tris/glycine buffer	100 mL
MetOH	200 mL
dH_2O	1 L

*Transfer buffer should be stored at 4ºC to use.

Tris-Buffered saline (TBS)	
10x TBS	**Volume/Quantity**
Tris	24.2 g
NaCl	80.0 g
dH_2O	1 L
1x TBS	**Volume**
10x TBS	100 mL
Tween-20	0.5 mL

dH_2O	1 L

6.1.4. Immunoblotting gels

Stacking gel (5%)	**Volume**
dH_2O	4.5 mL
30% acrylamide/bis solution	1.3 mL
10% APS	80 µL
10% SDS	80 µL
Tris/HCl pH = 6.8	2.0 mL
TEMED	8.0 µL
Total volume	8.0 mL

Separating gel	**8%**	**10%**	**12%**	**15%**
dH_2O	9.3 mL	7.9 mL	6.6 mL	4.6 mL
30% acrylamide/bis solution	5.3 mL	6.7 mL	8.0 mL	10.0 mL
10% APS	200 µL	200 µL	200 µL	200 µL
10 SDS	200 µL	200 µL	200 µL	200 µL
Tris/HCl pH = 8.8	5.0 mL	5.0 mL	5.0 mL	5.0 mL
TEMED	12.0 µL	8.0 µL	8.0 µL	8.0 µL
Total volume	20 mL	20 mL	20 mL	20 mL

* Total volume represented is suitable for the preparation of 2 gels

6.1.5. Immunostaining and immunoblotting antibodies

6.1.5.1. Primary antibodies

Product	**Host**	**Manufacturer**	**Reference**	**Dilution**
4-hydroxynonenal (4-HNE)	Rabbit	Abcam	ab46545	1:100 (IHC)

Alpha-smooth muscle actin (α-SMA)	Rabbit	Merck	A 2547	1:800 (WB)
Beta-actin (β-ACTIN)	Mouse	Cell Signaling Technology	3700S	1:1000 (WB)
Cluster of differentiation 11b (CD11b)	Rat	BD	550282	1:500 (IF)
Cluster of differentiation 45 (CD45)	Rat	BD	550539	1:100 (IF)
Collagen I	Rabbit	Abcam	ab34710	1:100 (IHC)
CYP2E1 (Cytochrome P450)	Rabbit	Abcam	Ab28146	1:1000 (WB)
F4/80	Rat	Bio-Rad	MCA497	1:100 (IF)
Gliceraldehyde-3-phosphate dehydrogenase (GAPDH)	Mouse	Bio-Rad	MCA4739	1:5000 (WB)
Ki-67	Rabbit	Abcam	ab16667	1:100 (IHC)
PCNA	Mouse	Life Technologies	13-3900	1:1000 (WB)
Mucin-2	Rabbit	Santa Cruz	Sc-15334	1:800 (IF)
ZO-1 (IF)	Rabbit	Invitrogen	61-7300	1:100 (IF)

ZO-1 (WB)	Rabbit	Invitrogen	PA5-28858	1:500 (WB)
CD3	Rabbit	Abcam	Ab5690	1:100 (IF)
B220	Rat	Stemcell Technologies	RA3-6B2	1:100 (IF)
PV-1	Rat	BD Pharmingen	553849	1:100 (IF)
CD34	Rabbit	Abcam	Ab81289	1:100 (IF)
Hsp70/Hsp72	Rabbit	Enzo	ADI-SPA-812F	1:100 (IHC)
Hsc-70	Mouse	Santa Cruz	Sc-7298	1:1000 (WB)
CPT-1C	Mouse	Santa Cruz	Sc-514555	1:500 (WB)
CK19	Rabbit	Abcam	Ab15463	1:100 (IHC)
Occludin	Rabbit	ThermoFisher	71-1500	1:300 (WB)
Cleaved Caspase 3	Rabbit	Cell Signaling Technology	D175	1:1000 (WB)
Phalloidin, Fluorescein	*Amanita phalloides*	Sigma-Aldrich	Ab28146	1:1000 (IF)

Isothiocyanate Labeled			

6.1.5.2. Secondary antibodies

Product	Manufacturer	Reference	Dilution
Anti-mouse HRP	Bio-Rad	STAR207P	1:5000 (WB)
Anti-mouse biotinylated	Vector Laboratories	BA-9200	(IHC)
Anti-rabbit HRP	Cell Signaling Technology	70745	1:3000 (WB)
Anti-rabbit biotinylated	Vector Laboratories	BA-1000	(IHC)
Goat anti-Rat Alexa Fluor 488	Invitrogen	A11006	1:500 (IF)
Goat-Anti-Rabbit Alexa Fluor 488	Invitrogen	A11001	1:500 (IF)
Goat-Anti-Rabbit Alexa Fluor 546	Invitrogen	A11010	1:500 (IF)
Donkey-Anti-Rabbit Alexa 488	Invitrogen	A21206	1:500 (IF)

6.1.5.3. Flow cytometry antibodies

5.1.5.3.1. Flow cytometry antibodies for liver

Antibody	Fluorochrome	Manufacturer	Reference
Anti-mouse CD45.2	Brilliant Ultra Violet (BUV) 805	BD Biosciences	569200
Anti-mouse I-A/I-E (MHC-II)	Alexa Fluor 700	Biolegend	107622

Anti-mouse-CD11c	Brilliant Violet (BV) 650	Biolegend	117339
Anti-mouse- CD11b	BV605	Biolegend	101257
Anti-mouse-CD64	PercpCy5	Biolegend	139308
Anti-mouse-Ly6C	BV711	Biolegend	128037
Anti-mouse-Ly6G	PE	BD Biosciences	551461
Anti-mouse- F4/80	BV421	BD Biosciences	565411
Anti-mouse-NK1.1	FITC	Biolegend	108706
Anti-mouse- CD8	BUV737	Invitrogen	3670081-82
Anti-mouse-CD3	A594	Biolegend	152318
Anti-mouse-TCRδ	A750	Biolegend	118136
Anti-mouse-TCRβ	BV510	Biolegend	109233
Anti-mouse CD4	BV 570	Biolegend	100542
Anti-mouse CD16/CD32 (clone 2.4G2)	-	Tonbo Bioscience	70-0161-M001
Foxp3 / Transcription Factor Staining Buffer Kit	-	Tonbo	TNB-0607-KIT
Precision Count Beads™	-	Biolegend	424902
LIVE/DEAD® Fixable Aqua Dead Cell Stain Kit	405 nm excitation	Thermo Fisher	L34957

5.1.5.3.2. Flow cytometry antibodies for colon

Antibody	Fluorochrome	Manufacturer	Reference
Anti-mouse CD19	BV421	Biolegend	115537
Anti-mouse CD3	A647	BD Biosciences	557869
Anti-mouse NK1.1	Alexa Fluor 700	Biolegend	108730
Anti-mouse CD4	PE-Cy7	Biolegend	100528

Anti-mouse CD8	Percp-Cy5	Biolegend	100734
Anti-mouse-TCRδ	A750	Biolegend	118136
Anti-mouse CD45.2	BV786	BD Biosciences	563894
Anti-mouse Foxp3	FITC	Invitrogen	115773-82
Anti-mouse CD25	BV710	BD Biosciences	740714
Anti-mouse CD16/CD32 (clone 2.4G2)	-	Tonbo Bioscience	70-0161-M001
Foxp3 / Transcription Factor Staining Buffer Kit	-	Tonbo	TNB-0607-KIT
Precision Count Beads™	-	Biolegend	424902
LIVE/DEAD® Fixable Aqua Dead Cell Stain Kit	405 nm excitation	Thermo Fisher	L34957

6.1.6. Primer sequences for RT-qPCR

Primers were designed and checked for specificity with Primer Blast tool from NCBI and purchased from Sigma-Aldrich (MO, USA).

Gene	Forward (5'-3')	Reverse (5'-3')
α-Sma	CCCCTGAAGAGCATCGGACA	TGGCGGGACATTGAAGGT
Asbt	TCGTTTAAGGCATCCGTGTAGA	CACCCCATAGAAAACATCACCA
Ccl2	TAAAAACCTGGATCGGAACCAAA	GCATTAGCTTCAGATTTACGGGT
Cd36	CAAATGCAAAGAAGGAAAGCC	AATGGTCCCAGTCTCATTTAGC
C-myc	AGTGCTGCATGAGGAGACAC	GGTTTGCCTCTTCTCCACAG
Collagen I	TGTGTGCGATGACGTGCAAT	GGGTCCCTCGACTCCTAC
Cyclin A1	GATACCTGCTCGGGGAAAGAG	GCATTGGGGAAACTGTGTTGA

Cyclin E	GAAAAGCGAGGATAGCAGTCAG	CCCAATTCAAGACGGGAAGTG
Cyp27a2	AGGGCAAGTACCCAATAAGAGA	TCGTTTAAGGCATCCGTGTAGA
Cyp7a1	GCTGTGGTAGTGAGCTGTTG	GTTGTCCAAAGGAGGTTCACC
E.Coli 16s	AGAGTTTGATCCTGGCTCAG	CTTGTGCGGGCCCCCGTCAATTC
Gapdh	TGTTGAAGTCACAGGAGACAACCT	AACCTGCCAAGTATGATGACATCA
Fxr	GGCAGAATCTGGATTTGGAATCG	GCCCAGGTTGGAATAGTAAGACG
Ntcp	CAAACCTCAGAAGGACCAAACA	GTAGGAGGATTATTCCCGTTGTG
Ost-α	TCTGCACCCACGGTGGTAT	GGCCATTTCTACAAGTGTGAGG
Ost-β	AGATGCGGCTCCTTGGAATTA	TGGCTGCTTCTTTCGATTTCTG
Pparγ	CACAATGCCATCAGGTTTGG	GCTGGTCGATATCACTGGAGATC
Scd-1	GTTCCAGAATGACGTGTACGA	GGCTTGTAGTACCTCCTCTG
Tlr2	CACCACTGCCCGTAGATGAAG	AGGGTACAGTCGTCGAACTCT
Tlr4	TGGCTGGTTTACACATCCATCGGT	TGGCACCATTGAAGCTGAGGTCTA
Tlr9	ACGGGAACTGCTACTACAAGA	CCCAGCTTGACAATGAGGTTAT
Tnf-α	CCTCTTCTCATTCCTGCTTGTGG	GAGAAGATGATCTGAGTGTGAGG
Xbp-1	CTGAGTCCGAATCAGGTGCAG	GTCCATGGGAAGATGTTCTGG

Zo-1	GCTTTAGCGAACAGAAGGAGC	TTCATTTTTCCGAGACTTCACCA

6.1.7. Mice

6.1.7.1. Diet

Diet	Reference	Manufacturer
Chow diet	LASQC diet® Rod18-H	Altromin LASQC diet Rod18-H, Germany
Western diet (WD)	D1602230	Research Diets, New Brunswick, NJ

6.1.7.1.1. Macronutrients of diets

Macronutrients (% kcal)	Groups	
	Control	DUAL
Protein	16	20
Fat	10	40
Carbohydrate	73	40

6.1.7.1.2. Composition of chow diet

Main nutrients (%)		Amino acids/kg (g)	
Protein	18.9	Arginine	9.0
Fat	5.3	Cysteine	4.0
Fibre	3.9	Histidine	4.5
Ash	7.0	Isoleucine	7.0
N-free-Extracts	53.1	Leucine	21.0
Dry Matter	88.0	Lysine	9.0
Kcal/g	3.0	Methionine	4.5
Minerals/kg (g)		Phenylalanine	10.0

Calcium	10	Threonine	6.5
Phosphorus	6.5	Tryptophan	2.0
Sodium	3.0	Tyrosine	7.0
Magnesium	2.5	**Vitamins/kg**	
Trace element/kg (mg)		Vit. A	15.000 I.E.
Iron	200.0	Vit. D3	1.200 I.E.
Iodine	4.0	Vit. E	90 mg
Copper	15.0	Vit. K	5 mg
Cobalt	1.5	Thiamine (B1)	15 mg
Manganese	120.0	Riboflavin (B2)	10 mg
Selenium	0.2	Pyridoxine (B6)	10 mg
Zinc	75.0	Cobalamin (B12)	50 mg
Fatty acids/kg (g)		Biotin	200 mcg
C16, Palmitic	7.5	Choline	1000 mg
C18, Stearic	3.0	Folate	2 mg
C18:1, Oleic	13.0	Niacin	40 mg
C18:2, Linoleic	21.0	Pantothenate	20 mg
C18:3, Linolenic	13.0		
C:20, Arachidonic	0.2		

6.1.7.1.3. Composition of WD (D1602230)

Main nutrients	**g%**	**kcal%**
Protein	22	20
Fat	45	40
Carbohydrate	20	40
Total		100
Kcal/g	**4.5**	
Ingredients	**g**	**kcal**
Casein	200	800
L-Cystine	3	12
Maltodextrin 10	100	400
Fructose	200	800
Sucrose	96	384
Cellulose	50	0
Soybean Oil	25	225
Primex Shortening	135	1215
Lard	20	180
Mineral Mix S10026	10	0
DiCalciumPhosphate	13	0
Calcium Carbonate	5.5	0
Potassium Citrate, 1 H20	16.5	0
Vitamin Mix V10001	10	40
Choline Bitartrate	2	0

Cholesterol	18	0
TOTAL	**904.05**	**4056**
Total FAT (g)	**180**	
C16, Palmitic	29.80	
C18, Stearic	14.42	
C18:1, Oleic	58.90	
C18:2, Linoleic	26.65	
C18:3, Linolenic	2.32	
C:20, Arachidonic	0.620	
C18:1, Oleic	58.90	
FAT	**(%)**	
Saturated	34.4	
Monounsaturated	44.0	
Polyunsaturated	21.6	
Transfat	29.2	

6.1.7.2. Drinking water DUAL feeding

Substance	Manufacturer
Glucose	Sigma-Aldrich, MO, USA
Ethanol absolute	AppliChem, Darmstadt, Germany

6.1.7.3. Cocktail of antibiotics

Antibiotics	Concentration	Manufacturer
Gobemicina Normon (Ampicillin)	100 mg/L	Lab. Normon, Madrid, Spain
Ceftazidime Kabi	100 mg/L	Fresenius Kabi Singapore

Ciprofloxacin Normon	125 mg/L	Lab.Normon, Madrid, Spain
Metronidazole Normon	100 mg/L	Lab. Normon, Madrid, Spain
Sulfate of Streptomycin Reig Jofré	50 mg/L	Lab. Reig Jofré, Barcelona, Spain
Vancomycin Sala	50 mg/L	Lab. Reig Jofré, Barcelona, Spain

6.1.7.4. Microbiome modulation

Product	Manufacturer
Omeprazol Cinfa 20 mg	Cinfa, Pamplona, Spain
Citrafleet	Casen Recordati S.L., Madrid, Spain

6.1.7.5. Probiotics and placebo

Product	Ingredients	Manufacturer
VSL#3 Probiotic	Liver lactic bacteria and bifidobacterial in carrier	Actial Farmaceutica SRL, Rome, Italy
VSL#3 Placebo	Carrier: corn starch, maltose, anti-caking agent: silicon dioxide	Actial Farmaceutica SRL, Rome, Italy

6.1.8. Instruments and equipment

Instrument/Equipment	Manufacturer
ACCU-CHECK glucometer	Roche, Basel, Switzerland
Antigen 2100-Retriever	Aptum Biologics, Hants, UK
Centrifuge 5415 D	Eppendorf AG, Hamburg, Germany
Centrifuge Z233M-2 and refrigerated	Hermle Labor Technik GmbH, Wehingen, Germany
Confocal system IXplore SpinSR	Olympus, Tokyo, Japan
Cryostat CM1950	Leica Biosystems, Wetzlar, Germany

Digital microscope camera Moticam 2500	Ryf AG, Bettlachstrasse, Switzerland
DISKUS Z16 APO	Leica Biosystems, Wetzlar, Germany
Drying and sterilizing ovens natural convection	J.P. selecta, Barcelona, Spain
Eclipse Ci optical microscope	Nikon, Tokyo, Japan
FastPrep-24™5G	MP Biomedicals, Illkirch-Graffenstaden, France
FACSSymphonyTM	BD Biosciences, NJ, USA
Gel chamber MINI-Protein	Bio-Rad, CA, USA
ChemiDoc	Bio-Rad, CA, USA
Glass homogenizers	Omni International, Inc. Kennesaw, GA, USA
Leica EG1160 embedding center, dispenser + hot plate	Leica Biosystems, Wetzlar, Germany
Leica AF6000 LX with Leica type microscope DMI6000B	Leica Biosystems, Wetzlar, Germany
LI-COR Odyssey	LI-COR, NE, USA
Manual microtome RM2125 RTS	Leica Biosystems, Wetzlar, Germany
Microcentrifuge IR 220 VAC	Carl Roth, Karlsruhe, Germany
Microplate reader Fluorescence	Biotek, PC, Italy
NanoDrop™ One Microvolume UV-Vis spectrophotometer	Thermo Fisher Scientific, MA, USA
Real Time PCR System 7300	Thermo Fisher Scientific, MA, USA
SPECTROstar^{Nano} spectrophotometer	BMG LABTECH, Ortenberg, Germany
T100 Thermal Cycler	Bio-Rad, CA, USA
Thermomixer	Eppendorf, Hamburg, Germany
Thermo Scientific Forma Steri-Cycle i250 CO_2 incubator	Thermo Fisher Scientific, MA, USA
Transmission electron microscope. JEOL 1010	JEOL, MA, USA

Vertical laminar flow workbench, mini-V/PCR	Azbil Telstar Technologies Slu, Barcelona, Spain
Vortex Heidolph Reax 200	Heidolph, Schwabach, Germany
Water bath HI1210	Leica Biosystems, Wetzlar, Germany
ZEISS Axio Lab.A1 microscope	Carl Zeiss Microscopy GmbH, Jena, Germany

6.1.9. Software

Software	Manufacturer
Applied Biosystems 7300 Real-Time PCR System software	Thermo Fisher Scientific, MA, USA
AxioVision SE64. Rel.4.9	Carl Zeiss Microscopy GmbH, Jena, Germany
BioRender	BioRender.com (2022)
FACSDiva 6.0	BD Biosciences, NJ, USA
Flowjo sofware	Tree Star, NJ, USA
GraphPad Prism version 8.0	San Diego, CA
ImageJ Version 1.52u	LOCI, University of Wisconsin, USA
Image Lab software, Version 6.1.0	Bio-Rad, CA, USA
LAS_X_Core_3.5.7	Leica Microsystems, Wetzlar, Germany
Microsoft Office	Microsoft, NM, USA
Quantity One software	Bio-Rad, CA, USA
Spectronaut®	Biognosys, MA, USA
String-dbApp 11.5	String consortium (core data CPR, EMBL, SIB, KU, TUD and UZH)

6.1.10. Consumables

Product	Manufacturer
1.1 mL serum-gel polypropylene microtubes	Sarstedt Inc, Nümbrecht, Germany

96 well black bottom plate, TC surface with lid	Thermo Fisher, MA, USA
384 well plate barcoded for PCR	Thermo Fisher, MA, USA
Blood agar (TSA with 5% Sheep Blood/MacConkey) agar plate	Thermo Fisher Scientific, MA, USA
Cell culture plate sterile, 96 Well, flat-bottom with lid	Greiner Bio-One, Kremsmünster, Austria
CellStar® cell culture multiwell plates (6-wells, 12-wells)	Greiner Bio-One, Kremsmünster, Austria
Cell strainer sterile (100, 70 µm)	Thermo Fisher Scientific, MA, USA
CellTrics (35 µm)	Sysmex, SJD, Spain
Coverslips	Hirschmann, Eberstadt, Germany
Cryogenic tubes	Thermo Fisher Scientific, MA, USA
Eppendorf reference 2G single-channel, fixed volume (10 - 1000 µL)	Eppendorf AG, Hamburg, Germany
Eppendorf tubes (1.5 mL, 2.0 mL)	Thermo Fisher Scientific, MA, USA
Falcon tissue culture treated flasks (50 mL, 250 mL)	Thermo Fisher Scientific, MA, USA
Falcon tube (15 mL, 50 mL)	Labbox, Barcelona, Spain
Graduated filter tip (sterile) 10 µL, 200 µL, 1000 µL	Starlab, Hamburg, Germany
Histology cassettes	Deltalab, Barcelona, Spain
MicroAmp™ optical adhesive film	Thermo Fisher, MA, USA
Micropipete tips (100 µL, 200 µL and 1 mL)	Grenier Bio One, Kremsmünster, Austria
Mini Trans-Blot® electrophoretic transfer cell	Bio-Rad, CA, USA
Needle (22, 27G)	BD Plastipak, NJ, USA
Pipettes (5 mL, 10 mL, 25 mL)	Greiner Bio-One, Kremsmünster, Austria

Polyvinylidene difluoride (PVDF) membrane (0.45 µm or 0.22 µm)	Bio-Rad, CA, USA
Reactive strips (Ref: 06916686001)	Roche, Basel, Switzerland
Microscope KliniPath Silan printer slides.	Klinipath, Duiven, The Netherlands
Syringes 1 mL	BD Plastipak, NJ, USA
Syringe 1 mL with 27 x 13 needle	BD Plastipak, NJ, USA
Whatman® paper	Bio-Rad, CA, USA

6.2. METHODS

6.2.1. Maintenance of mice and animal experimentation

All animal experiments were designed and performed in accordance with the Spanish laws and regulations on animal protection (PROEX210/18; PROEX125.1/20). Mice were kept in a specific pathogen-free facility of the Faculty of Biology (at Universidad Complutense de Madrid) in a temperature-controlled room with 12-hour light/dark cycles, with free access to food and water, according to the guidelines of the Federation for Laboratory Animal Science Associations (FELASA). For the experiments, we used female and male mice in a C57BL/6J background at 10 weeks old, from Janvier Labs, France.

6.2.2. Experimental groups

The test group was fed with DUAL diet, which is composed of WD (40% kcal of fat, 20% kcal of fructose and 2% of cholesterol) and 10% ethanol (EtOH) in drinking sweetened water (6.75% D-glucose).

Three groups were used as controls: **i.** Control (fed with chow diet (Altromin) plus filtrated tap water), **ii.** WD (fed with WD and sweetened drinking water) and **iii.** EtOH (fed with chow diet plus 10% EtOH in sweetened drinking water) **(Fig. 15).** Sample size ranged from 5 to 7 animals per group.

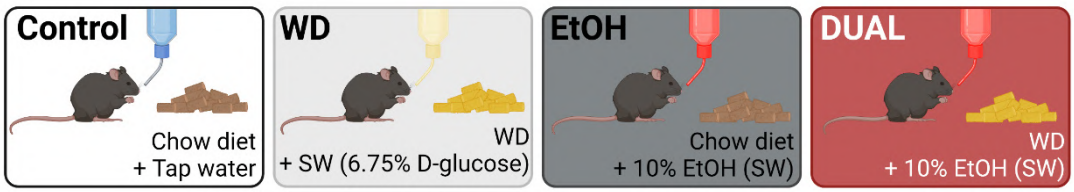

Fig. 15. Feeding groups in DUAL diet experiment. DUAL diet was established as a test group. Control, WD and EtOH feeding groups were established as controls.

6.2.3. Animal feeding

6.2.3.1. DUAL diet

The DUAL feeding was performed with 10-week-old mice with a body weight over 18 g.

Day 1-4: WD + ordinary tap water.

Day 5-7: WD + introduction of the 6.75% D-Glucose to the drinking water (sweetened water).

Day 8-10: WD + 1%vol/vol EtOH in sweetened water.

Day 11-12: WD + 2%vol/vol EtOH in sweetened water.

Day13-14: WD and 4% vol/vol EtOH in sweetened water.

Week 3: WD and 5% vol/vol EtOH in sweetened water.

From **week 4,** mice received WD and 10% vol/vol EtOH in sweetened drinking water until the end of treatment **(Fig. 16).**

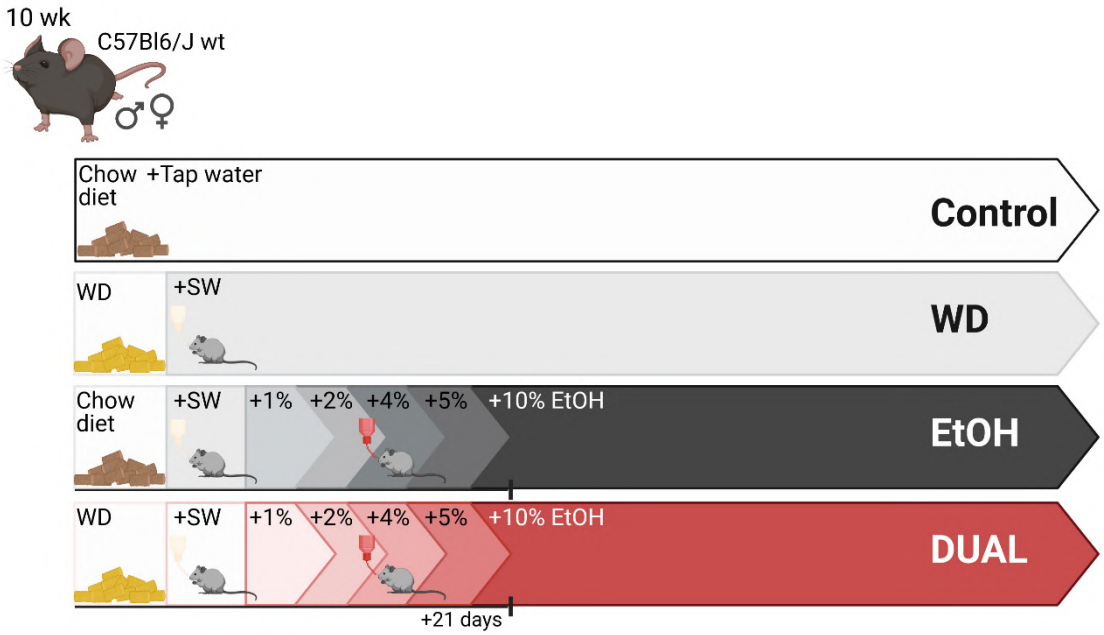

Fig. 16. Scheme of feeding for the different experimental groups. DUAL model.

The food was given *ad libitum* and placed directly in the cage dieting dish. In order to avoid EtOH evaporation and keep the constant concentration, the drinking bottle was changed twice a week. The time of the day, when the food and the water were changed was kept consistent through the experiment.

The duration of the feeding was 10, 23 or 52 weeks long (146, 147).

To further increase the ethanol concentration by over 10%, it needs to be raised a 5%/week. Initially we performed a pilot study to assess the optimal EtOH concentration.

Thus, on **week 5** EtOH concentration was 15% and on the **week 6** mice received 20% EtOH in the drinking water **(Fig. 17).**

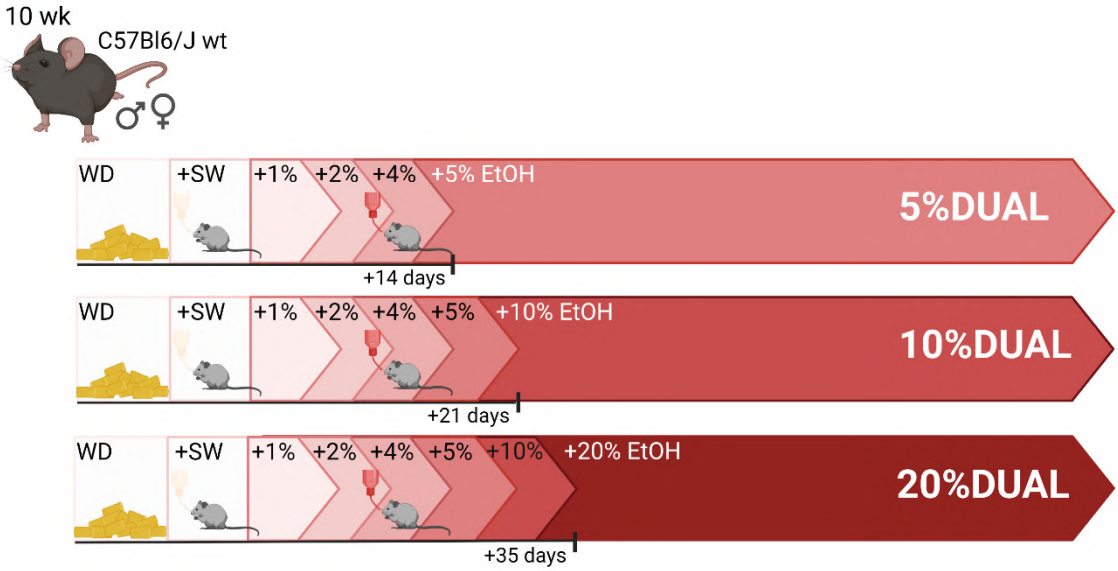

Fig. 17. Scheme of feeding for the assessment of optimal EtOH concentration.

6.2.3.2. DUAL + DEN model

14-day-old mice were injected with a single intraperitoneal (IP) DEN (Sigma-Aldrich) injection (25 mg/kg body weight). When animals were 10 weeks old, males were separated individually in cages and fed with DUAL or control diet. Feeding was 16 weeks long **(Fig. 18).**

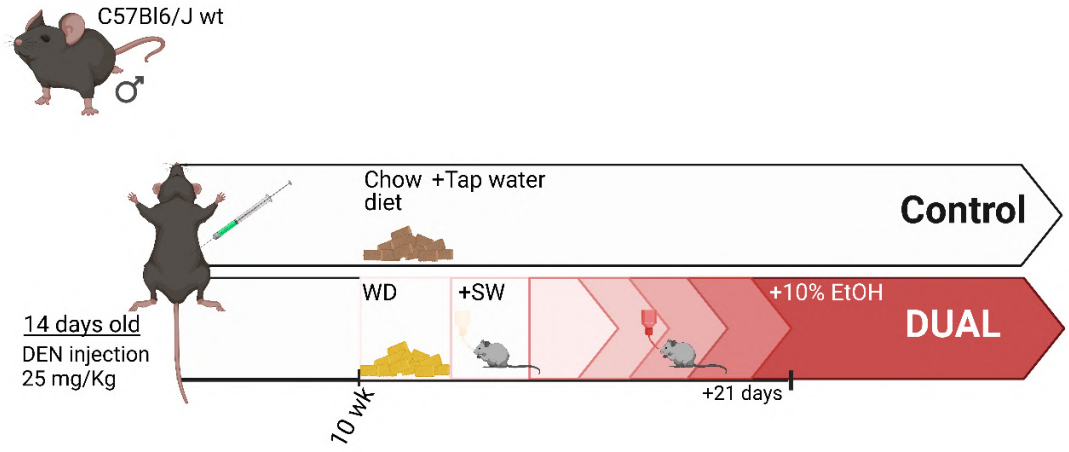

Fig. 18. Experimental design of DEN + DUAL model. DEN injection was administered at day 14 after birth. DUAL or control feeding started at the age of 10 weeks and was prolonged for 16 more weeks.

6.2.3.3. Antibiotic administration

A cocktail of antibiotics (ABX) was prepared and administered to DUAL, or control fed animals.

6.2.3.3.1. ABX administration in the drinking water

A cocktail of ABX in the specified concentration on the material section **6.1.7.3. Cocktail of absorbable and non-absorbable ABX** was added to the drinking water (sweetened, 10% EtOH) during the last 4 weeks of the short-term DUAL feeding (10 weeks) **(Fig. 19).** The fresh mixture of ABX was reconstituted every 2-days and drinking bottles were protected from the light to avoid degradation. Mice receiving only DUAL diet and only control diet were used as controls.

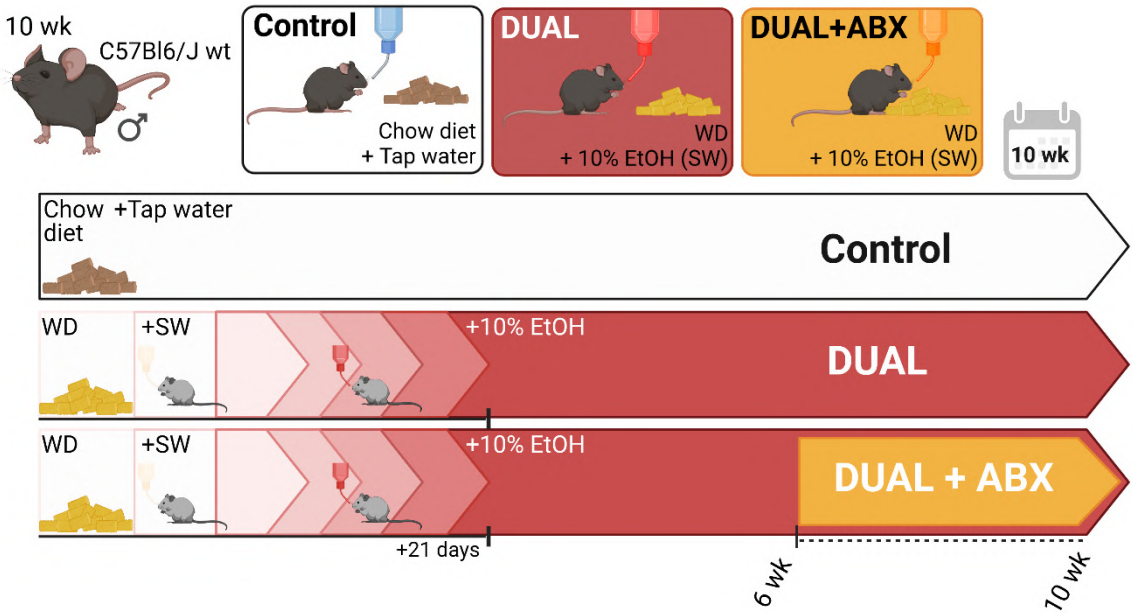

Fig. 19. Experimental design of ABX administration in the drinking water in the short-term feeding DUAL model of 10 weeks. A cocktail of ABX was administered into the drinking water during the last 4 weeks of feeding.

6.2.3.3.2. ABX administration by oral gavage

A total volume of 150 µL was administered to DUAL- or control- fed animals by oral gavage every 24 hours during the last 10 days of DUAL feeding **(Fig. 20).** The control mice were receiving either control or DUAL diet (148).

Mice were housed in separate ventilated cages to prevent cross-contamination among groups. Stool pellets were collected before ABX administration and at the end of the experiment.

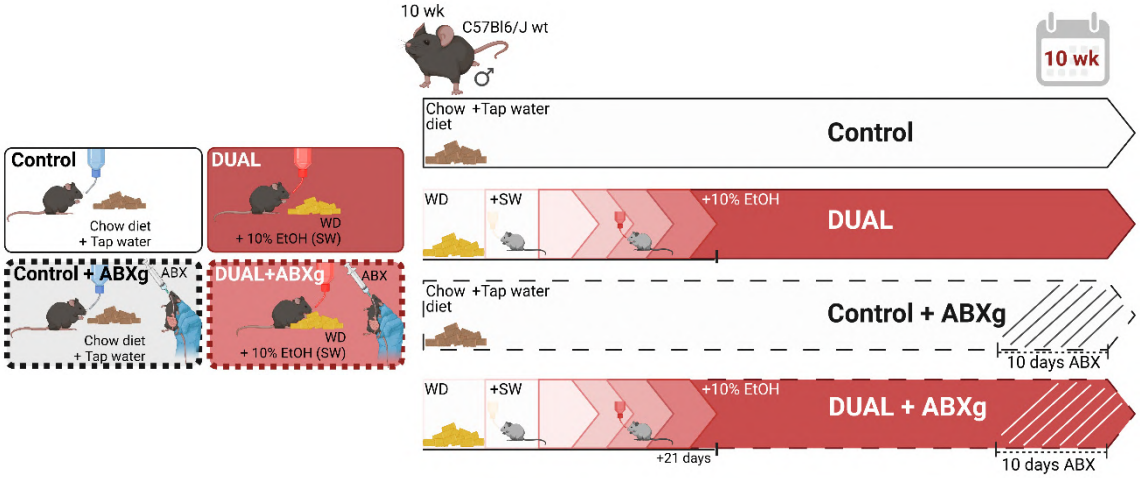

Fig. 20. Experimental design of ABX administration in the short-term fed DUAL model. 150 µL of cocktail of ABX were administered by oral gavage daily during the last 10 days of feeding.

6.2.3.4. Probiotic supplementation

Probiotic/placebo (Actial Farmaceutica SRL) supplementation maintaining DUAL diet was performed the last 4 weeks of short-term DUAL feeding (10 weeks) **(Fig. 21)**. Details can be found in the material section **6.1.7.5. Probiotics and placebo.**

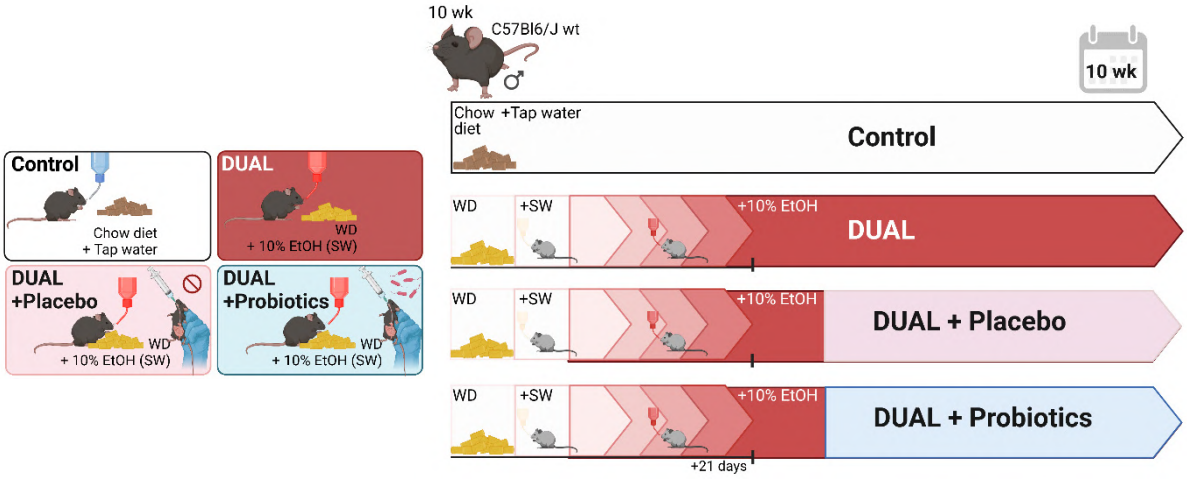

Fig. 21. Experimental design of probiotic/placebo supplementation in the short-term feeding DUAL model. Probiotic/placebo were administered by oral gavage during the last 4 weeks of short-term DUAL feeding (10 wk), twice per week.

To facilitate intestinal emptying, in week 6 of DUAL feeding a single oral dosage of 150 µL of CitraFleet® (Casen Recordati S.L.) was prepared following the manufacturer's instructions and given via oral gavage. 12 hours later, two additional doses of 100 µL of Citrafleet were orally administered (with 30 min gap between dosages). Mice were 12 h fasted. 100 µL of probiotic VSL#3® (Actial Farmaceutica SRL) corresponding to 4 billion bacteria were administered by oral gavage. VSL#3 contains four strains of *Lactobacillus (Lactobacillus plantarum, L. acidophilus, L. delbrueckii subsp. Bulgaricus* and *L. casei*), three strains of *Bifidobacterium* (*Bifidobacterium longum, B. breve* and *B. infantis*) and *Streptococcus salivarius subsp. Thermophilus*. The control group was fed with DUAL diet + 100 µL placebo following the same protocol that was above described (Actial Farmaceutica SRL).

During the four following weeks, the probiotic/placebo was administrated twice a week until the experimental end point **(Fig. 22).**

Mice were housed in separate ventilated cages to prevent cross-contamination among groups. Stool pellets were collected before probiotic administration and at the end of the experiment.

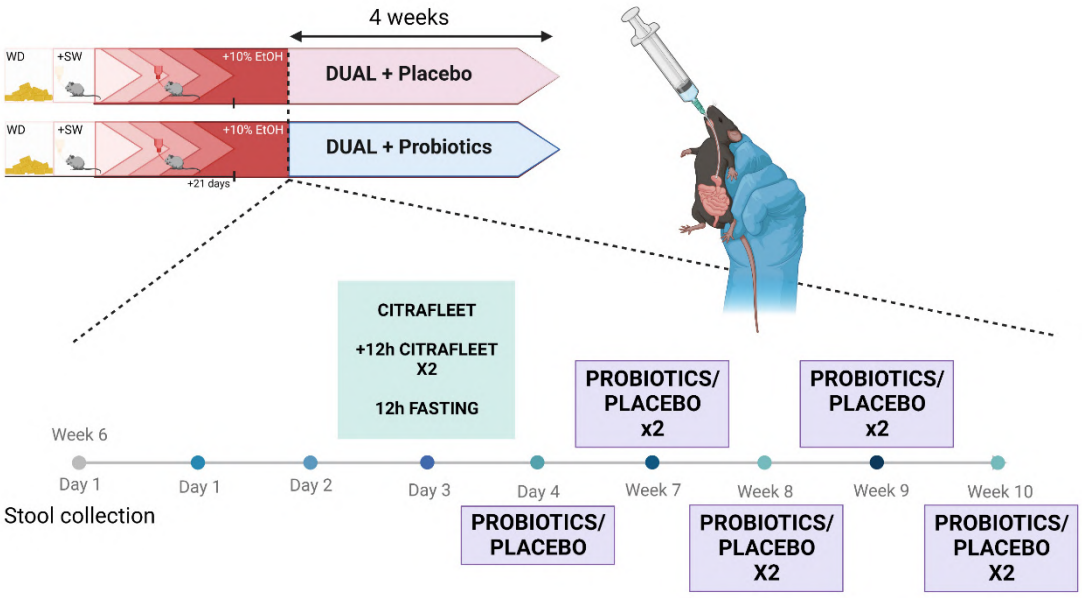

Fig. 22. Detailed experimental design of probiotic/placebo supplementation by oral gavage.

6.2.3.5. FMT

FMT maintaining DUAL diet was performed during the last 4 weeks of DUAL feeding (short 10- and long term 23-weeks experiments) **(Fig. 23)**.

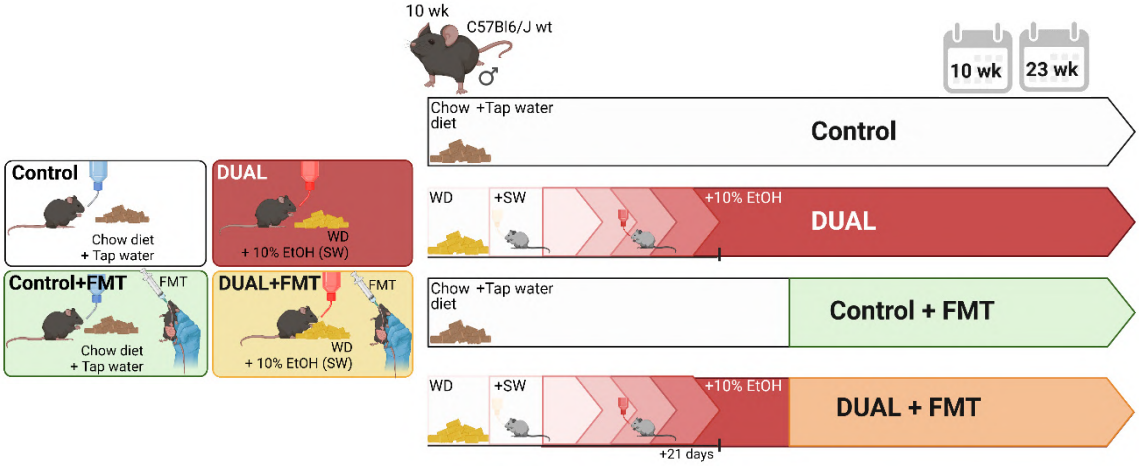

Fig. 23. Experimental design of FMT in the short-term DUAL feeding. FMT was performed with fresh stool from healthy donors to DUAL mice by oral gavage during last 4 weeks of DUAL feeding, twice per week.

At the beginning, 1 mg of Omeprazole® (Cinfa) was given to DUAL- or control-fed mice to prepare gastrointestinal track for FMT during three days in row. The third day, the Omeprazole ® gavage was accompanied by an oral dose of CitraFleet® (Casen Recordati S.L.) (150 µL). 12 hours later, two additional doses of 100 µL of Citrafleet were administered. After 12 h of fasting, 1 mg of Omeprazole® was again administered by gavage prior to FMT.

Fresh fecal pellets were collected from control mice (10 weeks old, kept on chow diet and normal water). Donor feces were manually homogenized, dissolved in saline solution (100 µg/µL), and filtrated through a cell strainer to remove debris. The supernatant was collected and used as transplant material within 10 min to prevent changes in bacterial composition. 150 µL of filtrated solution were administered by oral gavage to recipient mice. Donor and recipient mice were paired (same donor to same recipient) along the treatment.

From this point forward, 1 mg Omeprazole® administration plus FMT was performed twice a week until the end of the feeding. Feeding and FMT scheme for 10- and 23-weeks feeding are represented in **Fig. 24 A, B** respectively.

Control and DUAL-fed mice without gavage were used as controls.

Mice were housed in individual ventilated cages to prevent cross-contamination among groups. Stool pellets were collected before transplantation (at baseline) and at the end of the experiment.

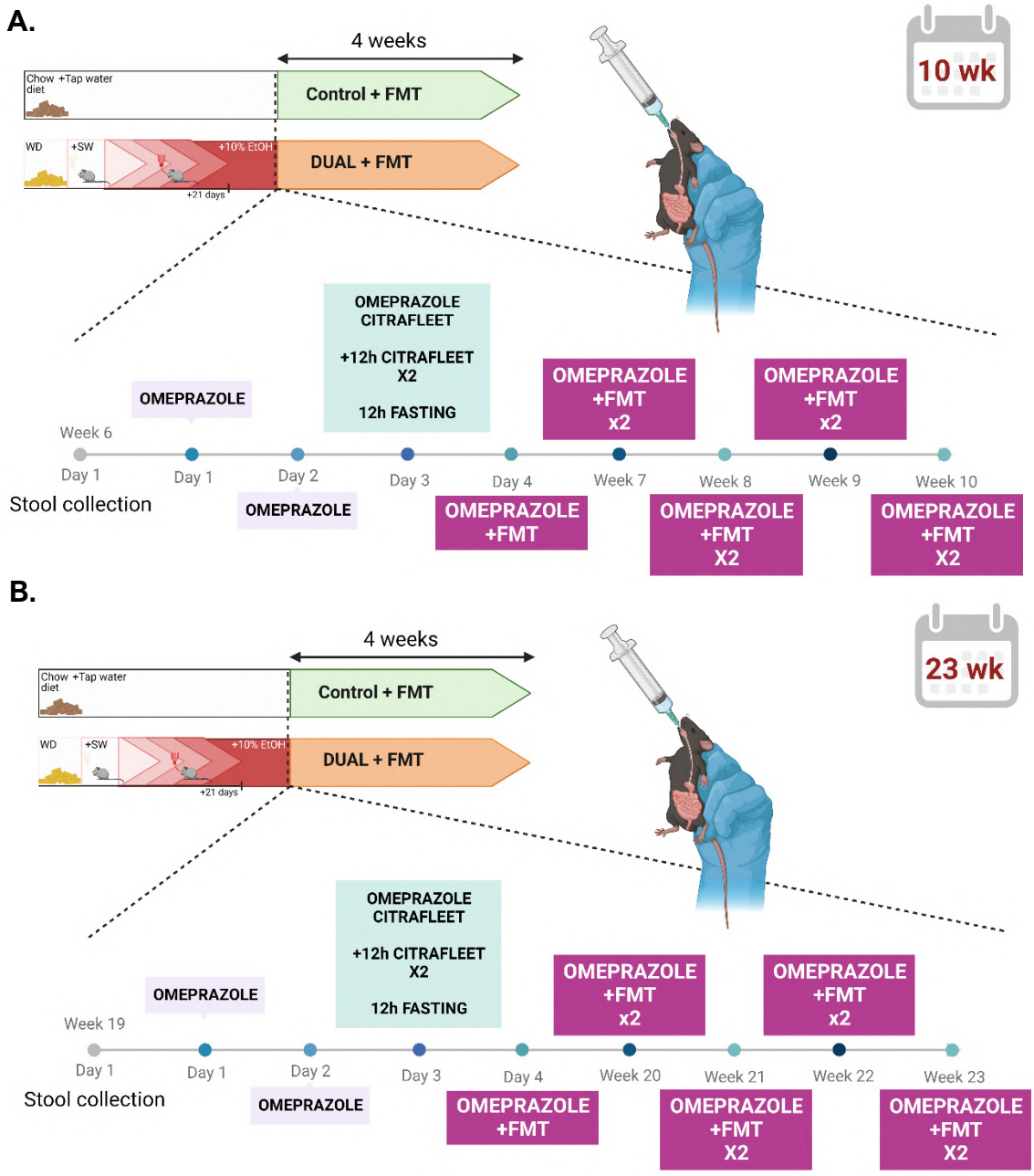

Fig. 24. Detailed experimental scheme of FMT in DUAL animals. FMT was performed with fresh stool pellets from healthy donors to DUAL mice by oral gavage during the last 4 weeks of feeding. **A.** Short-term DUAL feeding (10 wk). **B.** Long-term DUAL fed animals (23 wk).

6.2.3.6. DUAL withdrawal

Mice were exposed to DUAL diet for a period of 10 or 23 weeks; after that, the DUAL diet was removed, and DUAL feeding was replaced with chow diet and filtrated tap water for 21 days **(Fig. 25)**.

Mice were housed in separate ventilated cages to prevent cross-contamination among groups. Stool pellets were collected before transplantation (at baseline) and at the end of the experiment.

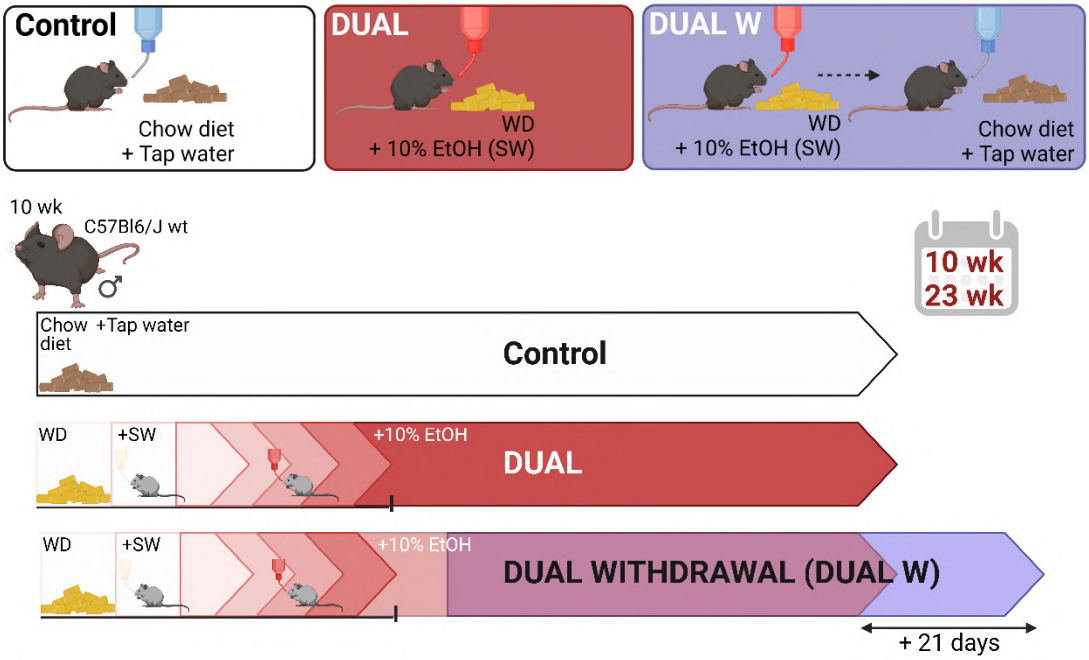

Fig. 25. Experimental design of DUAL withdrawal (DUAL W). After 10 weeks of DUAL feeding, DUAL diet was replaced with chow diet and normal water for the next 21 days.

6.2.4. Glucose Tolerance Test (GTT)

At the end of the feeding, glucose levels in blood were measured after a 12 h fasting. GTT was further performed through an IP injection of 7.5 g/kg body mass of 20% glucose solution (Braun). Glucose levels were measured using an Accu-Check glucometer (Roche) and reactive strips (Roche) after 15, 30, 60, 90 and 120 minutes after the injection, following the established protocols (149).

6.2.5. Insulin Tolerance Test (ITT)

At the end of the feeding, ITT was performed after a 6 h fasting through an IP injection of 0.75 IU/kg from an *Actarapid* stock solution (Sigma-Aldrich). Glucose levels were measured using an Accu-Check glucometer (Roche) and reactive strips (Roche) after 0, 15, 30, 60 and 90 minutes, following the established protocols (149).

6.2.6. FITC dextran

A dosage of 44 mg/100 g of body weight (from a stock solution of 100 mg/mL in saline solution) of FITC-dextran 4 kDa (TdB Labs) was administered by gavage to mice after 8 h of fasting. 4 hours after FITC administration, mice were sacrificed. FITC-dextran concentration in serum was determined by measuring the IF in serum (together with a standard curve) at a 485 nm excitation and 528 nm emission wavelength using IF plate reader (Biotek) (150).

6.2.7. Bodipy assay

Mice were fasted for 16 h and a 2 µg/g body weight dosage of BODIPY® 500/510 C1, C12 fatty acids (ThermoFisher) was administered by gavage. 2 h later, mice were sacrificed, and small intestines were excised, separated into three parts: duodenum, jejunum and ileum. For this experiment, the middle part was taken and frozen in O.C.T. media *Tissue-Tek* (Sakura) (151).

6.2.8. Mouse sacrifice

12-18 - hours fasted mice were sacrificed by an overdose of isofluorane (Solvet) inhalation. Body weight and mouse length were measured. The abdominal cavity was cut open along the *Linea alba*. Two relaxation cuts were placed along the costal arches at the lateral abdominal walls.

6.2.9. Liver extraction

The liver was removed by dissecting the ligaments and placed in cold PBS. Liver images were taken with a MZ16 Stereo microscope with a Leica DFC480 digital camera through the DISKUS Z16 APO (Leica Biosystems).
The gallbladder was separated. One piece of each left and right lobe was embedded in O.C.T. media *Tissue-Tek* (Sakura) and stored at -80ºC. Another piece of both big lobes was taken and placed in 4% PFA (AppliChem) for paraffin embedding. The rest of the liver lobes were cut into small pieces and snap frozen in liquid nitrogen and stored at -80ºC.

6.2.10. Extraction of gonadal WAT

After cutting the peritoneum transversely, both perigonadal fat pads were carefully dissected. Half of the WAT tissue from each side was placed into a plastic cassette for paraffin embedding; the other half was cut into small pieces and frozen in cryovials in liquid nitrogen and further placed at -80ºC.

6.2.11. Gut extraction

The gut was extracted from pylorus until the anus. Total gut, colon and caecum length were measured. The gut content was carefully washed out using a syringe with PBS. The small intestine was equally divided into three parts as it is shown in **Figure 26** to differ the duodenum, jejunum, and ileum. Colon was separated. The first part of each section was placed into a plastic cassette and fixed in Metacarn **(described in the material section 6.1.3. Standard buffer and media).** The second one, into O.C.T media (Sakura) and frozen at -80ºC. The third part was cut into small pieces and placed into a cryotube that was frozen in liquid nitrogen and stored at -80ºC **(Fig. 26).**

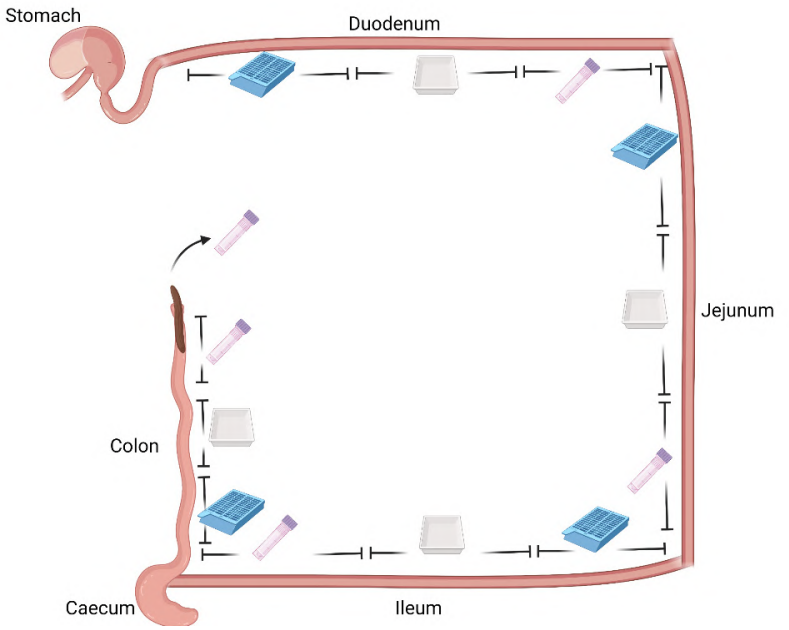

Fig. 26. Schematic representation of gut processing after mouse sacrifice. Made with BioRender.com.

6.2.12. Stool sample extraction

Prior to sacrifice, mice were placed in empty cages for fresh stool collection. On the day of sacrifice, stool was extracted from the rectum for analysis.

6.2.13. Serum analysis

Immediately after euthanasia, blood was collected from inferior vena cava using a 1 mL syringe and a 27G needle and placed in Serum-Gel Polypropylene (Sarstedt) microtubes. Blood was centrifuged at 12000 rpm, 10 min, 4ºC. Serum fraction was extracted and stored at -80ºC.

The subsequent measurement of Alanine Aminotransferase (ALT), Aspartate Aminotransferase (AST), Lactate dehydrogenase (LDH) and cholesterol levels was performed in the Central clinical routine laboratory at University Hospital RWTH Aachen (Germany).

6.2.14. Paraffin tissue processing

Liver, WAT, and intestine biopsies were placed into plastic cassettes and fixed in 4% PFA (AppliChem). After 48 h fixation, samples were washed 3 times for 10 minutes in PBS or distilled water (dH_2O). For dehydration, samples were

rinsed in increasing concentrations of alcohol (50- 70- 85- and 95% one hour each) and kept in 95% EtOH overnight. The day after, samples were rinsed twice in 100% EtOH (30 min each), cleaned in a mixture of xylene and absolute ethanol (1:1) and in pure xylene (Carl Roth) two times for 30 min. After complete dehydration, they were incubated in paraffin wax (Leica) at 71ºC, making 3 changes of 1 h each.

Finally, the samples were embedded in paraffin using an *Histocore Arcadia C + H* (Leica) and cut to a thickness of 5 µm using a rotatory microtome.

6.2.15.Haematoxylin and eosin staining (H&E)

Haematoxylin and eosin (H&E) staining was performed in paraffin sections of liver, WAT and gut tissue. Deparaffinization and rehydration of sections were performed through 3 changes of 5 min in xylene followed by 2 changes of 5 min in decreasing alcohol concentrations of 100-, 95-, and 70%. Then, samples were rehydrated in dH_2O two times of 5 min.

Nuclei were stained in blue by rinsing the slides in hematoxylin (AppliChem) for 2 min and washed in tap water for 10 min and 2x5 min in dH_2O. The cytoplasm and the rest of tissue were stained in eosin (Sigma-Aldrich) for 30 sec and further washed in dH_2O. Dehydration of the sample was performed by 2x10 sec in 95% EtOH followed by 100% EtOH and 3x5 min xylene.

Finally, stained sections were mounted with Roti®-Histokitt (Carl Roth) and covered with a coverslip. Samples were visualized using an optical microscope (Nikon) immediately after staining, photomicrographs were taken at 10x, 20x and 40x magnification.

6.2.16.Sirius red staining

Sirius red (SR) staining was performed in order to determine collagen deposition in the liver. For deparaffinization, slides were rinsed in xylene 2x5 min followed by 2x5 min changes in decreasing concentrations of ethanol from 100% to 70% ending in dH_2O as it has been previously described.

Subsequently, slides were rinsed in Picro-Sirius red solution for 1 h followed by a 4 min incubation in acidified water. Dehydration of the sample was

performed by 2x10 sec in 95% EtOH followed by 100% EtOH and 3x5 min xylene.

Finally, stained sections were mounted with Roti®-Histokitt (Carl Roth) and covered with a coverslip. Solutions are described in the material section **6.1.3. Standard buffer and media.** Samples were visualized using an optical microscope (Nikon) immediately after staining, photomicrographs were taken at 10x, 20x and 40x magnification.

6.2.17. Hass bilirubin staining

Hass bilirubin staining was performed to identify bilirubin accumulations in the liver parenchyma. For deparaffinization, slides were rinsed in xylene 2x5 min followed by 2x5 min changes in decreasing concentrations of EtOH from 100% to 70% ending in dH_2O as it has been previously described. Then, they were rinsed in *Fouchet's* reagent for 5 minutes and shortly washed in tap water followed by dH_2O.

Next, slides were incubated with *Van Gieson's* solution for 3-5 min and further washed in dH_2O. Dehydration of the sample was performed by 2x10 sec in 95% EtOH followed by 100% EtOH and 3x5 min xylene.

Finally, stained sections were mounted with Roti®-Histokitt (Carl Roth) and covered with a coverslip. Solutions used are described in the material section **6.1.3. Standard buffer and media.** Samples were visualized using an optical microscope (Nikon) immediately after staining, photomicrographs were taken at 10x, 20x and 40x magnification.

6.2.18. Pathological analysis of the samples

Liver histology, visible in the H&E and SR, was evaluated by an expert liver pathologist from Hospital Gregorio Marañón (Madrid, Spain) blinded to the dietary condition using *Bedossa* score system (152).

H&E staining in gut was carefully analyzed by measuring the size of the villi (length) and size of the crypts (depth) in each section using ImageJ software (151).

6.2.19.Immunohistochemistry (IHC) staining

Five µm sections were heated at 60ºC for 30 minutes and deparaffinization and rehydration of sections were performed through 3 changes of 5 min in xylene followed by 2 changes of 5 min in decreasing alcohol concentrations of 100-, 95-, and 70%. Then, samples were rehydrated in dH_2O twice of 5 min. Antigen unmasking was performed by boiling the sections in 10 mM sodium citrate buffer (citrate/PBS-T, pH=6.0) in a pressure cooker (Aptum Biologics). When finished, the slides were washed in dH_2O. Endogenous peroxidase was blocked using BLOXALL® (Vector Laboratories) solution for 10 min in a humid chamber.

Next, slides were rinsed in dH_2O followed by a wash of PBS. To prevent nonspecific binding of the secondary antibody, sections were blocked with horse serum solution (Vector Laboratories) for 30 min. Primary antibody, diluted in PBS, 1% BSA, 0.3% Triton, was added and incubated overnight at 4ºC.

On the following day, the sections were washed, and the corresponding biotinylated antibody was incubated for 1 h. After washing, the binding of the second antibody to first antibody was developed using DAB (Vector Laboratories), resulting positive staining labeled in brown. DAB reaction was further stopped in water and hematoxylin solution was used for counterstain. Dehydration of the sample was performed by 2x10 sec in 95% EtOH followed by 100% EtOH and 3x5 min xylene.

Finally, stained sections were mounted with Roti®-Histokitt (Carl Roth) and covered with a coverslip. Antibodies used are listed in **6.1.5. Immunostaining (primary and secondary antibodies)** in the material section.

Samples were visualized using an optical microscope (Nikon) immediately after staining, photomicrographs were taken at 10x, 20x and 40x magnification.

6.2.20.Immunofluorescence (IF) staining in paraffin

Five µm sections were heated at 60ºC for 30 minutes and treated with xylene and decreasing EtOH solutions ending in dH_2O for deparaffinization and rehydration, as it has been previously described.

Antigen unmasking was performed by boiling the sections in 10 mM sodium citrate buffer (citrate/PBS-T, pH=6.0) in a pressure cooker (Aptum Biologics). When finished, the slides were washed in dH_2O.

To prevent non-specific binding of the secondary antibody, sections were blocked with 5% goat serum (Thermo Fisher Scientific) in PBS in a humid chamber to prevent the tissue to dry for 1 h. When blocking solution was removed, slides were incubated in the primary antibody solution containing 1% goat serum in PBS overnight. The next day, samples were rinsed in PBS for washing and secondary IF antibody was added for 1 h. Finally, the slides were washed and Vectashield mounting medium containing DAPI (Vector Laboratories) was used for counterstain and mounting using a coverslip. Antibodies are listed in **6.1.5. Immunostaining (primary and secondary antibodies)** in the material section.

Pictures were taken through an AxioImager A1 microscope (Carl Zeiss Microscopy GmbH, Jena, Germany) and AxioVision software or in a Leica AF6000 LX with Leica type microscope DMI6000B together with LAS_X_Core software at 20x magnification. Positive cells (%) or positive area (%) were quantified using ImageJ software.

6.2.21.Frozen sections

Liver and gut samples were placed in O.C.T. media *Tissue-Tek* (Sakura) and preserved at -80ºC. Then they were cut into 7 and 5 µm using a cryostat (Leica Biosystems).

6.2.22.Oil red O staining

Neutral lipids and TG deposition in the liver were identified through Oil Red O (ORO) staining in 7 µm frozen sections. Samples were fixed in 4% PFA

(AppliChem) for 25 min and washed for 3x5 min in dH_2O. For staining, sections were rinsed in ORO working solution for 30 min, and color excess was removed by washing them, in dH_2O. Hematoxylin solution (AppliChem) was used for counterstain. After slides were washed, they were mounted using *Dako faramount aqueous* (Dako Agilent) mounting medium and covered with coverslips. ORO solution is described in the material section **6.1.3. Standard buffer and media.** Pictures were taken at 10x and 20x magnification and positive-ORO stained area (%) was quantified using ImageJ software (153). Samples were visualized using an optical microscope (Nikon) immediately after staining, photomicrographs were taken at 10x and 20x magnification.

6.2.23. IF staining in frozen sections

IF staining was performed in 5 µm frozen sections. Samples were fixed in 4% PFA (AppliChem) for 25 min and washed for 3x5 min in PBS. To prevent non-specific binding of the secondary antibody, sections were blocked with 5% goat serum in PBS in a humid chamber to prevent the tissue to dry for 1 h. When blocking solution was removed, slides were incubated in the primary antibody solution containing 1% goat serum in PBS for 1 h. Later, samples were rinsed in PBS for washing and secondary IF antibody was added for 1 h. Finally, slides were washed and Vectashield mounting medium containing DAPI (Vector Laboratories) was used for counterstain and mounting using a coverslip. Antibodies are listed in **6.1.5. Immunostaining (primary and secondary antibodies)** in the material section. Image acquisition was performed using an AxioImager A1 microscope (Carl Zeiss Microscopy GmbH, Jena, Germany) and AxioVision software or in a Leica AF6000 LX with Leica type microscope DMI6000B together with LAS_X_Core software. Pictures were taken at 20x magnification and positive cells (%) or positive area (%) were quantified using ImageJ software.

6.2.24. Phalloidin staining

IF staining was performed in 5 µm frozen sections. Samples were fixed in 4% PFA for 25 min and washed for 3x5 min in PBS. To prevent non-specific

binding of secondary antibody, sections were blocked with 5% goat serum in PBS in a humid chamber to prevent the tissue to dry for 1 h. When blocking solution was removed, 2 µg/mL of Phalloidin (Sigma-Aldrich) in PBS/1%BSA was added to the sample and stained for at least 30 minutes. Finally, slides were washed in PBS and Vectashield mounting medium containing DAPI (Vector Laboratories) was used for counterstain and mounting using a coverslip. Image acquisition was performed using an AxioImager A1 microscope (Carl Zeiss Microscopy GmbH, Jena, Germany) and AxioVision software or in a Leica AF6000 LX with Leica type microscope DMI6000B together with LAS_X_Core software. Pictures were taken through an IF microscope at 20x magnification and size of the cells was measured using ImageJ software.

6.2.25. Bodipy staining

10 µm thick gut frozen sections from animals challenged with BODIPY® 500/510 C1, C12 fatty acids (Thermo Fisher Scientific) were placed at room temperature and fixed in 4% PFA (AppliChem) for 25 min. Later, they were washed for 3x5 min in PBS. Vectashield mounting medium containing DAPI (Vector Laboratories) was used for counterstain and mounting using a coverslip. Image acquisition was performed using an AxioImager A1 microscope (Carl Zeiss Microscopy GmbH, Jena, Germany) and AxioVision software or in a Leica AF6000 LX with Leica type microscope DMI6000B together with LAS_X_Core software. Pictures were taken through an IF microscope at 20x magnification and positive BODIPY area (%) was quantified through ImageJ software.

6.2.26. Terminal deoxynucleotidyl transferase dUTP Nick end labeling (TUNEL)

Cell death was determined though TUNEL assay IF staining. 5 µm cryopreserved slides were defrosted and fixed in 4% PFA (AppliChem) for 25 min. After fixation, the sections were washed in PBS and incubated for 10 min in 3% H_2O_2 in methanol followed by washing for 10 min in PBS.

To have access to the DNA, nuclei were shortly (2 min) permeabilized in cold 150 mM Na-Citrate solution and washed in PBS.

Labeling reaction (Roche) was spread on each section and incubated overnight at 4ºC in a dark humidified chamber.

The following day, slides were washed with PBS 4 times of 10 min each. Vectashield mounting medium containing DAPI (Vector Laboratories) was used for counterstain and mounting using a coverslip. Solutions are described in the material section **6.1.3. Standard buffer and media.** Image acquisition was performed using an AxioImager A1 microscope (Carl Zeiss Microscopy GmbH, Jena, Germany) and AxioVision software or in a Leica AF6000 LX with Leica type microscope DMI6000B together with LAS_X_Core software. Pictures were taken through an IF microscope at 20x magnification and positive TUNEL cells (%) were quantified through ImageJ software.

6.2.27.Electron microscopy tissue processing and images

Fresh liver tissue was fixed in 4% PFA (AppliChem) and 2.5% glutaraldehyde buffer (Thermo Fisher Scientific) at 4ºC. The following day, after washing the samples, they were post-fixed in 1% osmium tetroxide and dehydrated in increasing concentrations of acetone (Applichem). Last, the tissue was embedded in *Spurr resin* (Electron Microscopy Sciences) and cut using an ultramicrotome (Leica, Microscopy CAI UCM). Finally, they were analyzed using a Transmission Electron Microscope *Jeol 1010* (Jeol) (Centro Nacional de Microscopía Electrónica, UCM).

6.2.28.Flow cytometry

6.2.28.1. Tissue processing for flow cytometry

- Isolation of immune cells from liver

Liver (1 g) was minced and transferred into a prepared digestion buffer containing DMEM (Thermo Fisher Scientific), collagenase (0.75 mg/mL) (Thermo Fisher Scientific) and DNAse I (0.05 mg/mL) (Thermo Fisher Scientific). Samples in the digestion media were preheated and placed in an

orbital shaker at 37ºC, 200 rpm, for 30 min. After the digestion, the content was poured into a new tube and filtered through a 100 µm cell strainer (Thermo Fisher Scientific). A syringe plunger was used to facilitate the filtration. Then, 15 mL of cold complete DMEM was added to stop any remnant enzymatic activity.

Hepatocytes were precipitated and discarded after 3 centrifugations at 50 xG, 3 min, 4ºC.

After a new centrifugation at 900 rpm, 7 min, 4ºC the rest of the cells were found in the pellet. Supernatant was discarded and 1 mL ACK lysis buffer (Thermo Fisher Scientific) was added and incubated for 5 min at room temperature to eliminate red blood cell contamination. The reaction was stopped by adding 10 mL of CMF PBS (Sigma-Aldrich) and subsequently filtered through 35 µm filters (Sysmex). After a centrifugation at 900 rpm, 7 min, 4ºC, immune cells were ready for staining.

- Isolation of immune cells from colon

The piece of the colon for flow cytometry analysis was weighted and cut longitudinally and placed in CMF cold PBS (Sigma-Aldrich). Later, it was cut into small pieces and placed into a pre-warmed CMF PBS/FBS and 2 mM EDTA solution and washed several times using an orbital shaker. After filtering with a cell strainer (Thermo Fisher), they were transferred to another tube where 10 mL of collagenase solution (Thermo Fisher) for digestion were added and incubated into an orbital shaker at 200 rpm for 45 min at 37ºC.

Then, the content was filtered through a 70 µm cell strainer and FACS buffer with FBS (1:1) was added. After centrifugation at 1500 rpm for 5 min at 4ºC, the supernatant was discarded and the cell pellet resuspended in ice-cold FACS buffer and filtered again through a 30 µm cell strainer (Sysmex).

6.2.28.2. Staining for flow cytometry

Cell suspensions from liver and colon were incubated with the viability marker LIVE/DEAD Fixable Aqua (Thermo Fisher) in PBS, following the manufacturers instructions for 1 h at 4°C. Cells were preincubated for 10 min at 4°C with anti-

mouse CD16/CD32 (clone 2.4G2, Tonbo Bioscience) at 1:200 dilution before staining with the antibody cocktails. Samples were then stained with the indicated antibodies at 1:200 dilution (see tables) for 20 min at 4ºC in FACS buffer (PBS supplemented with 3% FBS, 2 mM EDTA and 0.2% sodium azide). For intracellular staining, cells were fixed and permeabilized with a Foxp3/Transcription Factor Staining Buffer Kit (Tonbo Biosciences). Antibodies are listed in the material section **6.1.5.3. Flow cytometry antibodies.**

6.2.28.3. Flow cytometry analysis

Events were acquired on a FACSymphonyTM (BD) flow cytometer, in Centro Nacional de Investigaciones Cardiovasculares (CNIC), using the FACSDiva 6.0 software (BD Biosciences) and data were analyzed using Flowjo software (Tree Star).

6.2.29.Quantification of TG in the liver

A 40 mg cryopreserved liver sample was homogenized in 1 mL homogenization TG buffer (material section **6.1.3. Standard buffer and media)** and centrifuged for 10 min at 12000 rpm. For the standard curve, Biocal (Gernon RAL) (calibrator) was used following the manufacturers protocol. Sample and reagent were used in a 1:100 ratio in a 96-well plate. After 10 min incubation at room temperature, absorbance was read at 505 nm using a plate reader spectrophotometer (BMG LABTECH).

6.2.30.Quantification NEFA in serum

NEFA were determined in serum samples using a COBAS c311 analyzer (Roche) in collaboration with M. Ávila from CIMA (Universidad de Navarra).

6.2.31.Lipid extraction from feces

Feces were freshly collected from the mouse cage. 5 mL of saline solution were added to 1 g of feces and homogenized. Then, a chloroform: methanol

(1:1) solution was added and mixed. After centrifugation at 1000 xG for 10 min at room temperature, the lower liquid phase obtained contained the extracted lipids. A 22G needle was inserted into the base of the tube and lipid phase was eluted into a glass tube.
After evaporation, dry matter of lipids was visible and weighable (154).

6.2.32.Quantification of TBS in serum and in liver

BA content in serum and stool was measured through an enzymatic colorimetric assay based on the 3-α-hydroxyl group that can be oxidized to a 3-keto group by the enzyme 3-α-hydroxysteroid dehydrogenase. This experiment was performed in collaboration with F.Schaap, Maastricht University, The Netherlands. The Total Bile Acid Assay kit (Diazyme) was used.
Reagent 1 of the kit (210 µL) plus 4 µL of serum were added to the plate and incubated at 37ºC for 5 min. Then, 70 µL of reagent 2 were mixed and incubated at 37ºC for 2-3 min. Absorbance was read at 405 nm.
Total bile acid concentration was calculated using the following formula:
Sample A_{405}-Blank A_{405}/Calibrator A_{405}-Blank A_{405} x 50 µmol/L.

6.2.32.1. Determination of BA in serum

Serum samples were directly used for BA determination.

6.2.32.2. Determination of BA in liver

A piece of liver (50 mg) was homogenized in 1 mL 75% EtOH and the resultant mixture was incubated for 2 h at 50ºC in glass tubes. Then, it was centrifuged at 6000 xG, 10 min, 4ºC. The supernatant contained BAs fraction.

6.2.33.RNA

6.2.33.1. RNA isolation

Cryopreserved tissue was carefully homogenized in TRIzol (Thermo Fisher Scientific) using a FastPrep-24TM5G (MO Biomedicals, Illkirch-Graffenstaden, France). After homogenization, 200 µL of chloroform (AppliChem) were added per 1 mL TRIzol used. The solution was hand-shaken and incubated at 4ºC for 30 minutes. Later, samples were centrifuged at 12000 rpm for 12 min at 4ºC. The upper and transparent phase was transferred into a new tube without disrupting the interphase and additionally isopropanol (AppliChem) in a 1:1 ratio was added. The mixture was incubated for 20 min at 4ºC and later centrifuged at 12000 rpm, 10 min, 4ºC.

Supernatant was removed and RNA-containing pellet was washed 3 times with 1 mL ethanol followed by an 8500 rpm centrifugation of 5 min at 4ºC.

After the last wash, supernatant was discarded and the pellet was air dried for 30-40 min until it turns transparent. To solubilize the RNA, the pellet was resuspended in molecular H_2O (AppliChem) and dissolved at 65ºC in a Thermomixer (Eppendorf). Samples were stored at -80ºC.

6.2.34.RNA concentration determination and cDNA synthesis

RNA concentration and purity were determined by a NanoDrop Spectrophotometer (Thermo Fisher Scientific). Considering protein free RNA when A_{280}/A_{260}~1.8-2.0 and non-contaminated RNA A_{260}/A_{230}~2.2-2.4.

For complementary DNA (cDNA) synthesis, 1 µg of RNA was used. Reverse transcription was performed using Applied Biosystems™ high-capacity cDNA reverse transcription kit (Thermo Fisher Scientific) following the manufacturers protocol. **(Table 1).**

Table 1. RT reaction mix

Reagent	Volume (µL)
RNA (1 µg/µL)	10
Water for molecular biology	4.2
10x RT Buffer	2

25x dNTPs	0.8
10x Random primers	2
Enzyme Retrotranscriptase	1
Total volume	20

RT reaction was incubated in a thermocycler (T100 thermal cycler, Bio-Rad) using the following protocol (**Table 2**):

Table 2. RT thermocycler protocol

Temperature	Time (hh:mm:ss)
25ºC	00:10:00
37ºC	02:00:00
85ºC	00:05:00
4ºC	Infinite hold

Last, 85 µL of water for molecular biology (AppliChem) were added to the cDNA resulting from this reaction and samples were stored at -20ºC.

6.2.35.Quantitative Real-Time Polymerase Chain Reaction (RT-QPCR)

Real-Time Quantitative PCR (RT-qPCR) was performed in 10 µL reaction volume using SYBER Green Master Mix (Thermo Fisher Scientific, Invitrogen) **(Table3).**

Table 3. qPCR reaction mix. Volume/well.

qPCR reaction mix/well	Volume (µL)
cDNA	2.5
Forward primer	1
Reverse primer	1
SYBR Green ERTM qPCR	5
Water for molecular biology	0.5
Total volume	10

*Reaction mix for a total volume of 10 µL suitable for a 384-well plate.

The Real-time PCR System 7300 (Applied Biosystems) in the Genomics and Proteomics Facility (Facultad de Biología, Universidad Complutense de Madrid) was used following the program described in **Table 4.** For dissociation curve steps described in the second part of **Table** 4 were added to the PCR program. Relative expression was calculated using the $2^{-\Delta\Delta CT}$ method that normalizes gene expression to a housekeeping gene expression (*Gapdh) (155)*. Used primers are listed in **Primer sequences for RT-qPCR** in the material section.

Table 4. qPCR program

PCR program	Temperature	Time (hh:mm:ss)	Cycles
Activation	95ºC	00:00:10	
Denaturing	95ºC	00:00:15	X40
Annealing/Elongation	60ºC	00:01:00	
Conservation	4ºC	hold	

Dissociation curve (steps added to PCR program)	
Temperature	**Time (hh:mm:ss)**
95ºC	00:00:15
60ºC	00:01:00
95ºC	00:00:15

6.2.35.1. 3’ mRNA sequencing

3’ mRNA sequencing was performed and analyzed by the Genomics Facility of Aachen Interdisciplinary Center for Clinical Research (IZKF), Aachen, Germany. Briefly, input RNA was quantified using the QuantiFluor RNA System on a Quantus Fluorometer and quality control was performed using a Bioanalyzer 2100 with the Eukaryote Total RNA Nano assay. The sequencing library was prepared using the Collibri 3’mRNA Library Prep Kit following manufacturers instructions. Before sequencing, the library concentration was quantified using the QuantiFluor dsDNA System on a Quantus Fluorometer and quality was checked on an Agilent 4200 TapeStation System with the High

Sensitivity D1000 ScreenTape Assay. Library sequencing was performed on an Illumina NextSeq 500 with the NextSeq 500/550 High Output Kit v2.5.
The bioinformatic analysis was performed by the IZKF Genomics facility. First, FASTQ files were generated using bcl2fastq software. Data were processed by the nf-core/RNA-seq pipline which is publicly available (156) which works in Nextflow (157) together with Docker (158). Within this pipeline, reads were trimmed using Trim Galore (*https://github.com/FelixKrueger/TrimGalore)* followed to alignment to the mouse reference genome GRCm39 using STAR (159). Gene-level assignment was done using feature counts (160) and transcript-levels were quantified using Salmon (161). Downstream analysis was performed in R using DESeq2 (162).

6.2.36.Protein isolation and analysis

6.2.36.1. Protein isolation and quantification

Protein extraction was performed in cryopreserved tissue that was homogenized using RIPA buffer (50 mg tissue : 500 µL RIPA) in a FastPrep-24TM5G (MP Biomedicals). After homogenization, samples were incubated on ice for 30 min and then centrifuged at 12000 rpm, 10 min at 4ºC. The supernatant was transferred to a new tube.
Protein quantification was performed with the Pierce BCA Protein Assay Kit (Thermo Fisher Scientific), based on colorimetric detection. The measurement and plate preparation were done according to the manufacturer's instructions. The plate was incubated at 37ºC for 30 minutes and read using a spectrophotometer (BMG LABTECH) at 562 nm wavelength. Protein concentration was calculated using the standard curve of BSA contained in the BCA kit mentioned above.
Before the western blot, 4X Laemmli buffer was added to the samples, and they were denaturalized at 95ºC in the thermomixer for 10 min.

6.2.36.2. Western blotting (WB)

Handmade gels that ranged from 6 – 12% acrylamide, depending on the protein molecular weight that was going to be analyzed, were used to determine protein expression. 50-80 µg of protein were loaded in each well

and separated through an electrophoresis running at 120 V. Then, proteins were transferred to a PVDF membrane (0.45 µm) (BioRad) for ~ 1 h and 15 min – 2 h at constant 300 mA.

Gel, running, and transfer buffers were prepared as listed in section **6.1.3. Standard buffers** and media from the material part.

After the blotting, membranes were blocked either in 5% non-fat dry milk or BSA diluted in 0.01% TBST for 1 h. Then, membranes were incubated with the primary antibody in 2.5% blocking solution overnight at 4ºC. The following day, the primary antibody solution was removed, and membranes were washed 3 times for 10 min in TBST. Later, the second antibody was incubated in a 2.5% blocking at room temperature for 1 h. Next, membranes were washed with TBST and were incubated in Amersham ECL Prime (GE Healthcare, Amersham, UK) for 2 min. For band imaging, membranes were exposed in an Odyssey Fc Imaging system (LI-COR) or ChemiDoc (Bio Rad) until specific bands were detected. Antibodies used for WB are listed in **section 6.1.5. Immunostaining and Immunoblotting antibodies** in the material part. Specific bands corresponding to the proteins of interest were analyzed by densitometry using Image Lab (Bio-Rad) and ImageJ software.

6.2.37.Proteomic analysis

6.2.37.1. Proteomics sample preparation

The proteomic analysis was performed in collaboration with University Medical Center Groningen, Groningen, The Netherlands. Twenty microliters of the liver protein extract were mixed with LDS loading buffer (NuPAGE) and loaded on a precast 4-12% Bis-Tris gels (Novex). The samples were run shortly into the gel (approximately 5 min at 100 V). The gel was stained with Biosafe Coomassie G-250 stain (Biorad) and after destaining with milliQ-H2O, the band containing all proteins was excised from gel. The gel band was sliced into small pieces, washed subsequently with 30% and 50% v/v acetonitrile in 100 mM ammonium bicarbonate (dissolved in milliQ-H2O), each incubated at RT for 30 min while mixing (500 rpm) and lastly with 100% acetonitrile for 5 min, before drying the gel pieces in an oven at 37°C. The proteins were

reduced with 30 µL 10 mM dithiothreitol (in 100 mM ammonium bicarbonate dissolved in milliQ-H2O, 30 min, 55 °C) and alkylated with 30 µL 55 mM iodoacetamide (in 100 mM ammonium bicarbonate dissolved in milliQ-H20, 30 min, in the dark at RT). The gel pieces were washed with 100% acetonitrile for 30 min while mixing (500 rpm) and dried in an oven at 37°C) before overnight digestion with 30 µL 16 ng/µL trypsin (sequencing grade modified trypsin V5111, Promega) at 37 °C. The next day, the peptides were eluted from the gel pieces with 30 µL 75% v/v acetonitrile plus 5% v/v formic acid (incubation 20 min at RT, mixing 500 rpm). The elution fraction was diluted with 900 µL 0.1% v/v formic acid for cleanup with a C18-SPE column (SPE C18-Aq 50 mg/1 mL, Gracepure). This column was conditioned with 2x1 mL acetonitrile plus 0.1% v/v formic acid and re-equilibrated with 2x1 mL 0.1% v/v formic acid before application of the samples. The bound peptides were washed with 2x1 mL 0.1% v/v formic acid and eluted with 2x0.4 mL 50% v/v acetonitrile plus 0.1% v/v formic acid. The eluted fractions were dried under vacuum and resuspended in 50 µL 0.1% v/v formic acid.

6.2.37.2. Discovery-based proteomics analyses

Discovery mass spectrometric analyses were performed on a quadrupole orbitrap mass spectrometer equipped with a nano-electrospray ion source (Orbitrap Exploris 480, Thermo Scientific). Chromatographic separation of the peptides was performed by liquid chromatography (LC) on a nano-HPLC system (Ultimate 3000, Dionex) using a nano-LC column (Acclaim PepMapC100 C18, 75 µm x 50 cm, 2 µm, 100 Å, Dionex, buffer A: 0.1% v/v formic acid, dissolved in milliQ-H2O, buffer B: 0.1% v/v formic acid, dissolved in acetonitrile). One microliter from the liver or colon digests was injected using the µL-pickup method with buffer A as a transport liquid from a cooled autosampler (5 ˚C) and loaded onto a trap column (µPrecolumn cartridge, Acclaim PepMap100 C18, 5 µm, 100 Å, 300 µmx5 mm, Dionex). Peptides were separated on the nano-LC column using a linear gradient from 2-30% buffer B in 75 min at a flowrate of 300 nL/min. The mass spectrometer was operated in positive ion mode and data-independent acquisition mode (DIA) using

isolation windows of 9 m/z with a precursor mass range of 400-1200, switching the FAIMS between CV-45V and -60 V with three scheduled MS1 scans during each screening of the precursor mass range. LC-MS raw data were processed with Spectronaut (version 16.02.220606) (Biognosys) using the standard settings of the directDIA workflow except that quantification was performed on MS1. For the quantification, local normalization was applied, and the Q-value filtering was set to the classic setting without imputing.

6.2.37.3. Downstream protein analysis

Data from Spectronaut were exported and Volcano plots were represented though Prism 8.0. Protein candidates were represented, and proteins of interest highlighted.

Moreover, exported data were imported to StringApp-db for protein interaction, network, and pathway analysis.

6.2.38.Metabolomic analysis

6.2.38.1. Metabolite extraction

Metabolomic analysis was performed by Rubió Metabolomics S.L.U. (Bizkaia, Spain). Metabolite extraction was accomplished by fractionating the samples into pools of species with similar physicochemical properties, using appropriate combinations of organic solvents. Lipidomic analyses were performed using two separate liquid chromatography (LC)-time of flight (RoF)-mass spectrometry (MS)-based platforms that analyzed methanol (Platform 1) and methanol chloroform extract (Platform 2) (163). Lipidomic analyses were combined with a LC-single quadrupole- Then, three separate UHPLC-MS platforms optimized for extensive coverage of the hepatic or fecal metabolome were used allowing the optimal profiling of fatty acyls, bile acids, steroids, lysoglycerophospholipids, glycolipids, glycerophospholipids, sterol lipids, sphingolipids and amino acids and derivatives. Additionally, different types of quality control (QC) samples were used to assess the data quality (164).

6.2.38.2. Data analysis

Data pre-processing generated a list of chromatographic peak areas for the metabolites detected in each sample injection. An approximated linear detection range was defined for each identified metabolite, assuming similar detector response levels for all metabolites belonging to a given chemical class represented by a single standard compound.

Data normalization was performed following the procedure described by Martínez-Arranz et al. (165). Once normalized, the dimensionality of the complex data set was reduced to enable easy visualization of any metabolic clustering of the different groups of samples. This was achieved by multivariate data analysis, including the non-supervised principal components analysis (PCA). These multivariate data analyses were performed using the SIMCA software (version SIMCA 14.1. MSK Umetrics AB, Umea, Sweden). Data were centered and unit variance (UV)-scaled. Model quality was assessed using R2 and Q2 values, which indicate the explained fraction of variance and the goodness of prediction, respectively. The Q2 parameter was calculated by sevenfold cross validation.

Univariate statistical analyses were also performed calculating group fold-changes and Student's t-test p-value for the comparisons between mice which were treated with a DUAL diet and control mice. Univariate normality was assessed by the Shapiro-Wilk test. In order to help in the visualization, several heatmaps were generated displaying the results of the univariate data analysis. These heatmaps display the log2 (fold-change) of the metabolites included in the analysis together with the Student's t-test for each comparison. For each metabolite, changes between subgroups were calculated as the base 2 logarithm of fold-change. Darker blue and red colors indicate higher drops and elevations of the metabolite levels, respectively. These values are accompanied by a significance level based on p-values from Student's t-test. Three levels of increasing significance are considered: $p < 0.05$, $p < 0.01$, and $p < 0.001$. These different levels of significance are represented with lighter grey, darker grey or black lines, respectively. Lipids have been ordered in the

heatmap according to their carbon number and unsaturation degree of their acyl chains.

6.2.39.ELISA

6.2.39.1. LPS ELISA

LPS was determined in serum through LPS ELISA Kit (Antibodies). Kit reagent and standard preparation were performed according to the manufacturer's protocol. Serum samples were 1:5 diluted in diluent assay and 50 µl of sample were added in duplicate to the ELISA plate. After several steps with detection reagent incubation followed by several washes, the substrate of the enzyme was added and after 10-20 min of incubation at 37ºC, stop solution was added and the plate was immediately read in a spectrophotometer (BMG LABTECH) in a 450 nm wavelength.

6.2.39.2. Albumin ELISA

Albumin was determined in feces using mouse albumin ELISA Kit (Bethyl Laboratories). Reagent and standard curve were prepared according to the manufacturer's instructions. Mouse feces were homogenized in dilution buffer (75 mg/mL using a FastPrep-24TM5G (MP Biomedicals, Illkirch-Graffenstaden, France). Later, samples were centrifuged at 10000 xG, for 10 min at 4ºC. Supernatant was transferred to another tube and diluted 1:50 with dilution buffer.

100 µL of sample were added to the precoated plate of the kit and it followed subsequent steps of incubation and washes. Finally, the stop solution was added, and absorbance was immediately read in a spectrophotometer (BMG LABTECH) at 450 nm wavelength.

6.2.40.Bacteria culture in agar blood plates

Fresh blood from animals was extracted from vena cava in the sacrifice and plated into agar-blood plates (Thermo Fisher Scientific) under laminar flow hood (Telstar) and subsequently incubated at 37ºC for 72 h. Bacterial growth

was visually examined after 24-48 and 72 h. Fresh mouse feces were smashed, plated and incubated to be used as a positive control.

6.2.41.Human feces samples

Human feces samples were obtained from Val d'Ebron Hospital, Barcelona, Spain. Patient cohort is described in **Table 5.** This study was approved by *Comité de ética de la Investigación con medicamentos* of Val d'Ebron hospital with the code PR(AG)388/2021.

Table 5. Cohort of patients for 16s rRNA microbiome analysis from feces. Dual CLD etiology patients reported obesity/overweight features (Body Mass Index (BMI)>25 kg/m^2) and active alcohol consumption. Hepatic serum markers and liver disease scores were collected.

N	Diagn.	Gender	Age	EtOH (g)	DM2	BW (Kg)	BMI (kg/m^2)	ALT	AST	NAS Score	FIB4	Cirrhotic
01	DUAL	M	68	20	No	97,5	36,25	17	28	4	3.33	No
02	DUAL	M	73	10	Yes	96,7	31.22	59	47	3	3.04	Yes
03	DUAL	W	73	20	Yes	73,1	34.29	22	22	5	1.72	No
04	DUAL	M	73	20	Yes	98,1	37.38	51	59	3	3.16	No
05	DUAL	M	76	10	No	76,0	26.93	65	41	3	2.08	No
06	DUAL	M	62	10	Yes	95,9	33.58	47	54	3	4.32	Yes
07	DUAL	W	68	10	No	88,0	32.72	53	44	3	1.04	No
08	DUAL	M	79	20	Yes	113,3	37.42	22	22	3	2.75	Yes
09	DUAL	M	58	10	Yes	101,1	31.55	45	31	3	0.76	No
10	DUAL	M	69	40	Yes	106,3	36.78	12	19	¿	2.42	Yes
11	DUAL	M	59	20	Yes	98,5	28.47	48	52	6	3.10	Yes
12	Control	M	55	-	-	91		27	25	-	-	-
13	Control	W	47	-	-	55		16	21	-	-	-
14	Control	W	54	-	-	56		19	26	-	-	-
15	Control	W	47	-	-	67		20	20	-	-	-
16	Control	M	38	-	-	86		23	32	-	-	-
17	Control	M	42	-	-	70		12	18	-	-	-

6.2.42.16s microbiome analysis

16s microbiome analysis was performed in the Institute of Medical Microbiology, RWTH University Hospital, Aachen, Germany.

6.2.42.1. Isolation of metagenomic DNA

DNA was isolated using a modified protocol according to Godon et al. (166). Snap frozen samples were mixed with 600 µL stool DNA stabilizer (Stratec biomedical), thawed, and transferred into autoclaved 2-mL screw-cap tubes containing 500 mg 0.1 mm-diameter silica/zirconia beads. Next, 250 µL 4 M

guanidine thiocyanate in 0.1 M Tris (pH 7.5) and 500 µL 5 % N-lauroyl sarcosine in 0.1 M PBS (pH 8.0) were added. Samples were incubated at 70°C and 700 rpm for 60 min. A FastPrep instrument (MP Biomedicals) fitted with a 24 × 2 mL cooling adaptor filled with dry ice was used for cell disruption. The program was run 3 times for 40 s at 6.5 M/s. After each run, the cooling adapter was refilled with dry ice. An amount of 15 mg Polyvinylpyrrolidone (PVPP) was added and samples were vortexed, followed by a 3 min centrifugation at 15.000 xG and 4°C. Approximately 650 µL of the supernatant were transferred into a new 2 mL tube, which was centrifuged again for 3 min at 15.000 xG and 4 °C. Subsequently, 500 µL of the supernatant were transferred into a new 2 mL tube and 50 µg of RNase was added. After 20 minutes at 37°C and 700 rpm, gDNA was isolated using the NucleoSpin® gDNA Clean-up Kit from Macherey-Nagel. Isolation was performed according to the manufacturer's protocol. DNA was eluted from columns twice using 40 µL Elution buffer and concentration was measured with NanoDrop (Thermo Scientific). Samples were stored at -20 °C.

6.2.42.2. Illumina sequencing of 16S rRNA genes

Library preparation and sequencing were performed as described in detail previously (167) using an automation platform (Biomek400, Beckman Coulter). Briefly, the V3-V4 region of 16S rRNA genes was amplified in duplicates (25 cycles) following a two-step protocol (168) using primers 341F-785R (169). After purification using the AMPure XP system (Beckman Coulter), sequencing was conducted with pooled samples in paired-end modus (PE300) using a MiSeq system (Illumina, Inc.) according to the manufacturer's instructions and 25% (v/v) PhiX standard library.

6.2.42.3. 16s rRNA gene amplicon data analysis

Raw reads were processed using an in-house developed pipeline (www.imngs.org) (170) based on the UPARSE approach (171). In brief, sequences were demultiplexed and trimmed to the first base with a quality

score <3. The pairing, chimera filtering and Operational Taxonomic Unit (OTU) clustering (97% identity) was done using USEARCH 11.0 (172).

Sequences with less than 350 and more than 500 nucleotides and paired reads with an expected error >3 were excluded from the analysis. The remaining reads were trimmed by ten nucleotides on each end to avoid GC bias and non-random base composition. OTUs were clustered at 97% sequence similarity, and only those with a relative abundance >0.25% in at least one sample were kept. Sequence alignment and taxonomic classification was conducted with SINA 1.6.1, using the taxonomy of SILVA release 128 (173).

Downstream analysis was performed in the R programming environment using Rhea (https://lagkouvardos.github.io/Rhea/) (174). OTU tables were normalized to account for differences in sequence depth. ß-diversity was computed based on generalized UniFrac distances (175). α-diversity was assessed based on species richness and Shannon effective diversity (176). Zero values were removed from statistical calculations and P-values were calculated either using a non-parametric Wilcoxon Rank Sum Test or a Fisher's exact test corrected for multiple comparisons according to the Benjamini-Hochberg method. Only taxa with a prevalence of at least 30% samples in one given group were considered for statistical analysis.

Identity of OTUs of interest was confirmed using EZBioCloud (177).

6.2.43. Statistical analysis

Data are expressed as mean ± standard deviation. Statistical significance was determined when comparing two groups through Student's t-test. Meanwhile, one-way-ANOVA was applied when more than two groups went through the statistical analysis using a Tukey post-hoc test.

When more than one variant was studied at the same time, a two-way ANOVA plus Bonferroni post-hoc test was applied.

Significant differences are indicated as follows * p=0.05; ** p<0.01; *** p<0.001, **** p<0.0001.

Results

7. RESULTS

7.1. ESTABLISHING A DUAL MODEL

In the first part of the study, we established a physiological, fast and innovative experimental model of CLD which synergistically combined the effects of alcohol and WD – DUAL model.

The main limiting factor that has been previously found in ALD preclinical models, is the low EtOH intake due to natural aversion in mice (144). Thus, we masked the EtOH taste by adding 6.75% D-glucose in the drinking water. Moreover, EtOH was gradually introduced to drinking water as explained in detail in **Material and methods section 6.2.3.2. DUAL diet** and **Fig. 15, 16.**

Initially, we performed a pilot study to assess the optimal concentration of alcohol in the drinking water, establishing 3 different concentrations of 5, 10 and 20% alcohol as described in **Material and methods section 6.2.3.2. DUAL diet (Fig. 17)**.

We found that the concentration of EtOH significantly affected the volume and, as a result, the quantity of the daily consumed alcohol. When 20% EtOH was administered in the drinking water, mice significantly decreased consumption and the effects induced by alcohol were belittled. At 5% EtOH, the quantity of consumed alcohol remained relatively low.

Only mice receiving 10% vol/vol had a greater amount of consumed alcohol in comparison to the other two concentrations **(Fig. 27A).** Consequently, they developed more severe steatosis detectable by H&E **(Fig. 27B upper panel)**, greater fibrosis stained by SR and **(Fig. 27B mid; 27C)** higher levels of α-Smooth Muscle Actin (α-SMA), a marker of active HSCs, producers of collagen **(Fig. 27B low).**

Therefore, a concentration of 10% vol/vol EtOH was selected for all following experiments.

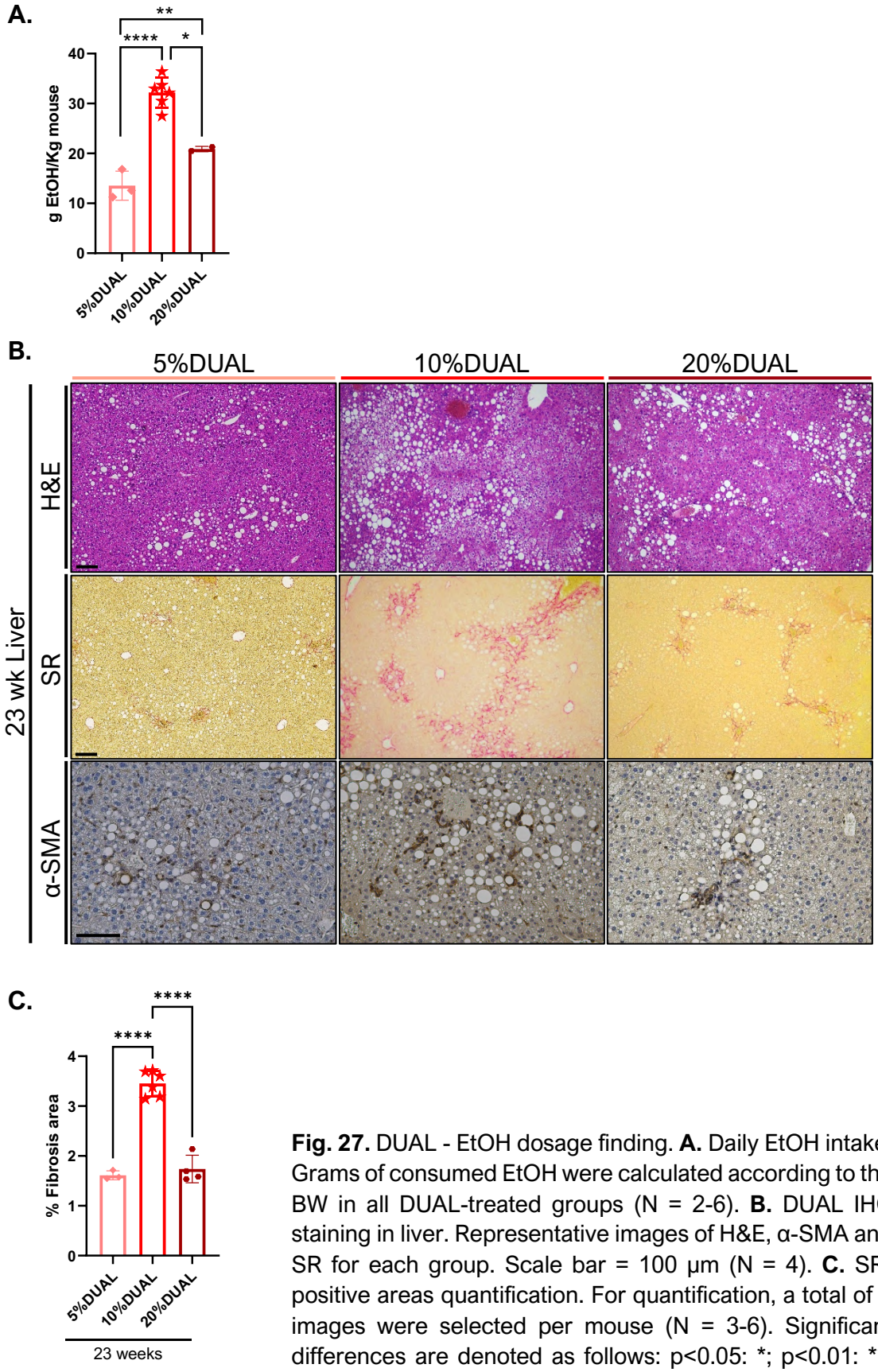

Fig. 27. DUAL - EtOH dosage finding. **A.** Daily EtOH intake. Grams of consumed EtOH were calculated according to the BW in all DUAL-treated groups (N = 2-6). **B.** DUAL IHC staining in liver. Representative images of H&E, α-SMA and SR for each group. Scale bar = 100 μm (N = 4). **C.** SR-positive areas quantification. For quantification, a total of 8 images were selected per mouse (N = 3-6). Significant differences are denoted as follows: $p<0.05$: *; $p<0.01$: **; $p<0.0001$: ****.

Animals were randomly assigned to four groups: (1) control group; (2) WD plus sweetened water group; (3) 10% vol/vol EtOH in sweetened drinking water plus chow diet group; (4) DUAL group fed with DUAL diet for 10 and 23 weeks **(Fig. 15)**.

7.2. MAIN EXTRAHEPATIC FEATURES OF THE DUAL MODEL: OBESITY, DYSLIPIDEMIA AND HYPERGLYCEMIA

Body weight gradually increased in all treated groups during the feeding. Previous studies in both humans and rodents showed a positive feedback loop between EtOH intake and dietary fat (178). Consistently, our model nicely reflected this positive correlation, since DUAL mice demonstrated significantly elevated EtOH consumption compared to the EtOH-fed animals **(Fig. 28A).** In turn, alcohol stimulated the ingestion of high-fat diet. This finally resulted in higher daily caloric consumption **(Fig. 28B, C)** and robust increase in the body weight and BMI in DUAL animals **(Fig. 28D, E).**

However, obesity is not only characterized by an increase in the body mass, but also is associated with profound changes in the WAT histology and function, which play an important role systemically and, more concretely, in the development of fatty liver disease (179). With the development of obesity, WAT undergoes a process of tissue remodeling in which adipocytes increase in size (hypertrophy) (48).

The morphometric evaluation of adipocytes in gWAT from perigonadal fat pad showed that DUAL diet led to an increase in adipocyte size of 93.2% after 23 weeks of feeding **(Fig. 29A upper panel; 29B).** Moreover, the unhealthy expansion of WAT in the DUAL group was accompanied by the infiltration of $F4/80^+$ macrophages and $CD45^+$ immune cells that aggregated around dying adipocytes and formed crown-like structures **(Fig. 29A middle panel).** Another deleterious effect typical of WAT failure is the accumulation of excessive amounts of ECM (48, 180). Consistently, collagen fiber deposition revealed by SR staining was increased in the DUAL group **(Fig. 29A lower panel; 29C).**

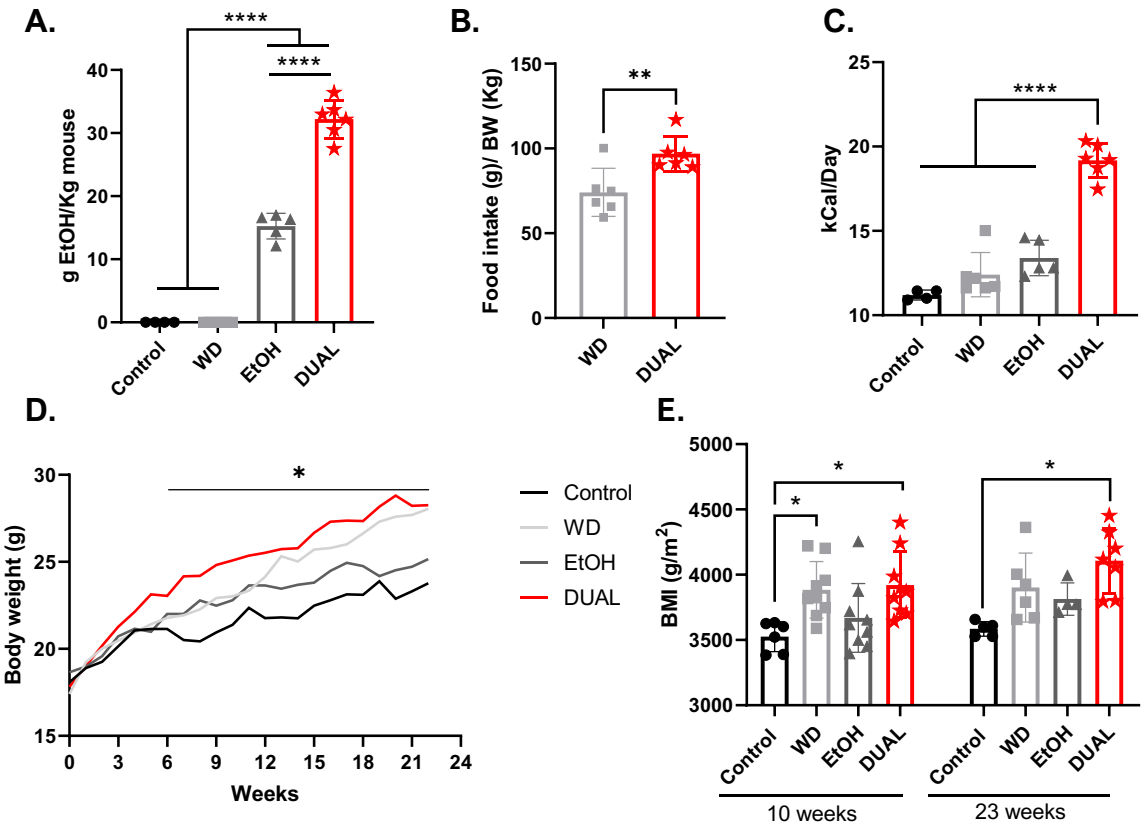

Fig. 28. A. Alcohol intake, g EtOH/ kg mouse (N = 4-6). **B.** Food intake, g WD/kg mouse BW (N = 4-6). **C.** Calorie intake per day including calories in food and in drinking water (D- glucose and/or EtOH) (N = 4-6). **D.** BW curve during the feeding period. Statistical differences between DUAL and control groups are shown (N = 5-7). **E.** BMI was calculated after 10 and 23 weeks of feeding (g/m^2) (N = 5-9). Significant differences are denoted as follows: p<0.05: *; p<0.01: **; p<0.0001: ****.

Obesity is strongly associated with other features of MS, including hyperglycemia and dyslipidemia (181). WAT dysfunction reduces insulin sensitivity which in turn increases the level of glucose in blood (hyperglycemia). Congruently, DUAL-fed animals developed hyperglycemia after 10 and 23 weeks of treatment **(Fig. 30A).** However, no significant difference between control animals and treated ones was detected by GTT **(Fig. 30B-C).** ITT after 6 hours of fasting showed the impaired insulin sensitivity only in WD and EtOH groups **(Fig 30D-E).**

Obesogenic diet and WAT adipose tissue dysfunction lead to dyslipidemia. We found constantly high levels of circulating serum cholesterol at 10 and 23 weeks in DUAL mice in comparison to the rest of the feeding groups **(Fig. 30F).**

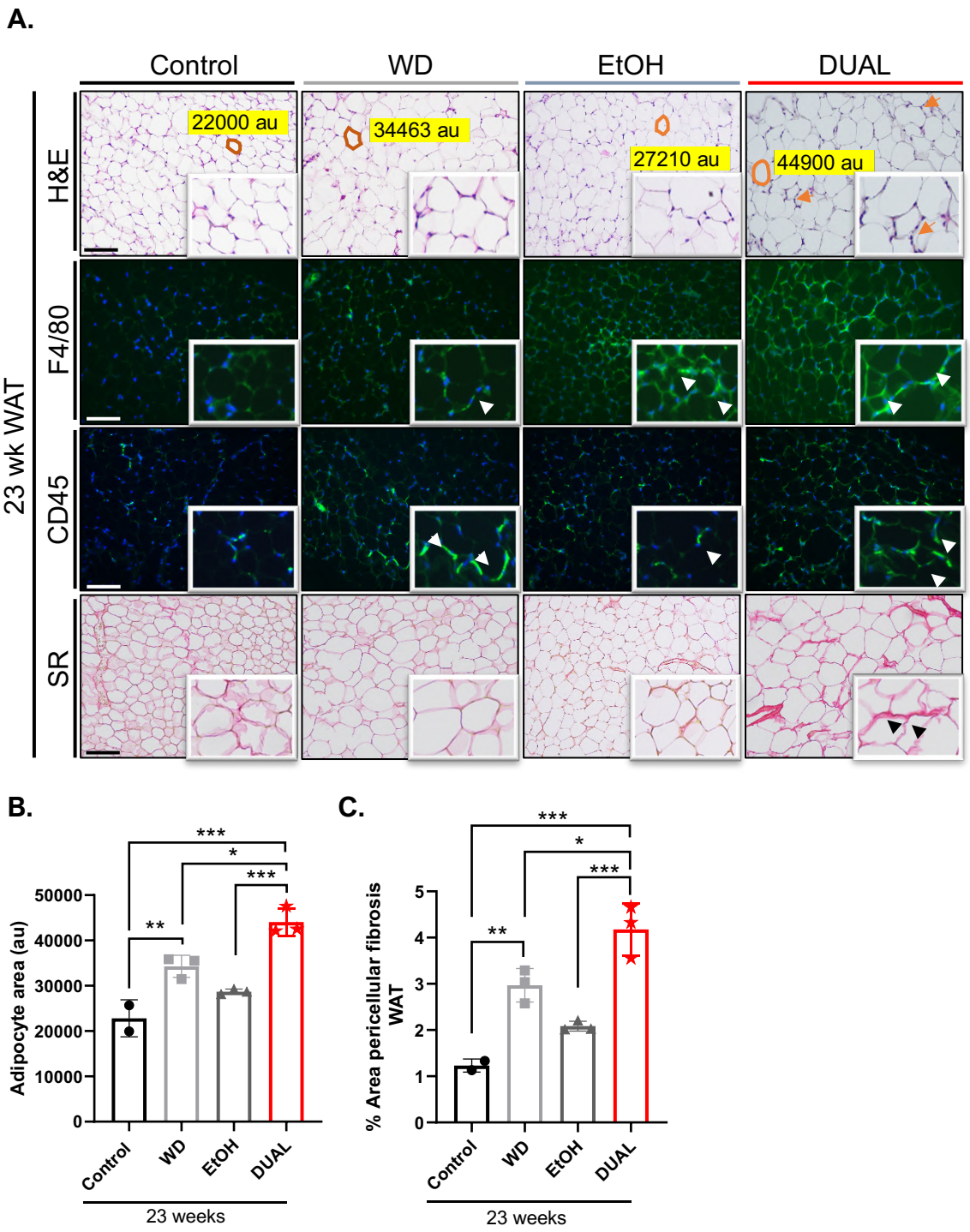

Fig. 29. A – upper. Representative WAT H&E. Scale bar = 100 µm. (N = 3). **A-middle.** Representative CD45 and F4/80 IF staining of WAT. Positive immune cells are stained in green. Nuclei are stained in blue using DAPI as a counterstain. Scale bar = 100 µm (N = 3). **A-low.** SR staining was performed in WAT. Scale bar = 100 µm. (N = 3). **B.** Size measurement of adipocytes in WAT tissue stained in H&E (N = 3). **C.** Quantification of pericellular fibrosis by measuring positive-SR-stained areas in WAT though ImageJ software. (N = 3) Significant differences are denoted as follows: $p<0.05$: *; $p<0.01$: **; $p<0.001$: ***.

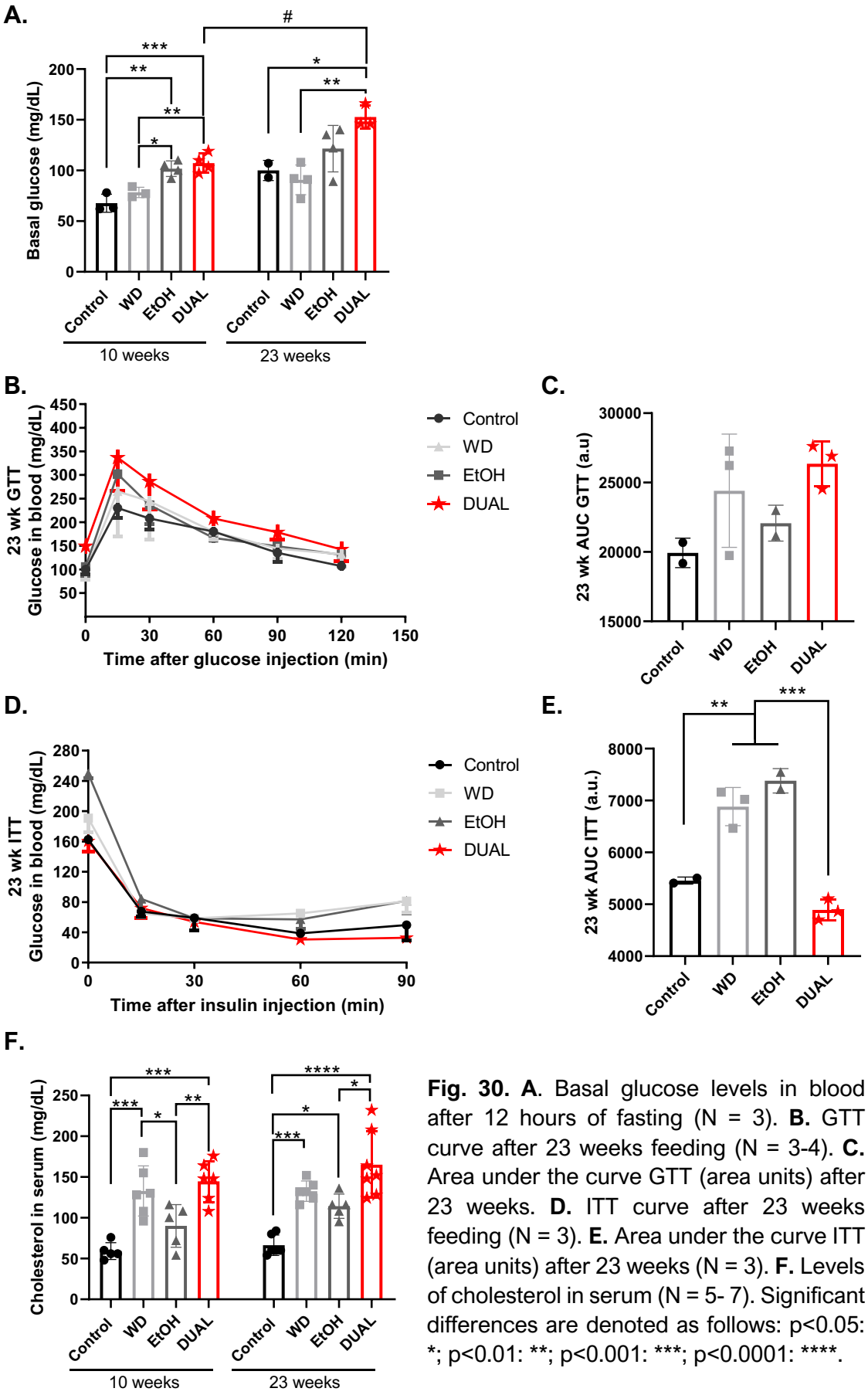

Fig. 30. A. Basal glucose levels in blood after 12 hours of fasting (N = 3). **B.** GTT curve after 23 weeks feeding (N = 3-4). **C.** Area under the curve GTT (area units) after 23 weeks. **D.** ITT curve after 23 weeks feeding (N = 3). **E.** Area under the curve ITT (area units) after 23 weeks (N = 3). **F.** Levels of cholesterol in serum (N = 5- 7). Significant differences are denoted as follows: p<0.05: *; p<0.01: **; p<0.001: ***; p<0.0001: ****.

7.3. DUAL FEEDING TRIGGERS HEPATOMEGALY AND FATTY LIVER DISEASE

WAT is a complex organ and has primary roles in energy homeostasis control, but it also regulates other metabolic tissues. In a high energy state, WAT can induce ectopic fat depositions in other tissues such as liver, skeletal muscle, heart, and pancreas (48). Obesity and MS prompt the development of fatty liver disease (182).

After 23 weeks of DUAL feeding, animals exhibited enlarged livers, which were pale and yellowish in color, indicating lipid accumulation **(Fig. 31A).** Accordingly, the hepatic mass was increased and the hepatosomatic ratio in DUAL animals reached 8.1±0.9% **(Fig. 31B-C).**

Microscopically, phalloidin IF staining revealed that hepatocytes of DUAL animals after 10 and 23 weeks of feeding lost their typical hexagonal shape and transformed into enlarged round cells **(Fig. 31D-E).**

Blinded quantitative analysis of H&E staining **(Fig. 32A)** performed by an experienced pathologist using *Bedossa system* (152) revealed that DUAL animals exhibited microvesicular and macrovesicular steatosis grade 2 **(Fig. 32B)** associated with hepatocyte ballooning **(Fig. 32C)**, reaching, in most of the animals, a S2A4 NAFLD score **(Fig. 32D)**.

All experimental groups after 23 weeks of treatment exhibited positive extensive ORO staining compared to control mice. However, numerous macrolipid and microlipid droplets were more profuse in DUAL-fed mice **(Fig. 33A-B).** Consistently, hepatic TG were increased in all mice, with the highest levels found in those treated with DUAL diet **(Fig. 33C).**

Dietary free fatty acids (FFAs) are the main source of TG in the liver. Interestingly, while NEFAs in the serum of WD-fed mice were significantly increased, the NEFA level in DUAL mice was not upregulated, indicating a massive FFA flux into the liver **(Fig. 33D).** Consistently. we found significant upregulation of *Cd36* expression (FA translocase) in the livers of DUAL animals **(Fig. 33E).** At the same time, the level of TG in serum of DUAL mice was not proportionally increased

(Fig. 33F), suggesting the possible impairment in hepatic secretion of VLDL (183).

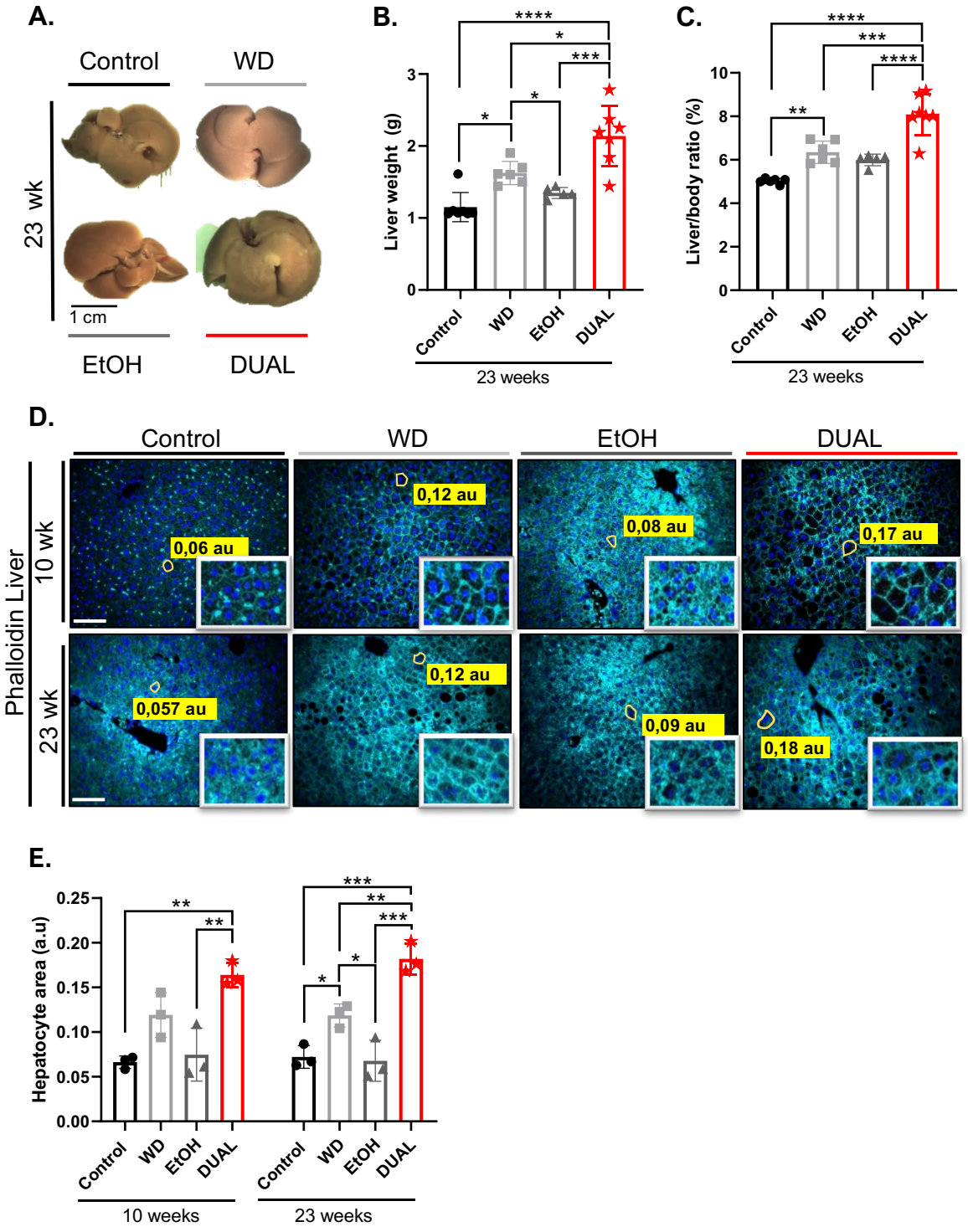

Fig. 31. A. Liver macroscopic images after 23 weeks of feeding. **B.** Liver weight (g) (N = 5-7). **C.** Liver weight to BW ratio (%) (N = 5- 7). **D.** Representative IF phalloidin- stained liver images. **E.** Size of hepatocytes in phalloidin- stained liver pictures quantified by ImageJ software. Scale bar = 100 µm (N = 3). Significant differences are denoted as follows: p<0.05: *; p<0.01: **; p<0.001: ***; p<0.0001: ****.

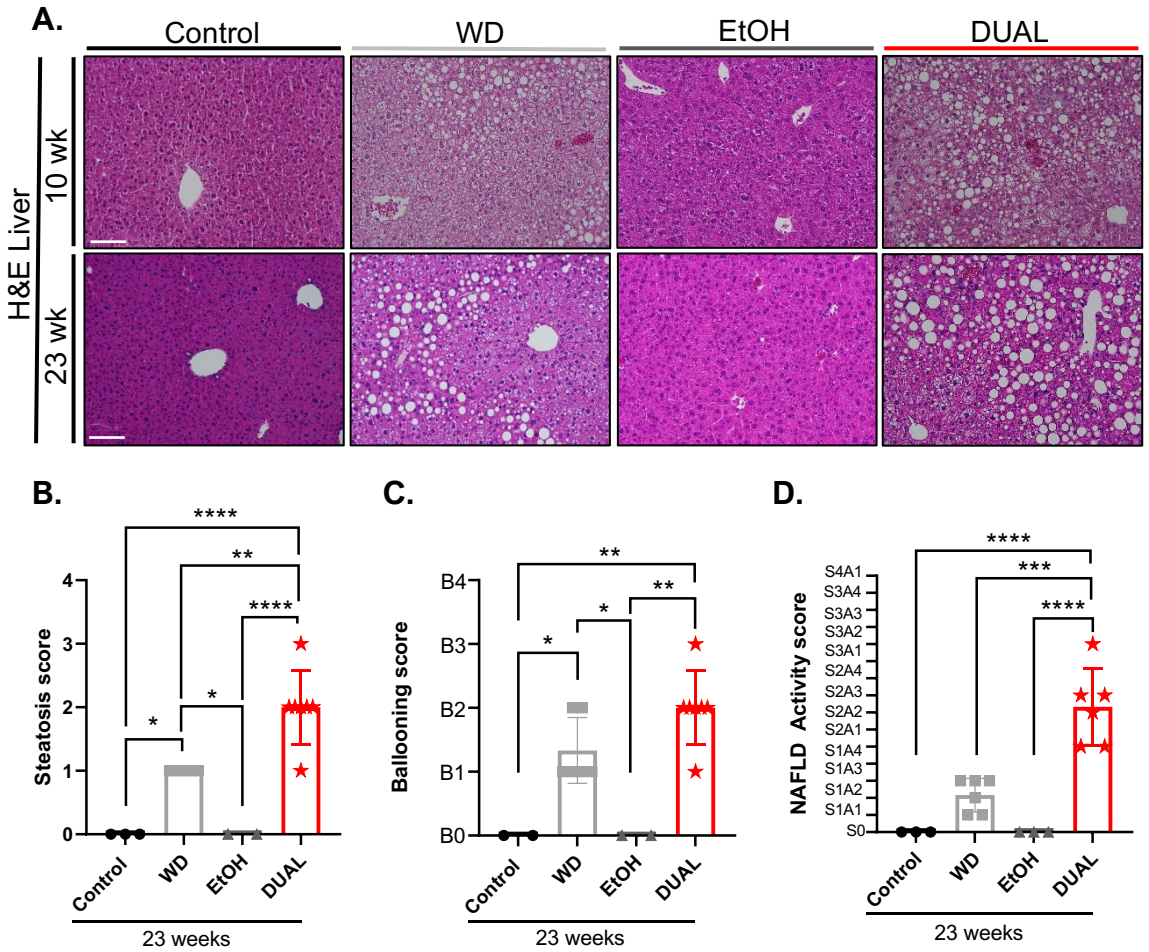

Fig. 32. A. H&E representative images after 10 or 23 weeks of feeding. Scale bar = 100 µm. **B.** Steatosis score assigned after 23 wk of treatment (N = 3- 7). **C.** Determination of 23 wk ballooning score in the liver. (N = 3-7). **D.** NAFLD activity score calculated at 23 wk timepoint. (N = 3-6). Significant differences are denoted as follows: p<0.05: *; p<0.01: **; p<0.001: ***; p<0.0001: ****.

To verify these results, we performed in-depth analysis of the hepatic metabolome. First, a clear separation between DUAL and control groups was observed. Results were displayed as a volcano plot, which highlighted a remarkable alteration of DG, TG, and cholesterol esters in the DUAL group **(Fig. 34A, B).**

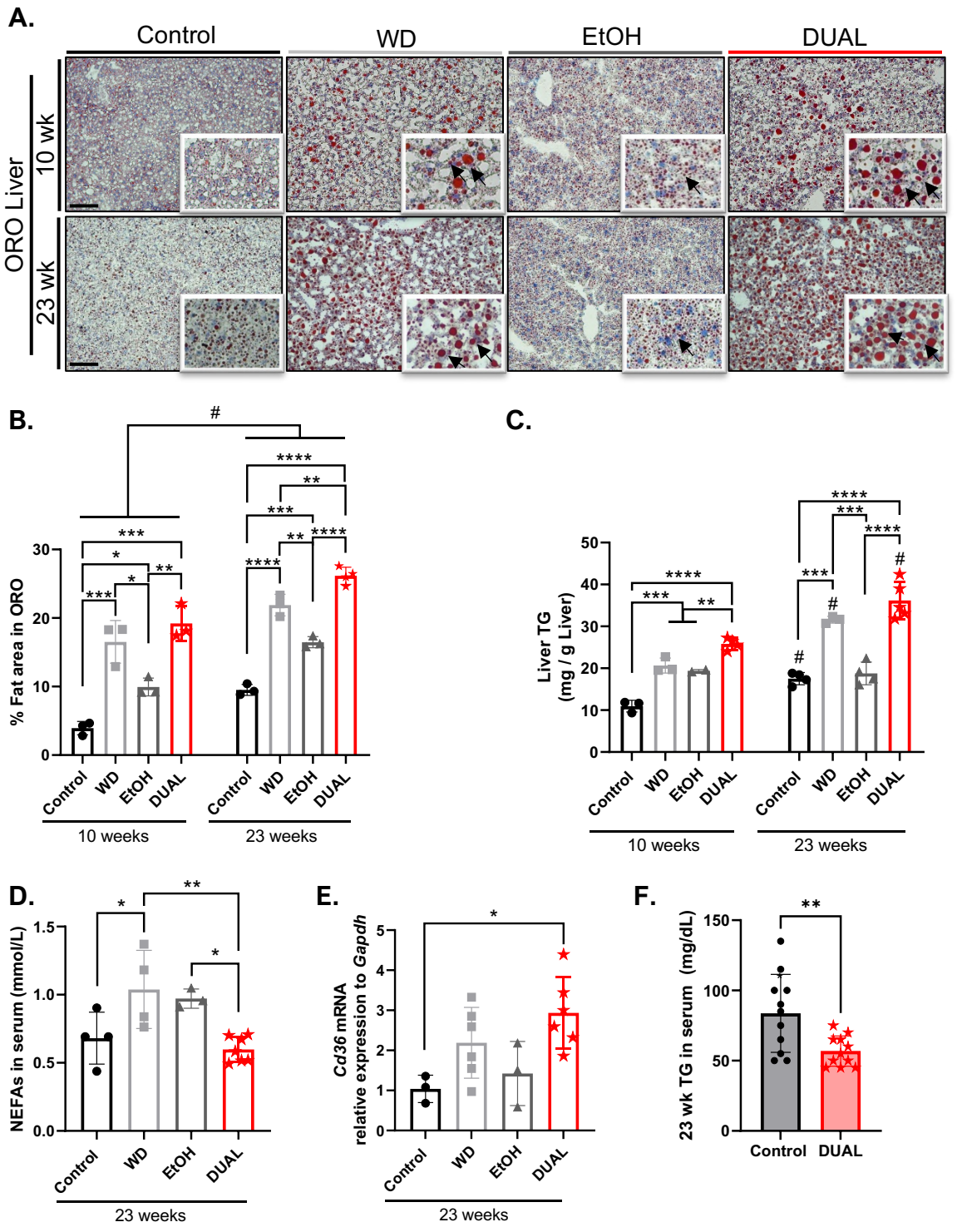

Fig. 33. A. Illustrative ORO- stained liver sections from each group and time- point feeding. Scale bar = 100 µm. **B.** Quantification of ORO- stained area (N = 3). **C.** Quantification of hepatic TG after 10 and 23 weeks feeding (mg/g liver). (N = 3-5). **D.** NEFAs in serum (mmol/L) (N = 3-7). **E.** *Cd36* mRNA relative expression to GAPDH through RT-qPCR (N = 3-6). **F.** TG in serum (mg/dL) after 12 h fasting. Significant differences are denoted as follows: p<0.05: *; p<0.01: **; p<0.001: ***; p<0.0001: ****; p<0.05: # in differences between 10 and 23 wk.

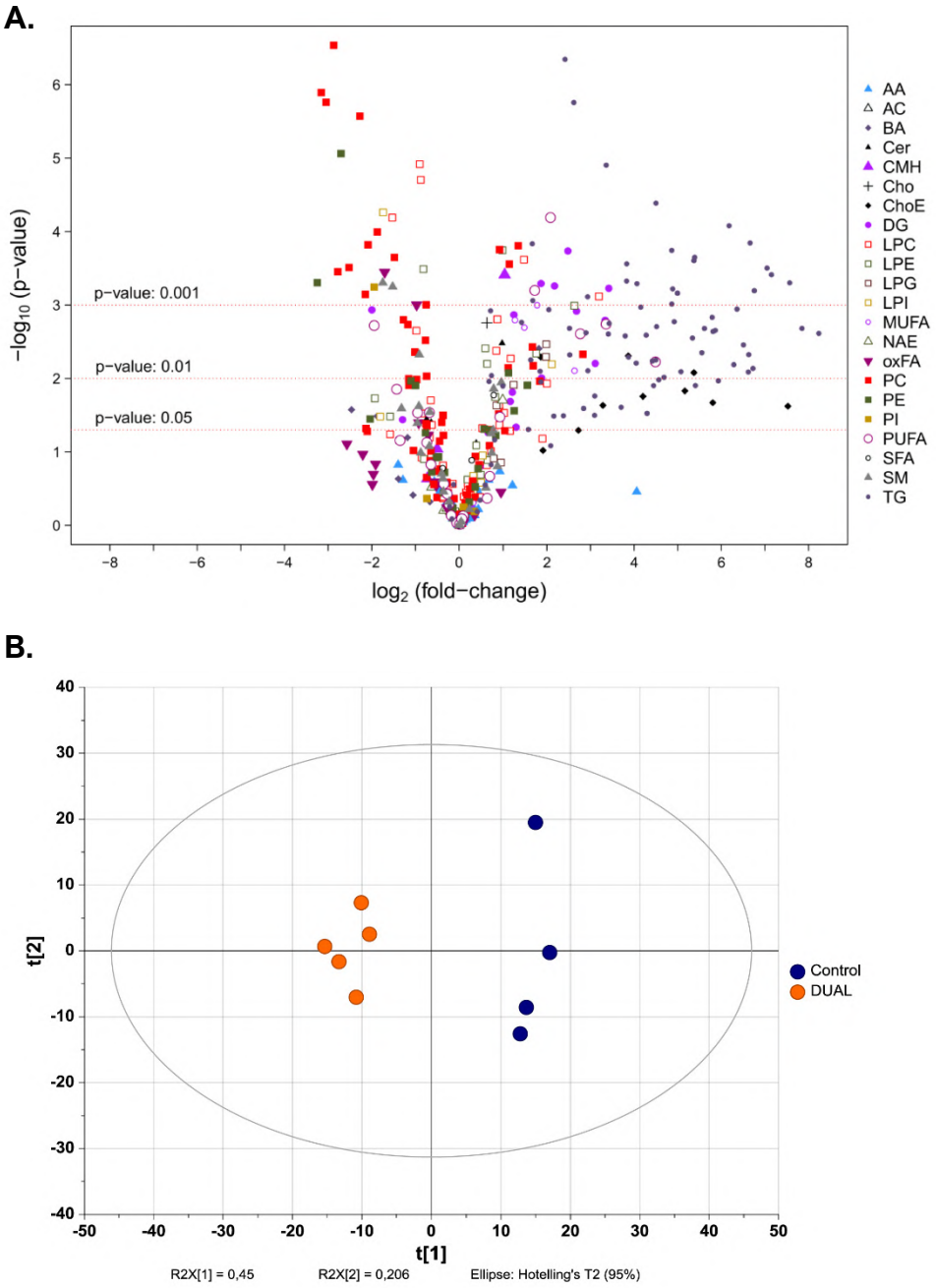

Fig. 34. A. Metabolomic study in the liver. Volcano plot [-log10(p-value) vs. log2(fold-change)] for the comparison DUAL vs. Control mice (hepatic tissue samples). Abbreviations: AA, amino acids; AC, acyl carnitines; BA, bile acids, Cer, ceramides; CMH, monohexosylceramides; Cho, cholesterol; ChoE, colesterol esters; DG, diglycerides; LPC, lysophosphatidylcholines; LPE, lysophosphatidylethanolamines; LPG, lysophosphatidylglycerols; LPI, lysophosphatidylinositols; MG, monoglycerides; MUFA, monounsaturated fatty acids; NAE, N-acyl ethanolamines; oxFA, oxidized fatty acids; PC, phosphatidylcholines; PE, phosphatidylethanolamines; PI, phosphatidylinositols; PUFA, polyunsaturated fatty acids; SFA, saturated fatty acids; SM, sphingomyelins; TG, triglycerides. **B.** Score scatter plot of the PCA model of liver samples. Model diagnostics (A=3; R2X=0.656; Q2X=0.382). The ellipse represents 95% confidence interval according to Hotelling's T2 test. (N = 5).

Interestingly, we found that the hepatic levels of SFA, such as palmitic acid or stearic acid, remained unaltered **(Table 6).** In contrast, monounsaturated fatty acids (MUFA) - oleic and palmitoleic acid - were increased. As the SFA are the substrates of the stearoyl-coenzyme A desaturase 1 (SCD-1) and the MUFA are the products of this enzyme, it may indicate an increment of the SCD-1 activity **(Table 7).** Consequently, we confirmed high expression of *Scd-1* in the livers of DUAL mice by qPCR **(Fig. 35A).**

Table 6. Changes (p-value<0.05) in the hepatic levels of non-esterified fatty acids between DUAL and control mice. Log2 (fold-changes) and Student's t-test p-values are indicated. Log2 (fold-changes) in blue denotes reduced levels in DUAL mice, while values in red indicate an increase.

Class	Metabolite	Metabolite (Common name)	Variable (Code OWL)	log_2(fc)	*p*-value
SFA	14:0	Myristic acid	FFA02	0.784908	1.68E-02
MUFA	16:1n-7	Palmitoleic acid	FFA04	1.486559	2.03E-03
	16:1n-9	Hypogeic acid	FFA05	2.635326	7.83E-03
	18:1n-9	Oleic acid	FFA08	1.270041	1.61E-03
	20:1n-6	-	FFA17	1.778511	1.01E-03
PUFA	16:2n-4,7	9(Z),12(Z)-Hexadecadienoic acid	FFA32	-1.428413	1.40E-02
	18:2n-6	Linoleic acid	FFA11	-0.94906	2.93E-02
	18:2n-x	-	FFA12	3.35734	1.82E-03
	18:3n-3	Alpha-Linolenic acid	FFA14	-1.944134	1.90E-03
	18:3n-x	-	FFA16	2.083576	6.44E-05
	20:2n-x	-	FFA49	4.488449	5.94E-03
	20:3n-3	Eicosatrienoic acid	FFA20	0.925712	3.34E-02
	20:3n-9	Mead acid	FFA22	1.722569	6.32E-04
	20:5n-3	Eicosapentaenoic acid	FFA26	-0.680908	2.91E-02
	22:3n-x	-	FFA46	2.76735	2.46E-03

Table 7. Changes in the ratios associated with SCD1 activity. Log2 (fold-changes) and Student's t-test p-values are indicated. Log2 (fold-changes) in red indicates an increment of the activity in DUAL mice.

Ratio	Indicator	log_2(fc)	*p*-value
Palmitoleic acid (16:1n-7) / Palmitic acid (16:0)	SCD (n-7). SCD-1 activity in16C	1.485	**5.38E-04**
Oleic acid (18:1n-9) / Stearic acid (18:9)	SCD (n-9). SCD-1 activity in18C	1.006	**1.10E-03**

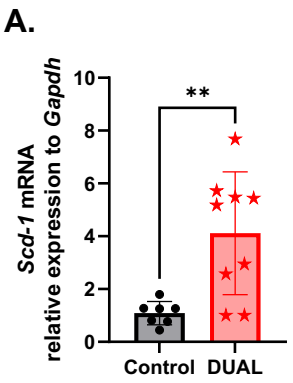

Fig. 35. A. *Scd-1* mRNA relative expression to *Gapdh* was quantified by RT-qPCR (N = 7). Significant differences are denoted as follows: p<0.01: **.

SCD1 is the rate-limiting step in the synthesis of MUFAs, which are the main components for TG and DG production. Hence, a remarkable increment of TG was found in the DUAL group. Moreover, we found that DUAL livers exhibited high concentrations of DG which have been described (16, 17) as lipotoxic and have been related with NASH **(Fig. 36A, B).**

Some of the most remarkable observed changes was the diminution of highly polyunsaturated PC **(Fig. 36C)**. It is interesting, as the formation of VLDL particles requires PC molecules rich in PUFA, such as docosahexaenoic acid (22:6n-3, DHA) or arachidonic acid (20:4n-6). The ratios of PC(22:6)/PC and PC(20:4)/PE(20:4), both of which are indicators of phosphatidylethanolamine N-methyltransferase (PEMT) activity, were reduced in DUAL mice in comparison to control animals. PEMT is needed for VLDL assembly and export, and its deletion makes mice more prone to the development of fatty liver (184) **(Table 8).**

The increase of lipid load in turn induces an intensification of hepatic lipid oxidation. As expected, we observed a significant upregulation CPT-1c levels in mice fed with WD. However, the protein expression of CPT-1c in the DUAL livers was not adequately increased and was similar to control **(Fig. 37A)**.

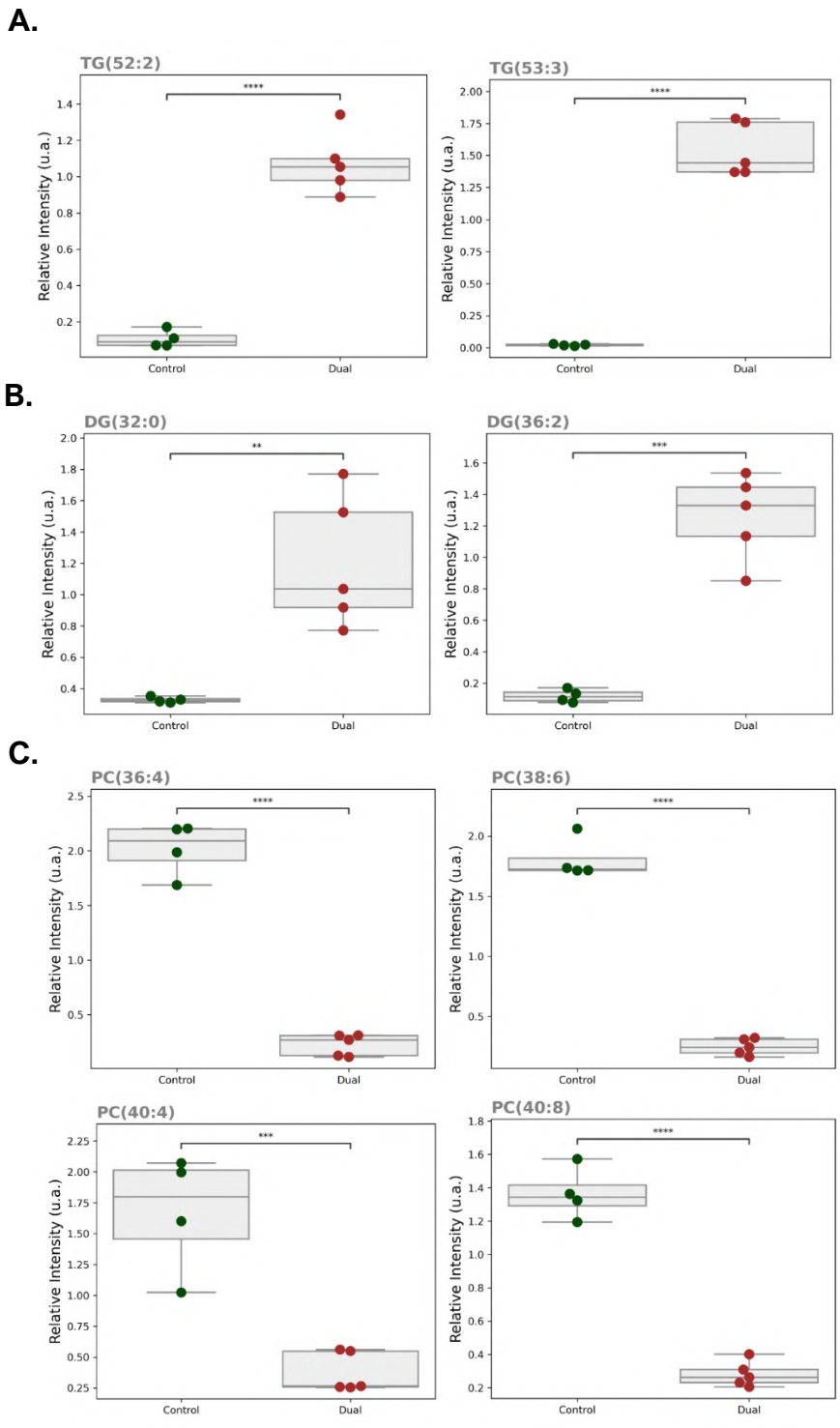

Fig. 36. A. Metabolomic study. Box plots representing the levels of TG(52:2) and TG(53:3) in liver tissue samples. Data represented as relative intensity (arbitrary units). **B.** Metabolomic study. Boxplots representing the levels of DG(32:0) and DG(36:2) in liver tissue samples. Data represented as relative intensity (arbitrary units). **(C).** Metabolomic study. Boxplots representing the levels of PC(36:4), PC(38:6), PC(40:4) and PC(40:8) in liver tissue samples. Data represented as relative intensity (arbitrary units). (N = 5). Significant differences are denoted as follows: p<0.01: **; p<0.001: ***; p<0.0001: ****.

Table 8. Changes in the ratios associated with PEMT activity. Log2 (fold-changes) and Student's t-test p-values are indicated. Log2 (fold-changes) in blue denotes reduced activity in DUAL mice.

Ratio	Indicator	log_2(fc)	*p*-value
PC(22:6) / PC	PC with DHA *vs*. total PC. Indicator of PEMT activity.	-0.454	**2.01E-03**
PC(20:4)/PE (20:4)	PC/PE with arachidonic acid. Indicator of PEMT activity.	-0.419	**5.27E-03**

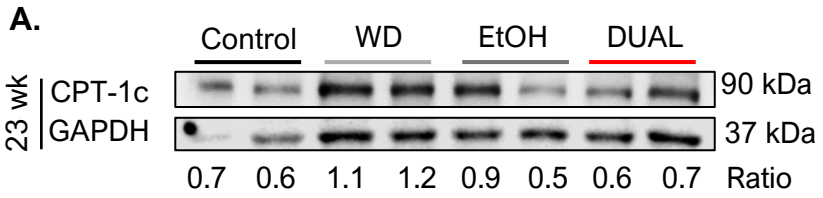

Fig. 37. A. CPT-1c immunoblot using GAPDH as loading control. Ratio between CPT-1c and GAPDH was calculated.

Altogether, the extraordinary FFA flux into the liver, poor TG secretion, combined with reduced lipid oxidation, contributed to the accumulation of a significant amount of fat in the liver parenchyma of DUAL mice.

Massive amounts of cholesterol were found in DUAL livers, moreover, conjugated and unconjugated cholesterol were similarly increased **(Fig. 38A)**. On the one hand, cholesterol accumulation in DUAL livers reflected high amounts of digested cholesterol from WD. On the other hand, the vast increase of unconjugated or free cholesterol (FC) was the result of unbalanced cellular cholesterol homeostasis, decreased cholesterol esterification, attenuation of cholesterol export and BA synthesis pathways. Moreover, accumulation of FC is well-known to be highly cytotoxic, leading to liver injury through the activation signaling pathways in KCs, HSCs, and hepatocytes, promoting inflammation and fibrogenesis (185, 186).

Cholesterol esters are a non-toxic path to store cholesterol, that was found to be increased in DUAL mice. Surprisingly, high levels of FC were also found in DUAL animals, which have been described to be toxic for hepatocytes, contributing to lipotoxicity.

A.

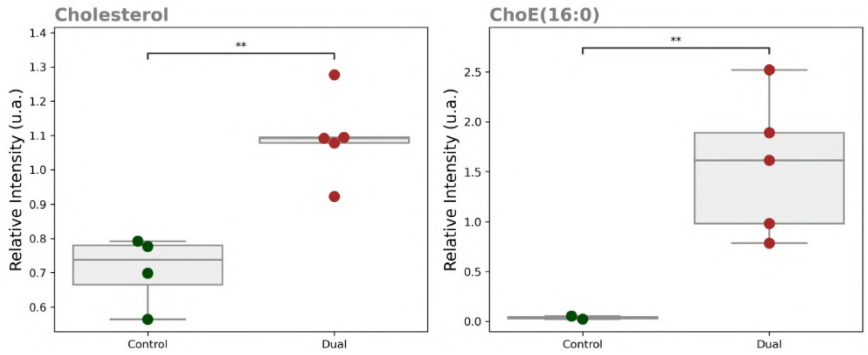

Fig. 38. A. Metabolomic study. Boxplots representing the levels of cholesterol and the cholesterol ester ChoE (16:0) in liver tissue samples. Data represented as relative intensity (arbitrary units). (N = 5). Significant differences are denoted as follows: p<0.01: **.

7.4. EXCESSIVE INTESTINAL ABSORPTION OF FAT CONTRIBUTED TO HEPATIC STEATOSIS IN DUAL MICE

Previously, it has been described that the overconsumption of energy-dense foods, especially rich in fat and sugars, induce elevated lipid absorption which contributes to obesity, MS, and fatty liver (187). However, fatty liver is the outcome of imbalance between dietary fat digestion, absorption, and metabolism. Thus, fat absorption was studied in the DUAL model. Fasted mice were gavaged with BODIPY® 500/510 C1, C12 fatty acids and, 2 h later, they were sacrificed. Following IF staining revealed higher rate of lipid absorption in DUAL intestine in the duodenum and in the jejunum **(Fig. 39A-D).**

Moreover, *Cd36*, a membrane protein that facilitates fatty acid uptake, was strongly upregulated in duodenum, jejunum and ileum of DUAL mice compared to controls **(Fig. 39E-G).**

Subsequently, we examined the amount of fat excreted by feces. The fat content in the stool of DUAL mice was isolated and weighted **(Fig. 40A).** The total amount of fat in DUAL feces was higher. However, the ratio between the amount of excreted fat vs amount of ingested fat was much lower in DUAL mice **(Fig. 40B).** This indicates a higher absorption rate of dietary lipids in DUAL animals.

Next, we decided to elucidate the qualitative aspects of fecal fat. As highlighted in the volcano plot **(Fig. 41A)** or the heatmap representation **(Fig. 41B),** most of the metabolites were significantly increased in DUAL mice, especially PC and

NEFA. The increment of TG, although also observed in these samples, was not so marked as in the liver study. The lower levels suggested a higher rate of absorption **(Table 9).**

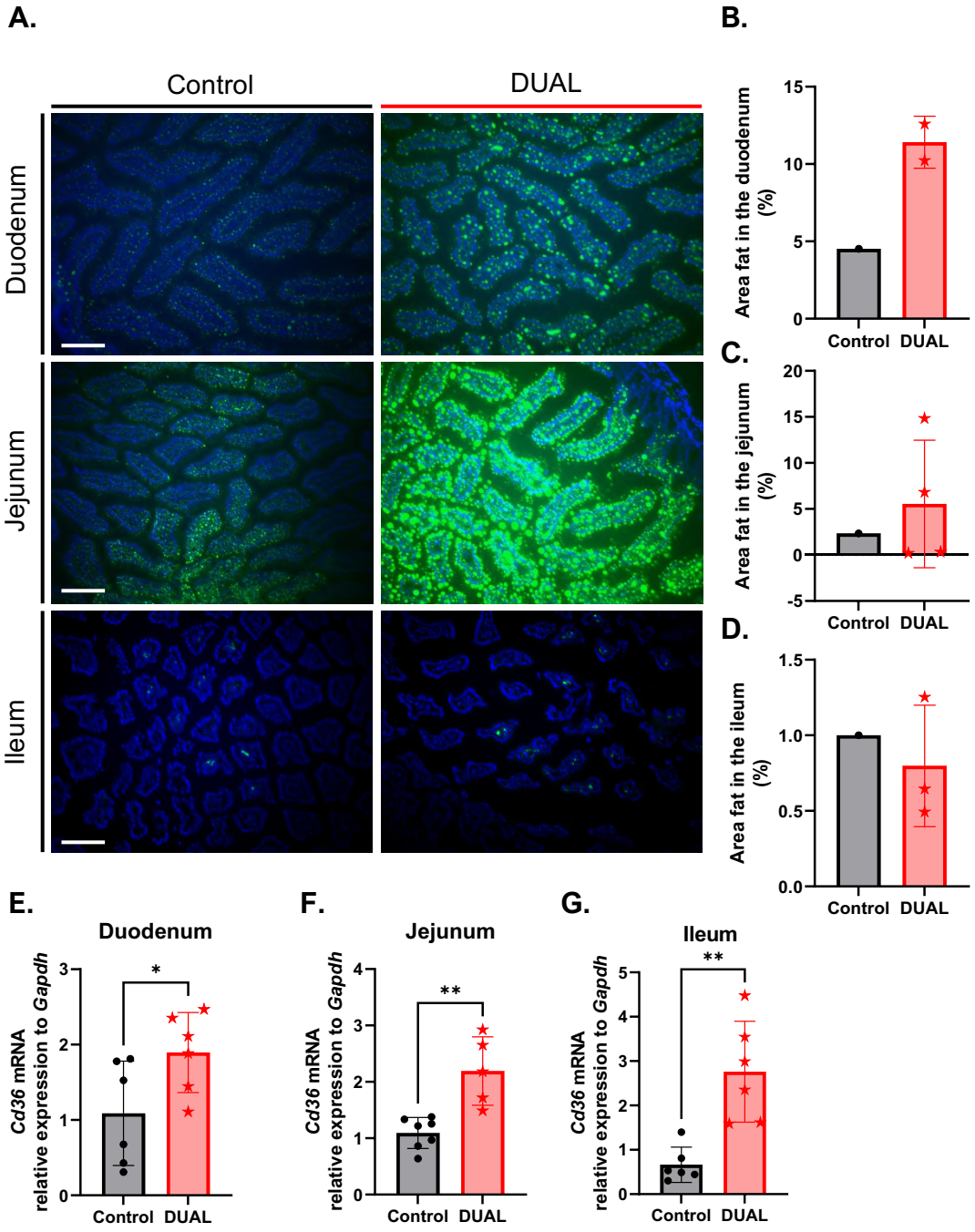

Fig. 39. A. Gut images (duodenum, jejunum, and ileum) of BODIPY® gavaged mice fed with Ctrl, WD and DUAL diet. **B-D.** Fat-positive area (stained in green) was quantified using ImageJ software (N = 1-3). **E-G.** *Cd36* mRNA relative expression to *Gapdh* was determined in duodenum, jejunum, and ileum respectively by RT-qPCR (N = 5-6). Significant differences are denoted as follows: p<0.05: *; p<0.01: **.

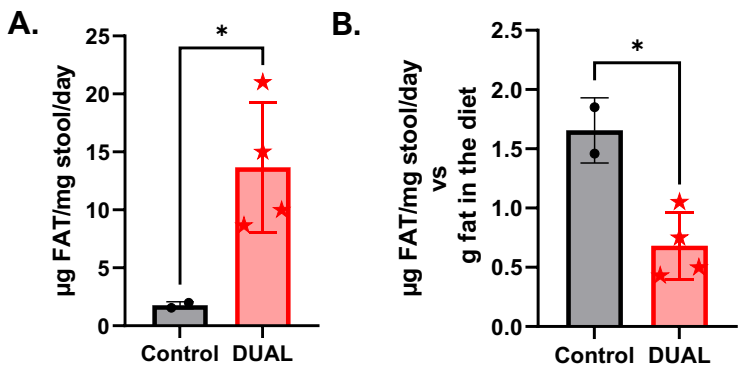

Fig. 40. A. Quantification of fat content in feces (µg fat/mg feces/day). **B.** Fat content in feces/g fat consumed ratio (µg fat/mg feces/day vs. g fat intake from diet). (N = 2–4) Significant differences are denoted as follows: p<0.05: *.

It is well known that the digestion and absorption of fat in the intestine is accomplished by BAs. They make lipids accessible to digestive enzymes and nutrient uptake machinery. Additionally, it has been described that high fat diets and CLD can alter the metabolism of BAs (188, 189).

Therefore, next we analyzed the enterohepatic cycle of BA circulation in DUAL mice. First, we identified increasing levels of BA in the serum of DUAL animals **(Fig. 42A)**. Second, to identify if the cause of increased BA in serum was an overcontent of BA in the liver, we measured the total bile salt (TBS) in the liver and performed Hall's Bilirubin Staining to confirm the presence of bile substances in the hepatic parenchyma **(Fig. 42B-D)**. Both methods revealed no difference between control and treated groups and were consistent with the levels of the CA and CDCA in the liver that were identified in the metabolome study; indicating that DUAL feeding does not induce cholestasis **(Fig. 42E-F).**

Consistently, we found no difference in the intrahepatic synthesis BA: the classical (*Cyp7a1)* and also the alternative regulator *(Cyp27a1)* of BAs synthesis were unaltered in DUAL livers **(Fig. 42G, H).**

Conjugated BAs are transported across the canalicular membrane into the bile and stored in the gallbladder. They were found to be decreased in DUAL animals, especially the glycine conjugated bile acid, Glycocholic acid (GCA) and the taurine conjugated bile acid, Taurolithocholic acid (TLCA) **(Fig. 42I, J).** The intrahepatic expression of bile salt export pump (BSEP), which regulates the efflux of BAs from the hepatocytes into the canaliculi, was subsequently downregulated in DUAL animals **(Fig. 42K)** (18).

A.

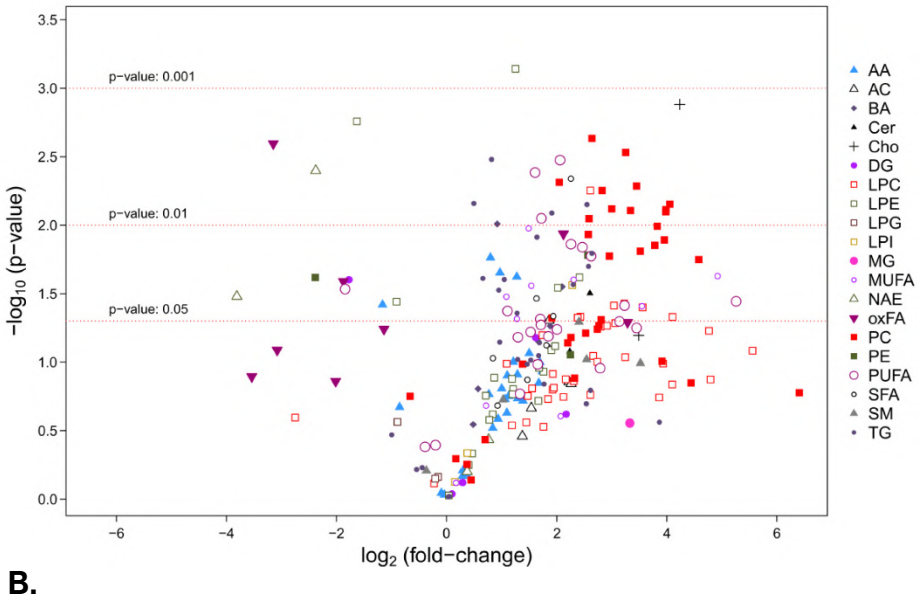

B.

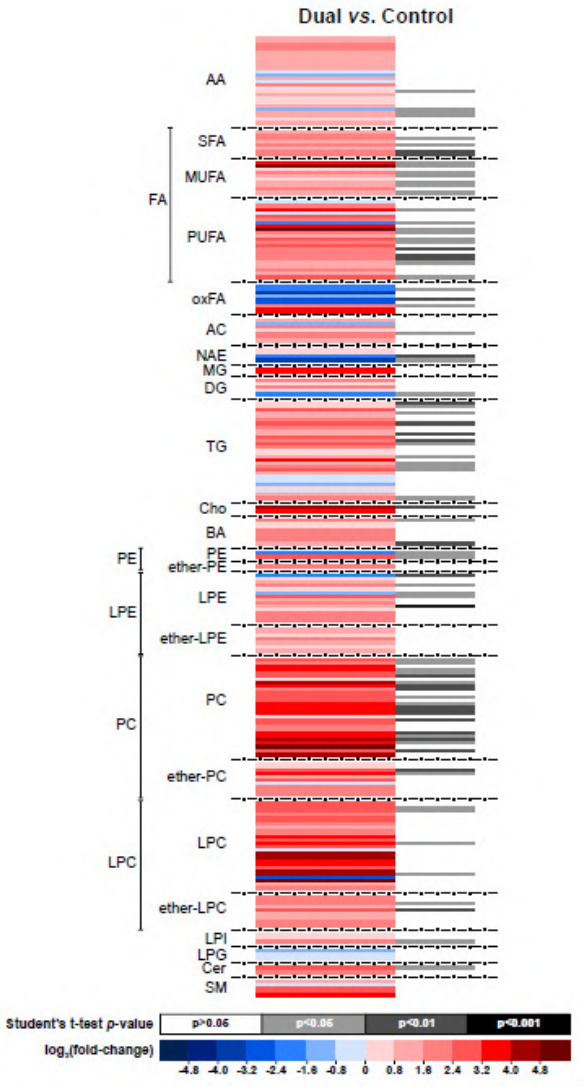

Fig. 41. A. Metabolomic study in feces. Volcano plot [-log10(p-value) vs. log2(fold-change)] for the comparison DUAL vs. Control mice (fecal samples). Abbreviations: AA, amino acids; AC, acyl carnitines; BA, bile acids, Cer, ceramides; Cho, cholesterol; DG, diglycerides; LPC, lysophosphatidylcholines; LPE, lysophosphatidylethanolamines; LPG, lysophosphatidylglycerols; LPI, lysophosphatidylinositols; MG, monoglycerides; MUFA, monounsaturated fatty acids; NAE, N-acyl ethanolamines; oxFA, oxidized fatty acids; PC, phosphatidylcholines; PE, phosphatidylethanolamines; PI, phosphatidylinositols; PUFA, polyunsaturated fatty acids; SFA, saturated fatty acids; SM, sphingomyelins; TG, triglycerides. **B.** Heatmap representing binary comparisons between DUAL and Control per metabolite (Study of fecal samples). Heatmap color codes for log2 (fold-change) and Student's t-test p-values are indicated at the bottom of the figure.

Table 9. Metabolites only detected in one of the groups (fecal samples).

Class	Metabolite	Variable (Code OWL)	Detected in group
Acylcarnitines	AC(14:1n-x)	AC06	DUAL
	AC(8:1n-x)	AC07	Control
	AC(16:1n-x)	AC17	DUAL
Cholesterol esters	ChoE(18:1)	ChoE_07	DUAL
	ChoE(20:4)	ChoE_12	DUAL
	ChoE(22:6)	ChoE_17	DUAL
Phosphatidylcholines	PC(40:7)	DAPC32	DUAL
	PC(36:5)	DAPC44	DUAL
	PC(37:4)	DAPE27	DUAL
Oxidized fatty acids	9,10-DiHOME	FFAox34	Control
Lysophosphatidylcholines	PC(0:0/20:1)	MAPC27	DUAL
	PC(0:0/20:2)	MAPC30	DUAL
	PC(20:3/0:0)	MAPC36	DUAL
	PC(0:0/22:4)	MAPC41	DUAL
	PC(22:4/0:0)	MAPC43	DUAL
	PC(0:0/22:5)	MAPC46	DUAL
	PC(22:5/0:0)	MAPC47	DUAL
Lysophosphatidylethanolamines	PE(22:4/0:0)	MAPE35	DUAL
	PE(22:6/0:0)	MAPE41	DUAL
Ether linked phosphatidylcholines	PC(P-36:2)	MEMAPC15_MEMAPC16	DUAL
Sphingomyelins	SM(d18:1/18:0)	SphLip_13	DUAL
TGs	TG(54:5)	TG53	DUAL
	TG(54:6)	TG55	DUAL

The food uptake stimulated gallbladder contraction, leading to the release of BAs into the intestine, where they solubilize and facilitate the absorption of dietary lipids. After performing these tasks, BA are reclaimed to the blood through a combination of passive absorption in the proximal small intestine and active transport in the distal ileum. In the ileum of DUAL mice, we found upregulation of ASBT - the transporter that moves BAs from the intestinal lumen across the apical brush border membrane **(Fig. 43A)**. OST-α and OST-β transporters, which further shuttle BA to the basolateral membrane and efflux them into the portal circulation, did not exhibit any changes in the DUAL group compared to controls **(Fig.43B, C).** The unaltered intestinal bile transporters were accompanied by intrahepatic downregulation of NTCP - the regulator of BA extraction from portal

blood **(Fig. 43D)**. These altogether leads to the increase of TBS level in serum in the DUAL group (190, 191).

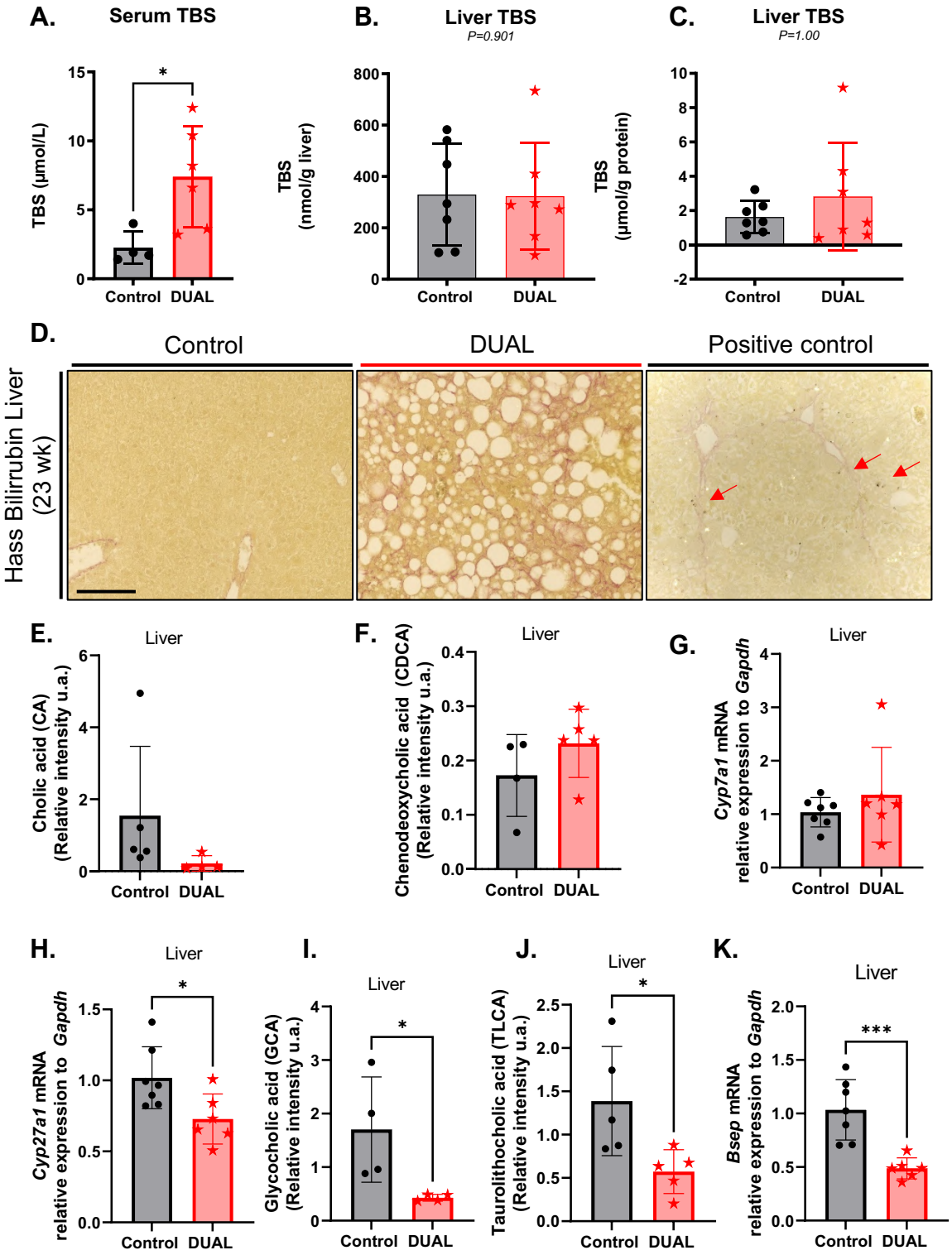

Fig. 42. A. TBS in serum (µmol/L). **B.** TBS in the liver nmol/g liver). **C.** TBS in the liver (µmol/g protein liver). **D.** Hass Bilirubin staining in the liver. Positive staining from positive control (treated with CCl_4) is showed and positive area (black dots) marked with arrows. **E-F.** CA and CDCA levels were determined in the liver though a metabolome study

(relative intensity u.a.). **G-H.** *Cyp7a1* and *Cyp27a11* mRNA relative expression to *Gapdh* in the liver was quantified by RT-qPCR respectively. **I-J.** Conjugated bile acids GCA and TLCA were respectively determined in the liver through a metabolome study (relative intensity u.a.). **K.** *Bsep* mRNA relative expression to *Gapdh* in the liver was quantified by RT-qPCR. (N = 4-7). Significant differences are denoted as follows: p<0.05: *; p<0.001: ***.

In line with these results, we found increased levels of Alkaline phosphatase (AP) in DUAL mice serum, whose increased activity has been described as a surrogate marker of BA retention **(Fig. 43E)** (192).

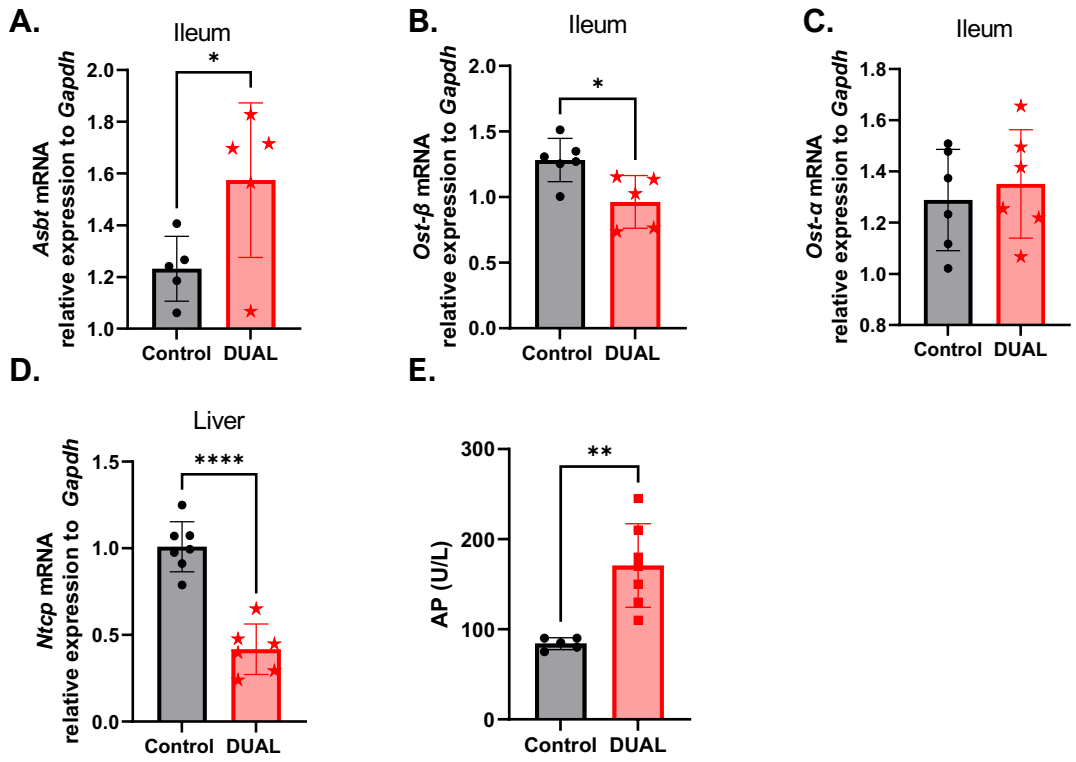

Fig. 43. A-C. *Asbt*, *Ost-β*, *Ost-α* mRNA relative expression to *Gapdh* was quantified in ileum by RT-qPCR respectively. **D.** *Ntcp* mRNA relative expression to *Gapdh* was quantified in liver by RT-qPCR. **E.** Alkaline phosphatase (AP) was determined in serum (U/L). (N = 5 – 7). Significant differences are denoted as follows: p<0.05: *; p<0.01: **; p<0.0001: ****.

A small part of BA is not recirculated but enters the colon where they are either dehydroxylated or deconjugated by bacteria and, mostly, excreted by fecal excretion. The metabolomic analysis of feces revealed increasing levels of primary bile acids (CA) **(Fig. 44A, B),** and conjugated bile acids (TCA) **(Fig. 44C),** consistently with the heatmap shown on **Fig. 41B.**

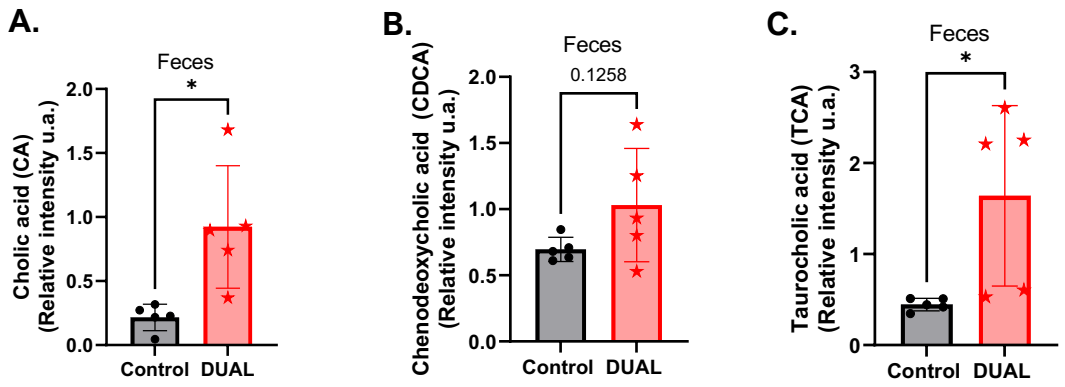

Fig. 44. A-C. Levels of CA, CDCA and TCA were determined in feces through the metabolome study (relative intensity u.a.). (N = 5). Significant differences are denoted as follows: p<0.05: *.

Moreover, FXR has been described to play an important role in bile salts homeostasis, as well as in glucose and lipid metabolism. FXR expression in ileum is able to induce FXR in the liver that critically regulates BA flux, suppresses DNL synthesis and increases lipid oxidation. Besides, it has been recently shown to play an important anti-inflammatory role (190, 193). DUAL animals exhibited decreased FXR expression in the ileum and, subsequently, in the liver **(Fig. 45A, B)**.

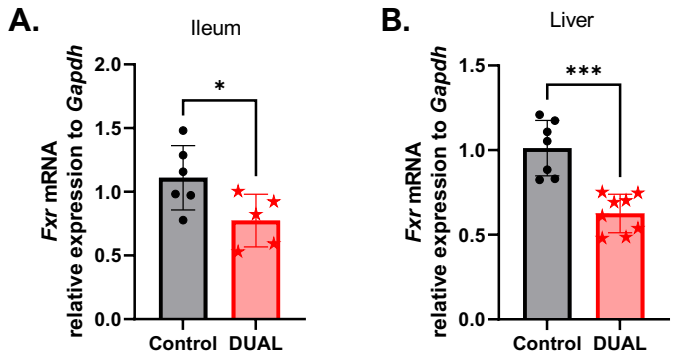

Fig. 45. A-B. *Fxr* mRNA relative expression to *Gapdh* was determined by RT-qPCR in the ileum and in the liver respectively. (N = 5-7). Significant differences are denoted as follows: p<0.001: ***.

Altogether, our results show a dysregulation in the BA cycle, that is resumed and represented in **Fig. 46A.**

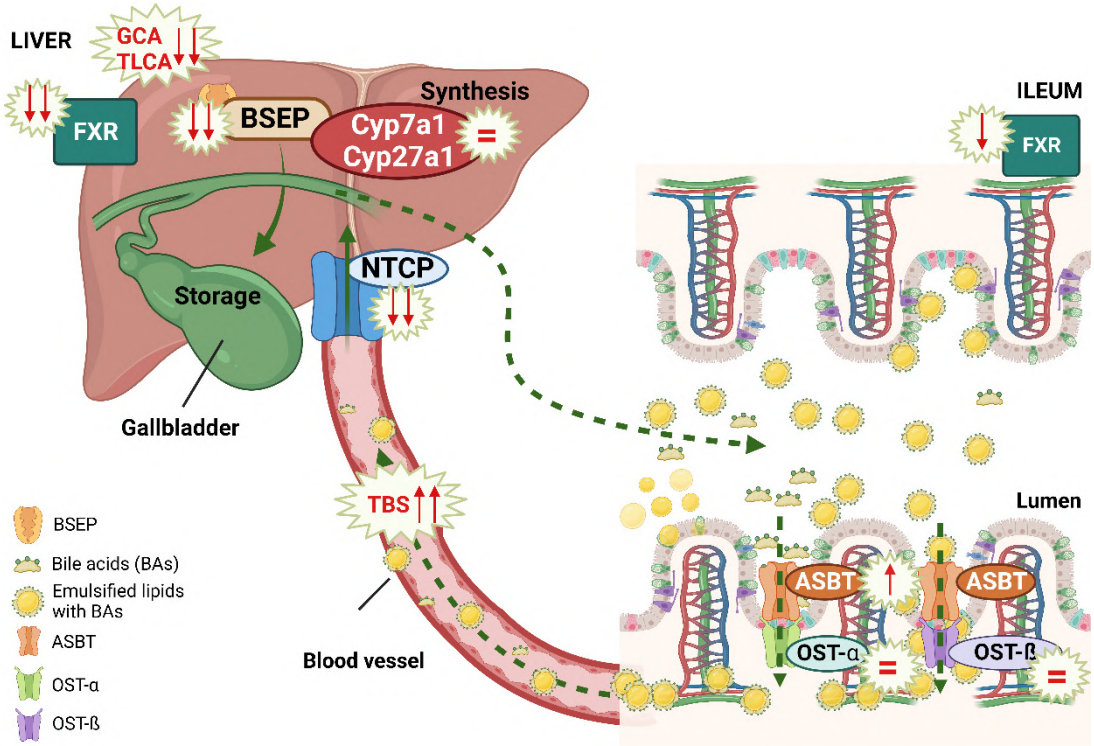

Fig. 46. Schematic representation of changes found in bile salts cycle in DUAL mice.

7.5. MASSIVE LIPID ACCUMULATION IN THE LIVER INDUCED LIPOTOXICITY, OXIDATIVE STRESS AND HEPATOCYTE CELL DEATH IN DUAL MICE

Massive deposition of fat in the liver tissue, coupled with alcohol consumption, induces oxidative stress (194). 23-week DUAL feeding showed an increased expression of cytochrome P450 (CYP2E1) **(Fig. 47A),** as well as significant induction of lipid peroxides in the liver, which we detected by 4-hydroxinonenal (4-HNE) staining **(Fig. 47B-C)**.

Oxidative stress caused ultrastructural morphological mitochondrial changes in DUAL animals, which were identified through transmission electron microscopy (TEM). Mitochondrial stress, induced by DUAL diet, led to irregular circled shapes, accumulation of cristae, and multiple electron dense particles in the mitochondria **(Fig. 47D).**

Rough ER enlargement and cisternae dilation were specifically found in DUAL mice **(Fig. 47D).**

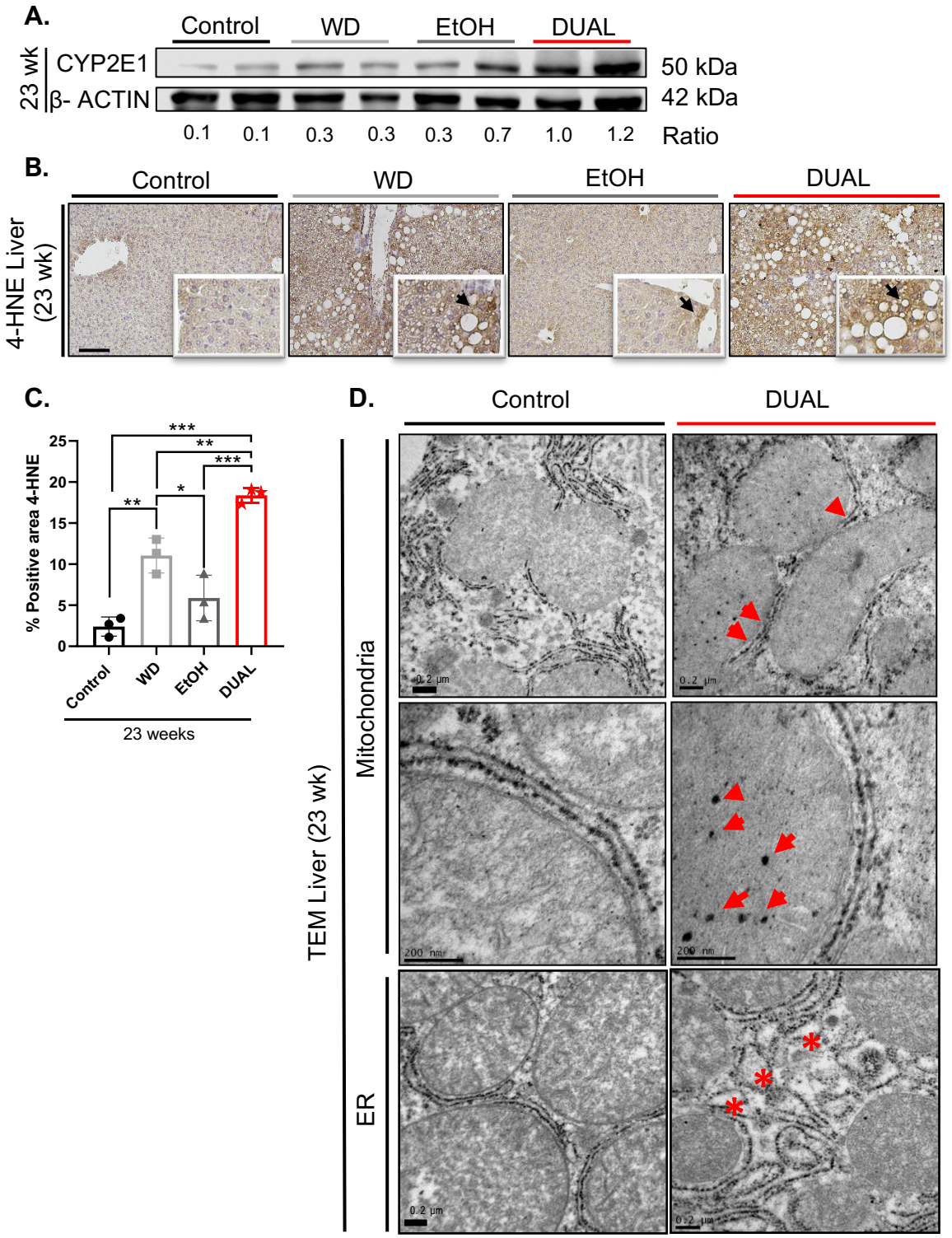

Fig. 47. A. CYP2E1 WB, β-actin used as a loading control. Ratio between CYP2E1 and β- actin was calculated. **B.** Illustrative 4-HNE- stained liver sections from each group after 23 weeks of feeding **C.** 4- HNE quantification (N = 3). Scale bar = 100 μm. **D.** Representative TEM pictures of control and DUAL groups. Mitochondria and endoplasmic reticulum are shown. Arrows mark cristae inclusions in mitochondrial matrix. Significant differences are denoted as follows: p<0.05: *; p<0.01: **; p<0.001: ***.

Oxidative and mitochondrial stress likely contributed to liver damage and caused significant increases in the plasma levels of ALT, AST, and LDH, all major clinical indicators of cellular liver injury **(Fig. 48A-C).**

In this line, cell death revealed by TUNEL IF staining in DUAL-fed mice livers was significantly higher compared to other experimental groups **(Fig. 48D-E).**

Death of hepatocytes may trigger compensatory proliferation in surrounding cells to maintain tissue homeostasis, as indicated by higher cellular proliferation in DUAL mice compared to the rest of experimental groups, which was assessed by Ki-67 IHC staining **(Fig. 48F-G).**

7.6. DUAL FEEDING INDUCED EXTENSIVE HEPATIC INFLAMMATION

Lipid deposition and cell death in the liver resulted in the infiltration of immune cells and liver inflammation (195). Mice fed either with WD or EtOH showed an increase in the accumulation of KCs/macrophages (positive CD45/F480), assessed by IF staining. However, this infiltration was more significant in DUAL animals **(Fig. 49A-C).**

This result was confirmed by flow cytometry analysis in the liver where we detected significantly increased monocytes, KCs, T-lymphocytes ($CD3^+$) and cytotoxic T lymphocytes ($CD8^+$) in DUAL animals. In contrast, the population of T helper ($CD4^+$) was reduced **(Fig. 50A-I).**

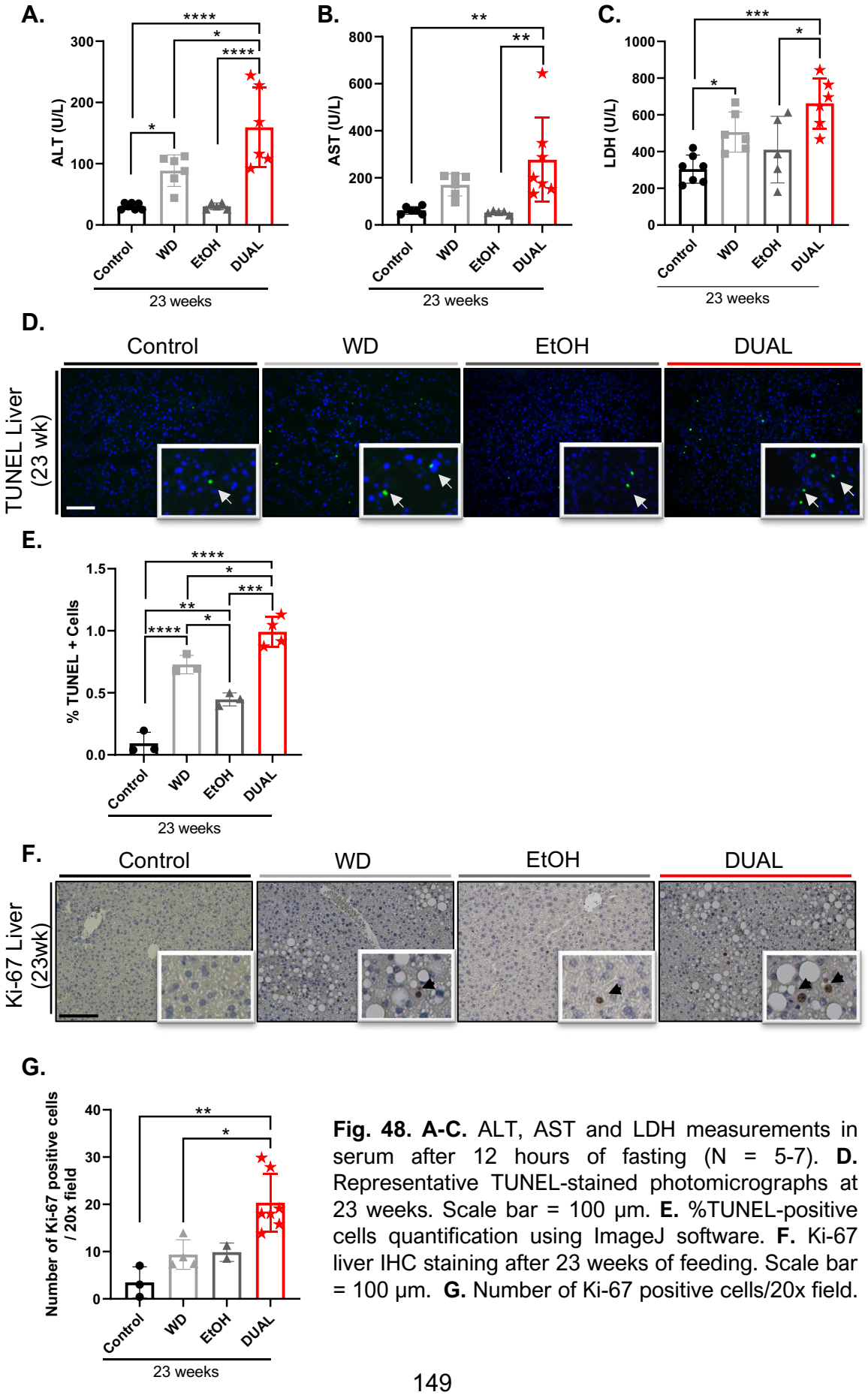

Fig. 48. A-C. ALT, AST and LDH measurements in serum after 12 hours of fasting (N = 5-7). **D.** Representative TUNEL-stained photomicrographs at 23 weeks. Scale bar = 100 µm. **E.** %TUNEL-positive cells quantification using ImageJ software. **F.** Ki-67 liver IHC staining after 23 weeks of feeding. Scale bar = 100 µm. **G.** Number of Ki-67 positive cells/20x field.

Significant differences are denoted as follows: p<0.05: *; p<0.01: **; p<0.001: ***; p<0.0001: ****.

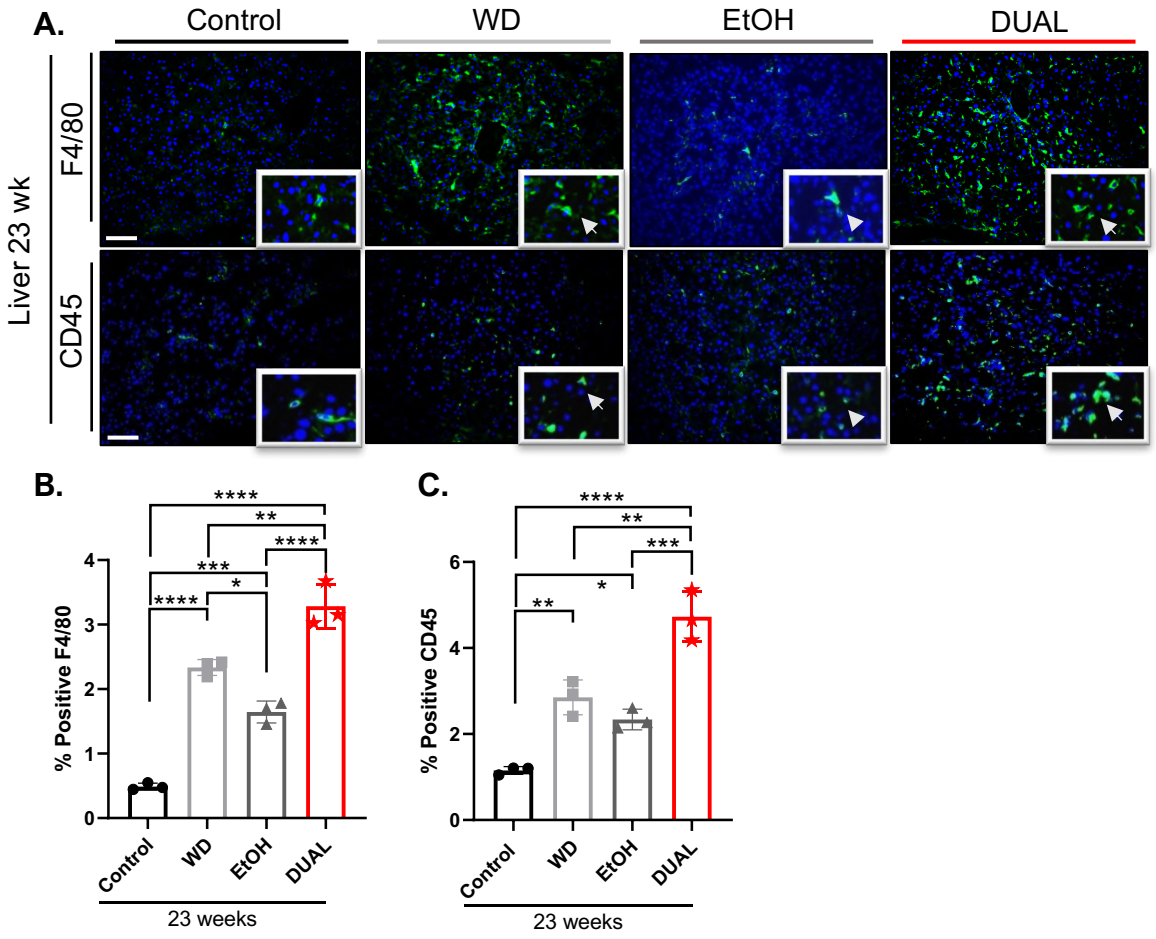

Fig. 49. A. Illustrative CD45 and F4/80 IF staining in liver sections of mice fed for 23 weeks. Positive immune cells are stained in green. Nuclei are stained in blue using DAPI as a counterstain. Arrows indicate CD45 or F4/80 positive cells. Scale = 100 µm. **B, C.** Quantification of %CD45 and F4/80 positive cells, respectively, using ImageJ software (N = 3). Significant differences are denoted as follows: p<0.05: *; p<0.01: **; p<0.001: ***; p<0.0001: ****.

The infiltrating cells actively produced various cytokines and contributed to the creation of a pro-inflammatory microenvironment. As expected, the mRNA expression of tumor necrosis factor-α (*Tnf-α*) was significantly increased in mice fed with the DUAL diet, particularly after 23 weeks of feeding **(Fig. 51A).**

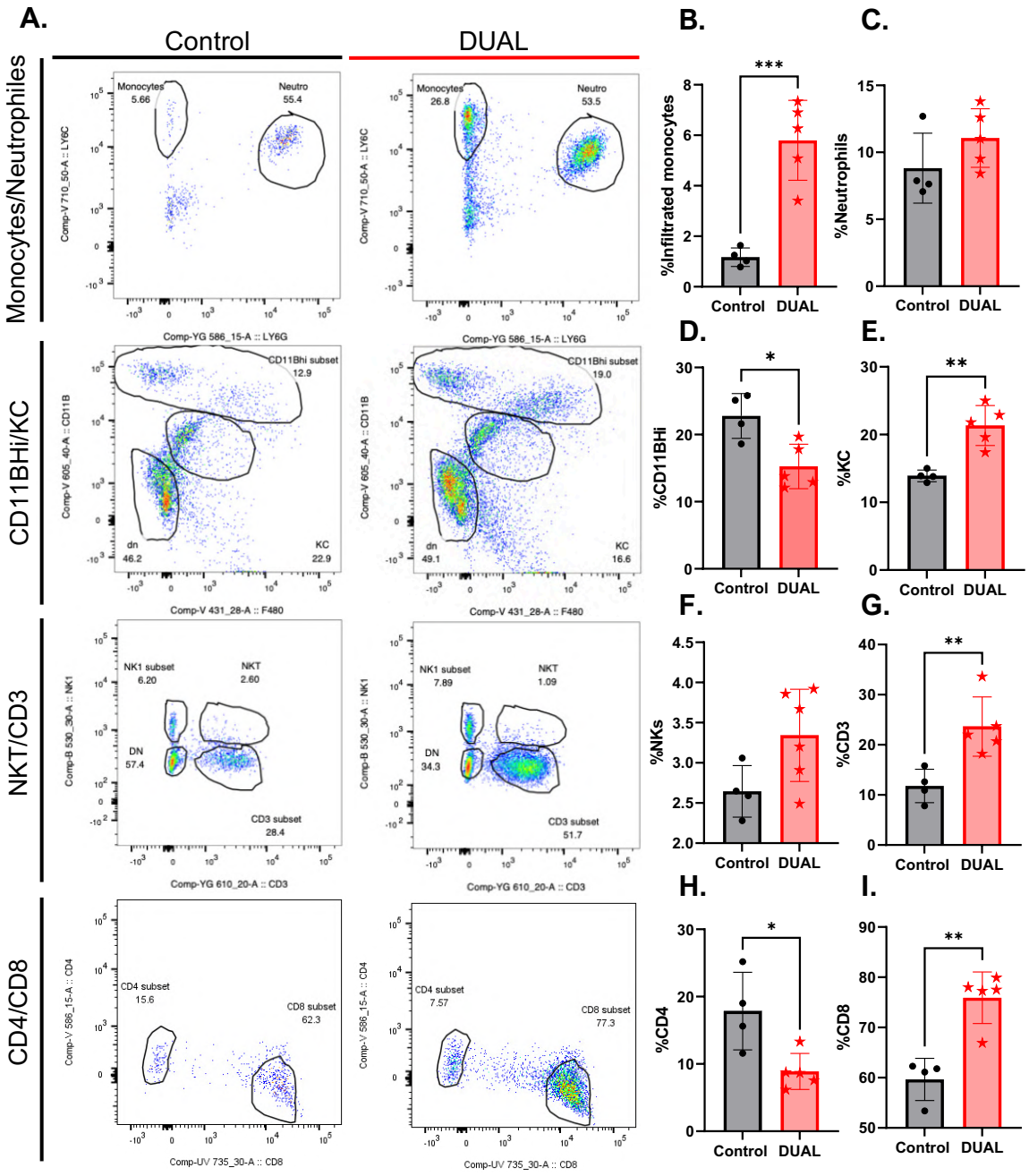

Fig. 50. A. Flow cytometry dot plots in liver. **B-I.** % of infiltrated monocytes, neutrophils, CD11BHi, KCs, NKs, CD3, CD4 and CD8 was calculated. (N = 4-5). Significant differences are denoted as follows: p<0.05: *; p<0.01: **.

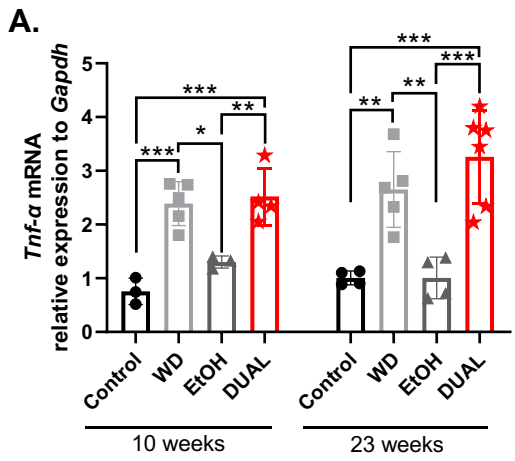

Fig. 51. A. *Tnf-α* mRNA relative expression to *Gapdh* after 10 and 23 weeks on diet (N = 3- 6). Significant differences are denoted as follows: p<0.05: *; p<0.01: **; p<0.001: ***.

7.7. DUAL DIET LED TO ADVANCED STAGES OF CLD

An excessive production of TNF-α triggers the activation of HSCs in the liver (196). Congruently, in DUAL-fed animals, WB and IHC analyses showed a strong expression of α-SMA, a marker of HSCs activation **(Fig. 52A-B).**

Activated HSCs are the main source of ECM during the progression of fibrosis. Therefore, SR staining demonstrated that the feeding of WD or EtOH alone can induce minor collagen deposition in the liver, while the rapid and severe progression of fibrosis was a remarkable feature of DUAL mice.

Advanced signs of fibrosis were noticeable after 23 weeks of feeding **(Fig. 52B-C).**

These findings were confirmed by IF staining for Collagen I **(Fig. 52B-D)**. Histopathological evaluation of fibrosis revealed F1a stage after 10 weeks and F1b in all DUAL animals after 23 weeks of feeding according to *Bedossa* index (152) **(Fig. 52E).**

Additionally, TEM analysis in the liver further identified collagen fibers in DUAL mice **(Fig. 52F)**. Finally, the upregulation of the pro-fibrogenic gene *CollagenI* was identified in DUAL livers by qPCR **(Fig.52G).**

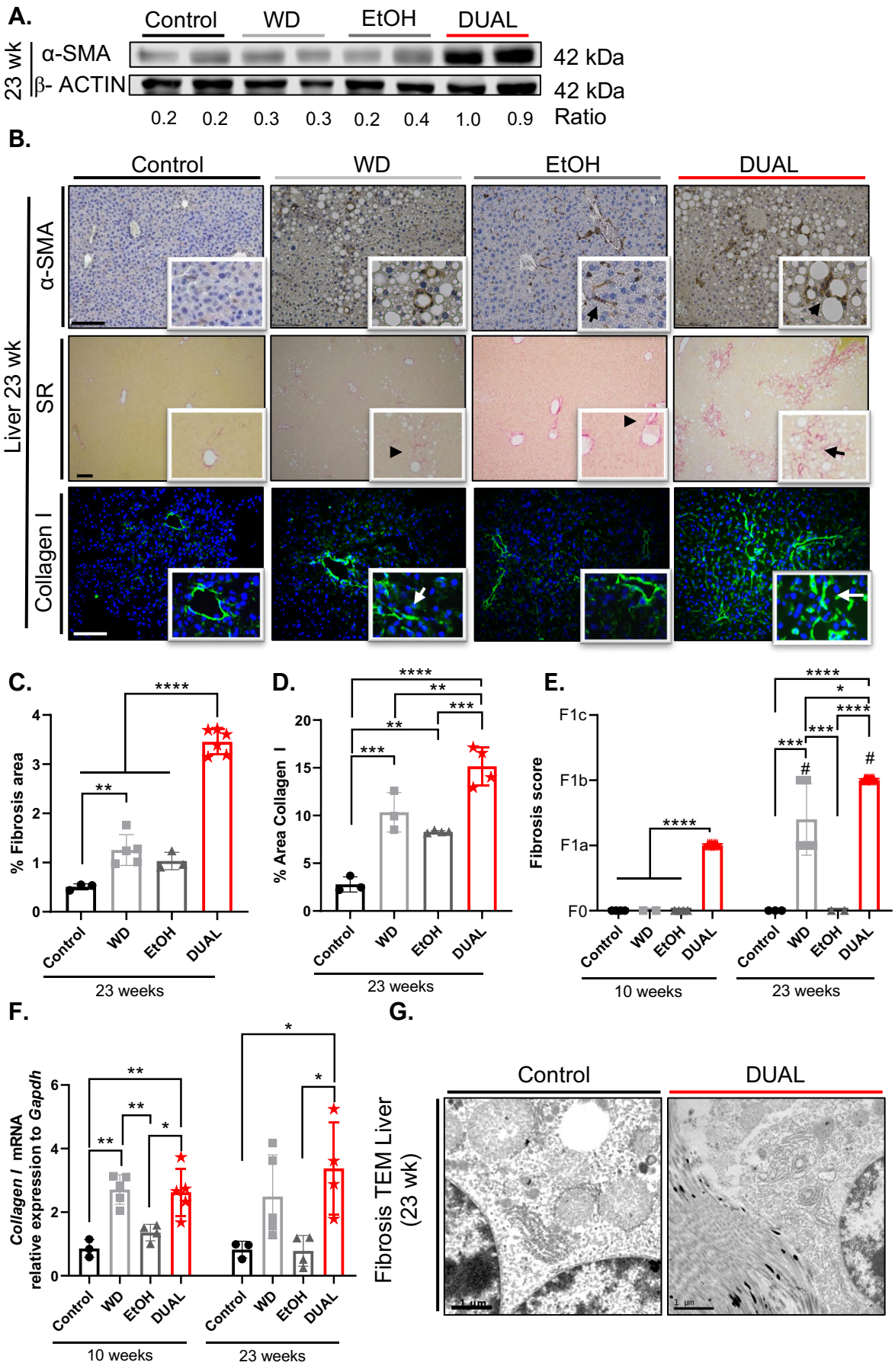
A.
Control
WD
EtOH
DUAL
23 wk
α-SMA
β- ACTIN
42 kDa
42 kDa
0.2 0.2 0.3 0.3 0.2 0.4 1.0 0.9
Ratio
B.
Control
WD
EtOH
DUAL
Liver 23 wk
α-SMA
SR
Collagen I
C.
% Fibrosis area
23 weeks
D.
% Area Collagen I
23 weeks
E.
Fibrosis score
F0
F1a
F1b
F1c
10 weeks
23 weeks
F.
Collagen I mRNA relative expression to Gapdh
10 weeks
23 weeks
G.
Fibrosis TEM Liver (23 wk)
Control
DUAL

Fig. 52. A. α- SMA western blot using β- actin as a loading control. Ratio between α- SMA and β-actin is calculated. **B.** HSCs and fibrosis- related stainings in liver. Representative liver images stained with α- SMA (IHC), SR, and collagen I (IF). Scale bar = 100 µm. **C, D.** Quantification of positive SR- stained and collagen I– stained areas after 23 weeks of treatment, respectively (SR, N = 3-6; collagen I, N = 3-4). **E.** Fibrosis score assigned after 10 and 23 weeks of feeding in all groups (N = 3-7). **F.** Respective *Collagen I* (10 and 23 weeks) mRNA expression relative to *Gapdh* (N = 3-6). **G.** Descriptive TEM pictures of collagen fibres in Control and DUAL group at 23 weeks. Significant differences are denoted as follows: p<0.05: *; p<0.01: **; p<0.001: ***; p<0.0001: ****.

7.8. DUAL DIET DRIVED CIRRHOSIS AND TUMORIGENESIS

Epidemiological evidence suggests that the combination of alcohol and metabolic factors increases the risk of cirrhosis and cancer (197). Thus, to test this further, we challenged mice to long-term DUAL feeding. After 52 weeks, we observed enlarged livers, yellowish in color, with pronounced scar tissue and single or multiple nodules in the liver surface, in some but not in all mice **(Fig. 53A-C).** DUAL mice also presented enlarged spleens and showed increased levels of plasma AST, ALT, LDH and serum cholesterol **(Fig. 53D-H).**

H&E staining showed immune cell infiltration and significant fatty changes **(Fig. 53I).** Meanwhile, SR staining showed extensive collagen deposition, and well differentiated micronodules surrounded by fibrotic connective tissue, indicating the stage of hepatic cirrhosis **(Fig. 53I).**

Next, we decided to analyze the tumor microenvironment. Notably, we found HSP70/HSP72 and CK19 positive staining, which both are markers of HCC **(Fig. 54A).** Besides, nodules exhibit positive proliferating cell nuclear antigen (PCNA) in the nuclei, a master indicator of proliferation and cell-cycle upregulation **(Fig. 54B).** Studying other components related to cell cycle regulation, we consistently found increased expression of *Cyclin E* mRNA in liver nodule tissue **(Fig. 54C).**

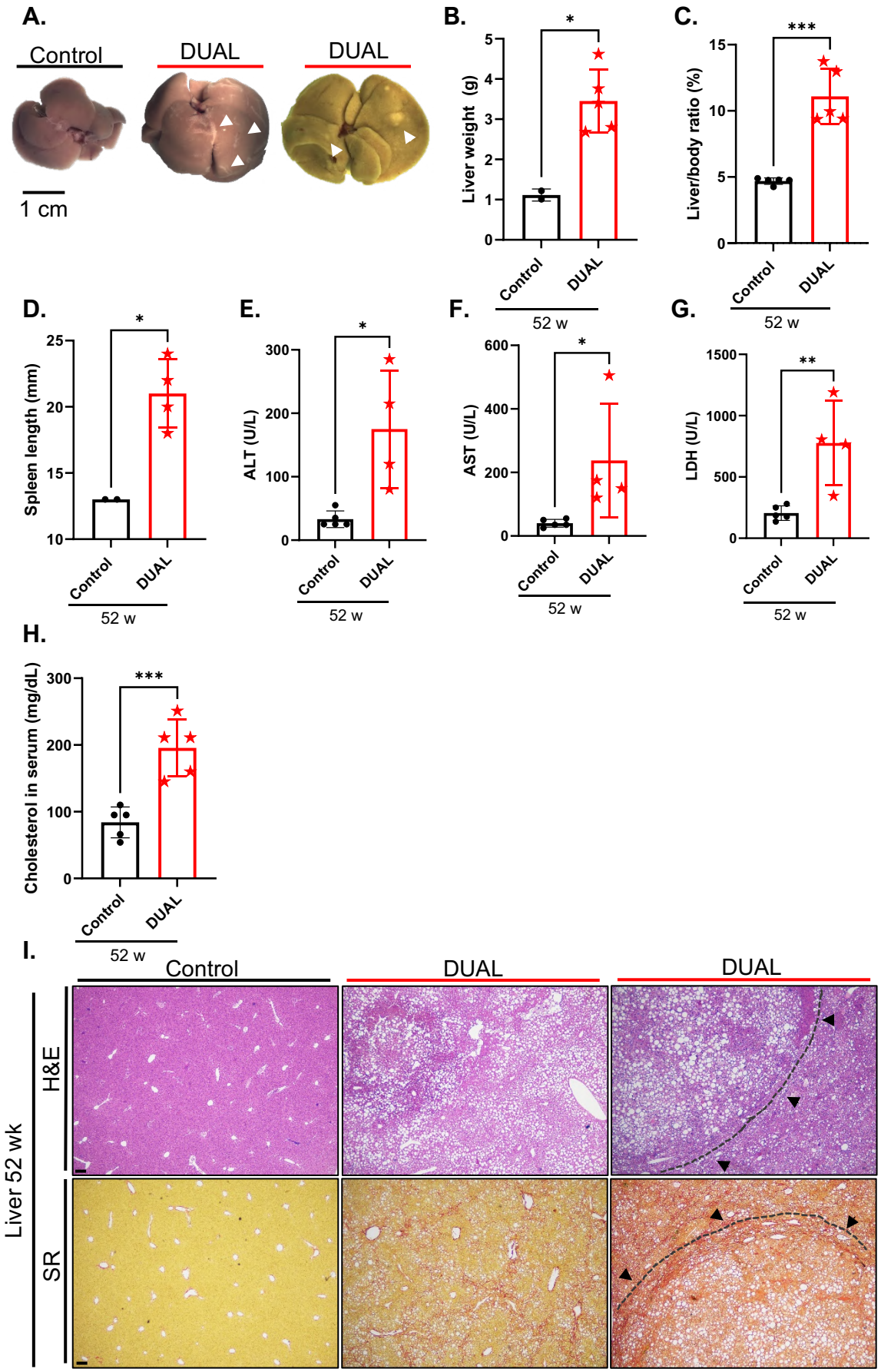
A.
Control
DUAL
DUAL
1 cm
B.
Liver weight (g)
C.
Liver/body ratio (%)
D.
Spleen length (mm)
E.
ALT (U/L)
F.
AST (U/L)
G.
LDH (U/L)
52 w
H.
Cholesterol in serum (mg/dL)
I.
Control
DUAL
DUAL
Liver 52 wk
H&E
SR

Fig. 53. A. Liver pictures after 52 weeks of feeding: control, DUAL and DUAL with regenerative nodule. Fibrotic scars and nodules on the surface are marked with arrows. **B-C.** Liver weight and liver body ratio (%) respectively (N=5). **D.** Spleen length (mm). **E-G**. ALT, AST and LDH (U/L) levels in serum. **H.** Cholesterol in serum (mg/dL). **I.** Representative pictures of H&E and SR staining after 52 weeks: control, DUAL and DUAL with regenerative nodule. Scale = 100 µm. (N = 4-5). Significant differences are denoted as follows: p<0.05: *; p<0.01: **; p<0.001: ***.

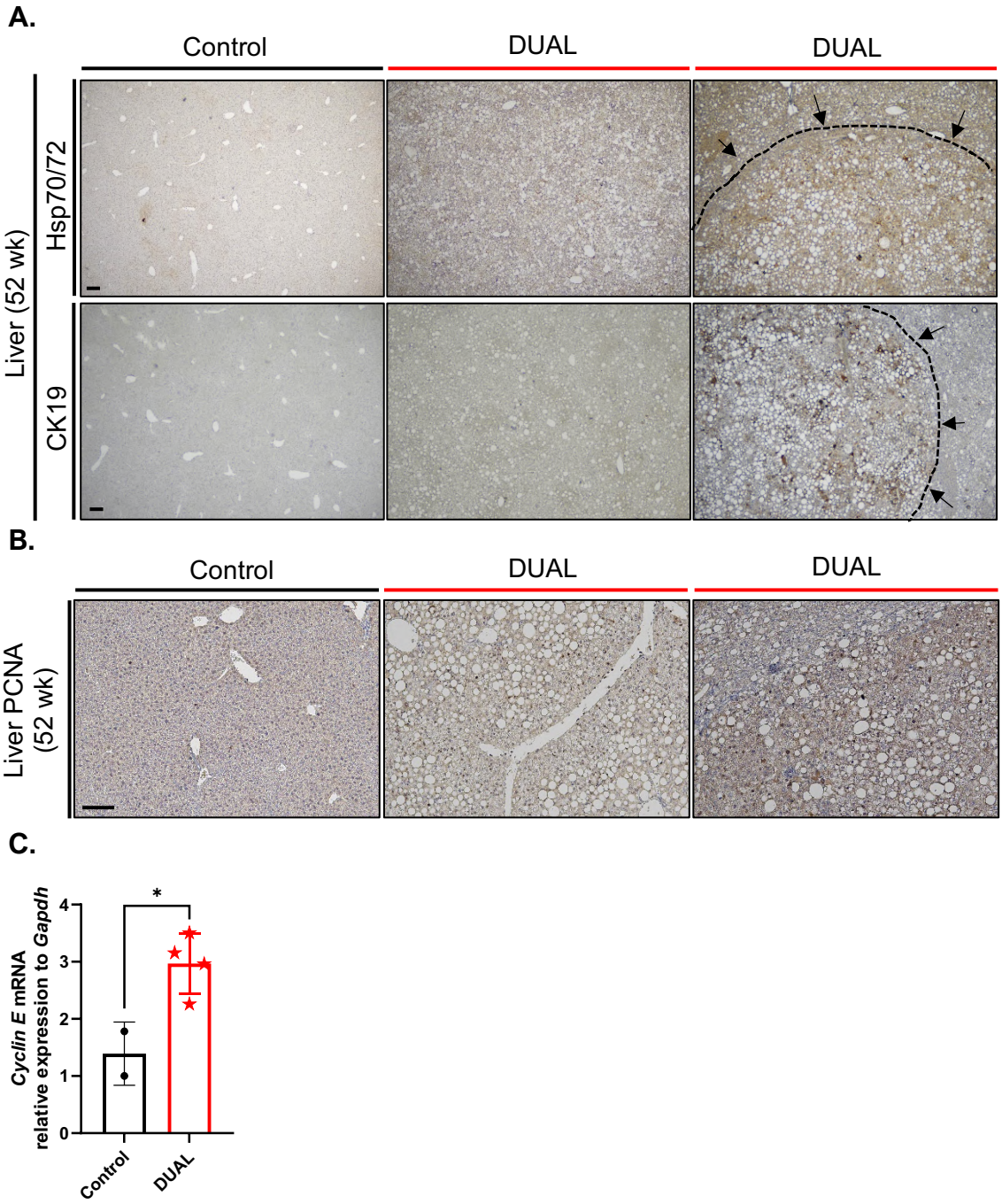

Fig. 54. A. Representative pictures of Hsp70/72 and CK19 after 52 weeks treatment. Control, DUAL and DUAL with regenerative nodule. Scale = 100 µm. **B.** Representative PCNA staining after 52 weeks treatment. Scale = 100 µm. **C.** *Cyclin E* mRNA relative expression to *Gapdh* though RT-qPCR (N = 2-4). Significant differences are denoted as follows: p<0.05: *.

7.9. A FAST TRACK TO HEPATIC TUMORIGENESIS: DUAL FEEDING PLUS DEN

To further investigate how our DUAL model affects tumor progression, a single dose of DEN was administered to 14-day-old mice by IP injection. After eight weeks, DEN-treated mice were split into two groups: one group was fed a DUAL diet while the other group was fed a control chow diet for 16 weeks, as it was described in section **6.2.3.2. DEN + DUAL model and in Fig. 18.**

Macroscopic evaluation showed that all DUAL plus DEN treated mice presented single or multiple tumor nodules larger than 0.5 cm, while only one out of nine mice placed on Chow diet + DEN treatment developed DEN-induced nodules **(Fig. 55A, B).**

DUAL plus DEN treatment also increased the hepatosomatic ratio **(Fig. 55C)**, and the hepatic transaminases (ALT, AST and LDH) **(Fig. 55D-F)**.

Pathological examination of H&E staining revealed well-circumscribed lesions with compressed adjacent parenchyma, loss of lobular architecture, and moderate fatty changes in the tumor nodules of DUAL + DEN mice **(Fig. 55G)**.

All tumor nodules in these mice showed strong overexpression of HCC markers as CK19 and HSP70/HSP72, identified by IHC straining **(Fig. 55G).**

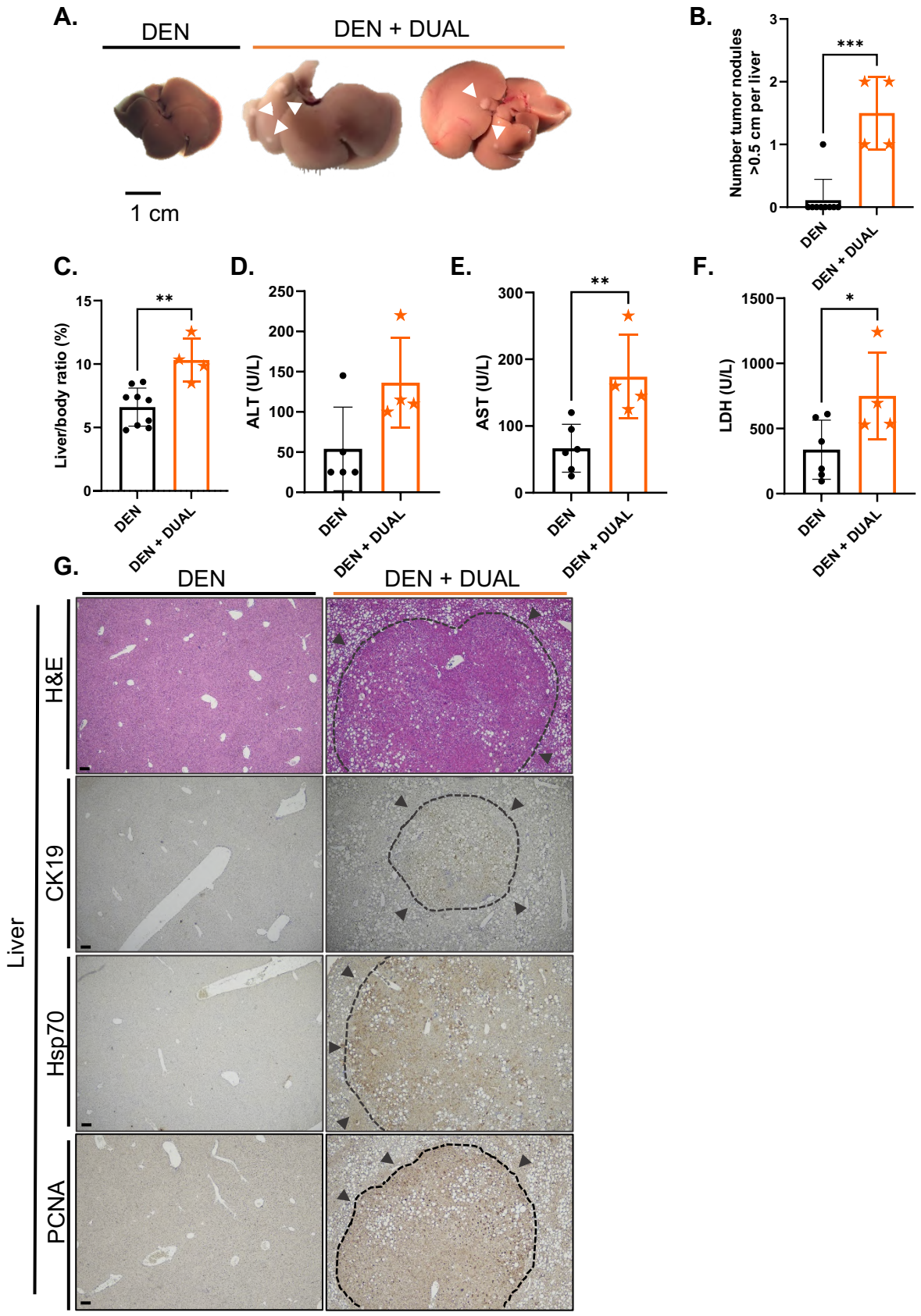

Fig. 55. A. Liver pictures of DEN and DEN + DUAL model. Tumor nodules are marked with arrows. **B.** Number of tumor nodules > 0.5 cm per liver (N = 4-9). **C.** Liver/body ratio (%) (N = 4-9). **D-F.** ALT, AST and LDH (U/L) levels in serum. **G.** Representative pictures of H&E, CK19, Hsp70/72, and PCNA respectively. Scale = 100 µm. Significant differences are denoted as follows: p<0.05: *; p<0.01: **; p<0.001: ***.

7.10. DUAL DIET MODIFIED GUT MORPHOLOGY

The latest compelling evidence showed that the increased consumption of obesogenic foods and alcohol may alter the intestinal function and gut microbiota. The interactions between the liver and the gut, the so-called “gut-liver axis”, play a critical role in onset and progression of CLD (99, 100, 198). Thus, we decided to evaluate the gut phenotype in 23 weeks DUAL diet fed animals.

First, in mice fed with DUAL diet for 23 weeks, we detected a remarkable reduction of the total gut/mouse length **(Fig. 56A, B)** caused by the shortening of the colon **(Fig. 56C)**.

Next, we performed H&E staining to analyze microscopically the gut morphology and to measure the size of the villi and the crypts in the different parts of the small intestine, as well as the size of crypts in colon. No differences were found either in duodenum or in jejunum **(Fig. 56D-I).**

However, DUAL diet slightly modified ileum structure, where villi were shorter **(Fig. 57A, B)** and crypts were shallower **(Fig. 57A, C)**. Importantly, DUAL diet induced strong structural deterioration of colon crypts, manifested by decreases in the crypt depth in DUAL mice compared to controls **(Fig. 58A, B)**.

In fact, gut shortening, and villus/crypt atrophy are biological markers in the assessment of the intestinal injury and inflammation (199). Based on morphological changes, we analyzed in detail the two parts of the gut most affected by DUAL feeding – ileum and colon.

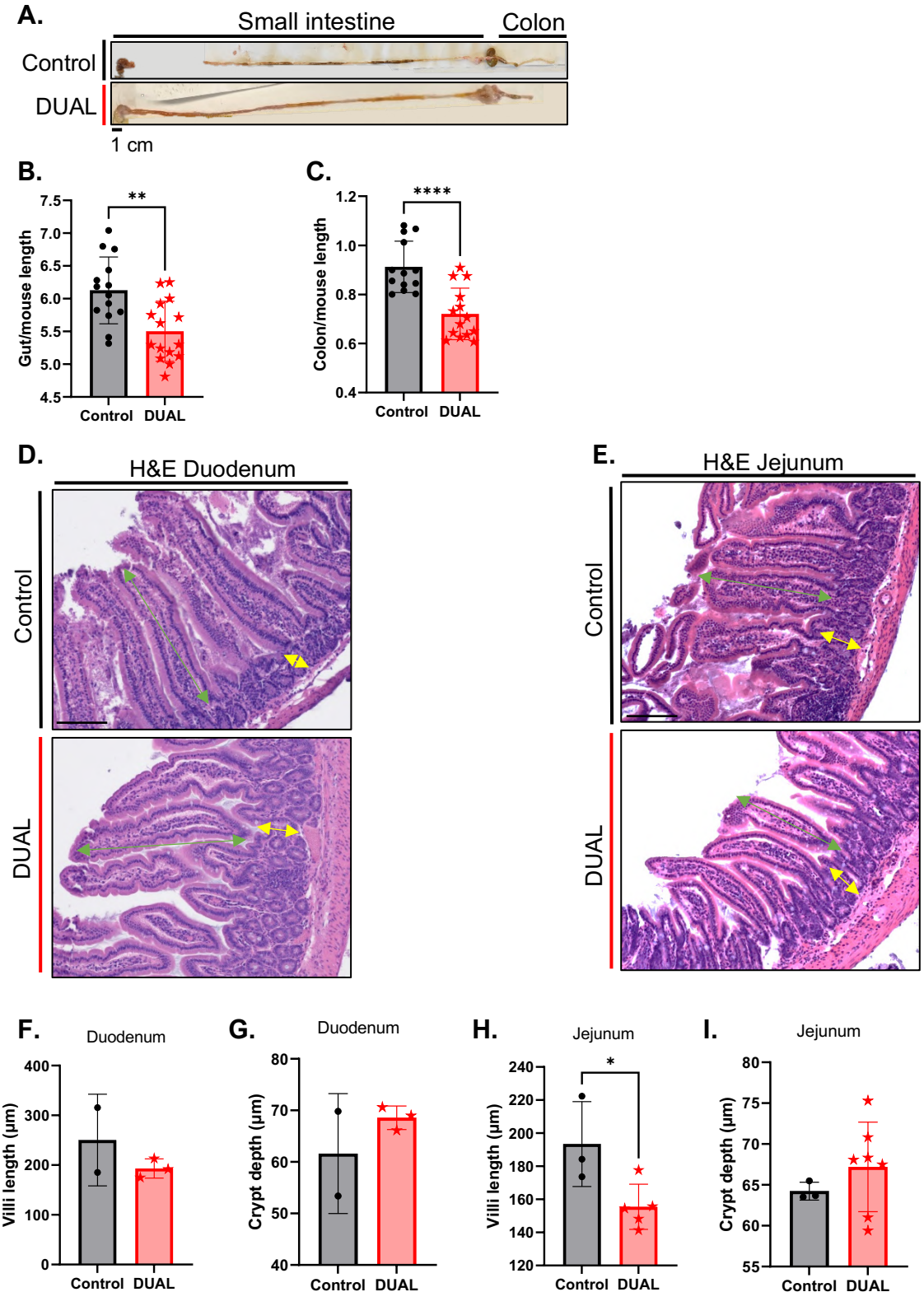

Fig. 1. A. Macroscopic images of gut. Scale = 1 cm. **B.** Gut/mouse length ratio (cm/cm). **C.** Colon/mouse length ratio (cm/cm). **D.** Representative H&E images of duodenum. Scale = 100 µm. **E.** Representative H&E images of jejunum. Scale = 100 µm. **F-G.** Duodenum villi length and crypt depth (µm) respectively. **H-I.** Jejunum villi length and crypt depth (µm) respectively. Villus length is labeled through a green arrow. Crypt depth is represented by the yellow arrow. (N = 2-7). Significant differences are denoted as follows: $p<0.05$: *.

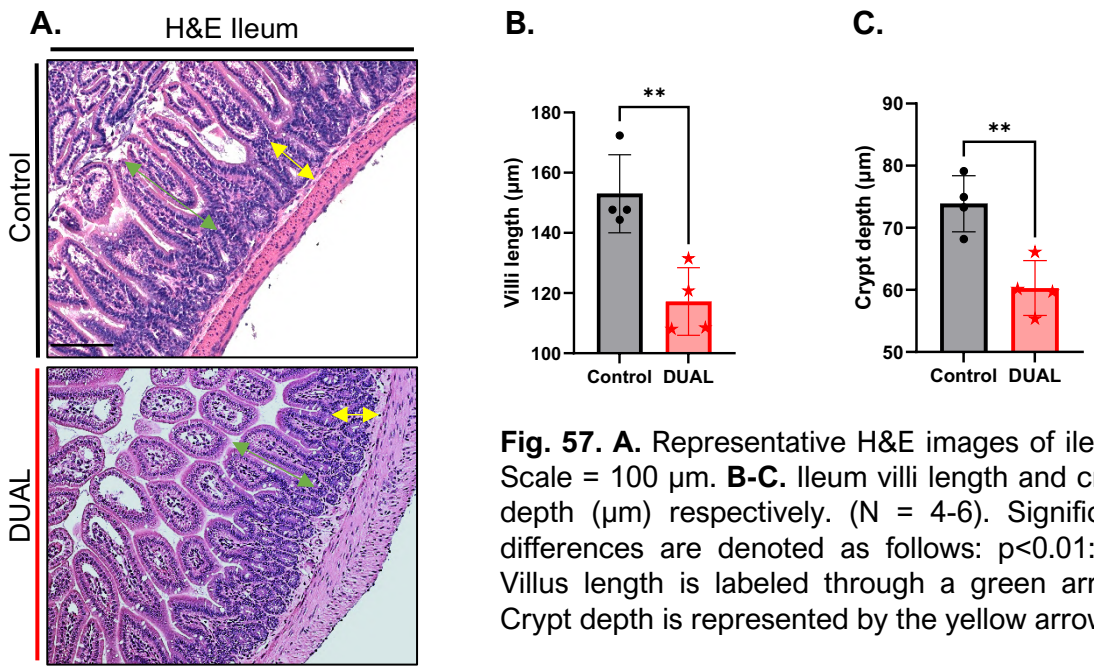

Fig. 57. A. Representative H&E images of ileum. Scale = 100 µm. **B-C.** Ileum villi length and crypt depth (µm) respectively. (N = 4-6). Significant differences are denoted as follows: p<0.01: **. Villus length is labeled through a green arrow. Crypt depth is represented by the yellow arrow.

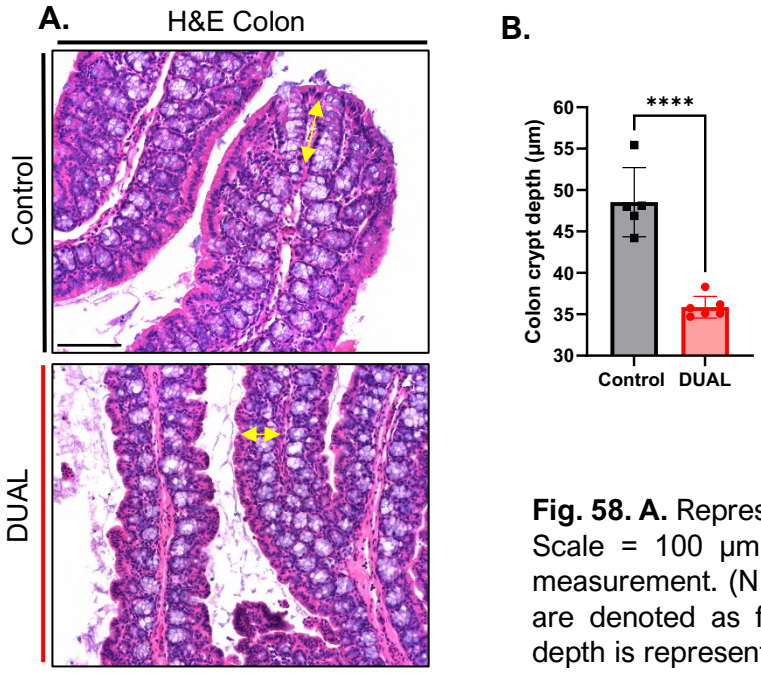

Fig. 58. A. Representative H&E images of colon. Scale = 100 µm. **B.** Colon crypt depth (µm) measurement. (N = 5-6). Significant differences are denoted as follows: p<0.0001: ****. Crypt depth is represented by the yellow arrow.

7.11. MILD INFLAMMATION AND MODERATE CELL DEATH WAS FOUND IN THE ILEUM OF DUAL-FED ANIMALS

Low inflammation rate was identified in the ileum of DUAL mice. Only minor infiltration of immune cells and the presence of monocytes ($CD11B^+$), macrophages ($F4/80^+$), and lymphocytes ($CD45^+/CD3^+$) was confirmed by IF

staining **(Fig. 59A)**. Hence, the expression of classical proinflammatory cytokines *Tnf-α* and *Ccl2* in ileum was not upregulated by DUAL feeding **(Fig. 59B-C)**.

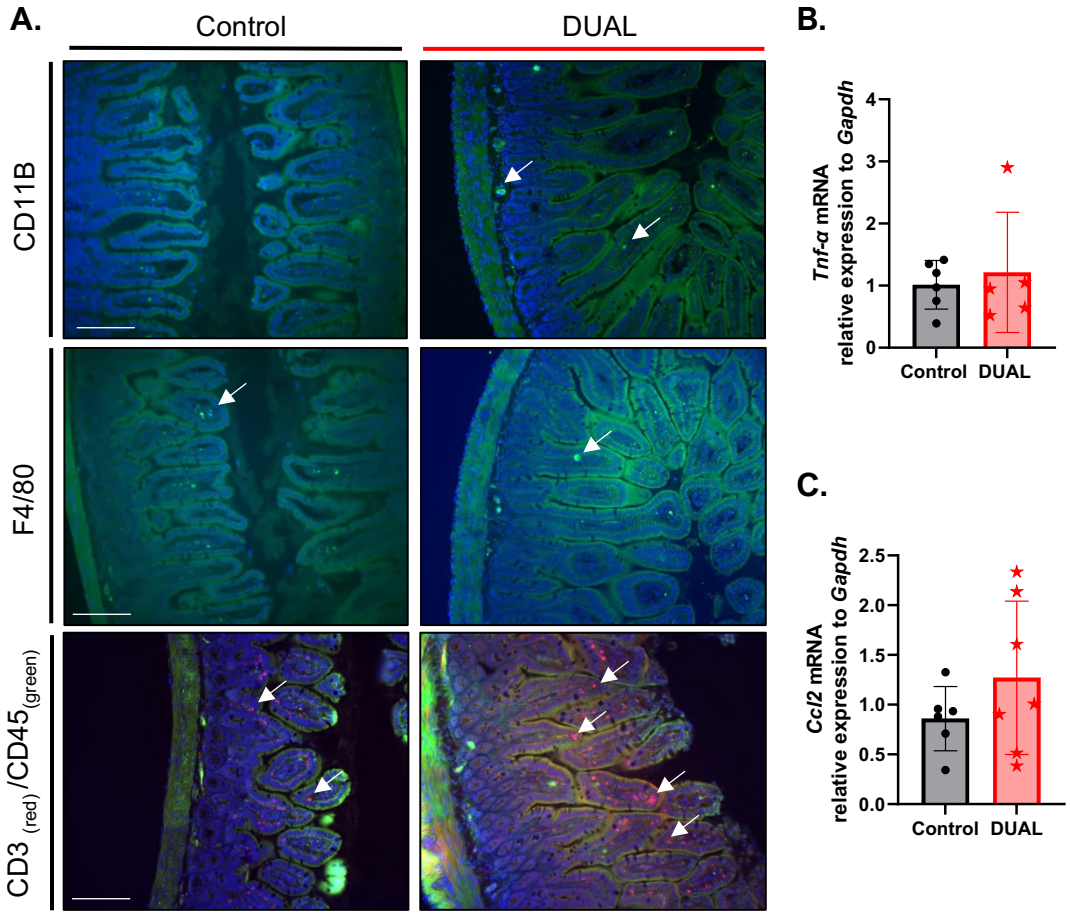

Fig. 59. A. Representative images of CD11B, F4/80, and CD3/CD45^{+} IF staining in ileum. **B-C**. *Tnf-α* and *chemokine (C-C motif) ligand 2* (*Ccl2)* mRNA relative expression to *Gapdh* was determined by RT-qPCR. Arrows point positive stained cells. (N = 6).

Mild inflammation in the ileum of DUAL mice was accompanied by moderate cell death assessed by TUNEL IF staining **(Fig. 60A-B)**. Cell death causes the compensatory proliferation in the surrounding cells, facilitating the tissue homeostasis (200). However, no significant cellular proliferation was detected by Ki-67 IHC staining in the ileum of DUAL animals **(Fig. 60A)**. Moreover, the expression *Cyclin E*, *Cyclin A* and *c-Myc*, genes directly implicated in cell cycle regulation and proliferation, remained unaltered **(Fig. 60C-E)**.

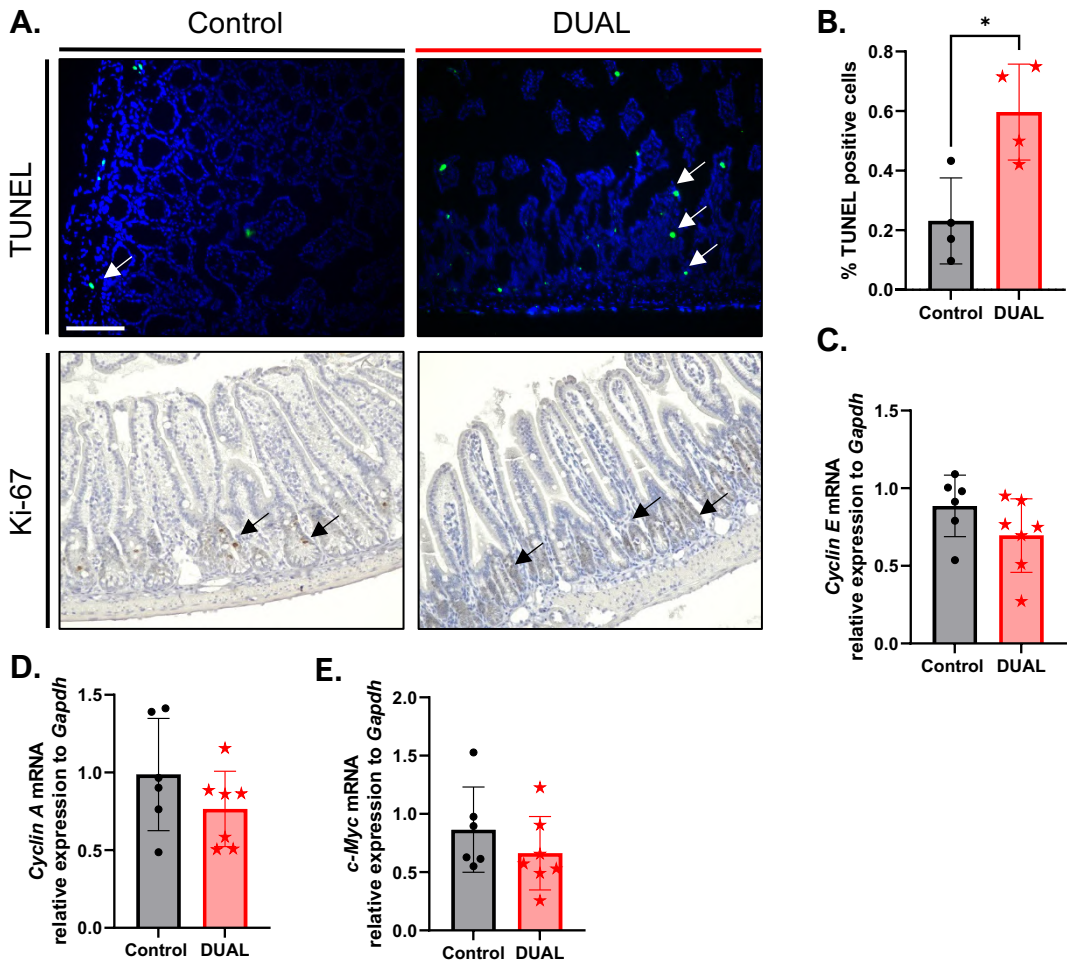

Fig. 60. A. TUNEL IF and Ki-67 IHC staining representative images. Scale = 100 µm. **B.** %positive-TUNEL cells was quantified though Image J software. (N = 4-7). **C-E.** *Cyclin E*, *Cyclin A,* and *c-Myc* relative expression to *Gapdh* was determined by RT-qPCR. (N = 6-7). Significant differences are denoted as follows: p<0.05: *. Arrows point positive stained cells.

Diet-induced intestinal damage and inflammation are likely to have important consequences, potentially resulting in the disruption of the gut barrier and gap formation in the epithelium (57). Thus, we quantified the amount of MUC2 protein as one of the main components of the mucus layer. The IF staining of MUC2 revealed that DUAL diet had no significant effect on the mucus layer in ileum **(Fig. 61A-B)**. Subsequently, we evaluated the possible damage in the next level of the gut barrier, the TJs. ZO-1 is one of the proteins that compose this protein complex. The quantification of ZO-1 in the ileum did not display any change under the DUAL feeding **(Fig. 61A, C)**.

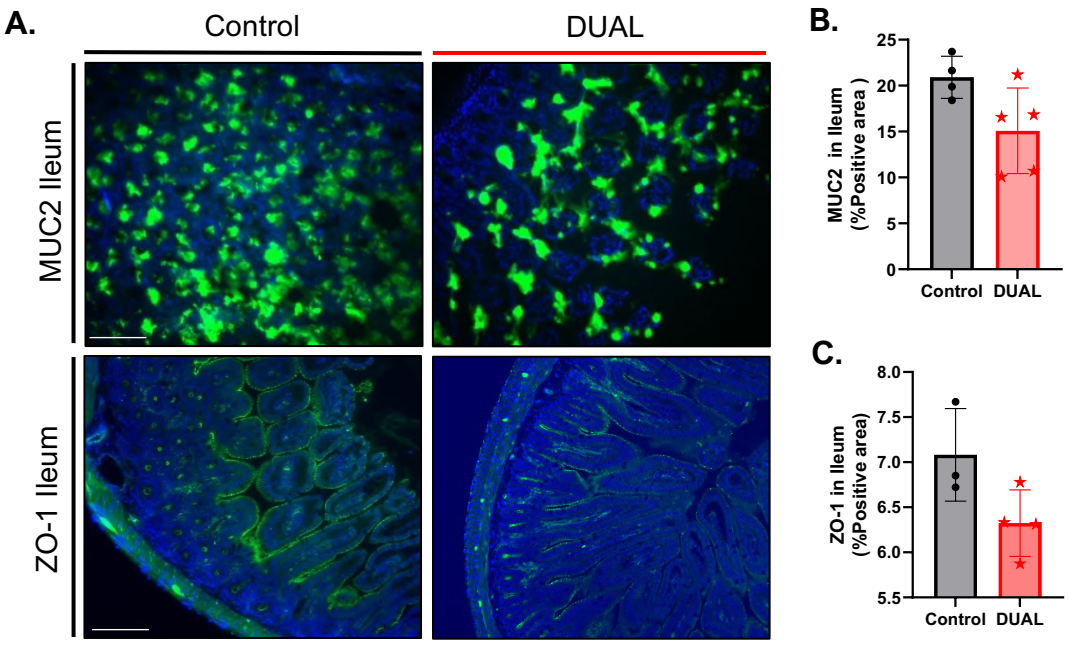

Fig. 61. A. MUC2 and ZO-1 IF staining in ileum representative images. Scale = 100 μm. **B.** Quantification of % positive area MUC2 by Image J software (N = 4-5). **C.** Quantification positive area (%) ZO-1 though Image J software (N = 4).

7.12. DUAL DIET TRIGGERED COLON INFLAMMATION AND INDUCED HYPERPLASIC GUT-ASSOCIATED LYMPHOID TISSUE IN COLON

Strong villus atrophy in the colon of DUAL-fed animals was accompanied by the presence of multiple lymphoid follicles visible in the H&E.

GALTs are immune structures located along the whole intestine as reservoirs of immune cells that control gut homeostasis for the efficient initiation and propagation of immune responses that generate from birth (69, 201). They can be further differentiated into PP or Solitary intestinal lymphoid tissues (SILTs) that develop differently and present dissimilar cellular organizations (202). However, hyperplasia and hypertrophy of GALT occur in a proinflammatory context. GALT structures were prominently increased in the colon of DUAL mice compared to controls **(Fig. 62A).**

We proceed to characterize them, since depending on the age and the stage, GALT can be composed of dendritic cells, T- or B-lymphocytes (201). We performed IF staining in order to characterize them and revealed that immune cell populations in GALT were mainly T-lymphocytes ($CD45^+$ $CD3^+$) and B-

lymphocytes (B220⁺); with minor presence of macrophages (F4/80⁺) and monocytes (CD11B⁺) **(Fig. 62B).**

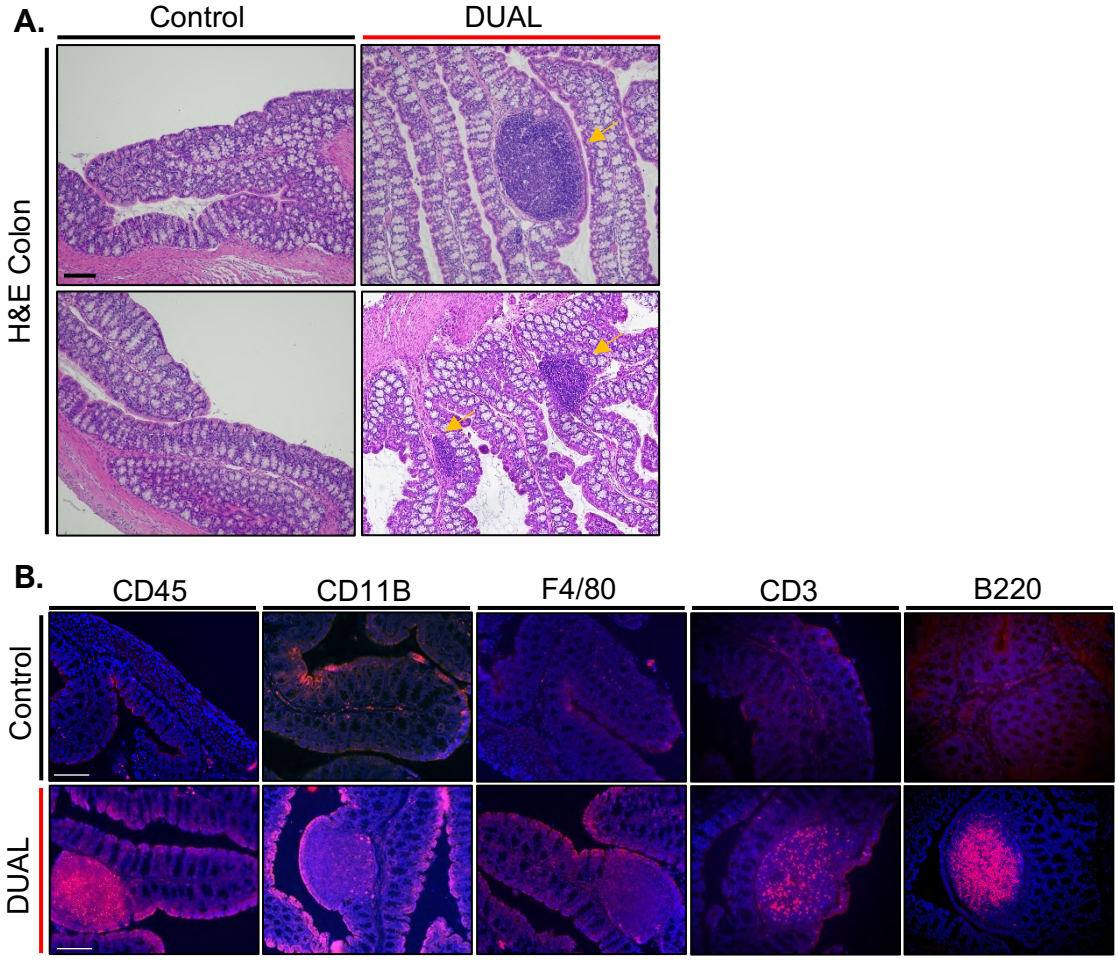

Fig. 62. A. H&E representative image of GALT in colon. Yellow arrow indicates GALT structures. **B.** GALT cell type-composition characterization by CD45, CD11B, F4/80, CD3 and B220 IF staining in colon. Scale = 100 μm.

Colon inflammation was further confirmed by flow cytometry, where we identified increased populations of T-lymphocytes (CD45/CD3⁺ cells) and expanded number of B-lymphocytes (CD45/CD19⁺ cells) **(Fig. 63A-C).** We found no difference in the levels of Treg (CD3/FOXP3⁺ cells) **(Fig. 63A, D)** and T-helper cells (CD3/CD4⁺ cells) **(Fig. 63A, E)**, but a significant increase in the cytotoxic CD3/CD8⁺ cells was found in the colon of DUAL mice **(Fig. 63A, F)**. Moreover, DUAL feeding induced a decrease in γδ-T-cells which have been associated to severe intestinal inflammation in preclinical studies (203) **(Fig. 63A, G).**

Additionally, boosted expression of *Tnf-α*, a proinflammatory cytokine, and *Xbp-1s,* an immune, mediator was detected in DUAL colon **(Fig. 63H-I).**

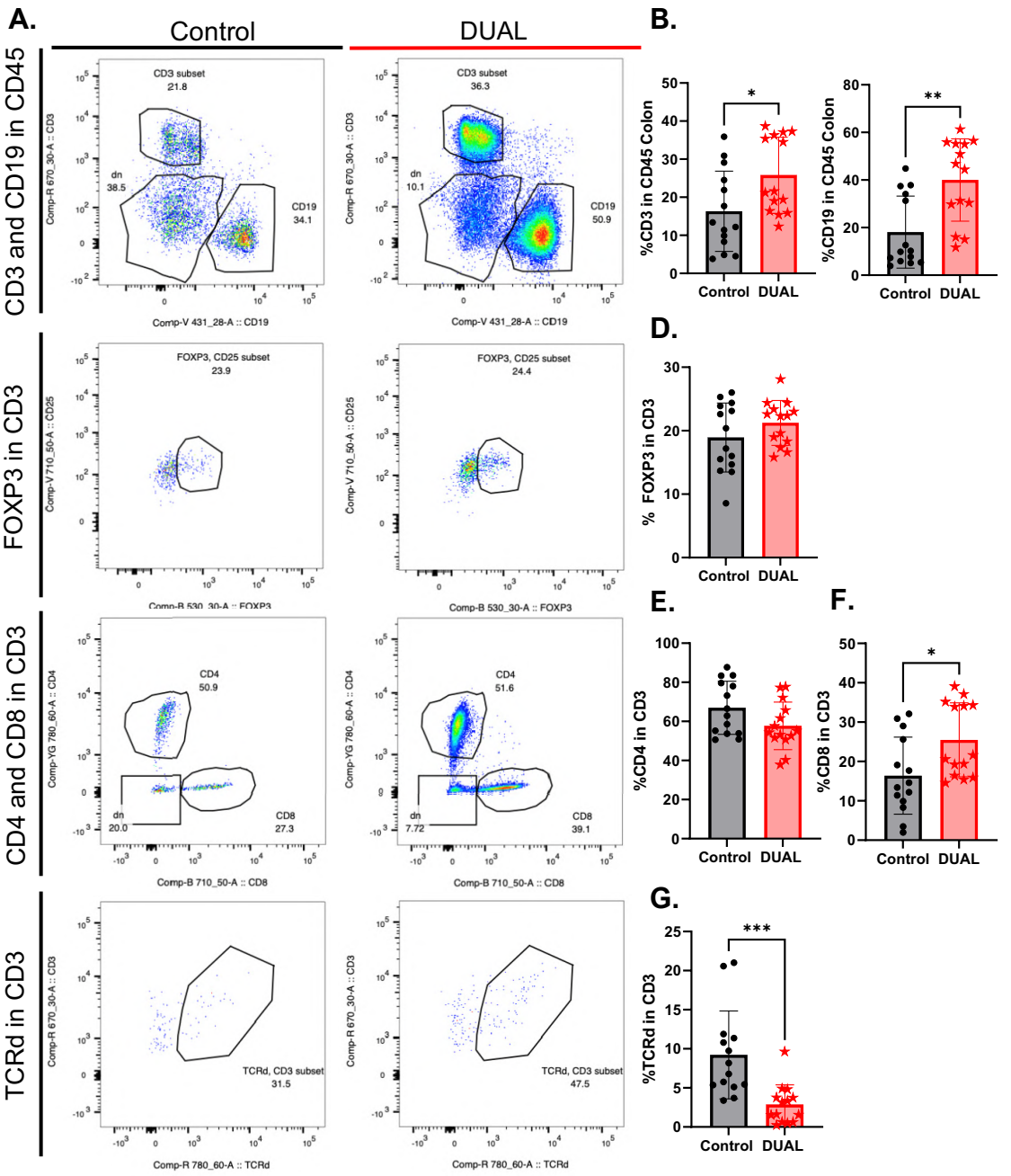

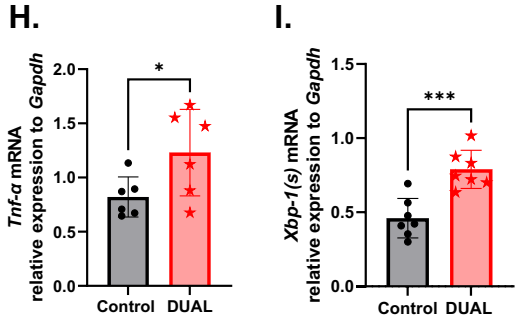

Fig. 63. A. Flow cytometry dot plots in colon. (N = 14). **B.** %CD3 in CD45 in colon. **C.** %CD19 in CD45 in colon. **D.** %CD4 in CD3. **E.** %CD8 in CD3. **F.** %TCRd in CD3. **G.** %FOXP3 in CD3. **H-I.** *Tnf-α* and *Xbp-1s* mRNA relative expression to *Gapdh* in colon was determined by RT-qPCR. (N = 7). Significant differences are denoted as follows: p<0.05: *; p<0.01: **; p<0.001: ***.

7.13. STRONG DAMAGE IN COLON PROMPTED BY DUAL DIET WAS NOT ACCOMPANIED BY ADEQUATE COMPENSATORY PROLIFERATION

Inflammation in colon triggered strong cell death of colonocytes that was identified though TUNEL IF staining. We found a remarkable fraction of dead cells in the colon of DUAL mice.

From previous publications, we know that fully differentiated enterocytes cover the flat surface of the colon and are continuously replaced by new generations of cells that exit the crypt pockets. The normal architecture of the crypt is maintained by a balance between cell proliferation at the base and apoptosis at the top of the crypt and surface epithelium (204). In DUAL animals, TUNEL positive cells were extended through the whole colon crypt **(Fig. 64A-B).**

Moreover, through Ki-67 IHC staining, we showed that the compensatory proliferation was not fully adequate to the level of cell death. Proliferation was not found to be more prominent in DUAL colon **(Fig. 64A, C).** This finding was further confirmed by PCNA protein expression, **(Fig. 64D-E)** and by mRNA expression of cell cycle effectors as *Cyclin A* and *Cyclin E* **(Fig. 64F-G).**

7.14. DUAL DIET CAUSED PROFOUND CHANGES IN THE GUT BARRIER

Next, we evaluated if the damage induced by DUAL diet was sufficient to disrupt the gut barrier. The first layer of the mechanical gut barrier is the mucose layer, which it is mainly constituted by MUC2 glycoprotein. MUC2 IF staining confirmed that DUAL diet led to an obvious decrease in colonic mucin coverage rate **(Fig. 65A-B).**

Epithelial cells are the second line of gut barrier defense. Key to this is the TJ, which seals the paracellular space and prevents unrestricted leakage. ZO-1 and occludin are key molecules in cell–cell contacts (61, 205). The distribution and expression of ZO-1 and occludin in DUAL colon were assessed by IF and WB analysis. The amount of ZO-1 was partially reduced in IF staining and WB. **(Fig. 65C-F).** Besides, a mild decrease of colonic occludin was detected by WB in DUAL-fed animals **(Fig. 65G-H).**

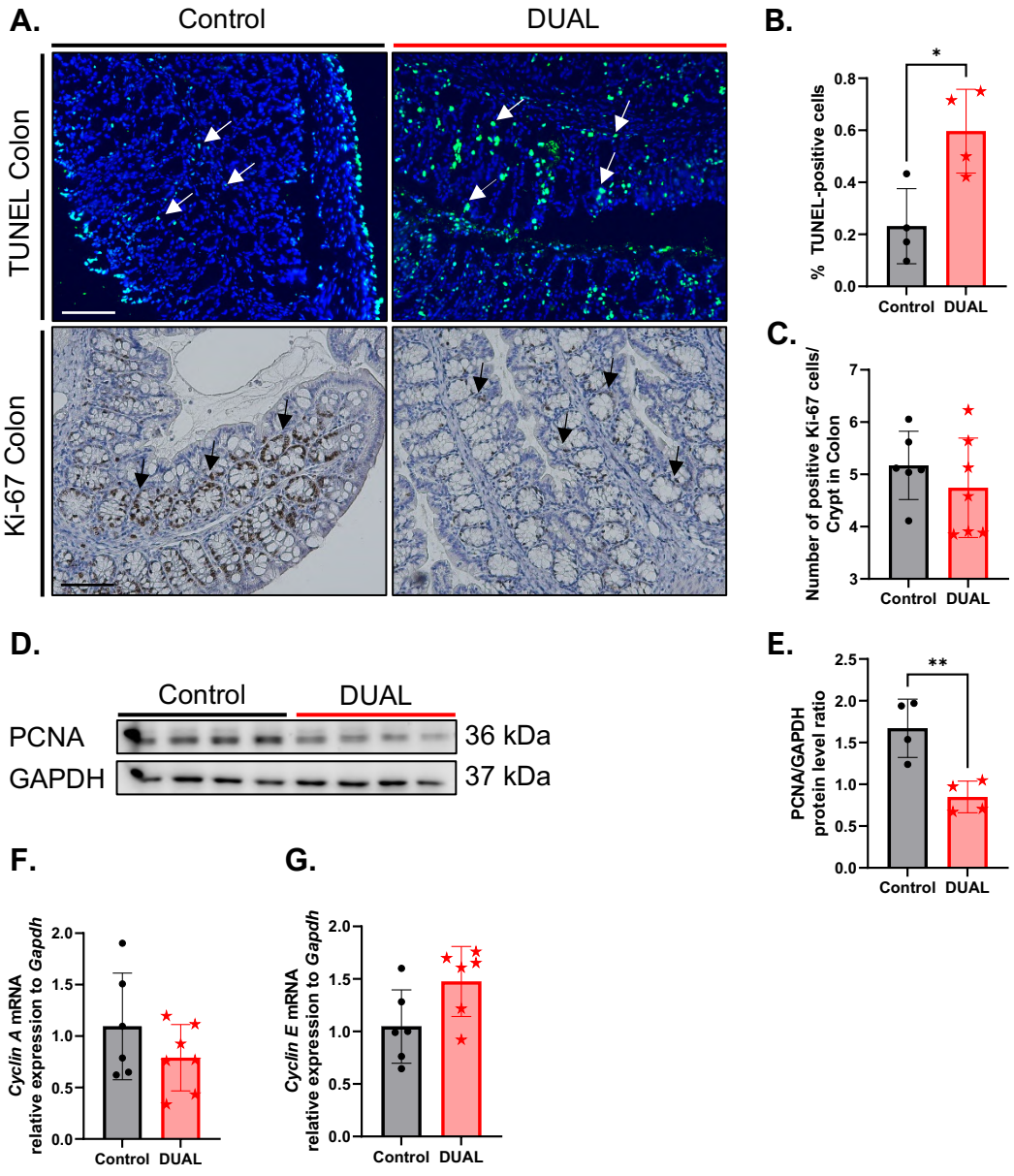

Fig. 64. A. TUNEL IF and Ki-67 IHC representative stainings in colon. Arrows point positive stained cells. Scale = 100 µm. **B.** Quantification of %-TUNEL positive cells in colon by Image J software. (N = 4). **C.** Number of positive Ki-67 cells in 20x area. (N = 6). **D.** PCNA WB in colon. GAPDH was used as a loading control. **E.** PCNA/GAPDH protein level ratio was calculated. (N = 4). **F-G.** *Cyclin A* and *Cyclin E* mRNA relative expression to *Gapdh* in colon was determined by RT-qPCR. (N = 6-7).Significant differences are denoted as follows: p<0.05: *; p<0.01: **.

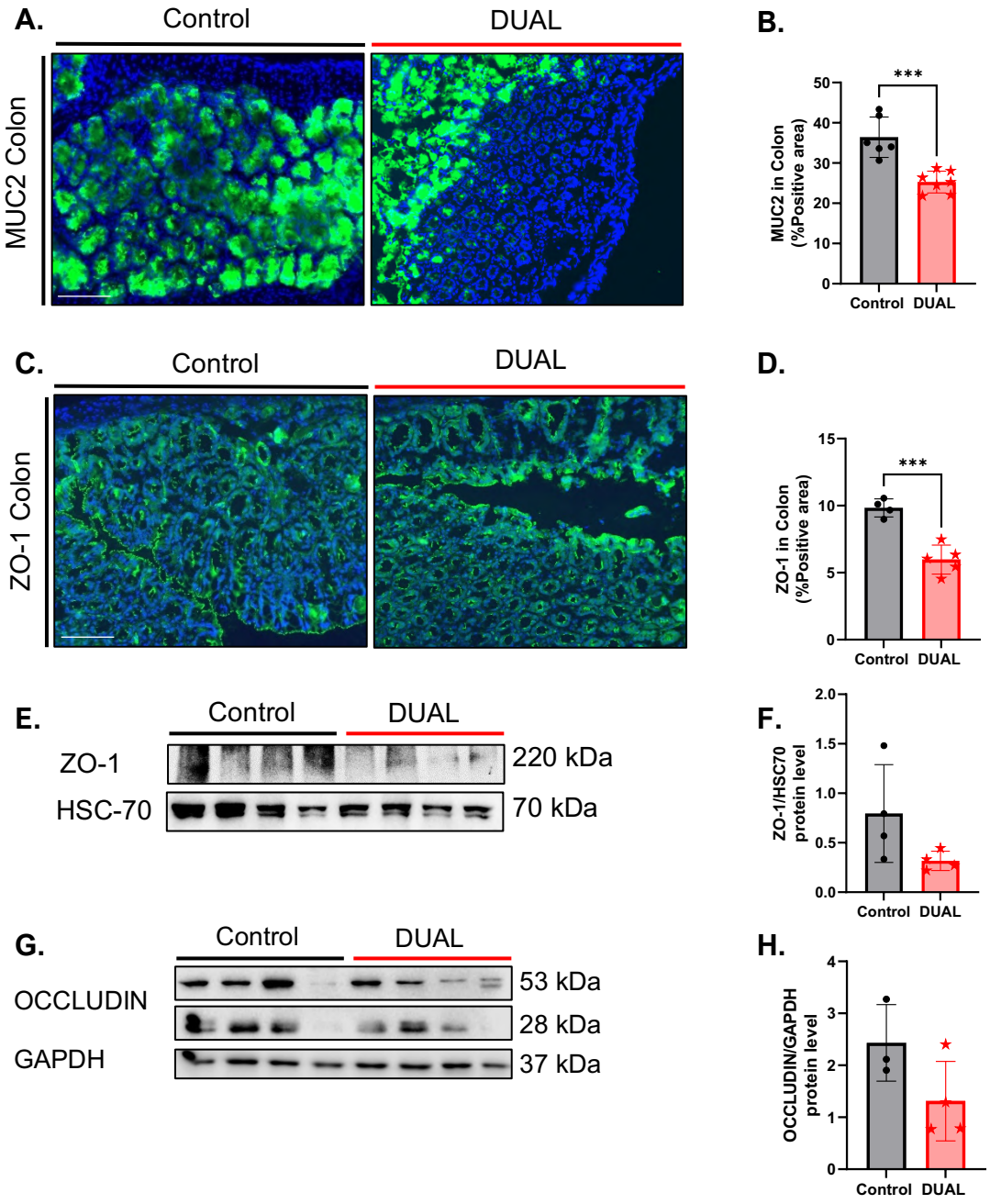

Fig. 65. A. IF staining MUC2 in colon. Scale = 100 μm. **B.** Quantification of positive MUC2 stained area (%) by Image J software. (N = 6-7). **C.** IF staining ZO-1 in colon. Scale = 100 μm. **D.** Quantification positive ZO-1 - stained area (%) by Image J software. (N = 4-5). **E.** ZO-1 WB in colon. HSC-70 was used as a loading control. **F.** ZO-1 WB quantification using ImageJ software. (N = 4). **G.** OCCLUDIN protein level analysis by WB. HSC-70 was used as a charge control. **H.** OCCLUDIN WB quantification using ImageJ software. (N = 4). Significant differences are denoted as follows: p<0.001: ***.

Finally, we assessed the GVB, which consists of a structured endothelium below the epithelial layer and play an important role for the pathogenesis of gut-liver axis (65). First, we analyzed CD34, a transmembrane glycoprotein that is expressed

on the surface of hematopoietic stem and endothelial cells. Consistently, the damage of endothelial cells induces a loss of CD34 expression (206). Thus, expression of CD34 in colon was significantly decreased in DUAL animals **(Fig. 66A-B)**.

To confirm the disruption of the GVB, we investigated PV-1, a protein primarily expressed on the membrane of endothelial cells, where it controls gut permeability (206). Upregulation of PV-1 has been described in various pathophysiological processes (207). We detect a non-significant increase of PV-1 by IF staining in the colon of DUAL mice which could be correlated to an increase in inflammation or injury **(Fig. 66A, C)**.

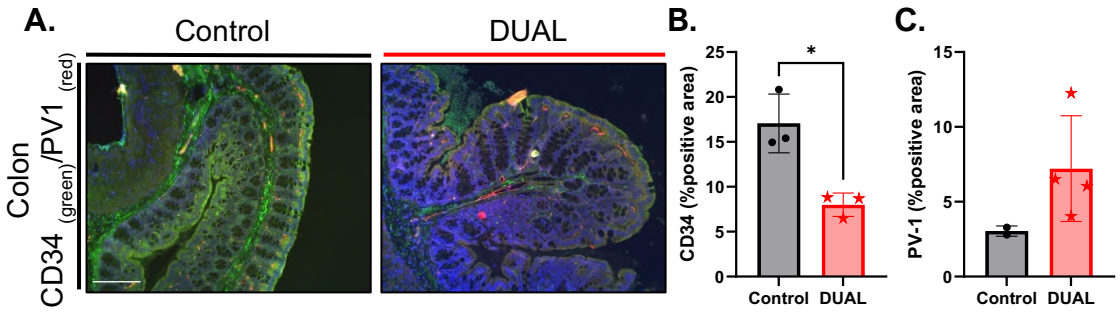

Fig. 66. A. Double IF staining CD34/PV1 in colon. **B-C.** Positive stained area of CD34 and PV-1 was calculated respectively using Image J software. Significant differences are denoted as follows: $p<0.05$: *.

7.15. GUT BARRIER DISRUPTION PROVOKED BY DUAL DIET INCREASED INTESTINAL PERMEABILITY

The defects in gut permeability, pose the risk of the translocation of luminal bacteria and their products (*e.g.*, LPS, lipoteichoic acid, bacterial DNA) to the blood which might affect other distant organs that drain and filter translocated bacteria.

Therefore, next we determine gut permeability in DUAL-fed animals. We administered 4 kDa FITC-dextran to mice by gavage, collected the blood 4 h later and determined the serum concentration of the FITC-dextran (208). Mice fed with DUAL diet revealed a significant increase of FITC dextran in the serum, confirming an increase in gut permeability **(Fig. 67A).**

The intestinal permeability is influenced, not only by the epithelial, but also by the GVB. Healthy capillary endothelium partly restricts molecules such as albumin, which has a molecular radius of 36 Å. When the GVB barriers are disrupted, big molecules are able to move from blood vessels across the mucosal barrier into the intestinal lumen by non-mediated diffusion. Thereby, measurement of albumin in fecal samples is a good indicator of a disrupted GVB and intestinal barrier (208). We measured albumin concentrations in fecal pellets from mice by a standard ELISA and we found a higher concentration in DUAL feces, indicative of gut barrier dysfunction **(Fig. 67B).**

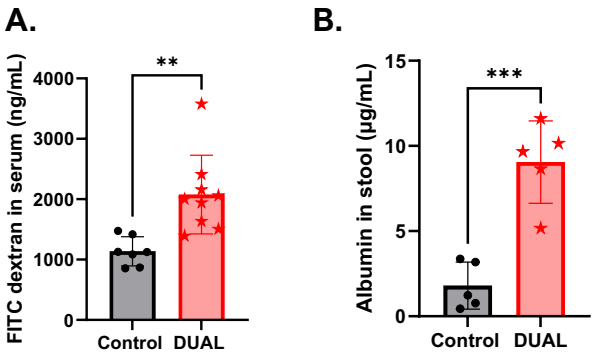

Fig. 67. A. FITC dextran measurement in serum (ng/mL). (N = 7). **B.** Albumin quantification in feces by ELISA (µg/mL). (N = 5). Significant differences are denoted as follows: p<0.01: **; p<0.001: ***.

7.16. DUAL FEEDING CAUSED NO DETECTABLE BACTERIEMIA BUT BACTERIAL SUBPRODUCTS ARAISED THE SYSTEMIC CIRCULATION

Patients in advanced stages of CLD, such as fibrosis and cirrhosis, exhibit boosted gut permeability and are under high risk of developing sepsis. Moreover, the presence of bacteria or bacterial subproducts in the systemic circulation is one major event in the underlying inflammation of CLD (209, 210).

It has been described that Gram-negative bacteria are responsible for about 60% of the bloodstream infections frequently observed in patients with liver cirrhosis (211).

Thus, the presence of Gram-negative bacteria in the circulation of DUAL mice was studied by platting blood in agar blood plates. After 72 h at 37ºC, plates were

visualized. We only detected one positive plate corresponding to one DUAL-fed mouse **(Fig. 68A, Table 10)**.

Moreover, the expression of *16s E.Coli* mRNA in the liver of DUAL mice was similar to control mice **(Fig. 68B).**

Although gut permeability was not strong enough for the passage of bacteria, we detected bacterial subproducts in the serum of DUAL animals. LPS are bacterial surface glycolipids, produced by Gram-negative bacteria. The alterations in the gut epithelial barrier allow microbiota to produce LPS to enter the bloodstream (212). Consistently, LPS in serum was analyzed by ELISA and revealed increased concentrations in DUAL mice **(Fig. 68C).**

Furthermore, the enlargement of MNL in DUAL animals exposed evidence of unleashed systemic inflammation **(Fig. 68D).**

TLRs are activated in response to bacterial, viral or fungi subproducts that reach the bloodstream, inducing an immune reaction towards them (213). Consequently, rising expression of TLRs was detected in DUAL livers by proteomic analysis where DUAL livers reported increased activity of TLR1, 2, 4 and 9, which triggered inflammation and caspase mediated cell death **(Fig. 68E)**. Additionally, innate immune response and immune activation were confirmed by mRNA sequencing analysis in the liver **(Fig. 68F).** The increased expression of *Tlrs* was further confirmed by RT-qPCR of *Tlr2, 4* and *9* **(Fig. 68G-I).**

7.17. DISBIOSIS WAS INDUCED AFTER 23 WEEKS OF DUAL FEEDING

Growing evidence has demonstrated that diet- or alcohol- induced intestinal dysbiosis also causes dysfunction of the gut-liver axis (214). Therefore, next we performed a comprehensive analysis of the microbiota with the help of *16s* rRNA sequencing in feces. We confirmed that DUAL diet induced strong dysbiosis in the intestinal microbiome communities in comparison to control fed animals **(Fig. 69A).** This imbalance was caused by 1. changes in relative abundance of microbes, 2. by gain or 3. by loss of community members.

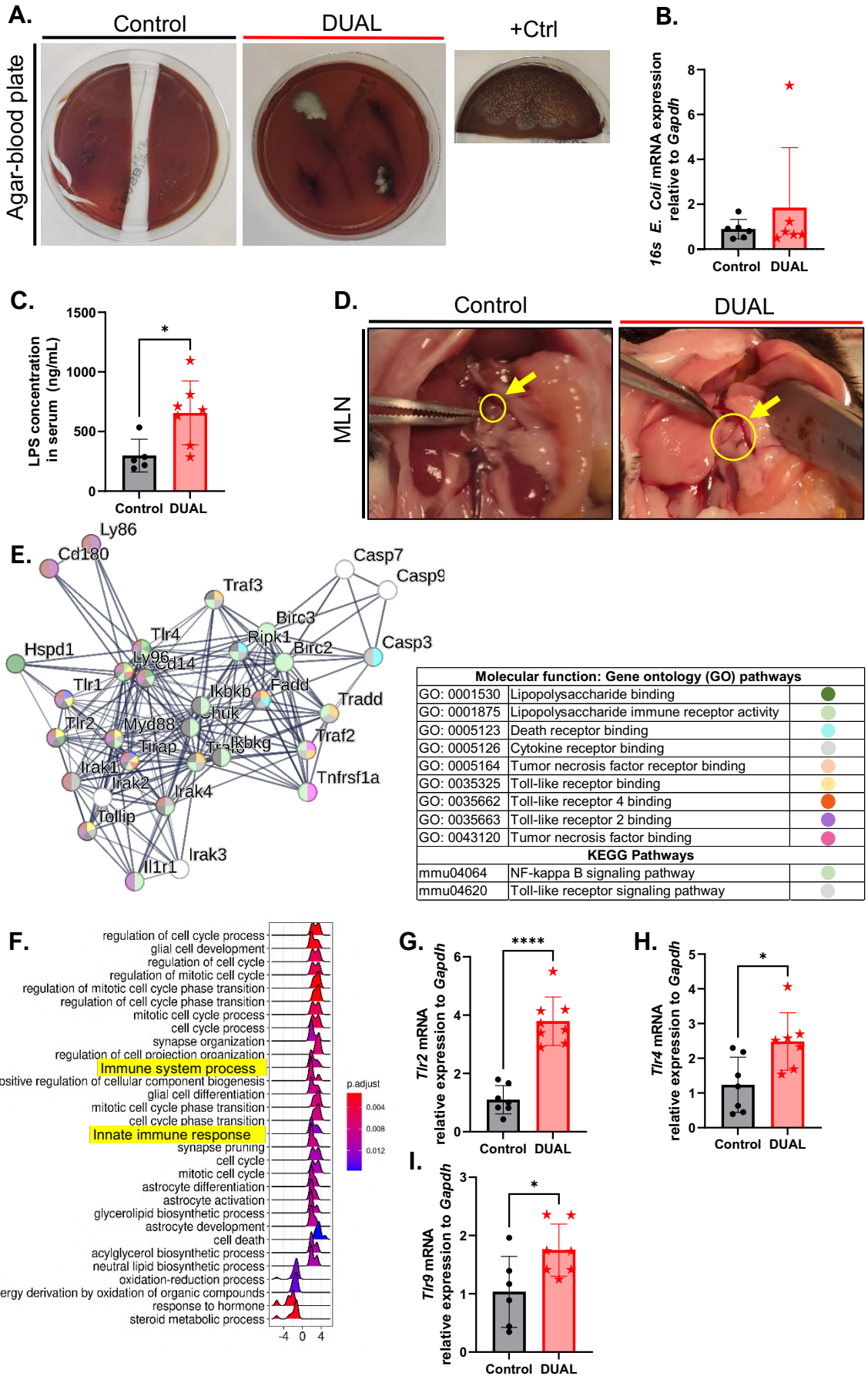
A.
Control
DUAL
+Ctrl
Agar-blood plate
B.
16s E. Coli mRNA expression relative to Gapdh
Control DUAL
C.
LPS concentration in serum (ng/mL)
Control DUAL
D.
Control
DUAL
MLN
E.
Ly86
Cd180
Casp7
Casp9
Traf3
Birc3
Tlr4
Ripk1
Birc2
Casp3
Hspd1
Ly96
Cd14
Tlr1
Ikbkb
Fadd
Tradd
Tlr2
Myd88
Ikbkg
Traf2
Tirap
Irak1
Irak2
Irak4
Tnfrsf1a
Tollip
Irak3
Il1r1
Molecular function: Gene ontology (GO) pathways
GO: 0001530 Lipopolysaccharide binding
GO: 0001875 Lipopolysaccharide immune receptor activity
GO: 0005123 Death receptor binding
GO: 0005126 Cytokine receptor binding
GO: 0005164 Tumor necrosis factor receptor binding
GO: 0035325 Toll-like receptor binding
GO: 0035662 Toll-like receptor 4 binding
GO: 0035663 Toll-like receptor 2 binding
GO: 0043120 Tumor necrosis factor binding
KEGG Pathways
mmu04064 NF-kappa B signaling pathway
mmu04620 Toll-like receptor signaling pathway
F.
regulation of cell cycle process
glial cell development
regulation of cell cycle
regulation of mitotic cell cycle
regulation of mitotic cell cycle phase transition
regulation of cell cycle phase transition
mitotic cell cycle process
cell cycle process
synapse organization
regulation of cell projection organization
Immune system process
positive regulation of cellular component biogenesis
glial cell differentiation
mitotic cell cycle phase transition
cell cycle phase transition
Innate immune response
synapse pruning
cell cycle
mitotic cell cycle
astrocyte differentiation
astrocyte activation
glycerolipid biosynthetic process
astrocyte development
cell death
acylglycerol biosynthetic process
neutral lipid biosynthetic process
oxidation-reduction process
energy derivation by oxidation of organic compounds
response to hormone
steroid metabolic process
p.adjust
-4 0 4
G.
Tlr2 mRNA relative expression to Gapdh
Control DUAL
H.
Tlr4 mRNA relative expression to Gapdh
Control DUAL
I.
Tlr9 mRNA relative expression to Gapdh
Control DUAL

Fig. 68. A. Bacterial colonies on blood agar plates after 72 h of incubation. Fresh blood from control and DUAL animals was plated. Feces were used as positive control. (N = 7). **B.** *16s E.Coli* mRNA relative expression to *Gapdh* in the liver was determined by RT-qPCR. (N = 6). **C.** LPS in serum (ng/mL). (N = 5-7). **D.** MNL representative image. MNLs are marked with arrows and circled. **E.** Proteomic analysis in the liver. Network diagram was performed using TLR4 activation found in DUAL livers as a central molecule. GO and KEGG pathways are summarized and classified by colors. **F.** mRNA most-changed genes analysis. Peaks in negative values represent downregulation meanwhile positive values show upregulation. Color scale shows significance from blue to red. **G-I.** *Tlr2, Tlr4* and *Tlr9* mRNA relative expression to *Gapdh* was determined in the liver by RT-qPCR. (N = 6-7). Significant differences are denoted as follows: $p<0.05$: *; $p<0.0001$: ****.

Table 10. Agar-blood plate results.

Agar blood plate	Positive	Negative
CONTROL	0	7
DUAL	1	6

First, we analyzed OTUs in both groups of mice and DUAL animals revealed a significant decrease. OTUs is a term that classifies groups of microorganisms based on their genetic similarity and it is usually utilized to study the diversity and abundance of microbial communities. However, OTUs do not always correspond to traditional taxonomic units due to limitations in the available genetic data and the resolution of the clustering methods used (215)**(Fig. 69B)**.

Additionally, we identified a significant decrease in the Shannon effective counts **(Fig. 69C).** The Shannon effective counts are known as equivalent number of species or true diversity. Taking both measurements, we can conclude that DUAL diet induced a decrease in microbiota diversity or a lower range of different bacteria.

At the level of phylum, we found a significant increase in the relative abundance (%) of *Actinobacteriota* **(Fig. 69D)**. Studies have shown that alterations in the composition and function of the gut microbiota, including an overgrowth of potentially harmful bacteria such as *Actinobacteria* can lead to increased gut permeability and endotoxemia, which in turn can contribute to the development of liver inflammation and steatosis (216).

Exploring in greater detail, at the level of family, we found a significant decrease in the abundance of *Muribaculaceae*. It is a family of bacteria that belongs to the

phylum *Bacteroidetes*. It is a Gram-negative bacterium that is commonly found in the gut of mammals, and it is believed to play an important role in the fermentation of dietary fiber and SCFAs production, which can provide energy to the host and modulate the immune system. It has been shown to be highly diverse and abundant. Importantly, the decrease in the *Muribaculaceae* abundance has been linked to obesity, diabetes and cirrhosis (217, 218). Additionally, beneficial physiological functions have been previously described in the family *Ruminococcaceae,* which resulted also diminished in DUAL microbiota (219) **(Fig. 69E)**.

More specifically, at the level of species, some bacteria present in the intestinal microbiota of the control mice disappeared after DUAL feeding: *Eubacterium xylanophilum*, *Muribaculum gordoncarteri, Paramuribaculum intestinale, Muribaculum gordoncarteri* and *Odoribacter laneus* **(Fig. 69F).**

In contrast, some families of bacteria increased or even appeared in DUAL microbiome such as *Peptostreptococcaceae, Rikenellaceae, Tannerellaceae* and *Oscillospirales* **(Fig. 69E).**

In addition, the following OTUs were identified only in DUAL microbiome: *Parabacteroides merdae*, *Acetifactor muris, Bacteroides acidifaciens, Desulfovibrio vulgaris, Faecalibacumum rodentium, Romboutsia timonensis* or *Massillimalia massilliensisl* **(Fig. 69F).**

All together we conclude that DUAL-diet induced dysbiosis could contribute to the activation of gut-liver axis in a number of different ways. It could lead to gain of bacteria with detrimental functions or loss of bacteria with functions beneficial to health.

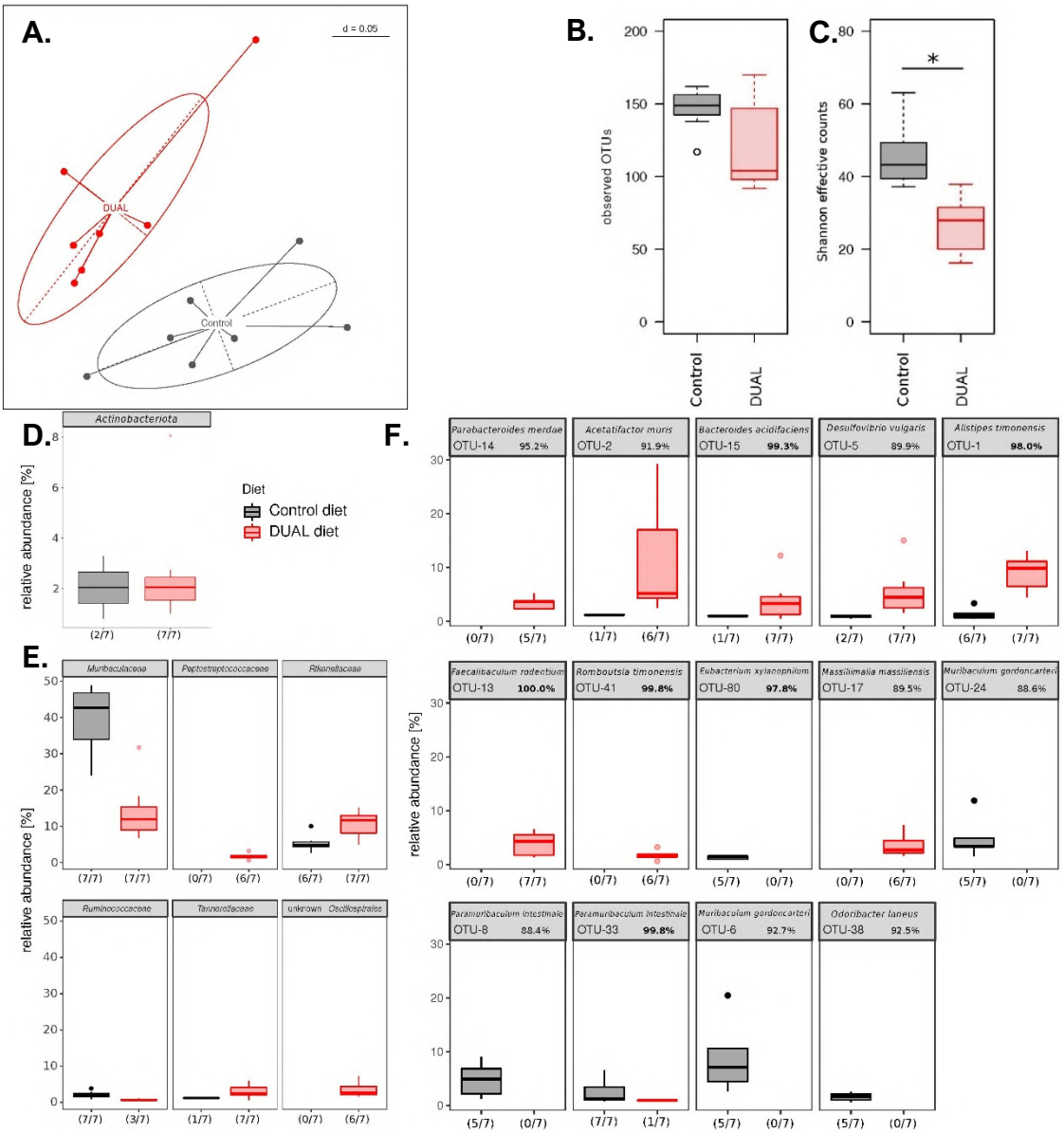

Fig. 69. A. Distinct clustering of mouse fecal microbiota profiles according to diet. This metaNMDS plot of microbial profiles is based on generalized UniFrac distances and shows a significant separation between mice given the DUAL (red) (N = 7) vs. control diet (grey) (N = 7) (p-value = 0.002). **B-C.** α-diversity of fecal microbiota decreased in mice fed a DUAL diet. The boxplots are based on a normalised OTU table with on average 61,324 ± 13,592 high quality reads per sample (97% identity level). The number of observed OTUs (left) (p-value = 0.099) and Shannon effective counts (right) (p-value=0.0011) of are compared between the two mouse groups (N = 7 each) fed either a control or the DUAL diet. Significant differences are denoted as follows: *, p < 0.05. **D-F.** Relative abundance of bacterial phylum, families and single molecular species (OTUs) influenced by DUAL diet. The relative abundance in % of total reads of **D.** phylum, **E.** families and **F.** OTUs differing significantly (corrected p-values<0.05) according to diet (each N = 7) are shown as box plots (control diet: grey; DUAL diet: red). The representative sequence of each OTU was assigned a taxonomy using EZBioCloud (Yoon et al., 2017), considering valid names only. The sequence identity (%) is displayed above each box plot. Species level identifications (i.e.>97 % identity) are shown in bold. The numbers below the x-axis indicate the number of positive samples for the given taxa out of the total number of samples (x/7).

7.18. DYSBIOSIS INDUCED BY DUAL DIET IN MICE WAS SIMILAR TO HUMAN DYSBIOSIS FOUND IN DUAL ETIOLOGY CLD PATIENTS

Next, we decided to evaluate if there existed any correlation between the microbiota changes that were identified in DUAL animals and those exhibited in patients with CLD of dual etiology (BASH patients). A cohort of patients in collaboration with Val d'Ebron Hospital was selected. DUAL etiology patients were selected for presenting NASH, being overweight (BMI greater than 25 kg/m^2), NAS activity score 3 or higher and reporting active and chronic alcohol consumption as described in section **6.2.41. Human feces samples** from materials and methods and in **Table 5.**

16s rRNA microbiota analysis was performed and, as expected, the presence of commensal bacteria was predominant in both microbiota of control mice and microbiota of healthy control humans.

Interestingly, dual etiology CLD, in both mice and humans, induced profound microbiome changes. The relative abundance of genus *Bacteroides* increased to 12.7% in mice and up to 12% in human. **(Fig. 70A-C)**. Moreover, in both human and mice, other genus slightly increased their percentage in comparison to control microbiota (e.g., *Blautia)* **(Fig. 70B, D)**. In contrast, the percentage of commensal bacteria, such as *Muribaculaceae,* decreased from 38.05% in controls to 12.18% in DUAL animals **(Fig. 70B, E)**. In dual etiology CLD patients the commensal bacteria, such as *Bifidobacterium,* was also reduced: from 5.18% in controls, until 1.18% **(Fig. 70B, F)**. Moreover, the genus *Prevotella* decreased a 6% in BASH patients **(Fig. 70G)**.

Altogether, our results are consistent with previous studies showing that microbiome changes have a direct impact on health and disease (220).

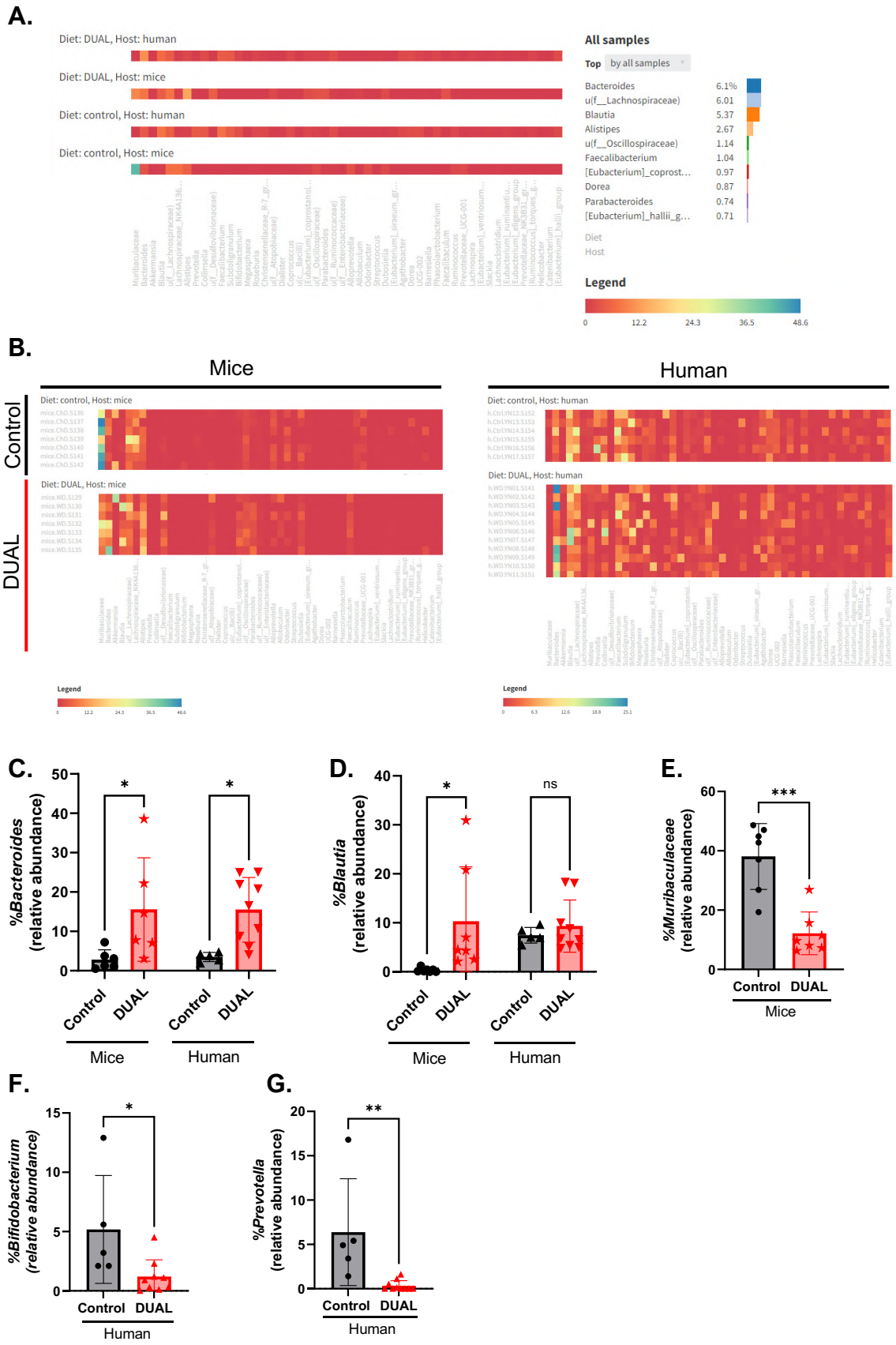

Fig. 70. A. Relative abundance grouped for DUAL vs. Control in human and mice samples. Representation at the genus level. **B.** Non-aggregate representation of DUAL vs. Control in human and mice samples. Genus level is showed. **C-D.** %*Bacteroides* and

Blautia relative abundance in mice and human. **E.** *%Muribaculaceae* relative abundance in mice. **F-G.** *%Biffidobacterium* and *Prevotella* relative abundance in human. KnomicsBiota service was used for the representation and analysis of the samples. Efimova, D., et al. (2018) Knomics-Biota - a system for exploratory analysis of human gut microbiota data. BioData Mining 11(1), 25. (N = 5-9). Significant differences are denoted as follows: $p<0.05$: *; $p<0.01$: **; $p<0.001$: ***.

7.19. ABX SUPPLEMENTATION IN THE DRINKING WATER REDUCED MS FEATURES AND SIGNIFICANTLY IMPROVED THE HEPATIC PHENOTYPE IN 10- WEEK FED DUAL MICE

Dysbiosis observed in DUAL mice was associated with decreased bacteria diversity, impaired epithelial barrier, LPS translocation and inflammation. Our results also demonstrated that microbiome changes observed in DUAL mice were very similar to those that displayed patients with CLD of dual etiology. Therefore, we proposed that: 1. The phenomenon of DUAL induced activation of gut-liver axis and consequent liver damage is mediated by gut microbiota; 2. The microbiome is a potential therapeutic target.

First, as a proof of concept, we performed antibiotic-induced microbiota-depletion (AIMD) in DUAL-fed and control animals. Mice received DUAL diet for 10 weeks and the last 4 weeks of feeding the DUAL diet was combined with a broad spectrum antibiotic mixture in the drinking water to remove the majority of the original gastrointestinal microflora. Mice receiving only DUAL or chow diet were used as controls as described in **6.2.3.3.1. ABX administration in the drinking water in material and methods section (Fig. 19)**.

The administration of ABX in the water significantly diminished the BMI reaching the value of the control group **(Fig. 71A).** Additionally, the gWAT/Body ratio was significantly reduced after ABX administration **(Fig. 71B).** Moreover, the high level of cholesterol in serum, a classical feature of MS, showed a significant decrease after ABX supplementation, reaching the control levels **(Fig. 71C).**

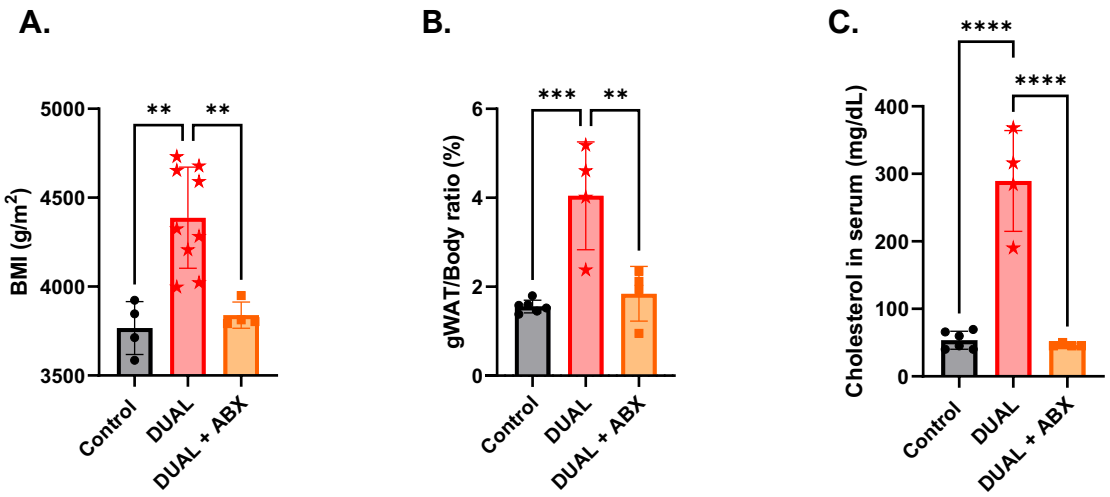

Fig. 71. A. BMI was calculated after 10 weeks of feeding (g/m^2) (N = 4-8). **B.** gWAT/Body ratio (%). (N = 4-5). **C.** Cholesterol levels in serum after 12 hours fasting (mg/dl). (N = 4-5). Significant differences are denoted as follows: p<0.01: **; p<0.001: ***; p<0.0001: ****.

Next, we focused on the liver phenotype. AIMD led to a significant decrease of liver weight compared to DUAL mice **(Fig. 72A).** H&E and ORO stainings confirmed the reduction of hepatic steatosis, since we observed that the size and number of lipid droplets in the liver parenchyma was significantly reduced compared to DUAL animals **(Fig. 72B-D).**

Consistently, TG content in the liver was also significantly reduced after ABX administration, although not down to control group **(Fig. 72E).**

The significant decrease of the hepatic cell death was confirmed by TUNEL IF staining, where the percentage of TUNEL-positive cells in hepatic parenchyma was reduced after ABX supplementation **(Fig. 72C low, F).** Moreover, the levels of AST, ALT and LDH in serum significantly decreased in DUAL+ABX compared to DUAL mice **(Fig. 72G-I).**

ABX supplementation also mitigated hepatic inflammation mainly by the reduction of the infiltrating macrophages and monocytes among other immune cells **(Fig. 73A-D).** Uniformly, mRNA expression of proinflammatory cytokine *Tnf-α* decreased after the ABX treatment **(Fig. 73E).** Finally, AIMD visibly reduced hepatic fibrosis, as confirmed by SR staining **(Fig. 73F).** Consistently, we found a remarkable decrease in the expression of *Collagenl* in the liver of DUAL + ABX animals **(Fig. 73G).**

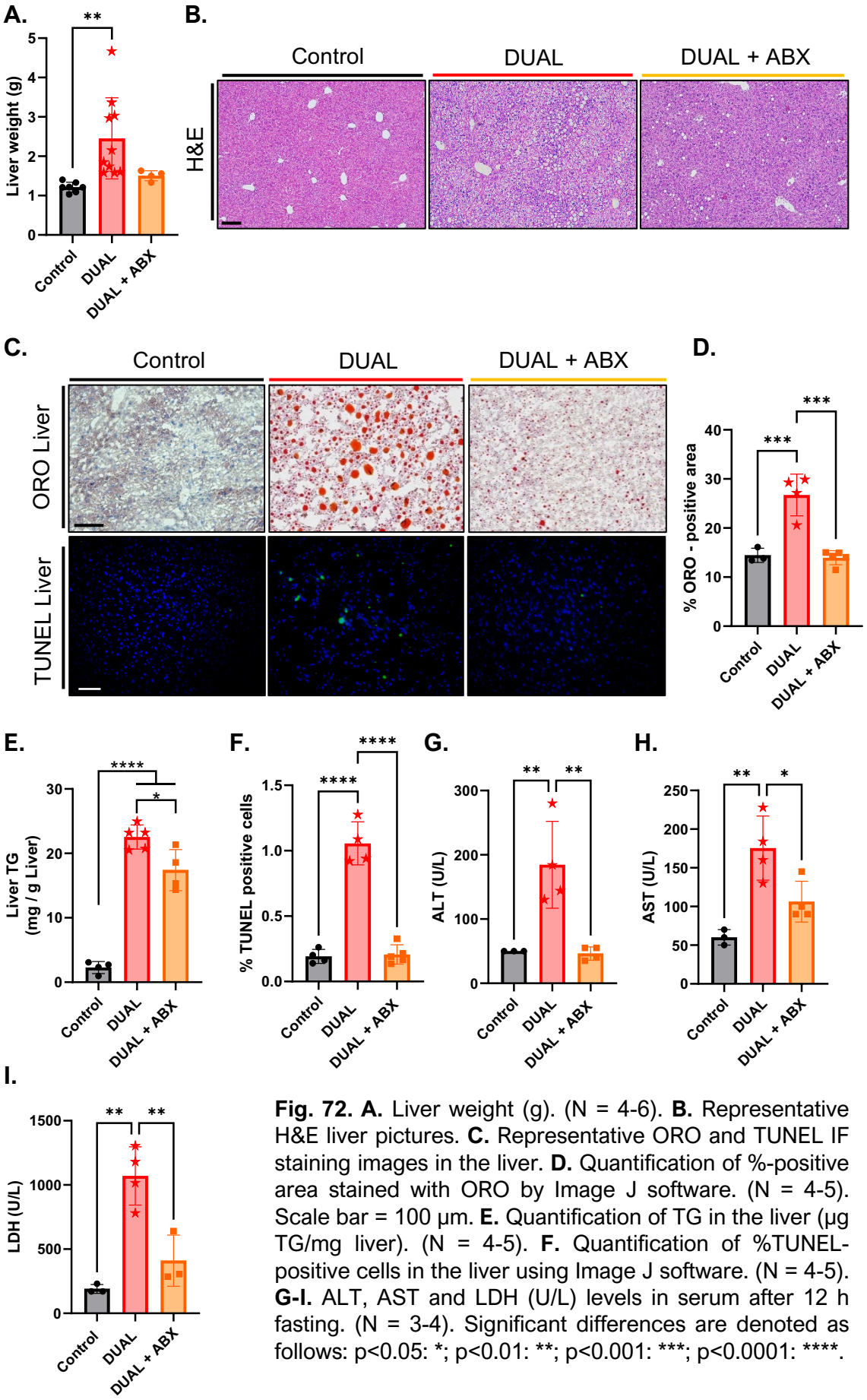

Fig. 72. A. Liver weight (g). (N = 4-6). **B.** Representative H&E liver pictures. **C.** Representative ORO and TUNEL IF staining images in the liver. **D.** Quantification of %-positive area stained with ORO by Image J software. (N = 4-5). Scale bar = 100 µm. **E.** Quantification of TG in the liver (µg TG/mg liver). (N = 4-5). **F.** Quantification of %TUNEL-positive cells in the liver using Image J software. (N = 4-5). **G-I.** ALT, AST and LDH (U/L) levels in serum after 12 h fasting. (N = 3-4). Significant differences are denoted as follows: p<0.05: *; p<0.01: **; p<0.001: ***; p<0.0001: ****.

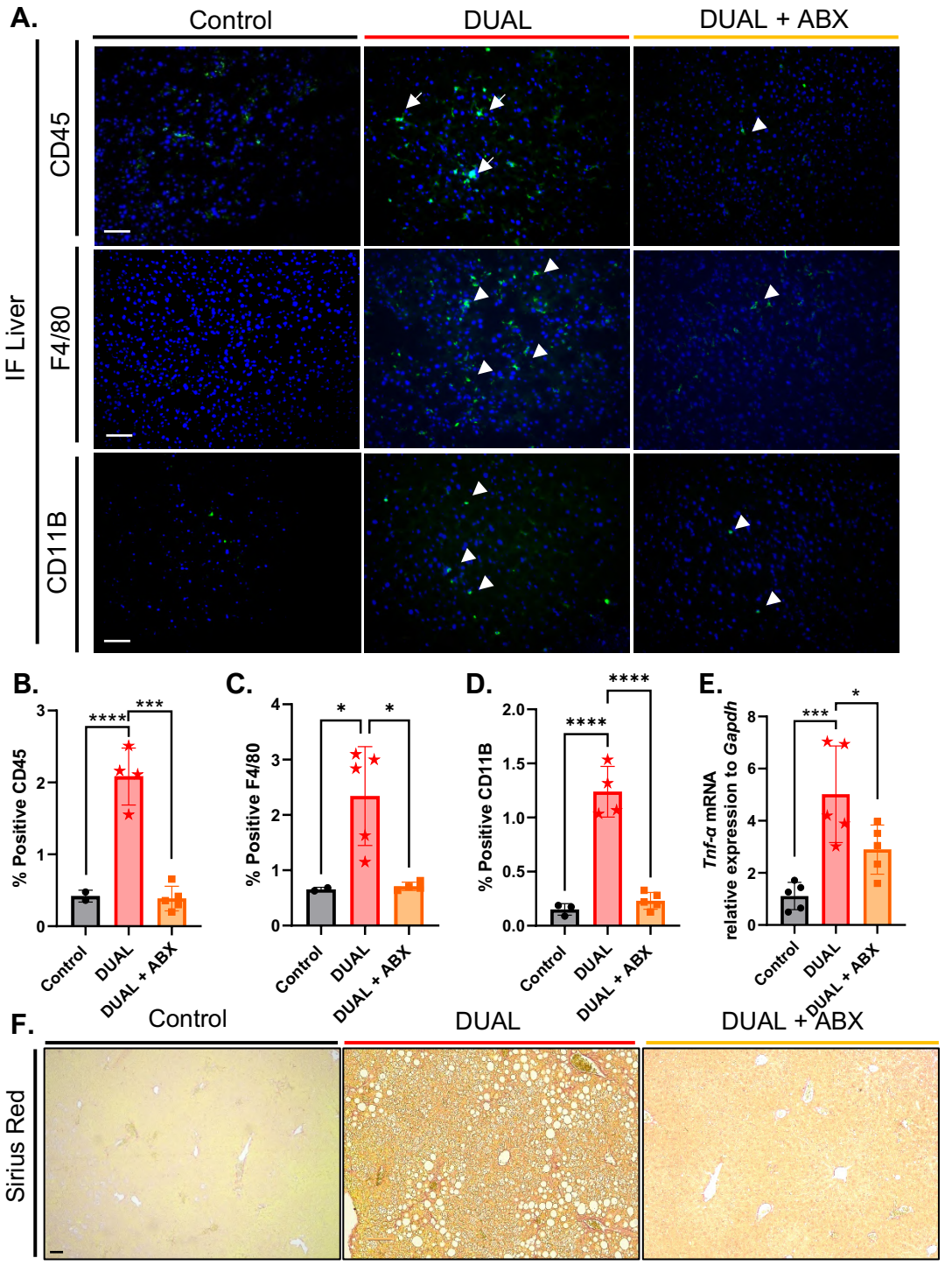

Fig. 73. A. Representative images of CD45, F4/80 and CD11B IF stained liver sections. **B-D.** Quantification of positive -CD45, -F4/80 and -CD11B (%) in liver using ImageJ software. (N = 3-5). **E.** *Tnf-α* mRNA relative expression to *Gapdh* was determined by RT-qPCR. (N = 5). **F.** Representative SR images in liver. Scale bar = 100 µm. **G.** *Collagen1* mRNA relative expression to *Gapdh* was determined in the liver by RT-qPCR. (N = 5). Significant differences are denoted as follows: p<0.05: *; p<0.001: ***; p<0.0001: ****.

7.20. ABX ADMINISTRATION BY ORAL GAVAGE DURING THE LAST 10 DAYS OF SHORT-TERM DUAL FEEDING ATTENUATED OBESITY, HEPATIC STEATOSIS, LIVER DAMAGE, INFLAMMATION AND FIBROSIS

To further verify that microbiota may play the principal role in the activation of the gut-liver axis and in the induction of DUAL- phenotype, we decided to use a second model of ABX administration by oral gavage. For rodents, oral gavage allows more precise volume and dose delivery and faster peak absorption of ABX, as compared with delivery in drinking water.

The identical cocktail of ABX was applied by oral gavage during the last 10 days of DUAL feeding as described in **material and methods** section **6.2.3.3.2. ABX administration by oral gavage (Fig. 20).** Moreover, to prove that ABX did not exert any secondary effect, the cocktail was administered to healthy control animals.

Consistent to our previous results, ABX administration by gavage induced a decrease in body weight. However, this time we did not find any differences in the gWAT deposits **(Fig. 74A-C).**

In the liver, we found that the administration of ABX by itself did not have any secondary effect in the controls, but significantly diminished hepatomegaly in DUAL-fed mice **(Fig. 74D).**

Next, ORO staining of liver samples revealed that ABX were able to diminish microvesicular and macrovesicular steatosis caused by DUAL feeding **(Fig. 75A, B).** Consistently, hepatic TG content was significantly decreased in ABX+DUAL compared to DUAL, but did not achieved similar levels as the control animals **(Fig. 75C).**

Dietary FFAs are the main source of TG in the liver. Consistently, we found significant upregulation of *Cd36* expression (FA translocase) in the livers of DUAL-fed animals. Reasonably, the administration of ABX simultaneously with DUAL feeding did not lead to the reduction of *Cd36* level in ABX+DUAL livers **(Fig. 75D).** In line, *Pparγ*, another steatogenic regulator mediating the expression of *Cd36* (221), had similar pattern of expression in all groups **(Fig. 75E).**

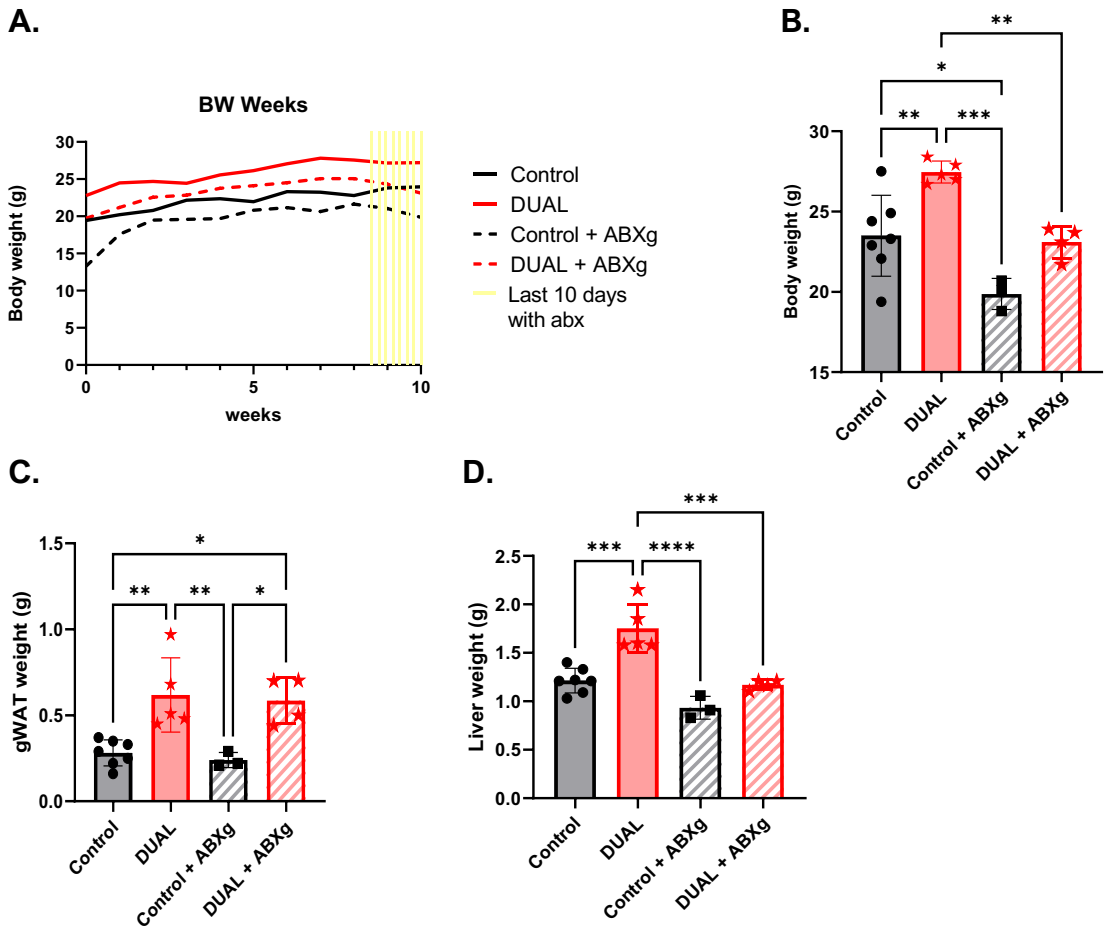

Fig. 74. A. BW curve during the feeding period. **B.** End point body weight (g). **C.** gWAT weight (g). **D.** Liver weight (g). (N = 4-7). Significant differences are denoted as follows: p<0.05: *; p<0.01: **; p<0.001: ***; p<0.0001: ****.

Intensive lipid load induces an increase in lipid oxidation. However, in consistency with our previous results, DUAL diet did not induce any rise in CPT-1c protein expression. CPT-1c expression in DUAL animals was similar to control mice. This finding indicates a reduction in lipid oxidation in DUAL fed animals resulting in lipid storage. Importantly, the administration of ABX increased the expression levels of CPT-1c in DUAL-fed animals **(Fig. 75F, G).**

The administration of ABX by gavage resulted in a reduction in the hepatic transaminases ALT, AST and LDH in DUAL fed animals **(Fig. 76A-C).**

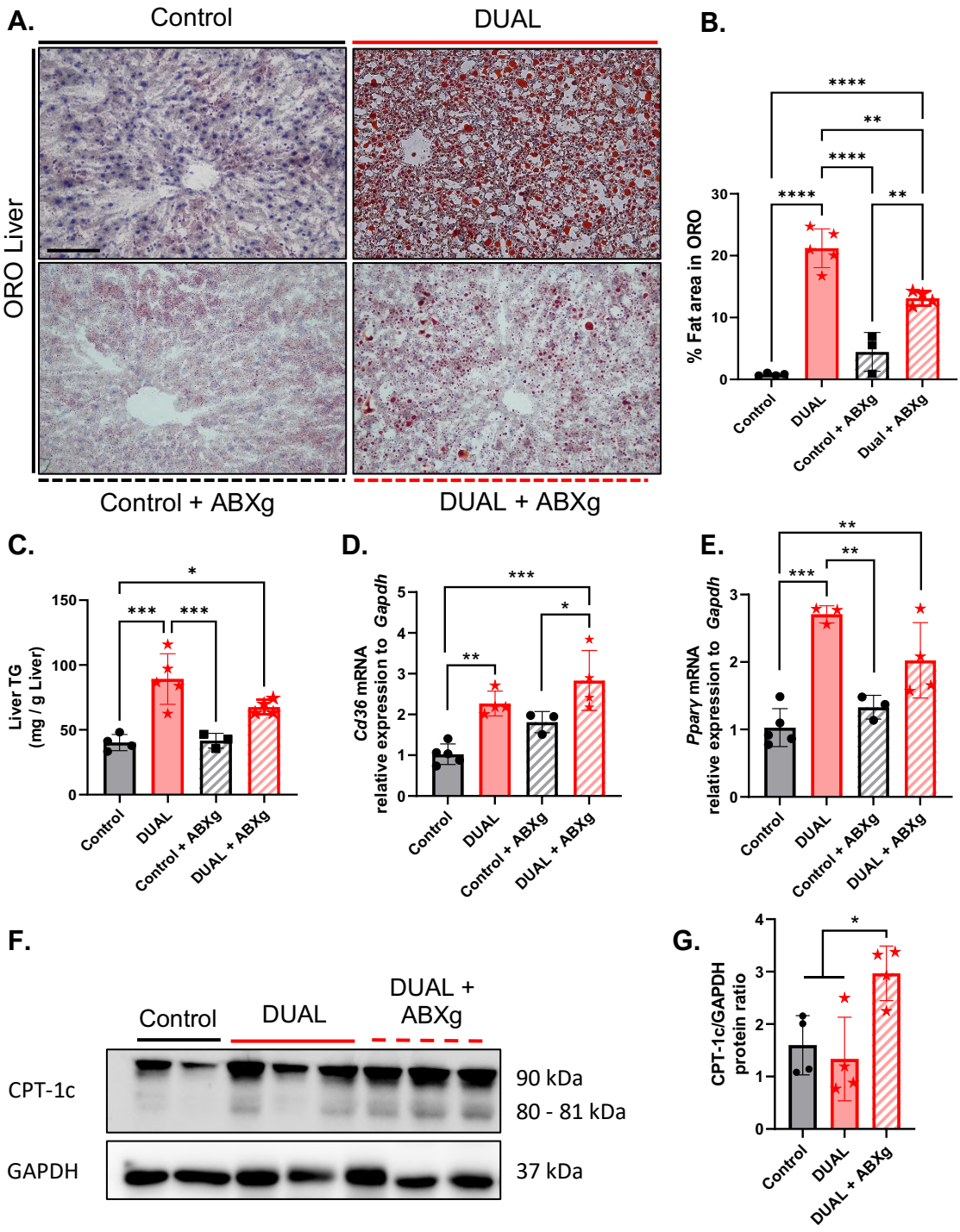

Fig. 75. A. ORO staining in the liver. Scale = 100 µm. **B.** Quantification of stained ORO area (%) through image J software. (N = 4-5). **C.** Quantification of TG in the liver (mg/g liver). (N = 4-5). **D-E.** *Cd36* and *Ppary* relative expression to *Gapdh* in the liver was determined by RT-qPCR. (N = 4-5). **F.** CPT-1c WB was performed in liver. GAPDH was used as a loading control. **G.** CPT-1c WB quantification using ImageJ software. CPT-1c/GAPDH ratio was calculated. (N = 4). Significant differences are denoted as follows: p<0.05: *; p<0.01: **; p<0.001: ***; p<0.0001: ****.

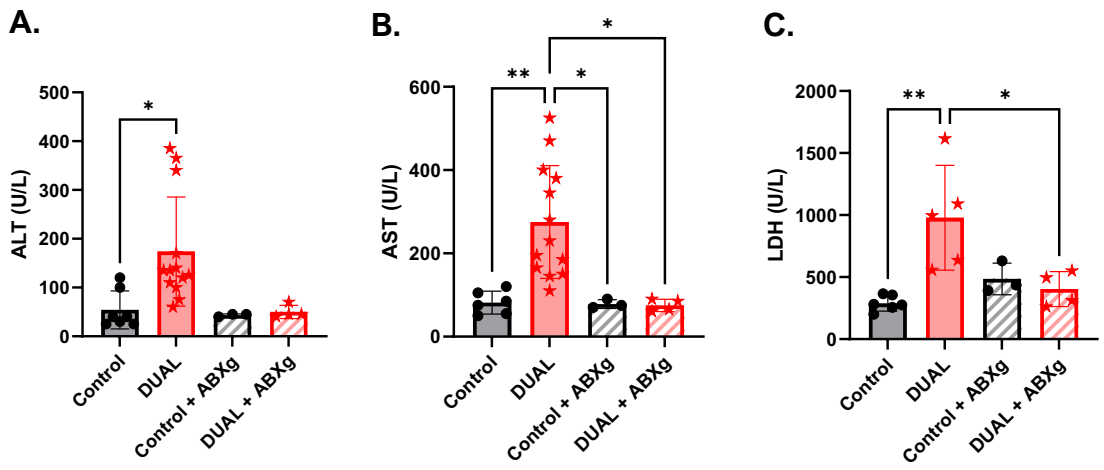

Fig. 76. A-C. ALT, AST and LDH (U/L) levels in serum after 12 h fasting. (N = 4-10). Significant differences are denoted as follows: p<0.05: *; p<0.01: **.

Consistently with the previous results, DUAL mice showed an increased accumulation of CD45 positive cells, as assessed by IF staining. Nevertheless, the combination of ABX+DUAL significantly reduced the numbers of immune cells infiltrating the hepatic parenchyma **(Fig. 77A, B).** As a result, *Tnf-α* expression was diminished **(Fig. 77C)** and the upregulation of *Tlr* expression was reduced **(Fig. 77D-F).**

Finally, SR staining and *CollagenI* mRNA expression clearly demonstrated that the application of ABX to DUAL fed animals reduced the level of fibrosis **(Fig. 77G-H).**

7.21. ABX SUPPLEMENTATION TO SHORT-TERM DUAL FED ANIMALS DID NOT INDUCE ANY IMPROVEMENT IN COLON INFLAMMATION OR DAMAGE BUT CHANGED COMPENSATORY PROLIFERATION AND INTESTINAL PERMEABILITY

Next, we checked if ABX administration by oral gavage had any effect on intestinal phenotype in DUAL mice. In spite of the total gut length was partially recovered in ABX+DUAL group, the colon was still shortened in comparison to the controls **(Fig. 78A-B).**

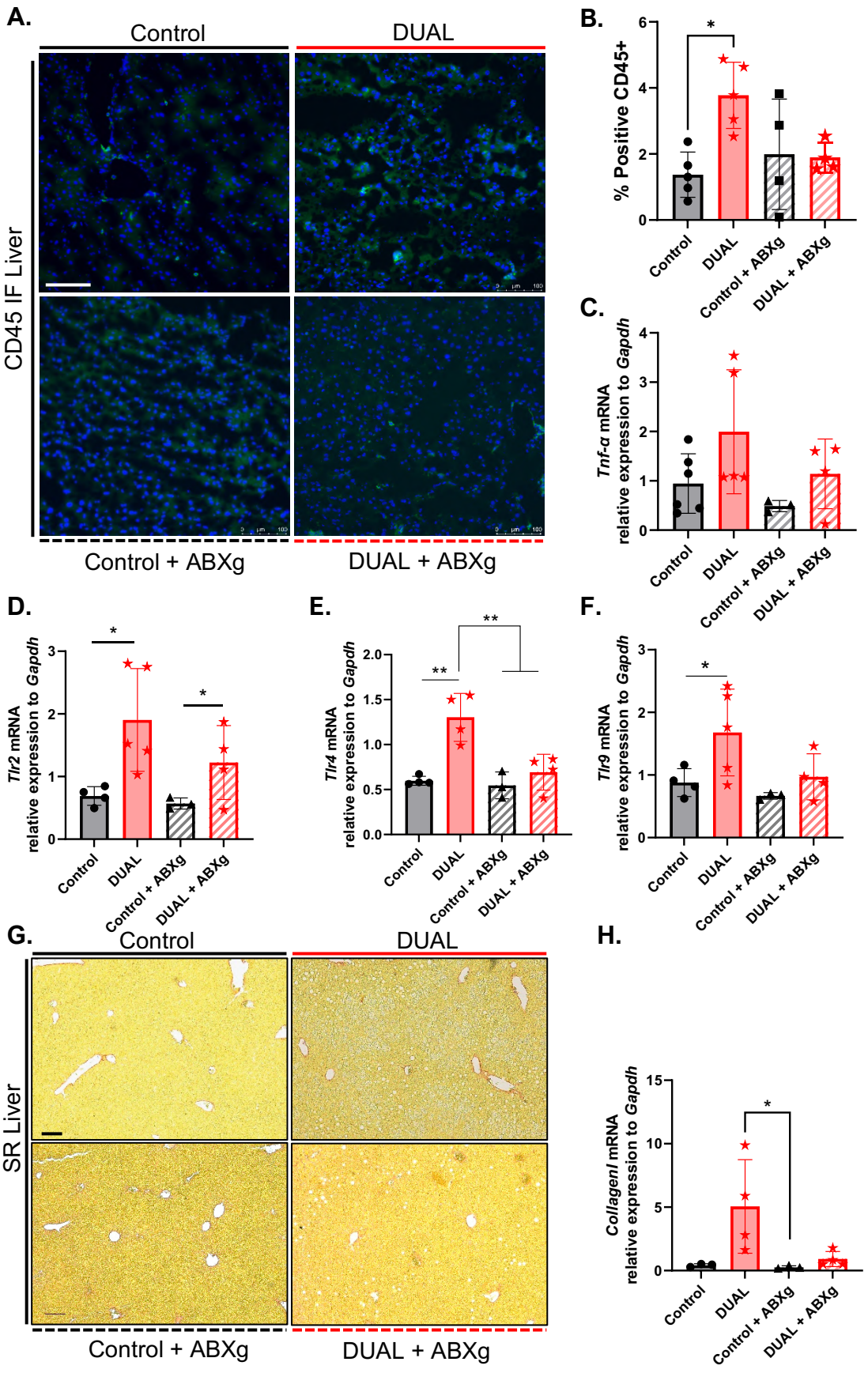
A.
Control
DUAL
CD45 IF Liver
Control + ABXg
DUAL + ABXg
B.
% Positive CD45+
C.
Tnf-α mRNA relative expression to Gapdh
D.
Tlr2 mRNA relative expression to Gapdh
E.
Tlr4 mRNA relative expression to Gapdh
F.
Tlr9 mRNA relative expression to Gapdh
G.
SR Liver
H.
Collagen1 mRNA relative expression to Gapdh
Control
DUAL
Control + ABXg
DUAL + ABXg

Fig. 77. A. Representative CD45 IF stained liver sections. Scale = 100 µm. **B.** Quantification CD45-positive cells in the liver (%) using ImageJ software. (N = 4-5). **C-F.** *Tnf-α, Tlr2, Tlr4, Tlr9* mRNA relative expression to *Gapdh* analysed by RT-qPCR in the liver. (N = 4-6). **G.** SR-stained liver sections. Scale = 100 µm. **H.** *CollagenI* mRNA relative expression to *Gapdh* determined by RT-qPCR. (N = 4). Significant differences are denoted as follows: p<0.05: *; p<0.01: **.

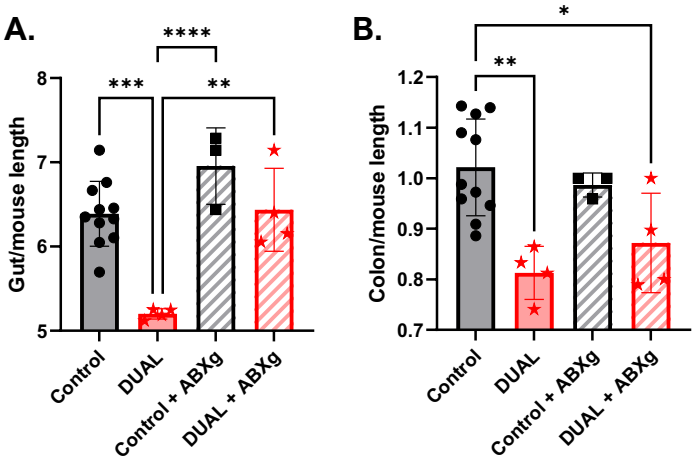

Fig. 78. A. Gut/mouse length (cm/cm). **B.** Colon/mouse length (cm/cm). (N = 4-7). Significant differences are denoted as follows: p<0.05: *; p<0.01: **; p<0.001: ***; p<0.0001: ****.

Moreover, the expression of the proinflammatory cytokine *Tnf-α* in colon remained high after ABX supplementation in comparison to controls animals **(Fig. 79A).**

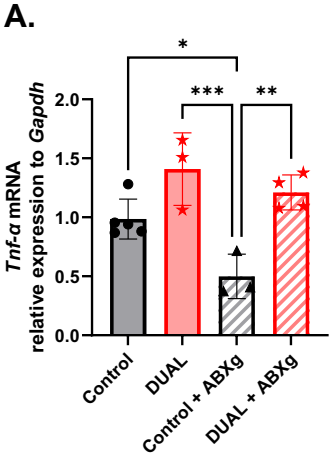

Fig. 79. A. *Tnf-α* mRNA relative expression to *Gapdh* was determined in colon by RT-qPCR. (N = 3-5). Significant differences are denoted as follows: p<0.01: **; p<0.001: ***.

Next, we evaluate the rate of colon damage by TUNEL IF staining. After 10 weeks of DUAL diet, the colon tissue was less damaged in comparison to long-term feeding **(Fig. 48D).** However, the application of ABX only mildly decreased DUAL-induced colon damage and the level of intestinal cell death did not drop to the levels of control groups **(Fig. 80A-B).** Importantly, ABX+DUAL administration

slightly increased the level of apoptosis in colon (Cleaved-caspase 3, (CC3) WB) and significantly increased colonic proliferation evaluated by PCNA **(Fig. 80C-D)**. Possibly, the administration of ABX stimulated compensatory proliferation in colon of DUAL-fed mice in order to maintain gut homeostasis **(Fig. 80E, F)**.

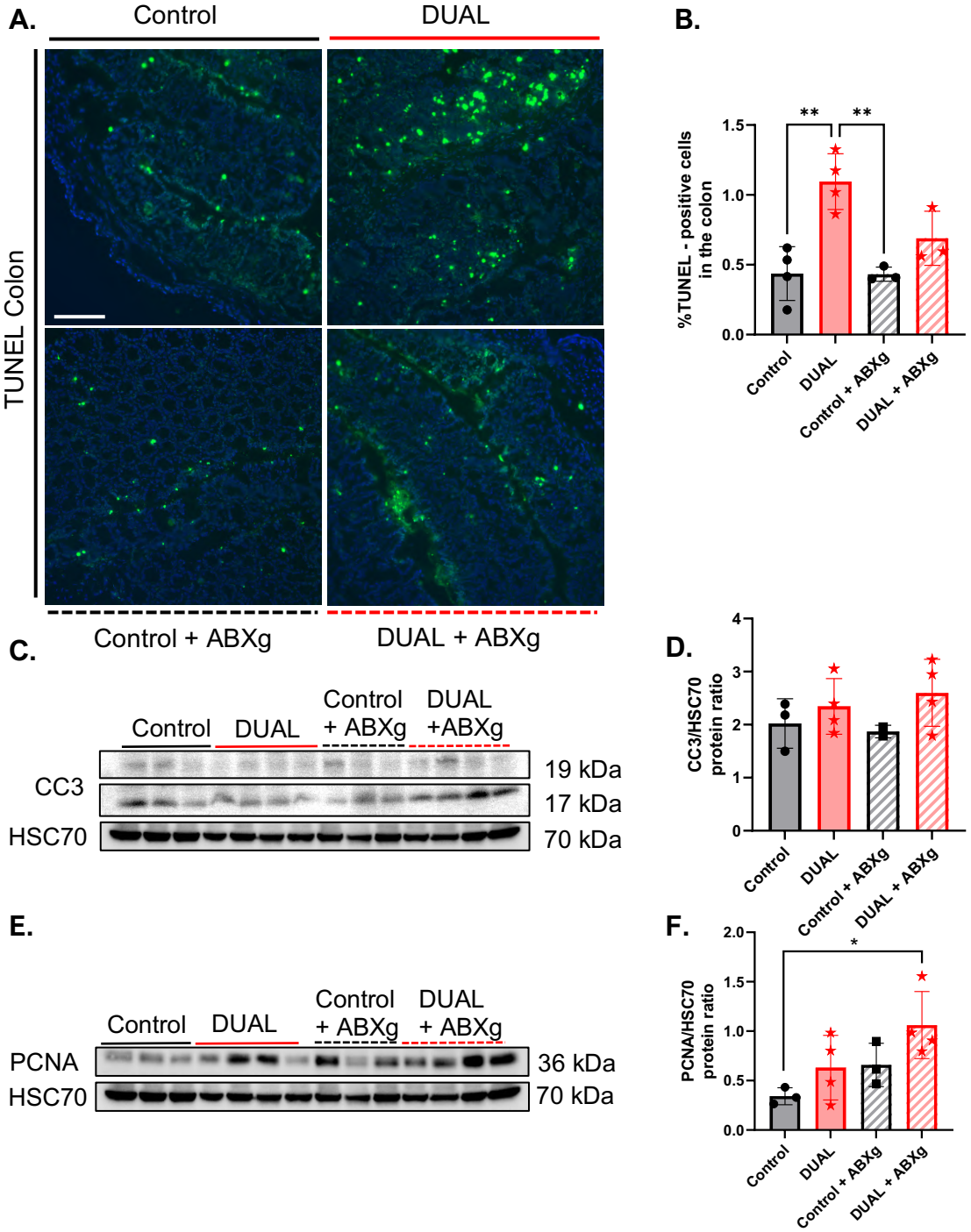

Fig. 80. A. Representative TUNEL IF staining in colon. Scale = 100 µm. **B.** Quantification of positive-TUNEL stained cells (%) using ImageJ software. (N = 3-4). **C.** CC3 WB using HSC70 as loading control in colon. **D.** Quantification CC3 WB by ImageJ software. CC3/HSC70 protein ratio was calculated. (N = 3-4). **E.** PCNA WB using HSC70 as loading control in colon. **F.** Quantification PCNA WB by ImageJ software. PCNA/HSC70 ratio was calculated. (N = 3-4). Significant differences are denoted as follows: $p<0.05$: *; $p<0.01$: **.

Finally, when we determined the concentration of LPS in serum, we found that the levels of LPS after the administration of ABX were depleted in comparison to DUAL fed mice. This indicates that: **1**. Gut permeability was significantly improved and **2**. ABX had a depletive effect on all types of bacteria, including the ones that exhibited detrimental functions for health **(Fig. 81A).**

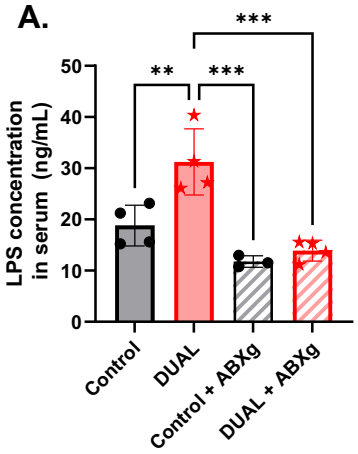

Fig. 81. A. LPS in serum determined by ELISA (ng/mL). (N = 3-4). Significant differences are denoted as follows: p<0.01: **; p<0.001: ***.

Consistently, when 16s microbiota analysis was performed, we found a decrease in the OTUs when we compared the microbiota prior to ABX administration vs. the microbiota after ABX gavage. Moreover, one animal reported an insufficient number of reads to perform any analysis **(Fig. 82A).** Principal component analysis (PCA) confirmed microbiome depletion after ABX administration. Additionally, different populations between DUAL fed animals and controls were observed **(Fig. 82B).**

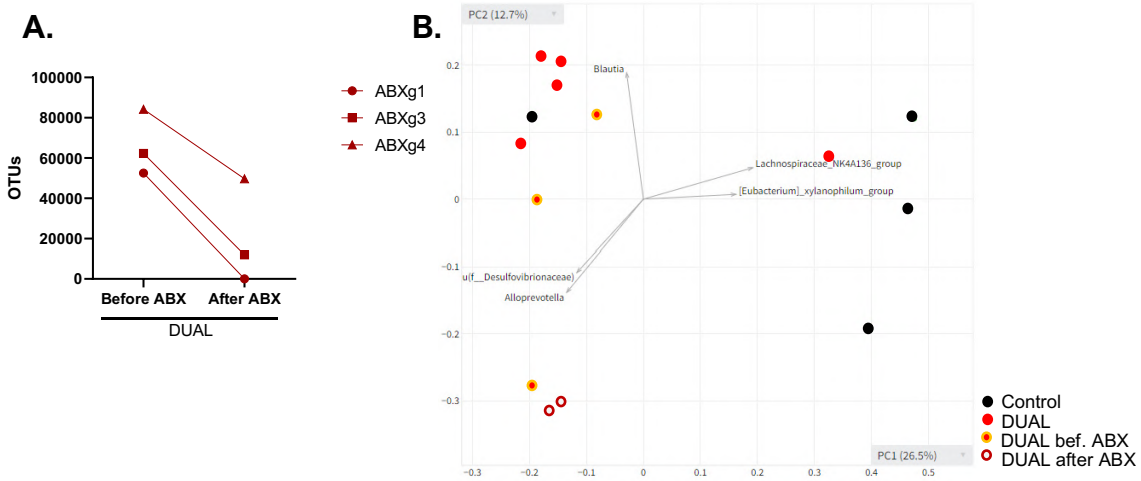

Fig. 82. A. Evolution of OTUs number before and after ABX administration in DUAL animals. **B.** Microbiome PCA representation (PC2 vs. PC1) in Control, DUAL, DUAL before ABXg and DUAL after ABXg.

7.22. PROBIOTIC ADMINISTRATION DID NOT REVEAL ANY IMPROVEMENT IN OBESITY FEATURES WHILE DUAL FEEDING OF 10 WEEKS

The administration of ABX proved that microbiome played an important role in steatohepatitis, liver damage and its consequent fibrosis induced by DUAL diet. As a potential therapeutical approach, we tested the probiotics as a treatment.

Mice were fed with DUAL diet for the 10 weeks short period and simultaneously received by oral gavage VSL#3 probiotic or placebo twice a week as described in **material and methods** section **6.2.3.4. Probiotic supplementation (Fig. 21, 22)**.

The administration of probiotics had no impact on DUAL-induced obesity. DUAL mice treated with probiotics strongly increased their body weight and had no differences in comparison to DUAL mice or DUAL + placebo groups **(Fig. 83A).** Moreover, the fat deposition and gWAT/body ratio did not show any decrease after probiotic administration **(Fig. 83B).** Consistently, the administration of probiotic did not produce any significant effect on dyslipidemia. Cholesterol levels in the serum of DUAL + Probiotics group remained elevated **(Fig. 83C).**

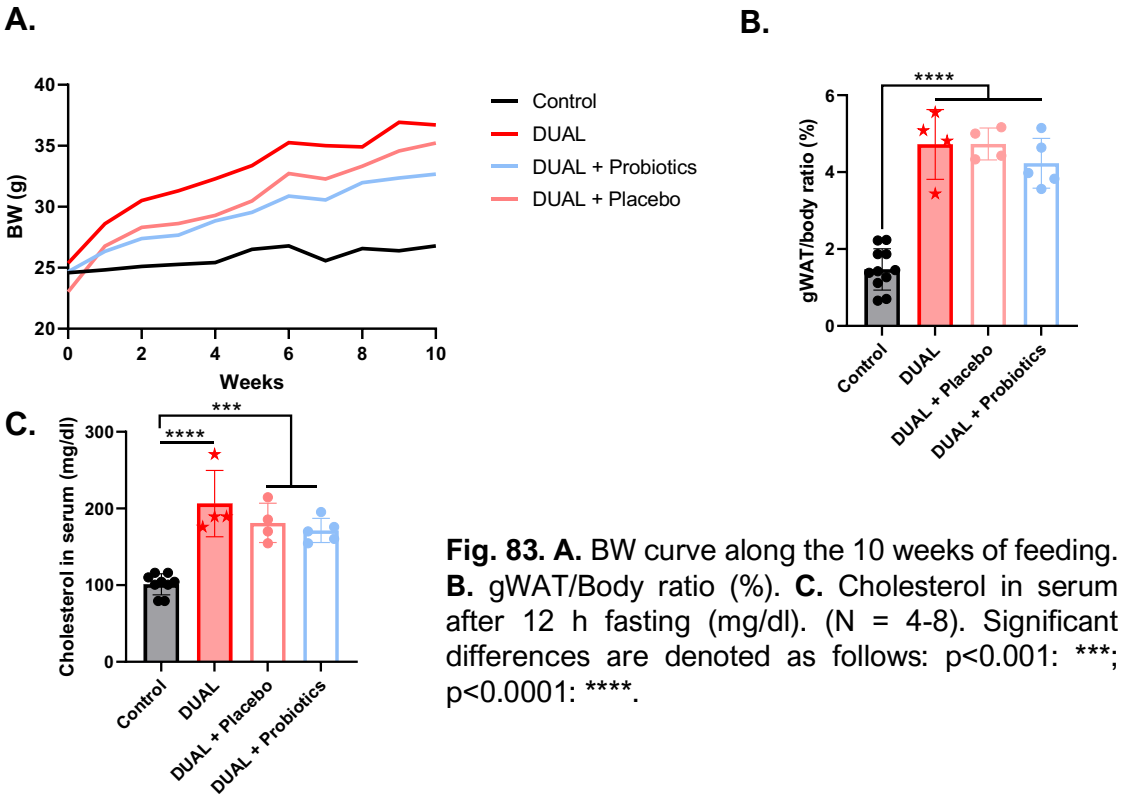

Fig. 83. A. BW curve along the 10 weeks of feeding. **B.** gWAT/Body ratio (%). **C.** Cholesterol in serum after 12 h fasting (mg/dl). (N = 4-8). Significant differences are denoted as follows: p<0.001: ***; p<0.0001: ****.

7.23. PROBIOTIC ADMINISTRATION DID NOT SHOW ANY POSITIVE EFFECTS ON SHORT-TERM DUAL-INDUCED STEATOHEPATITIS

The administration of probiotic induced a slightly decreased hepatomegaly in DUAL-fed animals. However, similar effects were demonstrated in the placebo group **(Fig. 84A).**

Next, we investigated hepatic steatosis. H&E and ORO staining clearly showed that the administration of probiotics had no effect on the lipid deposition in the hepatic parenchyma in the liver of DUAL-fed animals **(Fig. 84B; 85A, B).**

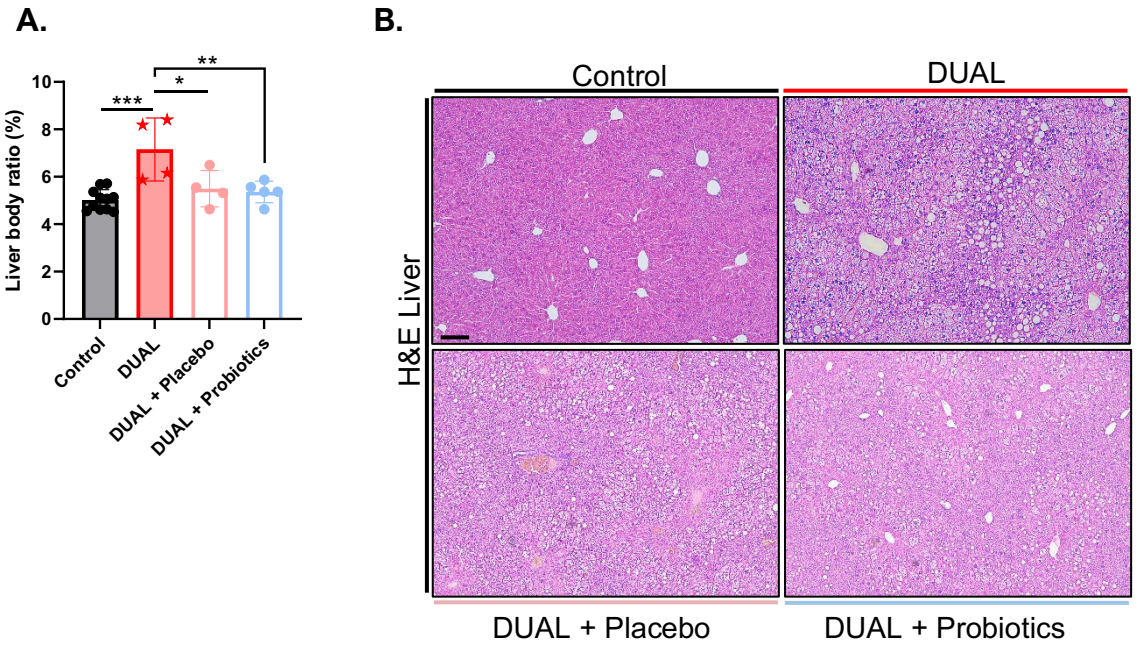

Fig. 84. A. Liver/body ratio (%). **B**. Representative images H&E in the liver. (N = 4-8). Scale = 100 µm. Significant differences are denoted as follows: p<0.05: *; p<0.01: **; p<0.001: ***.

These results were further confirmed by the quantification of TG in the liver, where we could neither find any differences between the DUAL + Probiotic group nor the DUAL/DUAL+Placebo groups **(Fig. 85C).**

Invariably, the expression of *Cd36*, a fat transporter, in the liver revealed no changes after probiotic administration **(Fig. 85D).**

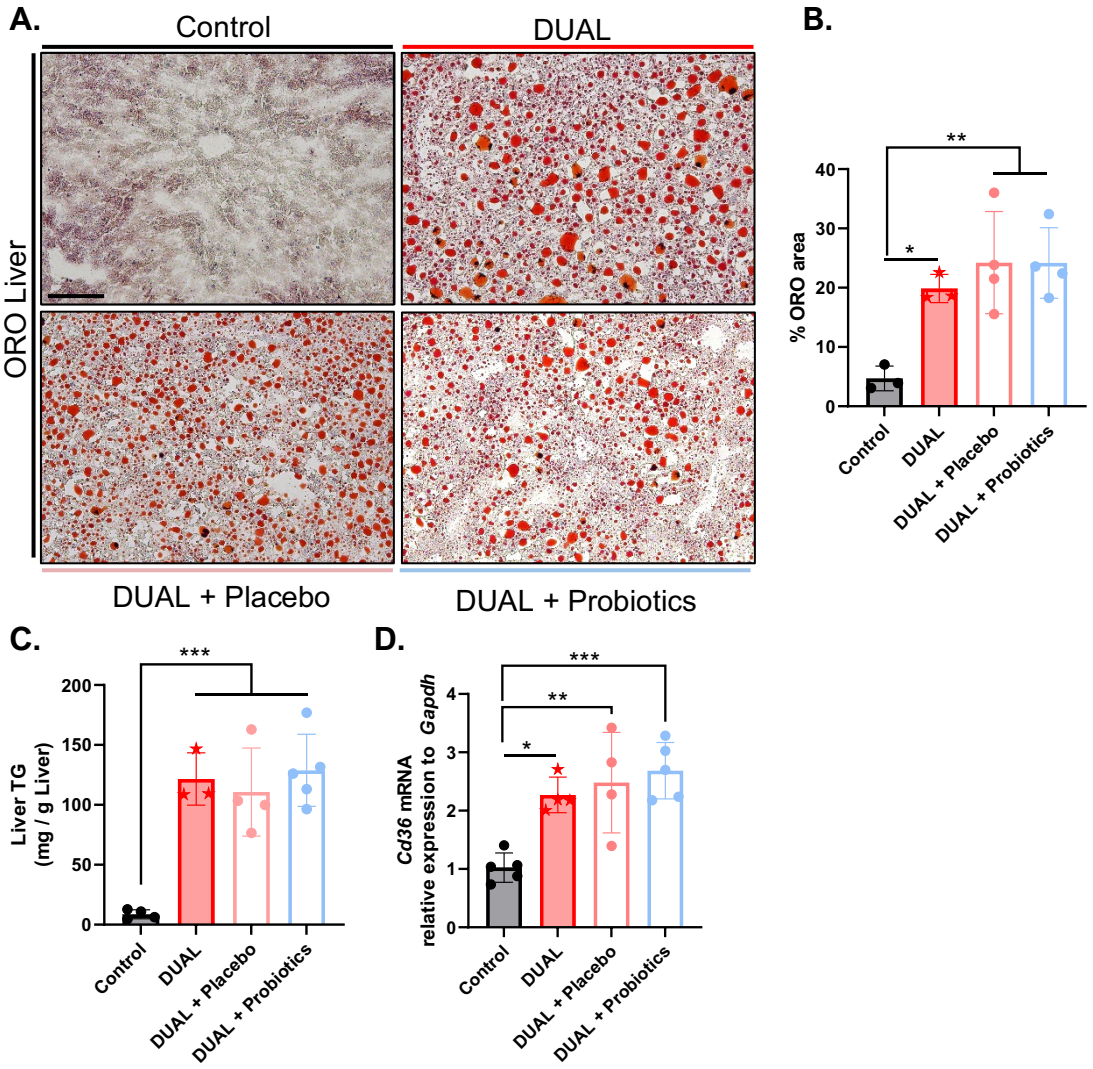

Fig. 85. A. ORO staining in liver, representative images. Scale = 100 µm. **B.** Quantification of positive-ORO area (%). (N = 3-4). **C.** TG quantification in the liver (mg/g liver). **D.** *Cd36* mRNA relative expression to *Gapdh* in the liver was measured by RT-qPCR. (N= 4-5). Significant differences are denoted as follows: p<0.05: *; p<0.01: **; p<0.001: ***.

Liver damage was characterized by the quantification of transaminases in serum. The level of ALT was slightly decreased in DUAL+Probiotics, but the levels of AST did not show any difference between DUAL and DUAL+Probiotics mice **(Fig. 86A, B).**

These results were confirmed by TUNEL IF staining, where both the DUAL + Probiotic and DUAL + Placebo group exhibited a very mild reduction in the liver cell death **(Fig. 86C-D).**

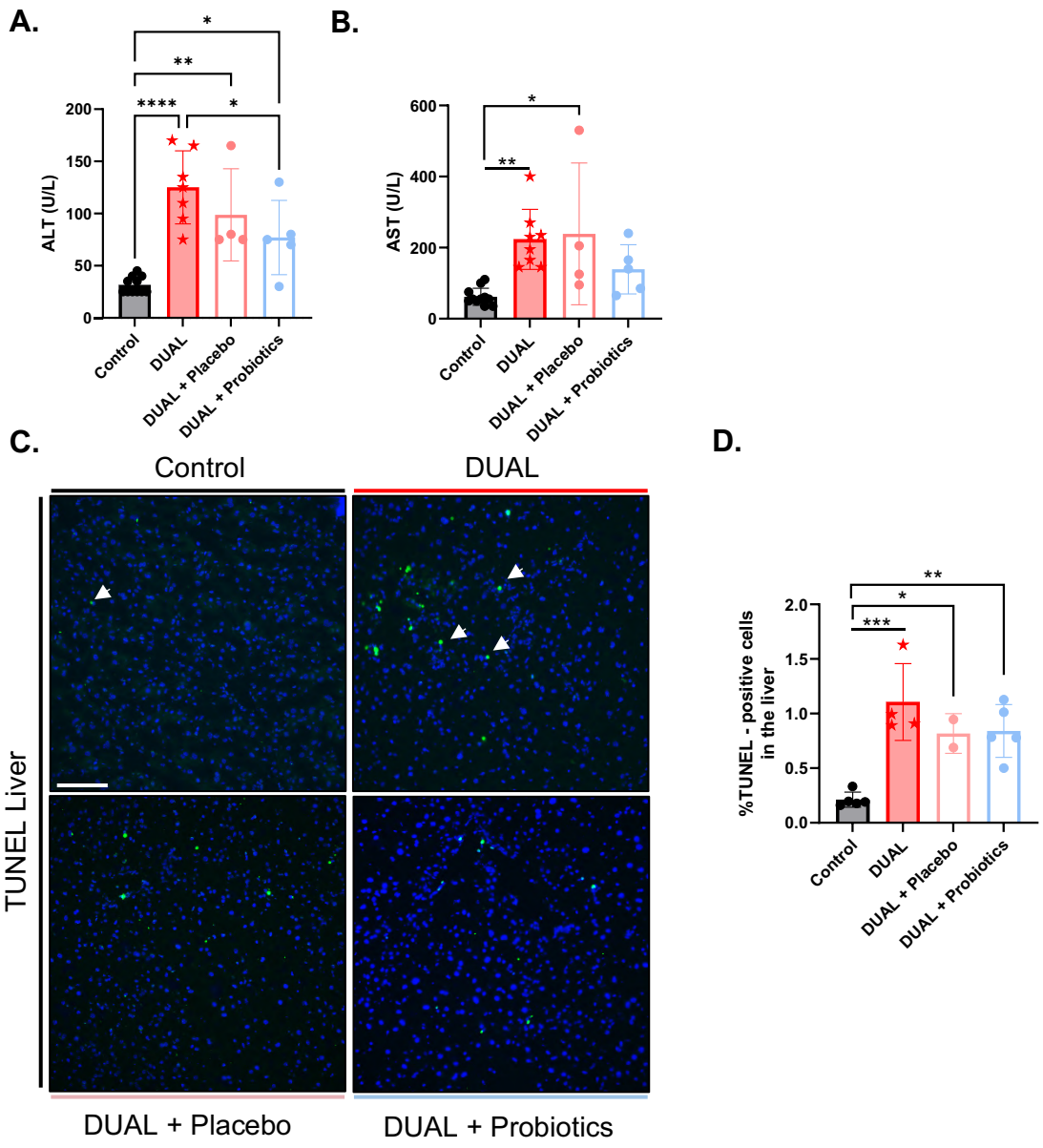

Fig. 86. A-B. ALT and AST levels in serum (U/L) respectively. (N = 4-7). **C.** Representative TUNEL IF images in the liver. Arrows show positive TUNEL cells. Scale= 100 µm. **D.** Quantification positive-TUNEL cells (%) using ImageJ software. (N = 2-5). Significant differences are denoted as follows: p<0.05: *; p<0.01: **; p<0.001: ***; p<0.0001: ****.

Our results showed that probiotic administration did not lead to any improvement in liver steatosis and hepatic cell death. In line, the immune cell infiltration after probiotic supplementation was similar between DUAL and DUAL + Probiotic fed animals. The number of immune cells ($CD45^+$) and, more concretely, macrophage infiltrates ($CD45/ F/480^+$) was still high in the hepatic parenchyma of DUAL mice after the application of probiotics **(Fig. 87A-D).**

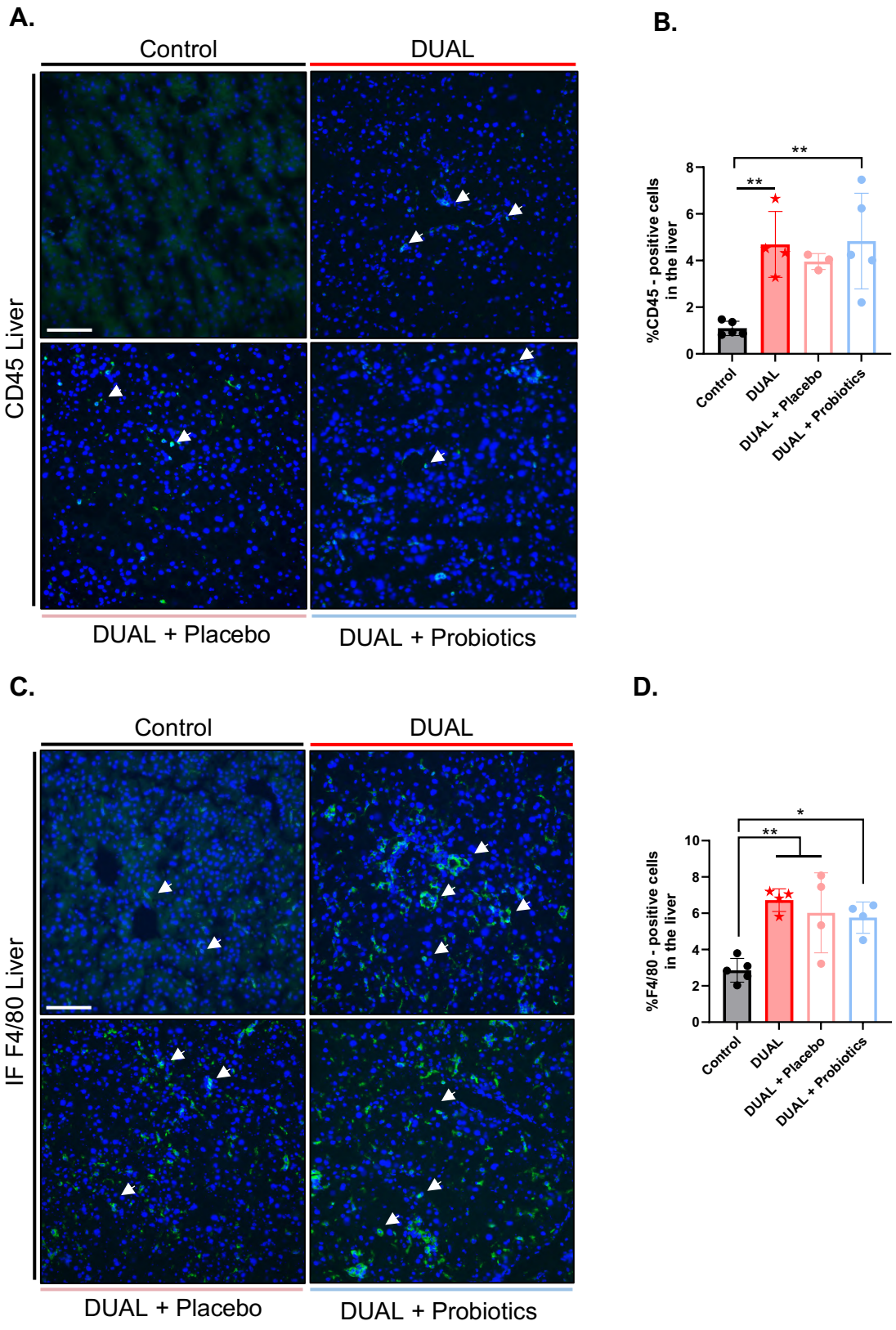

Fig. 87. A. CD45 IF staining in liver sections. Scale = 100 µm. **B.** Quantification of positive CD45 cells (%) using ImageJ software. (N = 3-5). **C.** F4/80 IF staining in liver sections. (N = 3-5). Scale = 100 µm. **D.** Quantification of positive F4/80 cells (%) using ImageJ software. (N = 3-5). Arrows show positive cells. Significant differences are denoted as follows: $p<0.05$: *; $p<0.01$: **.

Accordingly, no difference in mRNA expression of the immune response triggers *Tlr2*/4/*9* and *Tnf-α* was detected between groups **(Fig. 88A-D).**

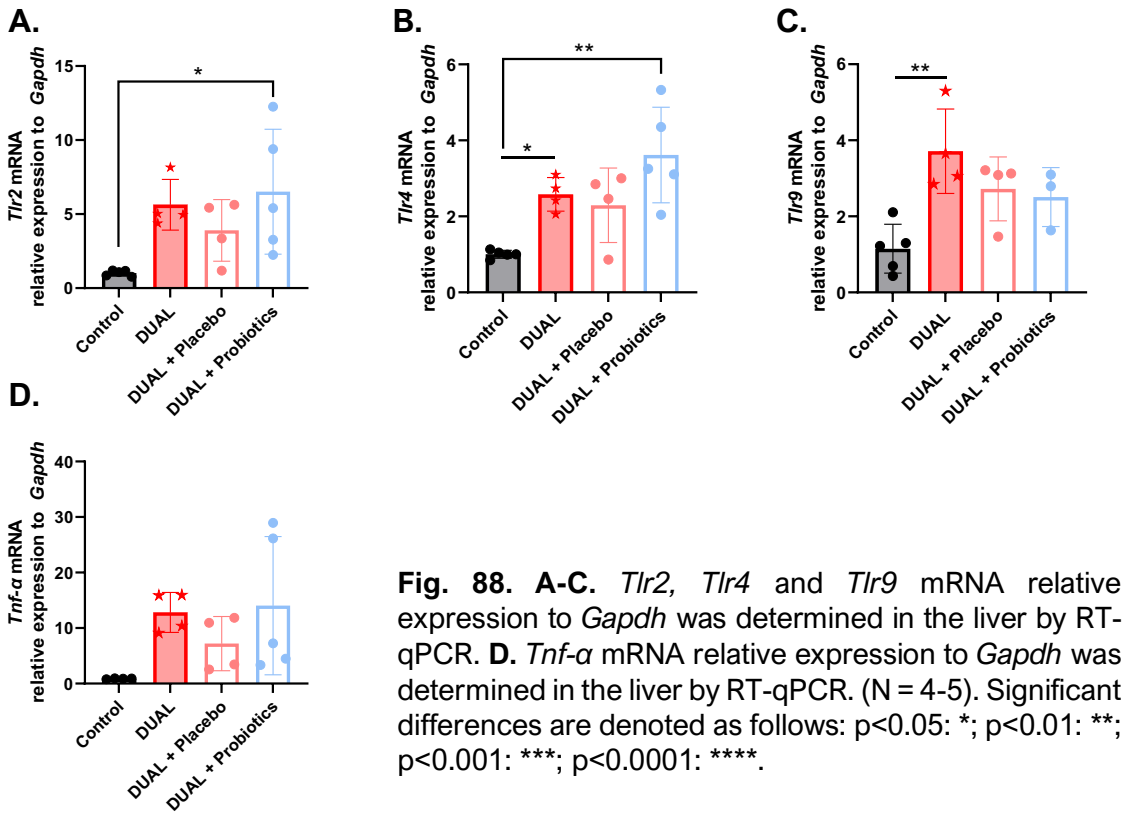

Fig. 88. A-C. *Tlr2, Tlr4* and *Tlr9* mRNA relative expression to *Gapdh* was determined in the liver by RT-qPCR. **D.** *Tnf-α* mRNA relative expression to *Gapdh* was determined in the liver by RT-qPCR. (N = 4-5). Significant differences are denoted as follows: p<0.05: *; p<0.01: **; p<0.001: ***; p<0.0001: ****.

Lastly, SR staining revealed that the administration of probiotics had no effect on the accumulation of collagen in the DUAL treated livers **(Fig. 89A-C).**

7.24. GUT PHENOTYPE AFTER 10 WEEKS OF DUAL DIET PLUS PROBIOTIC SUPPLEMENTATION REMAINED UNCHANGED

Probiotic administration did not exhibit any beneficial effect on the liver, but it remained unknown if locally it could have any effect on the gut.

Macroscopically, we calculated the ratio gut/mouse length and we found that gut length remained decreased after the administration of probiotics and had no significant differences versus DUAL animals. Moreover, the gut length remained significantly decreased compared to control mice **(Fig. 90A).**

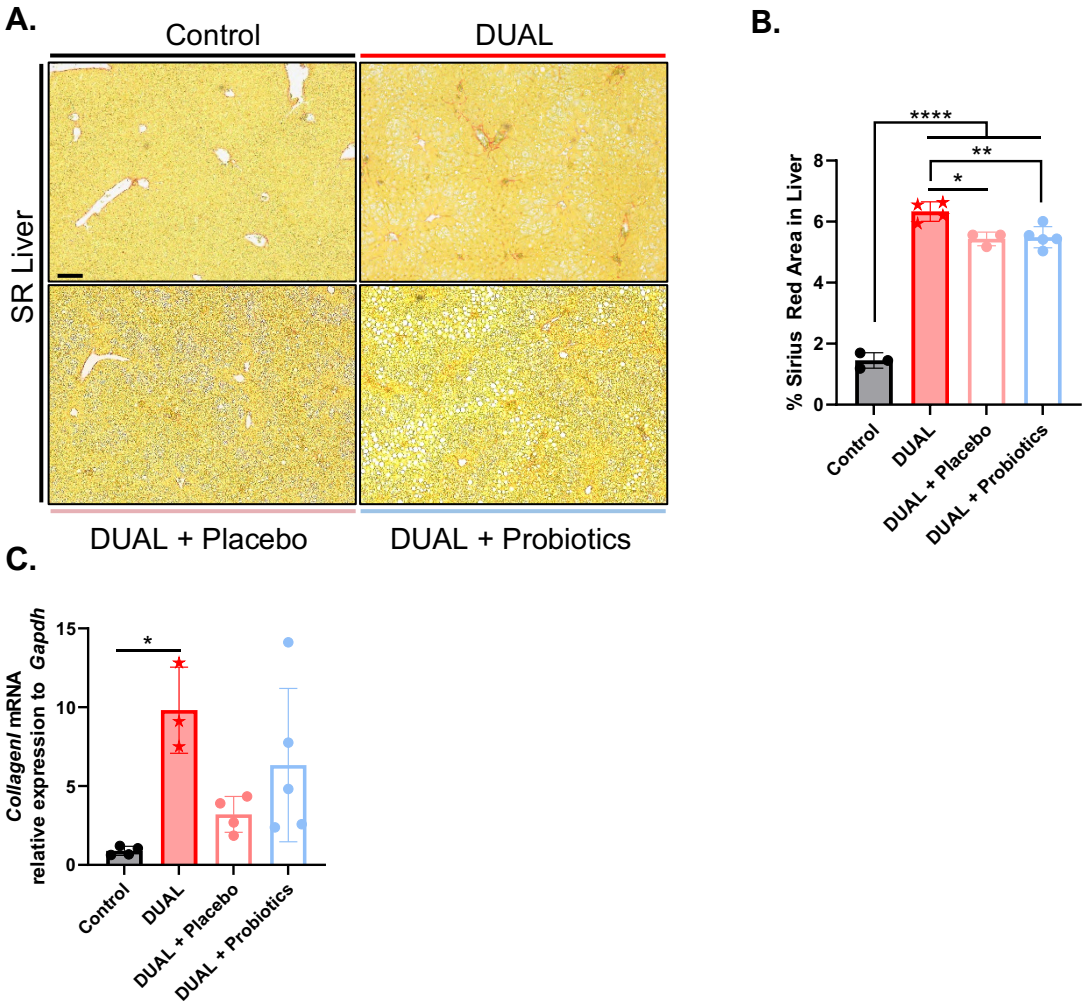

Fig. 89. A. SR representative images in the liver. Scale =100 µm. **B.** Quantification of positive SR-stained area (%) in the liver using ImageJ software. (N = 3-4). **C.** Collagen I mRNA expression in the liver analyzed by RT-qPCR. (N = 4-5). Significant differences are denoted as follows: p<0.05: *; p<0.01: **; p<0.0001: ****.

As previous results showed, the reduction in the gut length was due to a decrease in the colon length that was also observable in the DUAL + Probiotics group **(Fig. 90B).** Microscopically in the H&E we did not find any difference between the DUAL and the DUAL + Probiotic group **(Fig. 90B).**

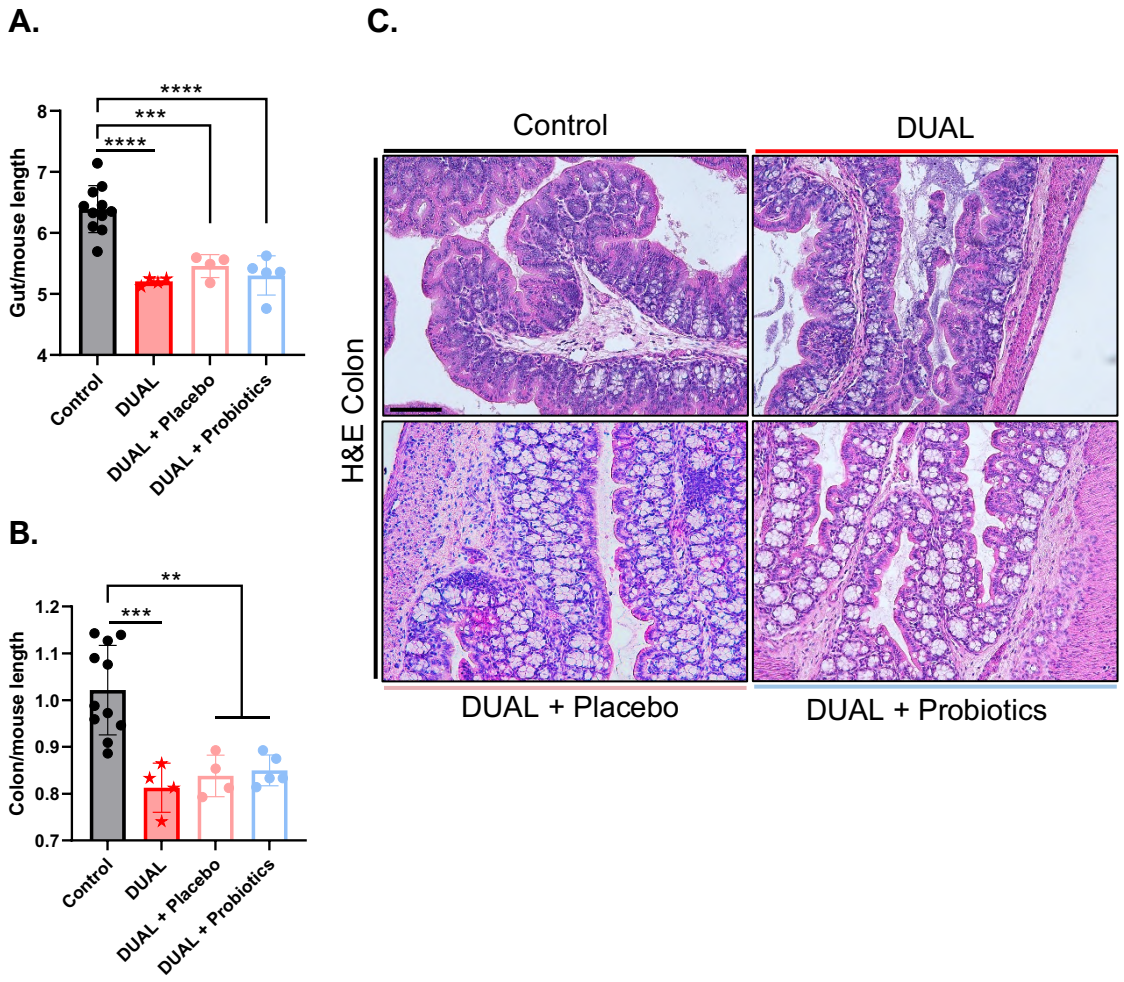

Fig. 90. A. Gut/mouse length ratio (cm/cm). **B.** Colon/mouse length ratio (cm/cm). **C.** Representative H&E-stained sections in colon. (N = 4-10). Scale = 100 µm. Significant differences are denoted as follows: p<0.01: **; p<0.001: ***; p<0.0001: ****.

Next, we analyzed in detail the effect of the probiotics on the gut barrier in DUAL mice. The probiotic administration did not ameliorate the damage induced by the DUAL diet to the mucus layer **(Fig. 91A-B).** Consequently, no significant differences in TJs ZO-1 protein expression were found in DUAL + Probiotic group **(Fig. 91C-D).**

Accordingly, FITC dextran challenge confirmed that the increased gut permeability induced by DUAL diet remained augmented after probiotic administration **(Fig. 92A).**

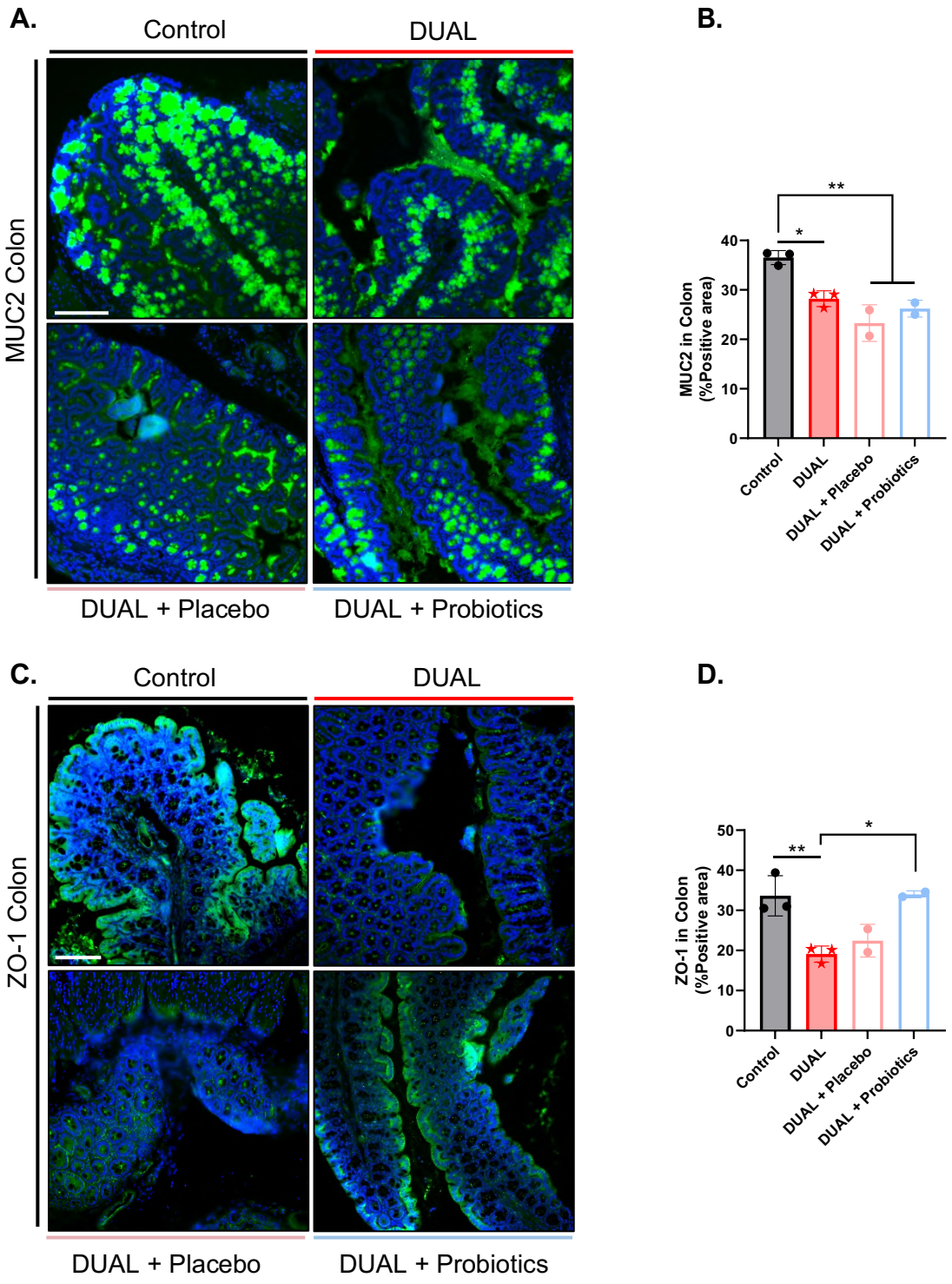

Fig. 91. A. Representative images MUC2 IF staining in colon. Scale = 100 µm. **B.** Quantification of positive MUC2 stained area (%) by ImageJ software. (N = 3). **C.** Representative images ZO-1 IF staining in colon. Scale = 100 µm. **D.** Quantification of positive ZO-1 area (%) in colon using ImageJ program. (N = 3). Significant differences are denoted as follows: $p<0.05$: *; $p<0.01$: **.

A.

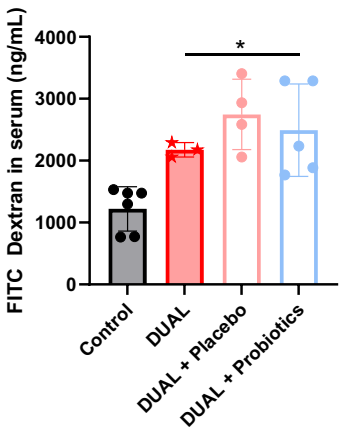

Fig. 92. A. FITC dextran concentration in serum (ng/mL). (N = 4-6). Significant differences are denoted as follows: p<0.05: *; p<0.01: **; p<0.001: ***; p<0.0001: ****.

7.25. MILD BUT SIGNIFICANT IMPROVEMENT OF THE DUAL LIVER PHENOTYPE FOUND AFTER 10 WEEKS WAS DETECTED AFTER FECAL MICROBIOTA TRANSPLANTATION

The absence of significant positive effects after probiotics in DUAL mice led us to the conclusion that the administration of the mixture of few bacterial strains is not significant for the microbiome modulation. Potentially, the application of a complete and balanced population of bacteria from living and healthy organisms can improve dysbiosis. Increasing evidence demonstrates that FMT, which is a new and underexplored method to alter the gastrointestinal microbiota, may be effective for the treatment of patients with CLD. However, the therapeutic potential of FMT-based intervention for CLD has been still poorly investigated to date (222, 223).

Here we aimed to assess the effectiveness of FMT treatment in DUAL fed mice. 10-weeks DUAL-fed animals were treated with multi-session FMT from healthy donors, via oral gavage as described in **6.2.3.5. FMT material and methods** section. For a better comparison, we used multiple controls: control (chow fed) animals, control (chow fed) + FMT; and treated animals: DUAL-fed mice, DUAL+ FMT as shown in **Fig. 23, 24.**

Firstly, body weight analysis did not show any significant differences between DUAL and DUAL + FMT groups **(Fig. 93A).** Moreover, no significant differences in BMI were found between DUAL and DUAL + FMT mice **(Fig. 93B).** Consistently, we did not observe any positive correlation in gWAT/body ratio after FMT administration **(Fig. 93C).**

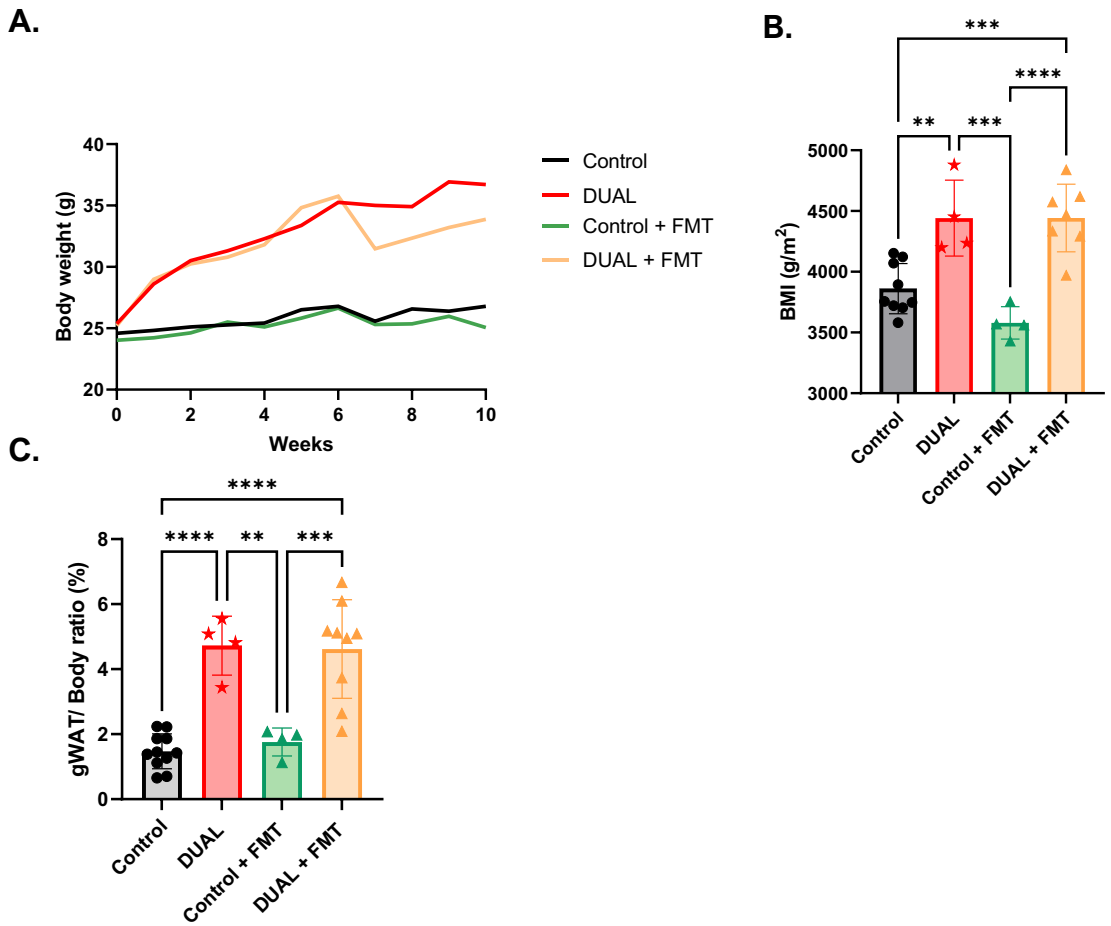

Fig. 93. A. Body weight recording during the 10 weeks of feeding. **B.** BMI was calculated after 10 weeks of feeding (g/m^2). **C.** gWAT/Body ratio (%). (N = 4-10). Significant differences are denoted as follows: p<0.01: **; p<0.001: ***; p<0.0001: ****.

Next, we analyzed the effects of FMT on the DUAL induced steatohepatitis.

Only a slight improvement was found in the liver weight and in the liver/body ratio after FMT administration to DUAL animals **(Fig. 94A-B).**

H&E and ORO stainings of the liver revealed notable changes. DUAL+FMT group showed significant improvement of hepatocellular morphology **(Fig. 94C; Fig.95A, B)** and attenuated hepatic steatosis with improved hepatic TG content, although not to the meanings of the control group **(Fig. 95C)**.

Mice were subjected to FMT during the last 4 weeks of DUAL feeding, and reasonably, the fat consumption was unaffected as well as the expression of the responsible genes implicated in the transport of fat inside the liver (*Cd36* and *Pparγ)* in DUAL+FMT group **(Fig. 95D-E).**

Importantly, in DUAL+FMT group, we found a mild increase, although not significant, in the protein levels of CPT-1c, associated with fat oxidation. This would explain the mild reduction of hepatic steatosis observed in DUAL mice subjected to FMT **(Fig. 95F-G).**

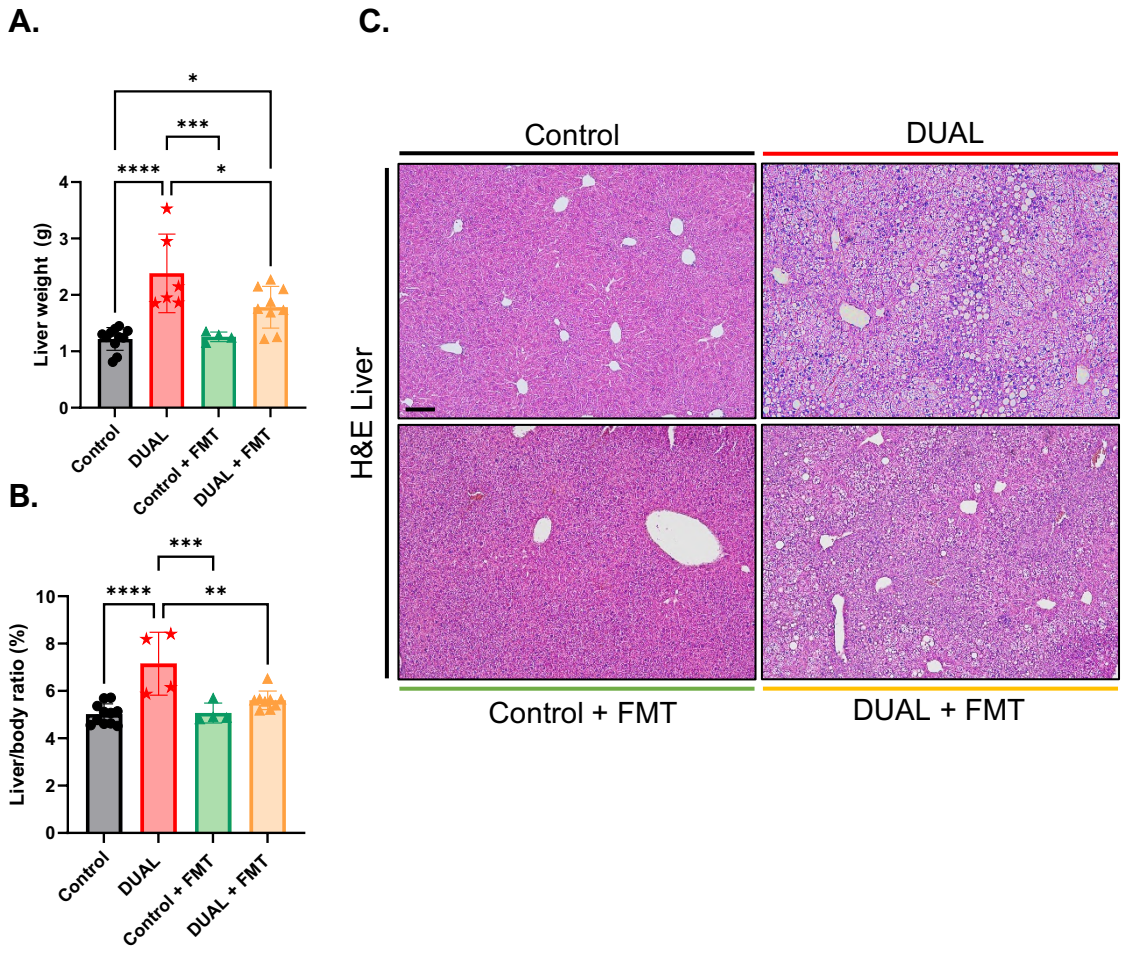

Fig. 94. A. Liver weight (g). **B.** Liver/Body ratio (%). **C.** Representative H&E-stained sections in liver. Scale = 100 µm. (N = 4-10). Significant differences are denoted as follows: p<0.05: *; p<0.01: **; p<0.001: ***; p<0.0001: ****.

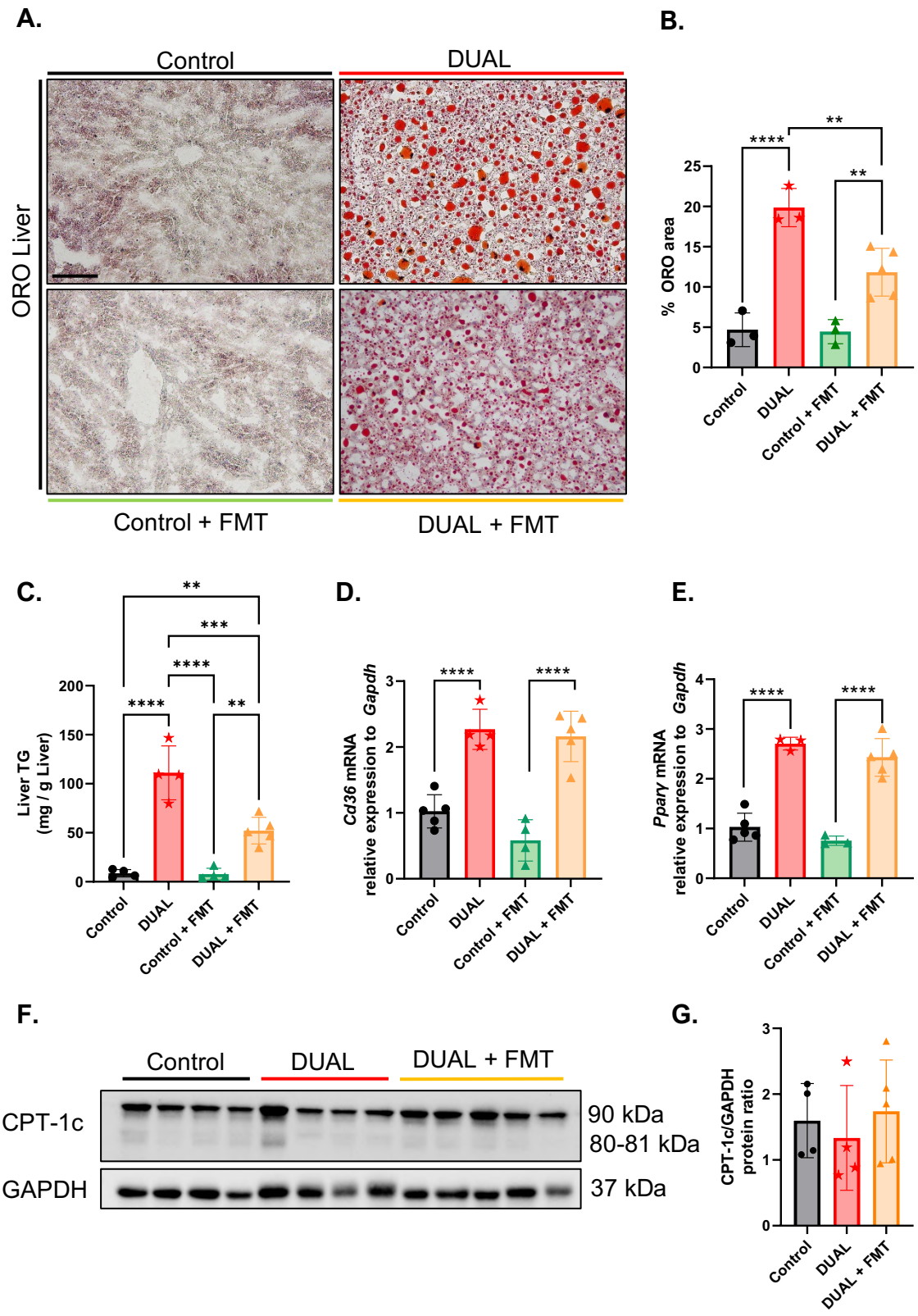

Fig. 95. A. ORO staining in liver. Scale = 100 µm. **B.** Quantification of positive-ORO area (%) using ImageJ software. (N = 3-5). **C.** TG quantification in the liver (mg/g liver). (N = 3-5). **D-E.** *Cd36* and *Ppary* relative expression to *Gapdh* in the liver determined by RT-qPCR. (N = 4-5). **F.** CPT-1c WB in the liver. GAPDH was used as a loading control. **G.** CPT-1c WB densitometry. CPT-1c/GAPDH protein ratio was calculated. (N = 3-5). Significant differences are denoted as follows: p<0.01: **; p<0.001: ***; p<0.0001: ****.

Major clinical indicators of hepatic injury, AST, ALT and LDH, were significantly reduced in DUAL-fed mice subjected to FMT **(Fig. 96A-C)**. Consistently, IF TUNEL staining was slightly but significantly ameliorated in DUAL+FMT livers **(Fig. 96D, E)**.

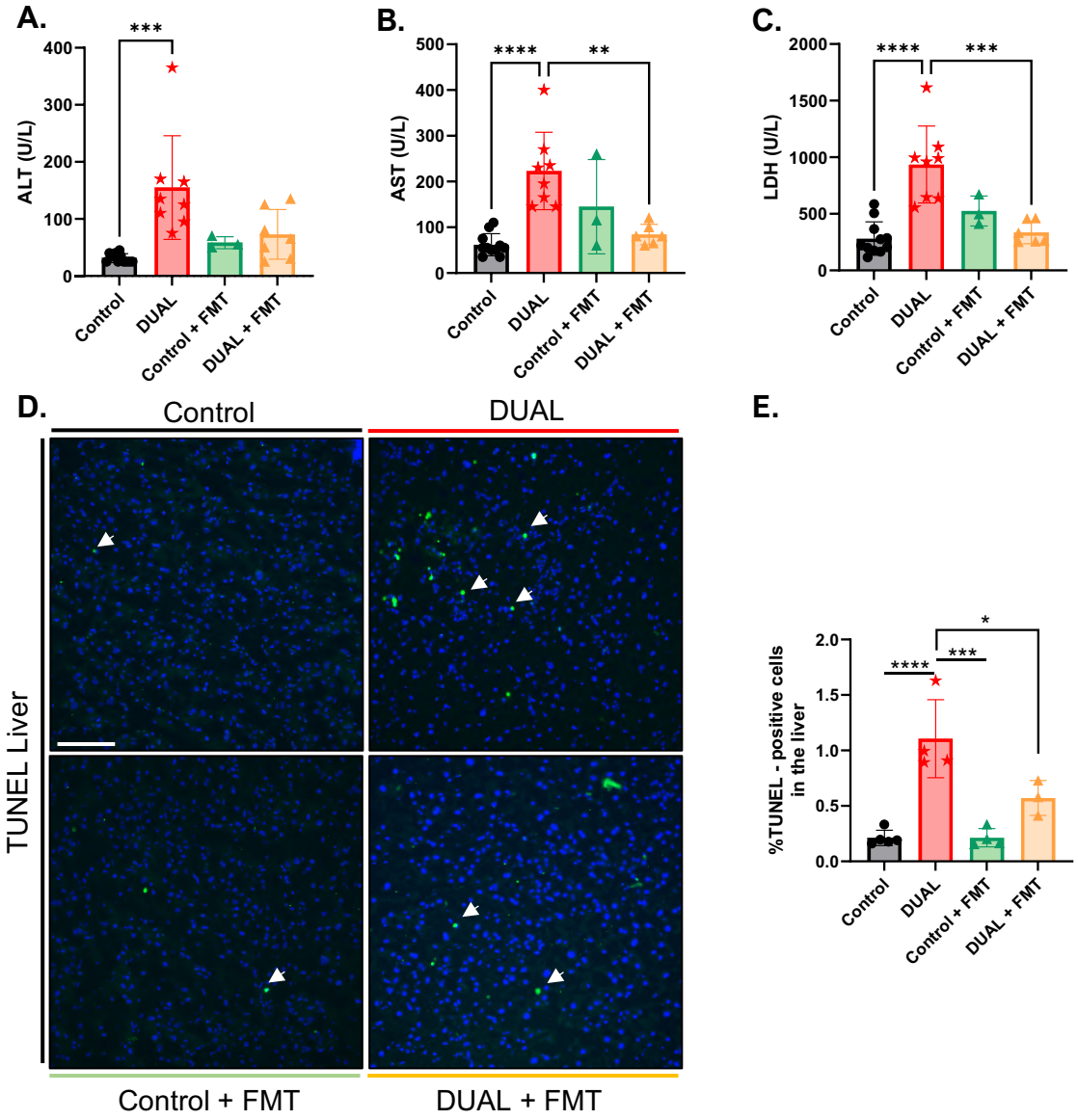

Fig. 96. A-C. ALT, AST and LDH concentration in serum (U/L). (N = 3-7). **D.** TUNEL IF staining in liver. Arrows show positive TUNEL cells. Scale = 100 µm. **E.** Quantification positive TUNEL cells (%) using ImageJ software. (N = 3-5). Significant differences are denoted as follows: p<0.05: *; p<0.01: **; p<0.001: ***; p<0.0001: ****.

Consequently, the decrease of hepatocyte cell death was directly associated with lower levels of hepatic inflammation. A reduction in the immune cell as macrophage infiltrates ($CD45^+$ $F4/80^+$) was identified in the liver of DUAL + FMT mice compared to DUAL animals **(Fig. 97A-D).**

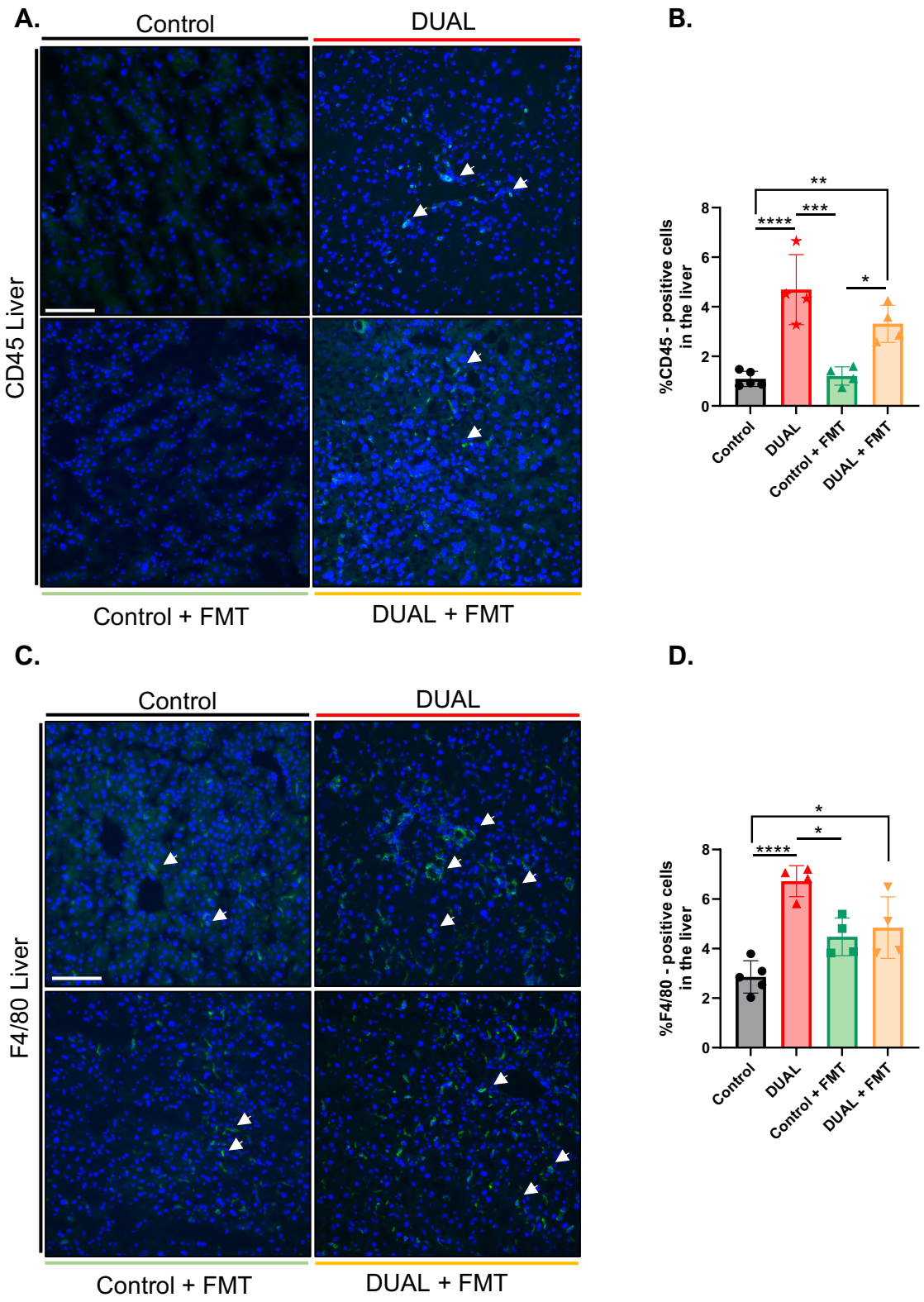

Fig. 97. A. CD45 IF staining in the liver. **B.** Quantification of positive CD45 cells (%) in the liver using ImageJ software. (N = 3-5). **C.** F4/80 IF staining in the liver. Scale = 100 µm. **D.** Quantification of positive F4/80 cells (%) in the liver by ImageJ software. Arrows show positive cells. (N = 4-5). Significant differences are denoted as follows: p<0.05: *; p<0.01: **; p<0.001: ***; p<0.0001: ****.

However, the inflammation was not reduced to the control levels. Accordingly, the hepatic expression of the proinflammatory cytokine *Tnf-α* was significantly reduced in DUAL + FMT compared to DUAL mice **(Fig. 98A).**

Finally, the inflammation triggered by the expression of *Tlr2, 4* and *9* showed a slight but not significant decrease in DUAL animals subjected to FMT **(Fig. 98B-D).**

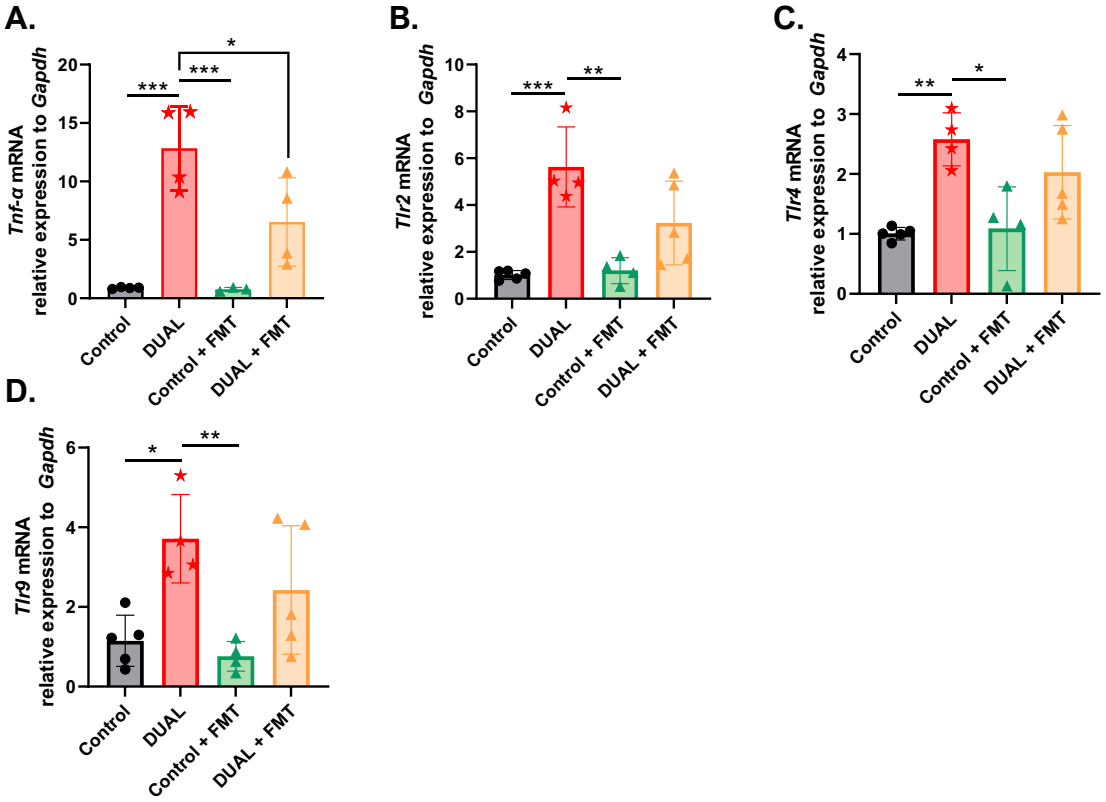

Fig. 98. A-D. *Tnf-α*, *Tlr2*, *Tlr4* and *Tlr9* mRNA relative expression to *Gapdh* was determined in the liver by RT-qPCR. (N = 3-4). Significant differences are denoted as follows: $p<0.05$: *; $p<0.01$: **; $p<0.001$: ***.

The mild reduction in the liver damage and inflammation induced by FMT consequently led to a decreased collagen deposition in the liver, as it is demonstrated by SR staining **(Fig. 99A).** mRNA expression of *CollagenI* was significantly reduced after FMT compared to DUAL animals **(Fig. 99B).**

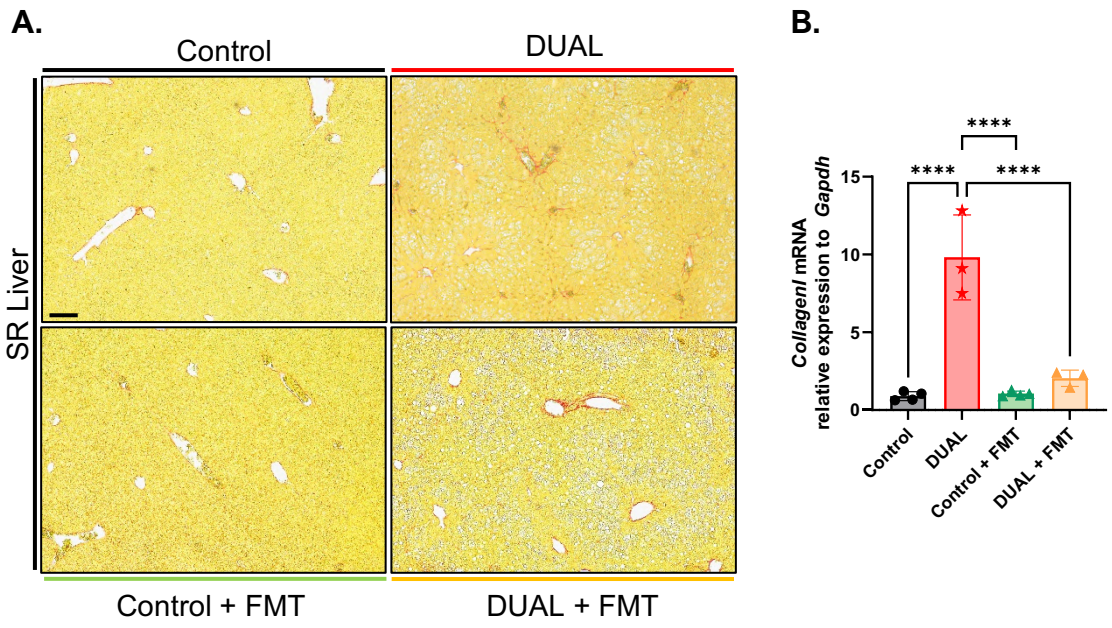

Fig. 99. A. SR staining in the liver. Scale = 100 μm. **B.** *CollagenI* mRNA relative expression to *Gapdh* in the liver was quantified through RT-qPCR. (N = 3-4). Significant differences are denoted as follows: p<0.0001: ****.

7.26. FMT SLIGHTLY IMPROVED SHORT-TERM DUAL-INDUCED INTESTINAL DAMAGE AND COLITIS AND AMELIORATED GUT BARRIER PERMEABILITY

To further connect the beneficial effects that were identified after FMT in the liver with alterations in gut physiology, the gut/mouse ratio and colon/mouse length were evaluated. Slight improvements were observed in DUAL mice subjected to FMT **(Fig. 100A, B).** Microscopically, the colon crypts in the DUAL+FMT group looked bigger than in the DUAL mice **(Fig. 100C).**

Since one of the major changes induced by DUAL diet was intestinal inflammation, we analyzed the inflammation in colon of DUAL mice after FMT administration. The level of the proinflammatory cytokine *Tnf-α* was slightly but not significantly decreased after FMT in comparison to control or DUAL mice **(Fig. 101A).**

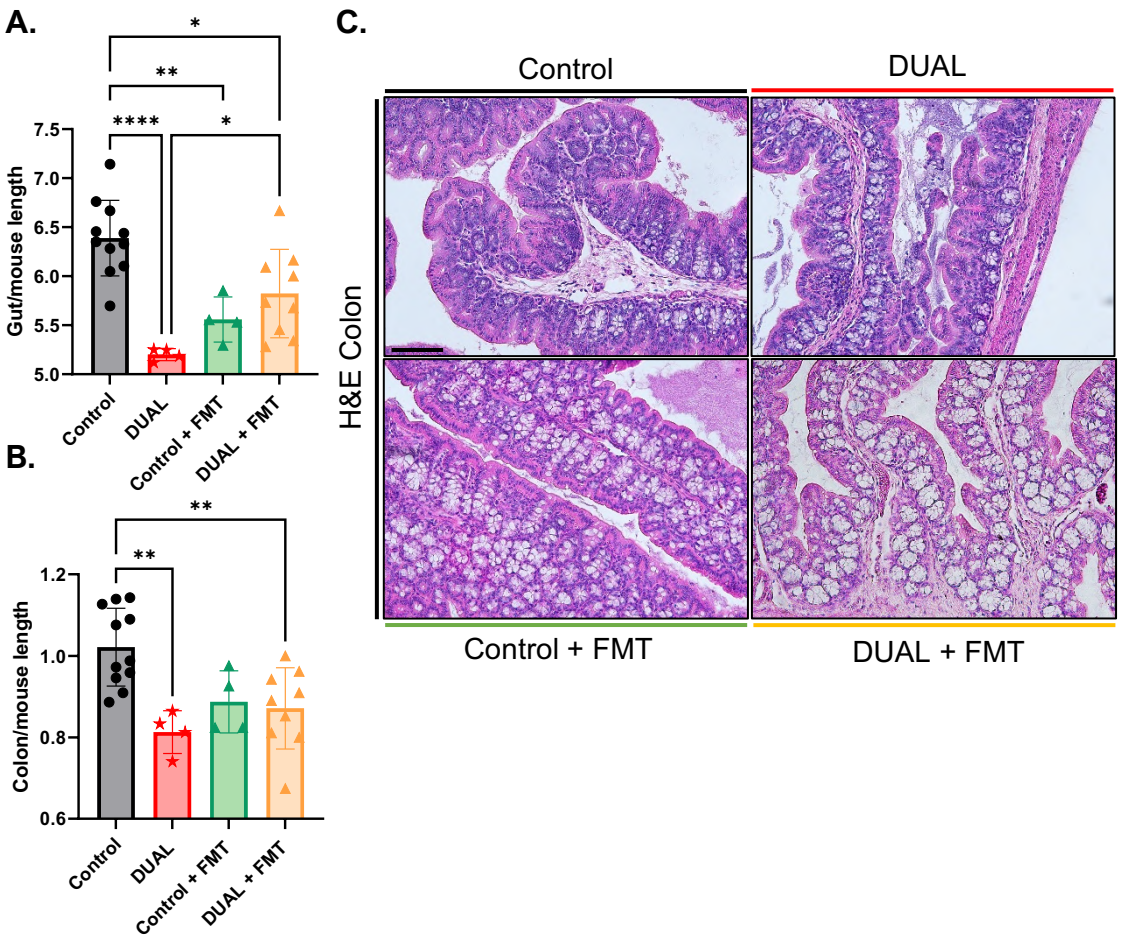

Fig. 100. A. Gut/mouse length ratio (cm/cm). **B.** Colon/mouse length ratio (cm/cm). **C.** Representative images from H&E in colon. Scale = 100 µm. (N = 4-10). Significant differences are denoted as follows: p<0.05: *; p<0.01: **; p<0.0001: ****.

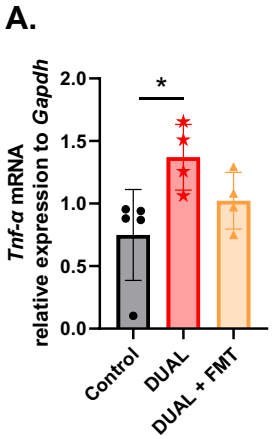

Fig. 101. A. *Tnf-α* mRNA relative expression to *Gapdh* in colon was determined by RT-qPCR. (N= 2-5). Significant differences are denoted as follows: p<0.05: *; p<0.01: **; p<0.001: ***; p<0.0001: ****.

Gut damage was further assessed by TUNEL IF staining. We found that intestinal cell death in colon of DUAL mice was significantly decreased after FMT **(Fig. 102A-B).** No significant difference between the groups was detected in the level of apoptosis as shown by CC3 WB on **(Fig. 102C-D)**. Interestingly, FMT administration to DUAL animals did not lead to significant compensatory proliferation **(Fig. 102D-E)**.

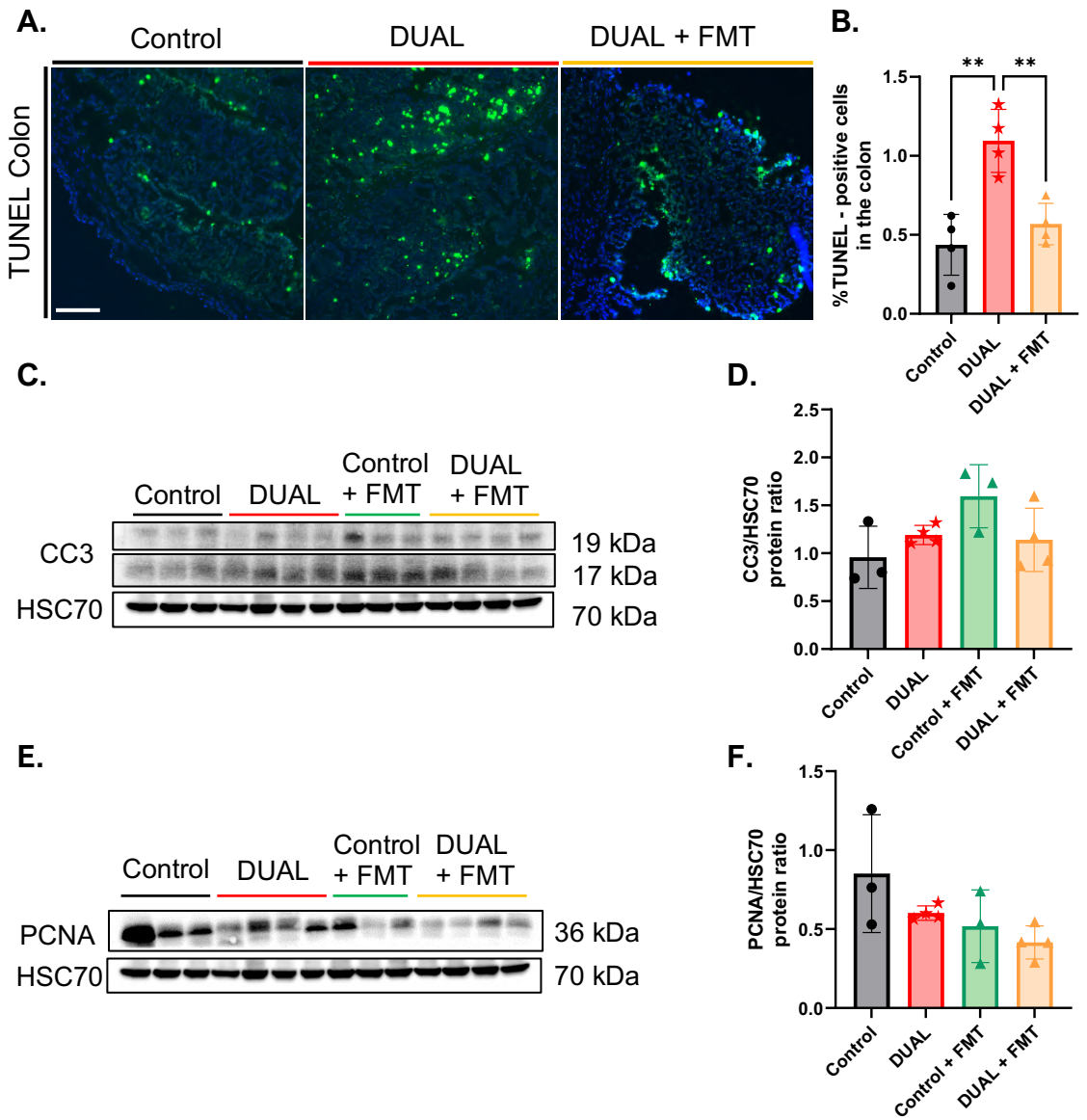

Fig. 102. A. TUNEL IF staining in colon. Scale = 100 μm. **B.** Positive-TUNEL cells (%) quantification using ImageJ software. (N = 4). **C.** CC3 WB using HSC70 as loading control. **D.** CC3 WB densitometry. CC3/HSC70 protein ratio was calculated. (N = 3-4). **E.** PCNA WB using HSC70 as a loading control. **F.** PCNA/HSC70 protein ratio was calculated. (N = 3-4). Significant differences are denoted as follows: p<0.01: **.

Following that, we investigate the effects of FMT on the impaired gut barriers of DUAL mice. On the first level, we identified an increase in the protein expression of MUC2 in the colon of DUAL + FMT group compared to DUAL mice **(Fig. 103A-B).**

Next, TJs were evaluated, and ZO-1 showed a slight but significant improvement between DUAL + FMT and DUAL mice **(Fig. 103C-D).** However, the protein levels of occludin, another TJs protein, were not ameliored after FMT administration to DUAL mice **(Fig. 103E-F).**

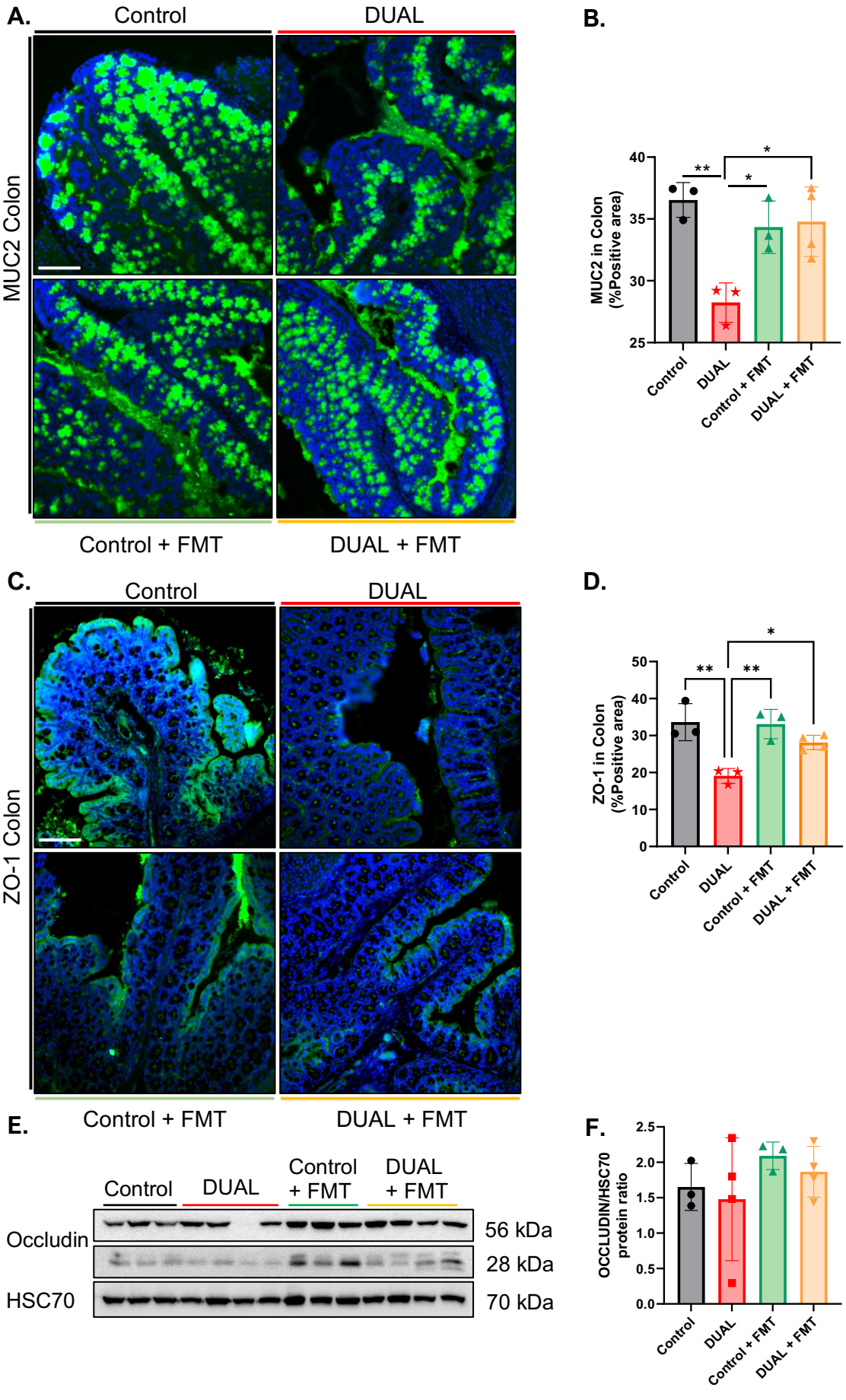
A.
Control
DUAL
MUC2 Colon
Control + FMT
DUAL + FMT
B.
MUC2 in Colon (%Positive area)
40
35
30
25
**
*
*
Control
DUAL
Control + FMT
DUAL + FMT
C.
Control
DUAL
ZO-1 Colon
Control + FMT
DUAL + FMT
D.
ZO-1 in Colon (%Positive area)
50
40
30
20
10
0
**
**
*
Control
DUAL
Control + FMT
DUAL + FMT
E.
Control
DUAL
Control + FMT
DUAL + FMT
Occludin
HSC70
56 kDa
28 kDa
70 kDa
F.
OCCLUDIN/HSC70 protein ratio
2.5
2.0
1.5
1.0
0.5
0.0
Control
DUAL
Control + FMT
DUAL + FMT

Fig. 103. A. MUC2 IF staining in colon, representative pictures. **B.** Quantification of positive MUC2 stained area (%) using ImageJ software. (N = 3-4). **C.** ZO-1 IF staining in colon. **D.** Quantification of positive ZO-1-stained area (%) using ImageJ software. (N = 3-4). **E.** OCCLUDIN WB. HSC70 was used as a loading control. **F.** OCCLUDIN WB densitometry by ImageJ software. OCCLUDIN/HSC70 protein ratio was calculated. (N = 3-4). Significant differences are denoted as follows: p<0.05: *; p<0.01: **.

As a result, the gut permeability analyzed by FITC dextran assay was moderately reduced in DUAL + FMT mice **(Fig. 104A).**

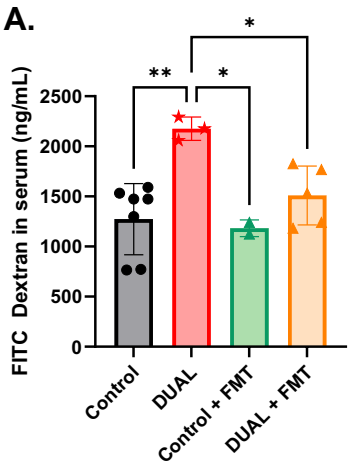

Fig. 104. A. FITC dextran concentration in serum (ng/mL). (N = 2-7). Significant differences are denoted as follows: p<0.05: *; p<0.01: **.

7.27. DUAL WITHDRAWAL REDUCED STEATOSIS, LIVER DAMAGE AND FIBROSIS

Nowadays, while no pharmacological therapy is approved for the treatment of CLD dual etiology, international guidelines advocate the use of lifestyle interventions that are based on changes in dietary habits and alcohol abstinence (224, 225). However, the adherence to clinical recommendations is compromised and tends to fail.

We decided to investigate if the DUAL withdrawal (DUAL W) could have any beneficial effect on early CLD induced by short term DUAL feeding. 10-week-old C57BL/6J male mice were fed with DUAL diet, control group was treated in parallel, for 10 weeks (short-term feeding). After DUAL feeding, treatment was replaced by normal filtered water and regular chow diet for 21 more days as is described in **material and methods 6.2.3.6. DUAL withdrawal section and in Fig. 25.**

The hepatic phenotype, liver weight and liver body ratio were significantly reduced after 21 days of DUAL W **(Fig. 105A-B).**

H&E staining revealed that DUAL W ameliorated lipid deposition in the liver **(Fig. 105C).**

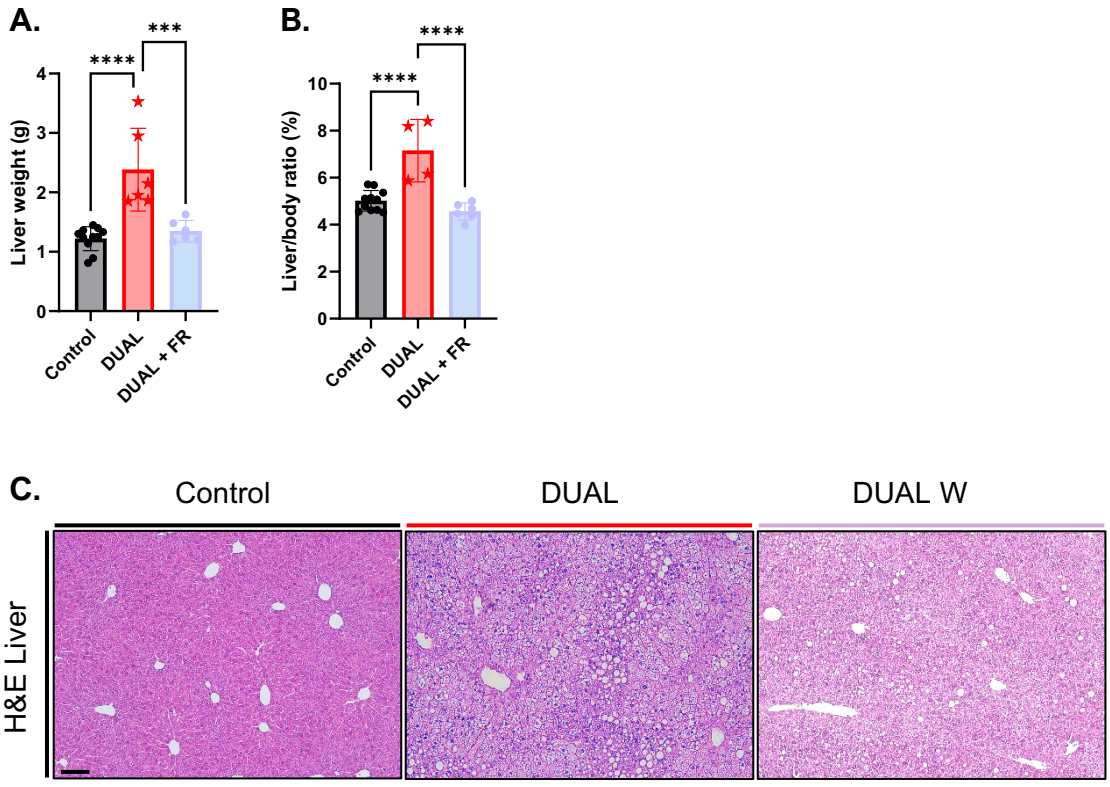

Fig. 105. A. Liver weight (g). **B.** Liver/Body ratio (%). **C.** Representative images from H&E in liver. (N = 6-10). Scale = 100 µm. Significant differences are denoted as follows: p<0.001: ***; p<0.0001: ****.

This result was confirmed by ORO staining, where DUAL W mice reduced the accumulation of lipid droplets exhibiting extent microsteatosis but not macrosteatosis **(Fig. 106A-B).** Consistently, the TG content in the liver was significantly reduced **(Fig. 106C).**

Some genes implicated in fat metabolism corroborated this result. The lipid transporter *Cd36* showed reduced expression in DUAL W group **(Fig. 106D).** Moreover, *Pparγ* expression, implicated in fat synthesis, was also decreased **(Fig. 106E)**.

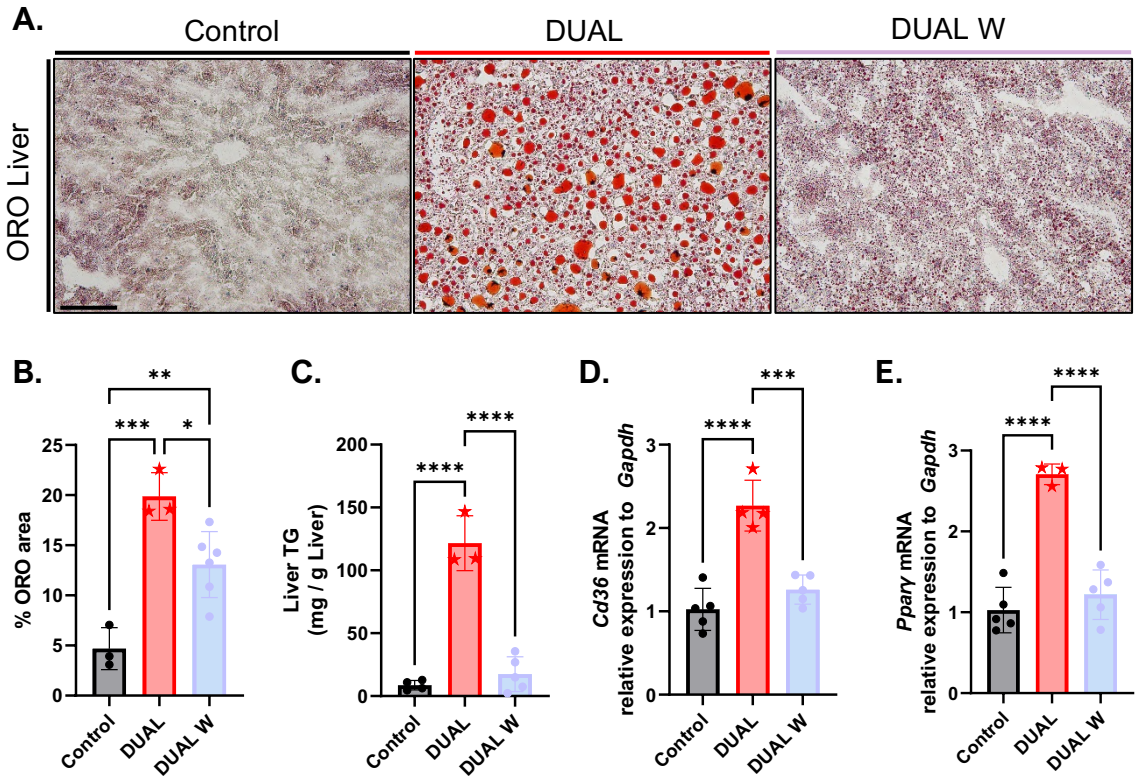

Fig. 106. A. ORO staining in liver. Scale = 100 µm. **B.** Quantification of positive-ORO area (%) using ImageJ software. (N = 3-6). **C.** TG quantification in the liver (mg/g liver). (N = 3-5). **D-E.** *Cd36* and *Ppary* relative expression in the liver determined by RT-qPCR. (N = 3-5). Significant differences are denoted as follows: p<0.05: *; p<0.01: **; p<0.001: ***; p<0.0001: ****.

Liver damage was further characterized. DUAL W mice exhibited a slight significant decrease in ALT concentration in serum **(Fig. 107A)**. However, the reduction in the levels of AST and LDH revealed no significant difference compared to DUAL-fed mice **(Fig. 107B-C).**

Consistently, DUAL W displayed a decrease in the hepatic cell death rate compared to DUAL mice, evaluated by TUNEL IF staining **(Fig. 107D-E).**

After diet withdrawal, the hepatic inflammation in DUAL mice was only slightly reduced. A significant number of $CD45^+$ $F4/80^+$ infiltrating cells was still present in liver parenchyma **(Fig. 108A-D).**

Uniformly, DUAL W was not associated with reduction in the expression of *Tlr2, 4* and *9* in the liver **(Fig. 108E-G).**

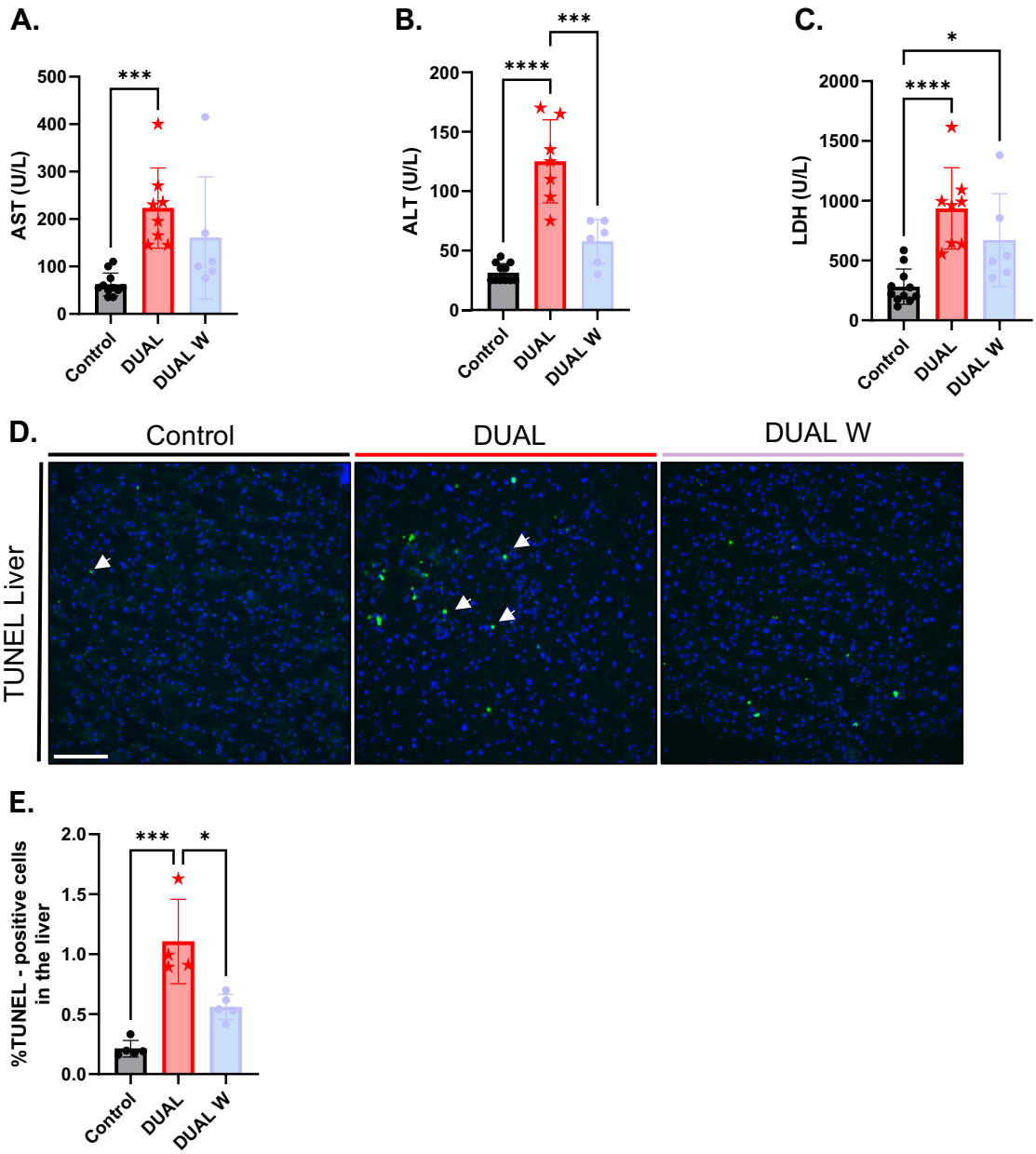

Fig. 107. A-C. ALT, AST and LDH concentration in serum (U/L). (N = 6 – 10). **D.** TUNEL IF staining in liver. Arrows show positive TUNEL cells. Scale = 100 µm. **E.** Quantification of positive TUNEL cells (%) using ImageJ software. (N = 4-6). Significant differences are denoted as follows: p<0.05: *; p<0.001: ***; p<0.0001: ****.

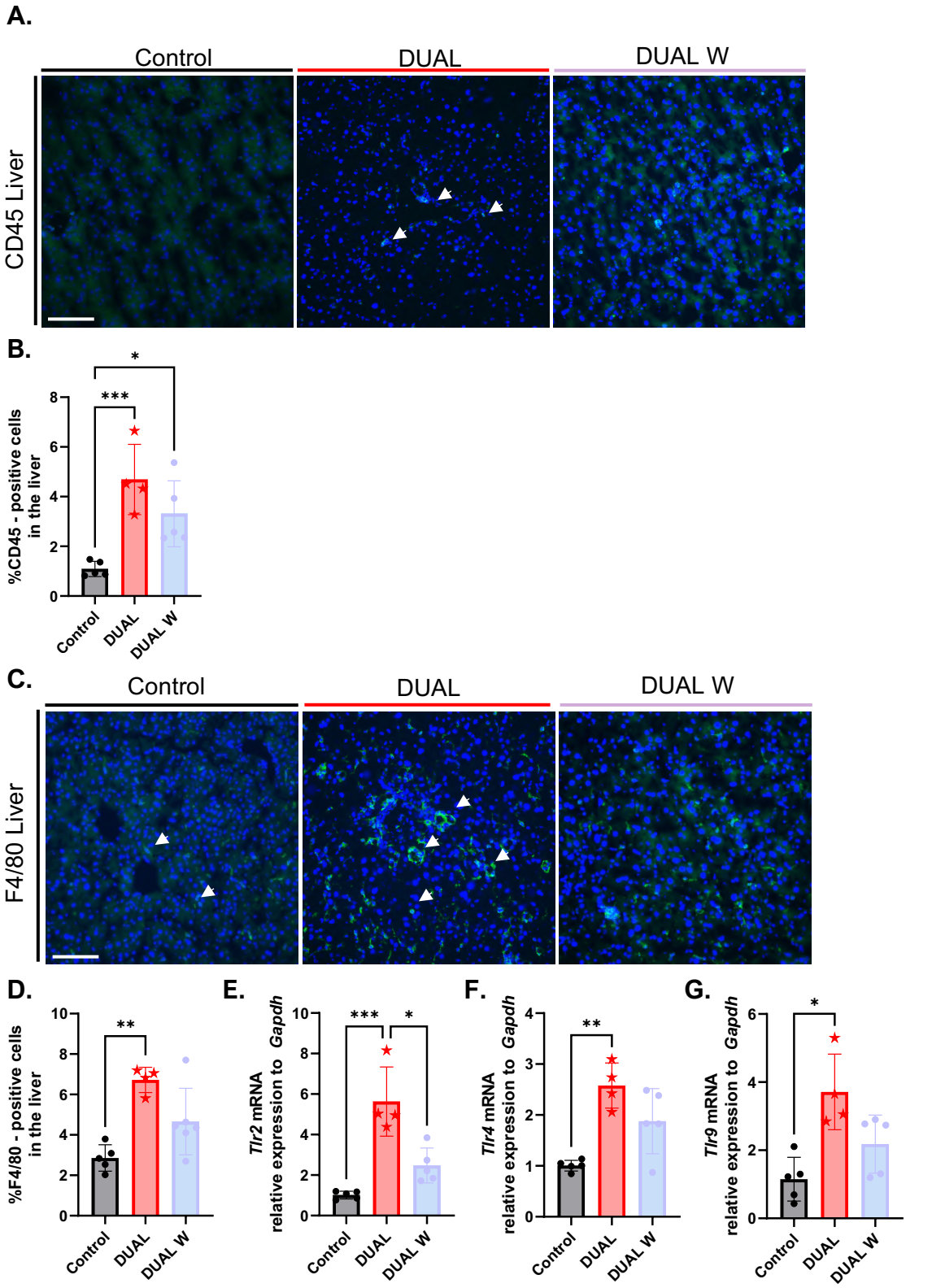

Fig. 108. A. CD45 IF staining in the liver. Arrows show CD45 positive cells. Scale = 100 µm. **B.** Quantification of positive CD45 cells (%) in the liver using ImageJ software. (N = 4-5). **C.** F4/80 IF staining in the liver. Arrows show F4/80 positive cells. Scale = 100 µm. **D.** Quantification of positive F4/80 cells (%) in the liver by ImageJ software. (N = 4-5). **E-G.** *Tlr2*, *Tlr4* and *Tlr9* mRNA relative expression to *Gapdh* was determined in the liver by RT-qPCR. (N = 4-5). Significant differences are denoted as follows: p<0.05: *; p<0.01: **; p<0.001: ***.

Lastly, liver fibrosis was identified by SR staining. DUAL W mice exhibited a reduction in the levels of liver fibrosis that were significantly different from DUAL mice **(Fig. 109A-B).** According to the latest results, we found a decrease in the *CollagenI* expression after DUAL withdrawal **(Fig. 109C).**

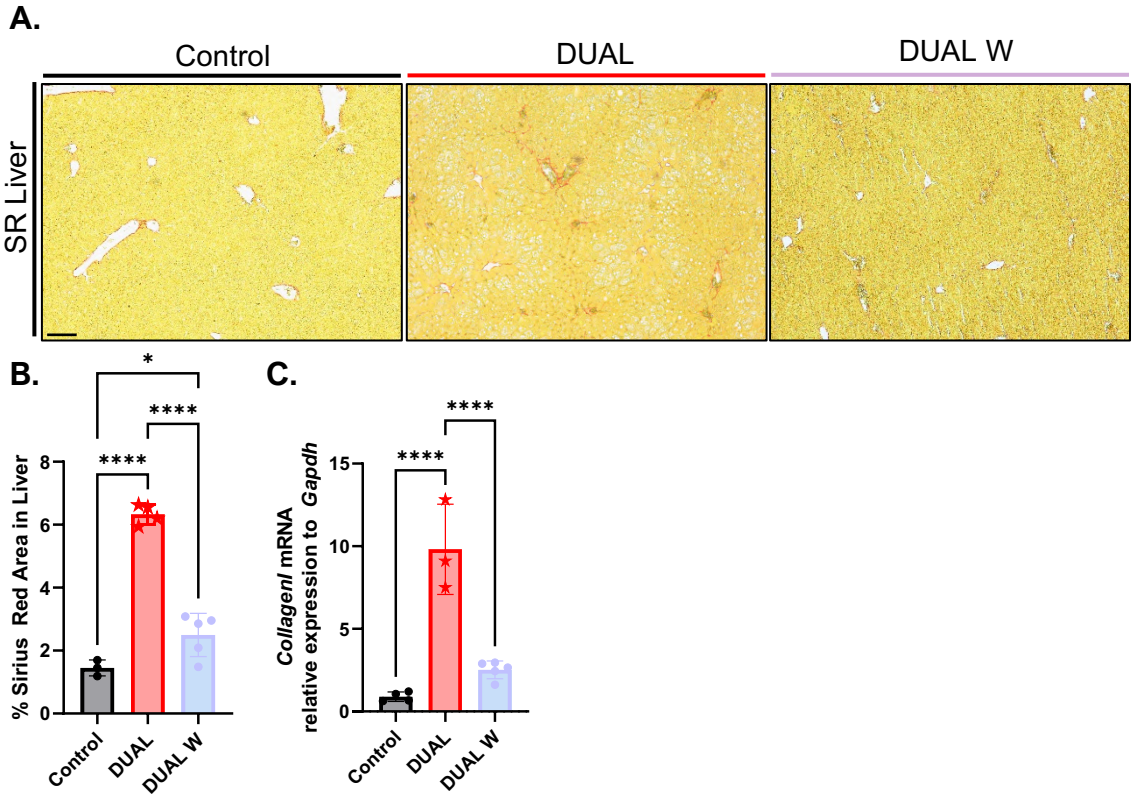

Fig. 109. A. SR staining in the liver. Scale = 100 µm. **B.** Quantification positive SR area (%) though ImageJ software. (N = 3-5). **C.** *CollagenI* mRNA relative expression to *Gapdh* in the liver was quantified though RT-qPCR. (N = 3-5). Significant differences are denoted as follows: p<0.05: *; p<0.0001: ****.

7.28. DUAL WITHDRAWAL AMELIORATED COLON INFLAMMATION AT MACROSCOPICAL AND MICROSCOPICAL LEVEL

Next, we investigated if DUAL W could induce any beneficial effect in the colon. We found that colon/mouse length ratio partially recovered to the control levels and the colon length increased **(Fig. 110A-B).** Moreover, the colonic crypts were bigger in DUAL W than in DUAL mice **(Fig. 110C).**

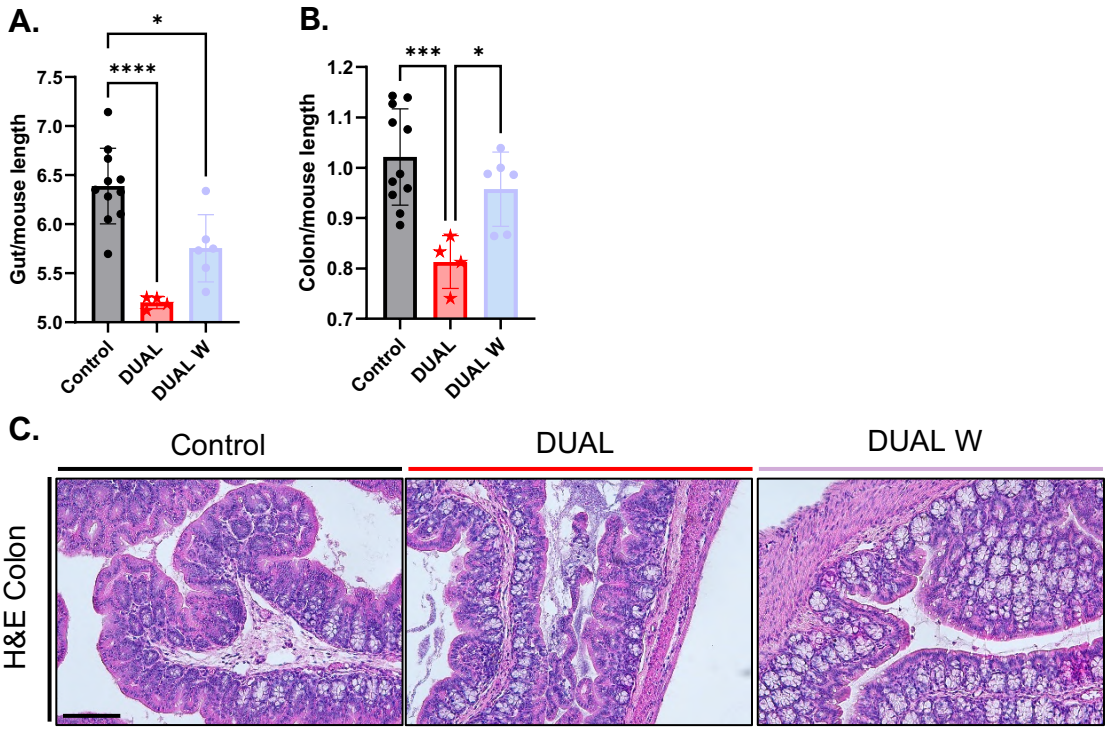

Fig. 110. A. Gut/mouse length ratio (cm/cm). **B.** Colon/mouse length ratio (cm/cm). **C.** Representative images from H&E in colon. (N = 4-10). Scale = 100 µm. Significant differences are denoted as follows: p<0.05: *; p<0.01: **; p<0.001: ***; p<0.0001: ****.

7.29. DUAL WITHDRAWAL REINFORCED THE GUT BARRIER

Finally, we decided to evaluate how DUAL withdrawal affected the gut barriers. We observed that the mucus layer was partially recovered as DUAL W mice exhibited higher levels of MUC2 protein **(Fig. 111A-B).** Besides, the levels of ZO-1 expression were also significantly increased after diet withdrawal **(Fig. 111C-D).**

Consistently, the levels of FITC-Dextran in the serum of DUAL W mice, showed a decreasing tendency, suggesting a restoration of gut barrier and an improvement of the intestinal permeability **(Fig. 112A).**

7.30. DUAL WITHDRAWAL AND FMT ARE THE BEST THERAPEUTIC OPTION FOR CLD INDUCED BY SHORT TERM DUAL FEEDING

After evaluating all therapeutic options, we found that the application of ABX returned the liver physiology to control levels. However, their impact was not strong enough to improve the extrahepatic features.

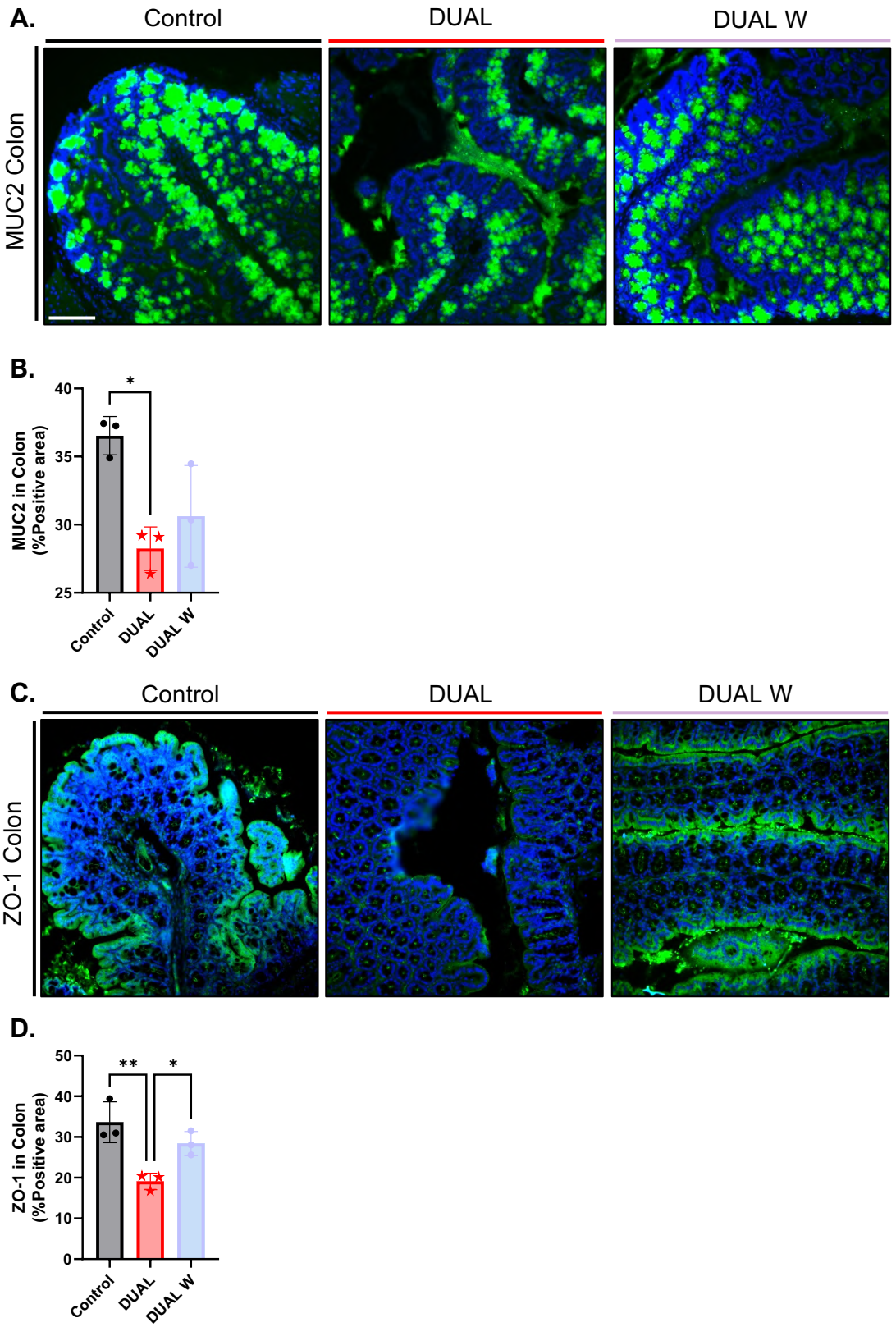

Fig. 111. A. MUC2 IF staining in colon, representative pictures. **B.** Quantification of positive MUC2 stained area (%) using ImageJ software. (N = 3). **C.** ZO-1 IF staining in colon. Scale = 100 µm. **D.** Quantification of positive ZO-1-stained area (%) using ImageJ software. (N = 3). Significant differences are denoted as follows: $p<0.05$: *; $p<0.01$: **.

A.

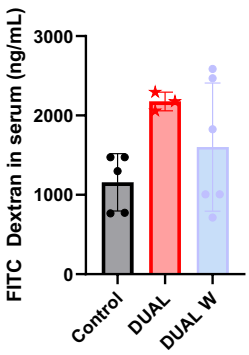

Fig. 112. A. FITC dextran concentration in serum (ng/mL). (N = 3-6).

FMT induced mild beneficial effects on the liver pathophysiology and gut phenotype, having less effect on the extrahepatic features.

The application of probiotics did not lead to any beneficial effect.

The DUAL W was the best therapeutic option in terms of extrahepatic and intrahepatic features: obesity was reverted and the liver phenotype was remarkably improved. Although changes in the gut were not so notable, altogether it was the most effective treatment.

7.31. FMT HAD NO EFFECT ON OBESITY IN LONG TERM DUAL FEEDING

The use of FMT in an early CLD model (10 weeks of DUAL feeding) showed mild improvement of the hepatic and intestinal phenotypes.

Our last step was to evaluate the effectiveness of microbiome modulation through FMT, maintaining the DUAL feeding but in a context of advanced CLD (23 weeks DUAL feeding), as described in **material and methods 6.2.3.5. FMT** and in **Fig. 23, 24.**

First, results showed that FMT had no effect on obesity: DUAL + FMT mice gained similar body weight **(Fig. 113A).**

Moreover, no difference was detected in WAT mass and the gWAT/Body ratio (%) between DUAL and DUAL + FMT animals **(Fig. 113B).**

In addition, the hypercholesterinemia induced by DUAL feeding remained unchanged after FMT **(Fig. 113C).**

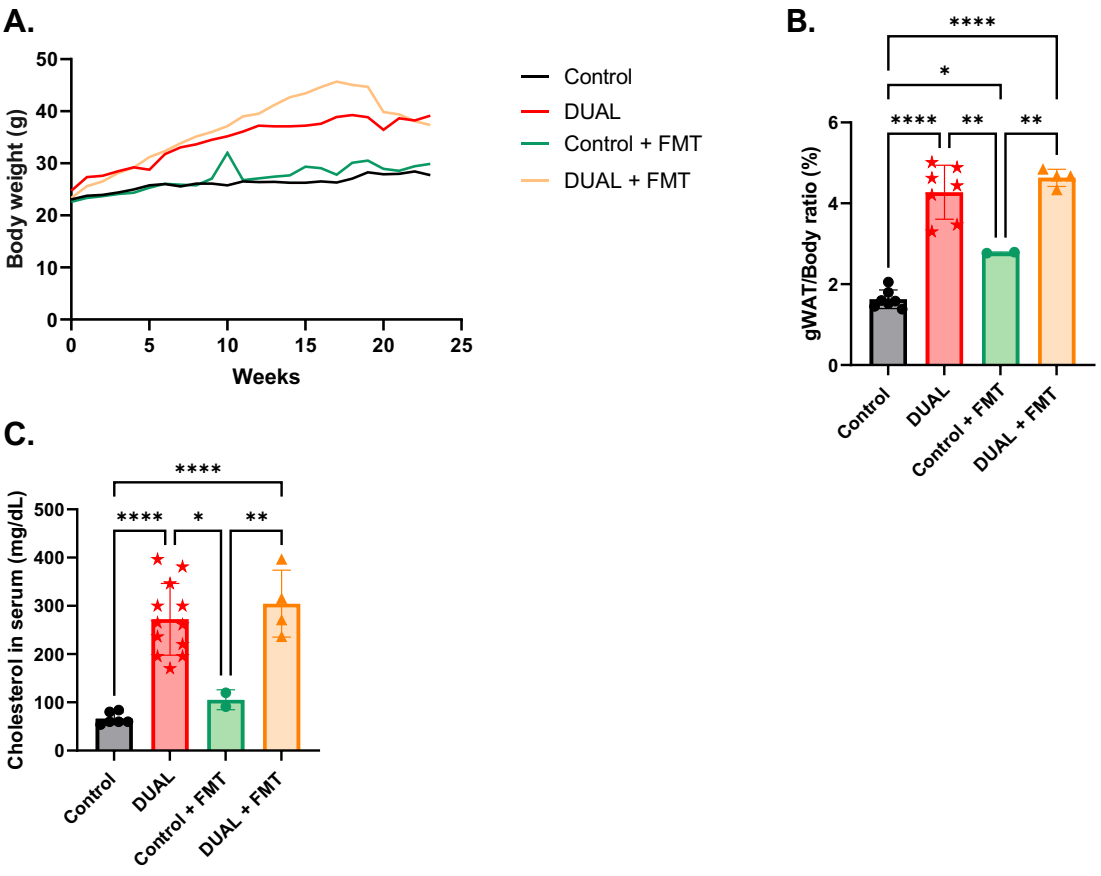

Fig. 113. A. BW recording during the 10 weeks of feeding. **B.** gWAT/Body ratio (%). **C.** Cholesterol level in serum after 12 h fasting (mg/dL). (N = 2-7). Significant differences are denoted as follows: p<0.05: *; p<0.01: **; p<0.0001: ****.

7.32. STEATOSIS, LIVER INJURY, HEPATIC INFLAMMATION AND FIBROSIS INDUCED BY LONG TERM DUAL FEEDING WERE NOT IMPROVED BY FMT

Macroscopic evaluation of the liver affirmed that FMT used in long term DUAL feeding had no effect on liver/body ratio (%) **(Fig. 114A-B)**. At a microscopical level, in the H&E staining, we could see only a little improvement in fat deposition; however, the hepatic parenchyma remained loaded by lipid droplets **(Fig. 114C).**

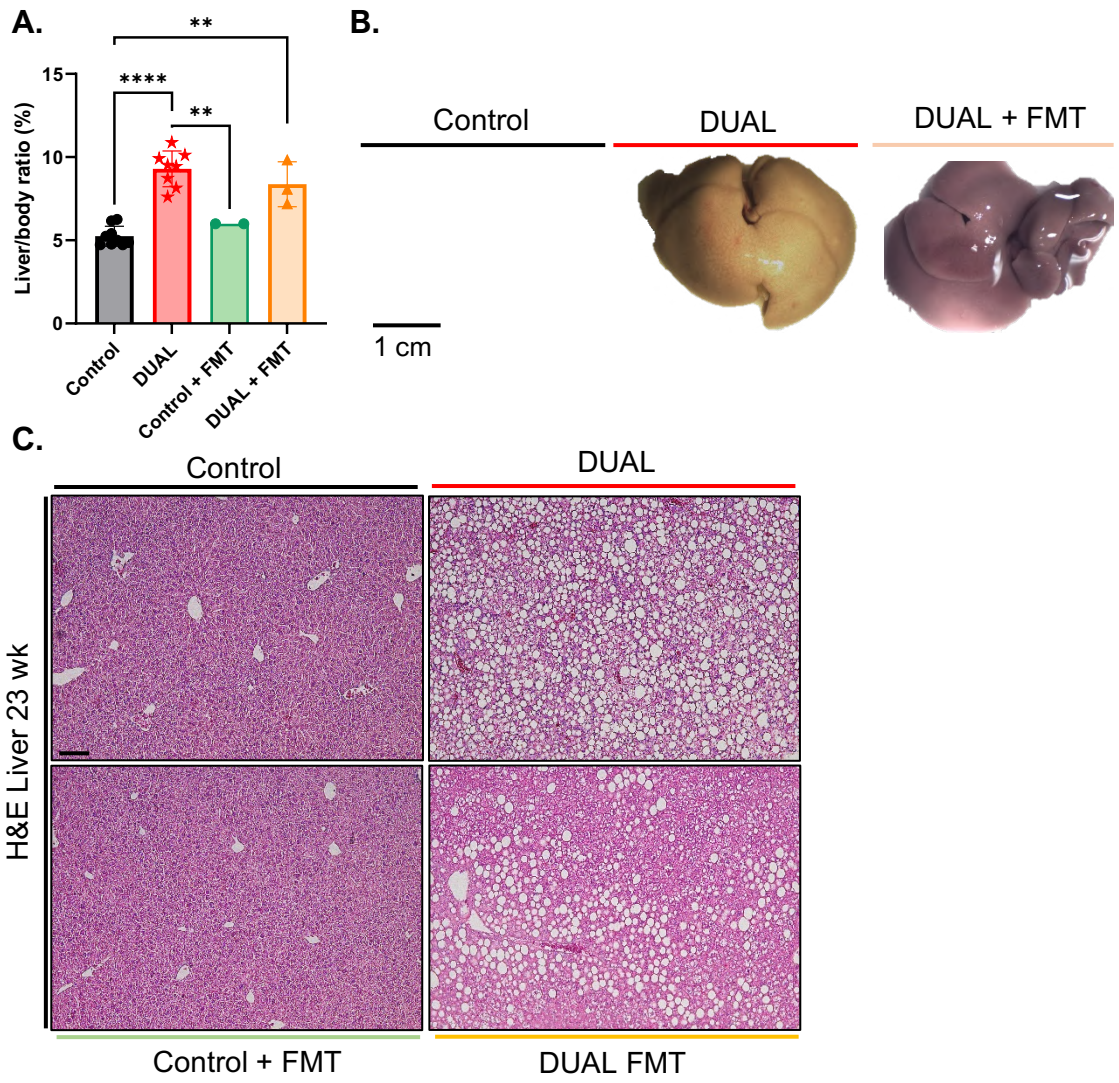

Fig. 114. A. Liver/body ratio (%) (g). (N = 2-7). **B.** Representative liver pictures. Scale = 1cm. **C.** Representative H&E-stained sections in liver. Scale = 100 µm. Significant differences are denoted as follows: p<0.01: **; p<0.0001: ****.

ORO staining further confirmed that, after FMT in long-fed DUAL mice, the intrahepatic lipid accumulation was still massive, mainly due to the microsteatosis **(Fig. 115A-B).** In line, the quantification of TG in the liver revealed no significant differences between the DUAL and DUAL + FMT animals **(Fig. 115C)**.

Next, we checked the fat transporter *Cd36* in the liver and we found that it exhibited a significant decrease after FMT in DUAL-fed animals **(Fig. 115D).** Similarly, *Pparγ,* implicated in lipid synthesis, showed a mild but not significant decrease compared to DUAL animals **(Fig. 115E)**. Importantly, no significant difference was found in CPT1-c protein expression in DUAL + FMT group **(Fig.**

115F, G). Altogether the balance between lipid uptake, oxidation and synthesis remained positive, as occurred in DUAL animals, contributing to fat accumulation.

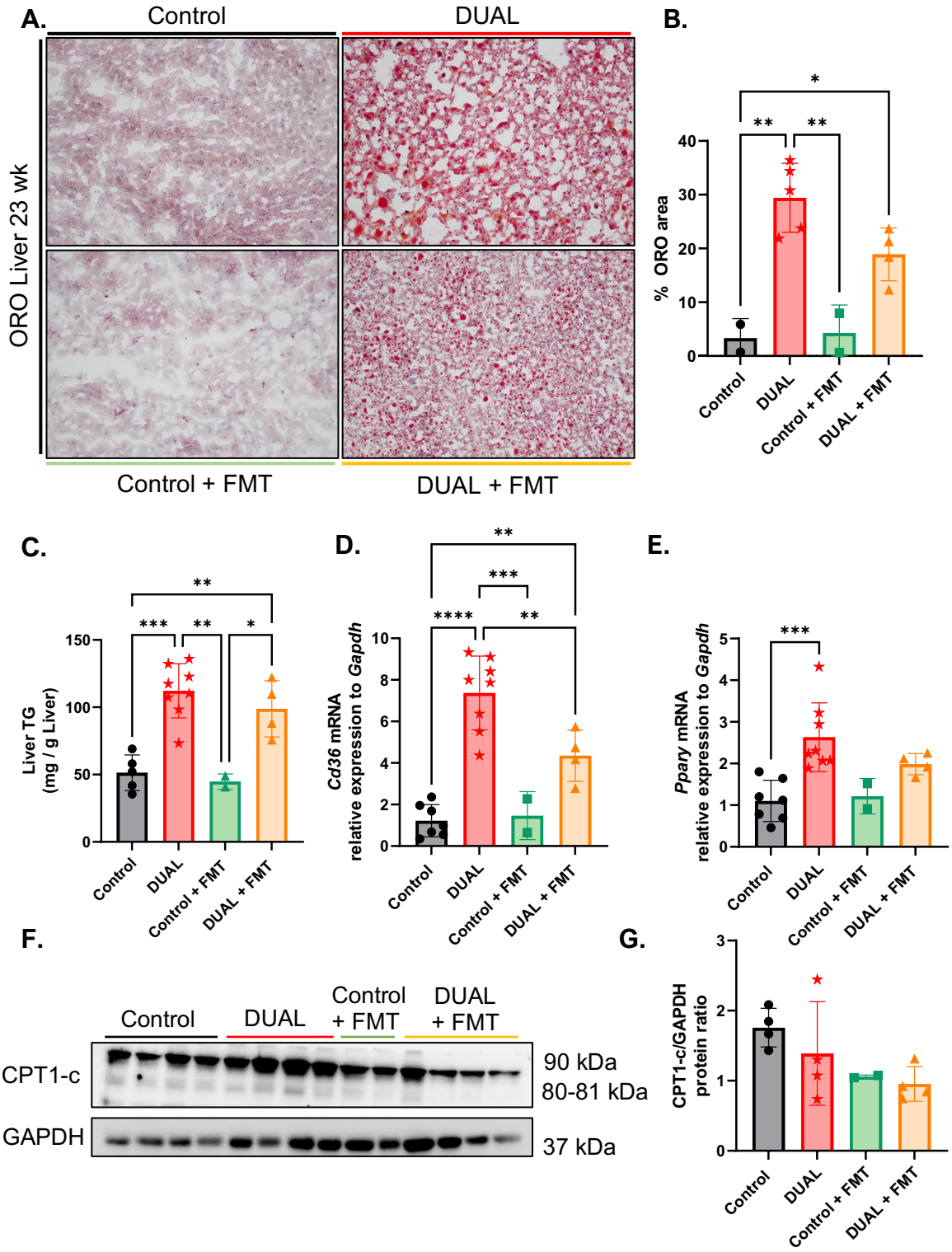

Fig. 115. A. ORO staining in liver. Scale = 100 µm. **B.** Quantification of positive-ORO area (%) using ImageJ software. (N = 2-5). **C.** TG quantification in the liver (mg/g liver). (N = 2-7). **D-E.** *Cd36* and *Ppary* relative expression in the liver determined by RT-qPCR. (N = 2-7). **F.** CPT1-c WB in the liver. GAPDH was used as a charge control. **G.** CPT1-c WB densitometry. CPT1-c/GAPDH protein ratio was calculated. (N = 2-4). Significant differences are denoted as follows: p<0.05: *; p<0.01: **; p<0.001: ***; p<0.0001: ****.

Our next step was to study the liver damage. After FMT in long-fed DUAL mice, hepatic transaminases in serum were still evaluated and no significant differences were found between DUAL and DUAL + FMT animals, although FMT revealed minor decrease **(Fig. 116A-B).** These data were further confirmed by TUNEL IF staining **(Fig. 116C-D).**

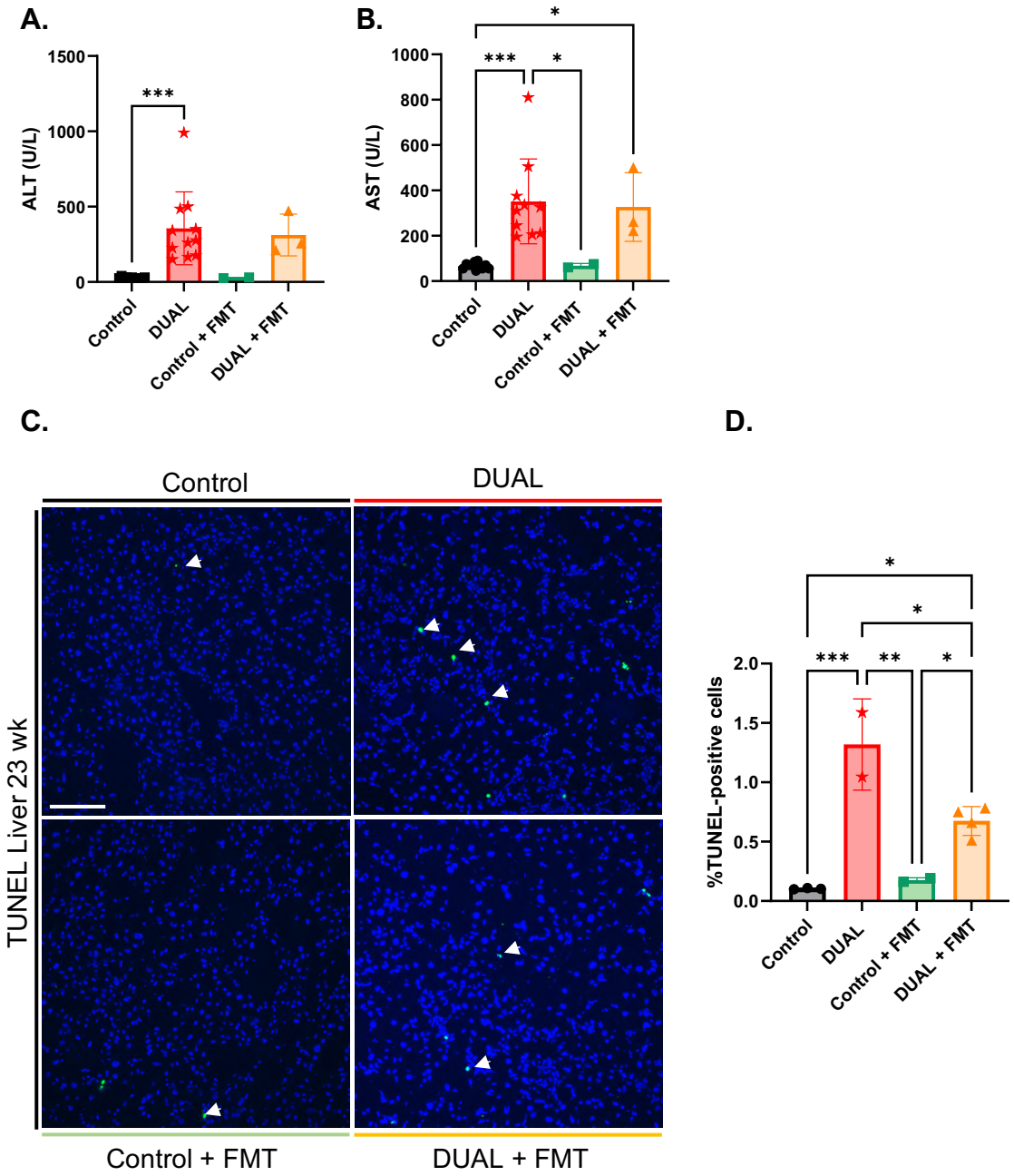

Fig. 116. A-B. ALT and AST concentration in serum (U/L). (N = 2-7). **C.** TUNEL IF staining in liver. Arrows show positive TUNEL cells. Scale = 100 μm. **D.** Quantification of positive TUNEL cells (%) using ImageJ software. (N = 2-4). Significant differences are denoted as follows: p<0.05: *; p<0.01: **; p<0.001: ***.

Consequently, the infiltrating CD45 positive immune cells in the liver remained increased in DUAL+FMT group **(Fig. 117A-B).** Consistently, the expression of *Tnf-α* was similarly increased in both DUAL and DUAL + FMT animals **(Fig. 117C).** Moreover, after FMT, the hepatic expression of *Tlr2* remained increased but the expression of *Tlr4* was slightly reduced although it was not significantly different **(Fig. 117D-E)** compared to DUAL fed animals.

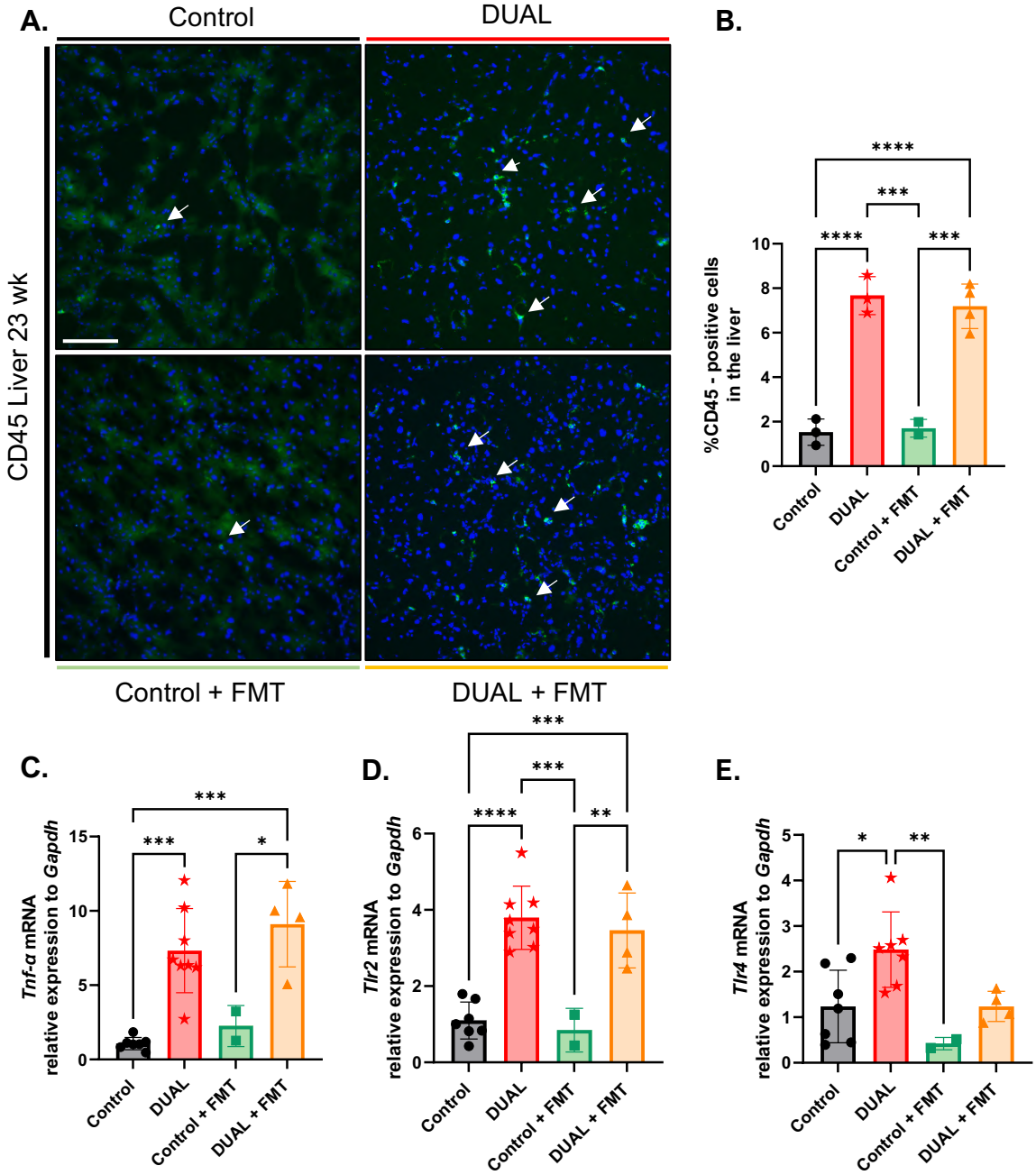

Fig. 117. A. CD45 IF staining in the liver. Arrows show positive CD45 cells. **B.** Quantification of positive CD45 cells (%) in the liver using ImageJ software. (N = 2-4). **C-E.** *Tnf-α, Tlr2*, and *Tlr4* mRNA relative expression to *Gapdh* was determined in the liver by RT-qPCR. (N = 2-7). Significant differences are denoted as follows: p<0.05: *; p<0.01: **; p<0.001: ***; p<0.0001: ****.

Altogether, after FMT in long term DUAL feeding, the inflammation remained increased, showing in most of the experiments any significant reduction compared to DUAL animals.

The quantification of SR staining in liver after long-term DUAL feeding revealed no differences in collagen fiber deposition between DUAL and DUAL + FMT mice **(Fig. 118A-B).** The increased expression of hepatic *Collagenl* in both DUAL and DUAL + FMT mice confirmed this result **(Fig. 118C).**

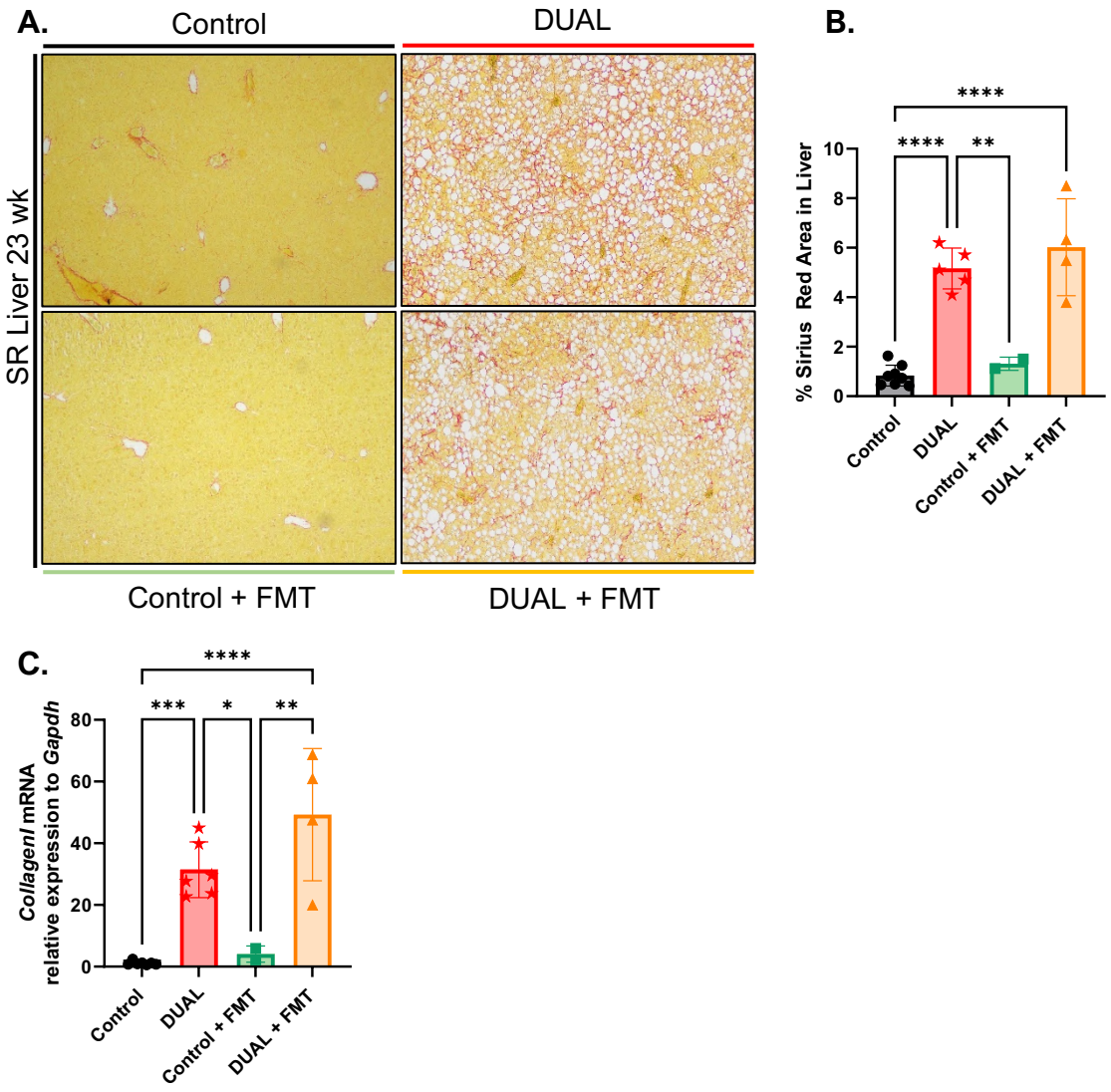

Fig. 118. A. SR staining in the liver. Scale = 100 µm. **B.** Quantification of positive SR area (%) though ImageJ software. (N = 2-7). **C.** *Collagenl* mRNA relative expression to *Gapdh* in the liver was quantified through RT-qPCR. (N = 2-6). Significant differences are denoted as follows: p<0.05: *; p<0.01: **; p<0.001: ***; p<0.0001: ****.

7.33. FMT DID NOT INDUCE ANY PHENOTYPICAL CHANGES IN COLON OF LONG-TERM DUAL-FED ANIMALS

Lastly, we decided to evaluate if FMT application to long DUAL feeding could induce any improvement in colon morphology. Macroscopically, colon remained as short as it was after 23 weeks DUAL diet **(Fig. 119A-B).** Moreover, we did not detect any visual differences in colonic H&E staining **(Fig. 119C).**

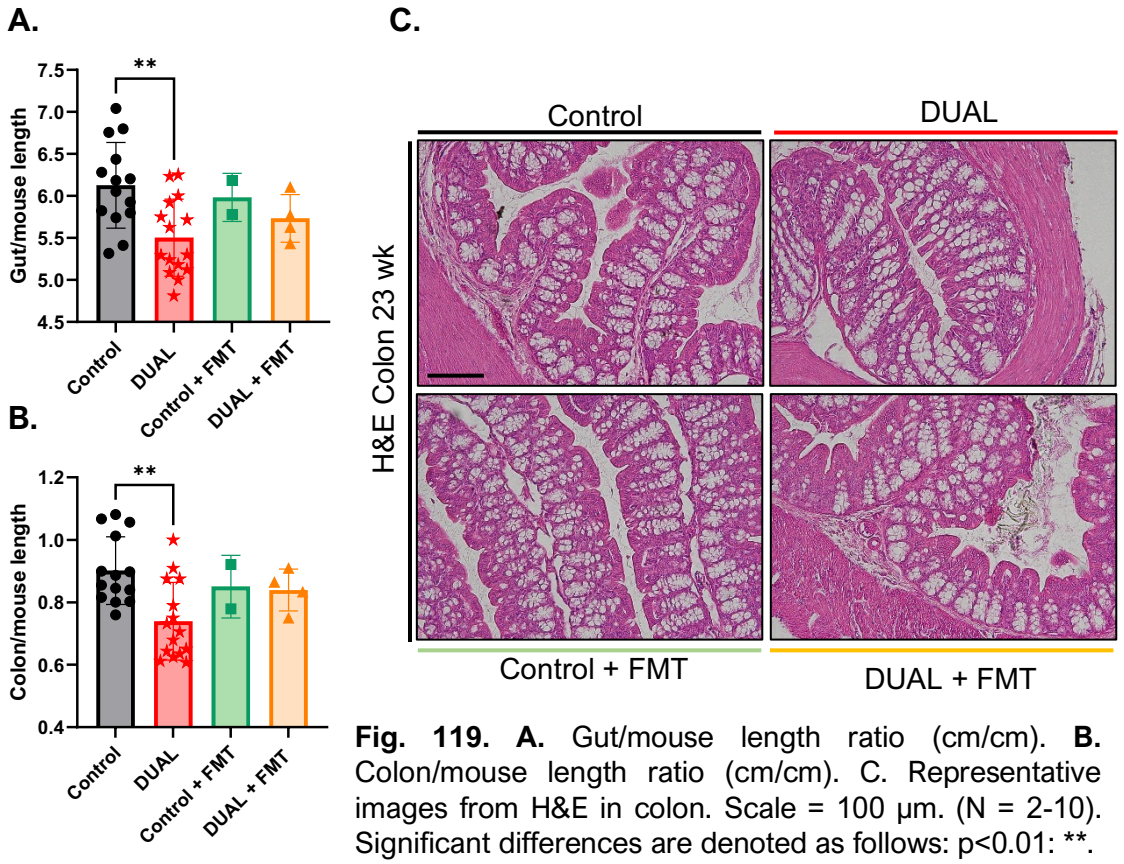

Fig. 119. A. Gut/mouse length ratio (cm/cm). **B.** Colon/mouse length ratio (cm/cm). C. Representative images from H&E in colon. Scale = 100 µm. (N = 2-10). Significant differences are denoted as follows: p<0.01: **.

Then we decided to evaluate the inflammatory stage in colon after FMT and we found no significant differences in the levels of T-($CD3^+$ in $CD45^+$) or B ($CD19^+$ in $CD45^+$) lymphocytes. Additionally, T helper lymphocytes ($CD4^+$ in $CD3^+$) remained increased as well as the cytotoxic lymphocytes ($CD8^+$ in $CD3^+$) in DUAL and DUAL + FMT groups. **(Fig. 120A-E).**

Although the levels of effector cells remained unchanged compared to DUAL diet, we found no significant changes in γδ-cells ($TCR\delta^+$ in $CD3^+$) compared to controls. Treg cells ($FOXP3^+$ in $CD3^+$) showed an increase compared to DUAL and control animals **(Fig. 120F-G).** The increased population of Treg has been

described in association with chronic intestinal inflammation or tolerogenic responses to microbiome - two potential hypothesis that could be considered in DUAL + FMT animals (226).

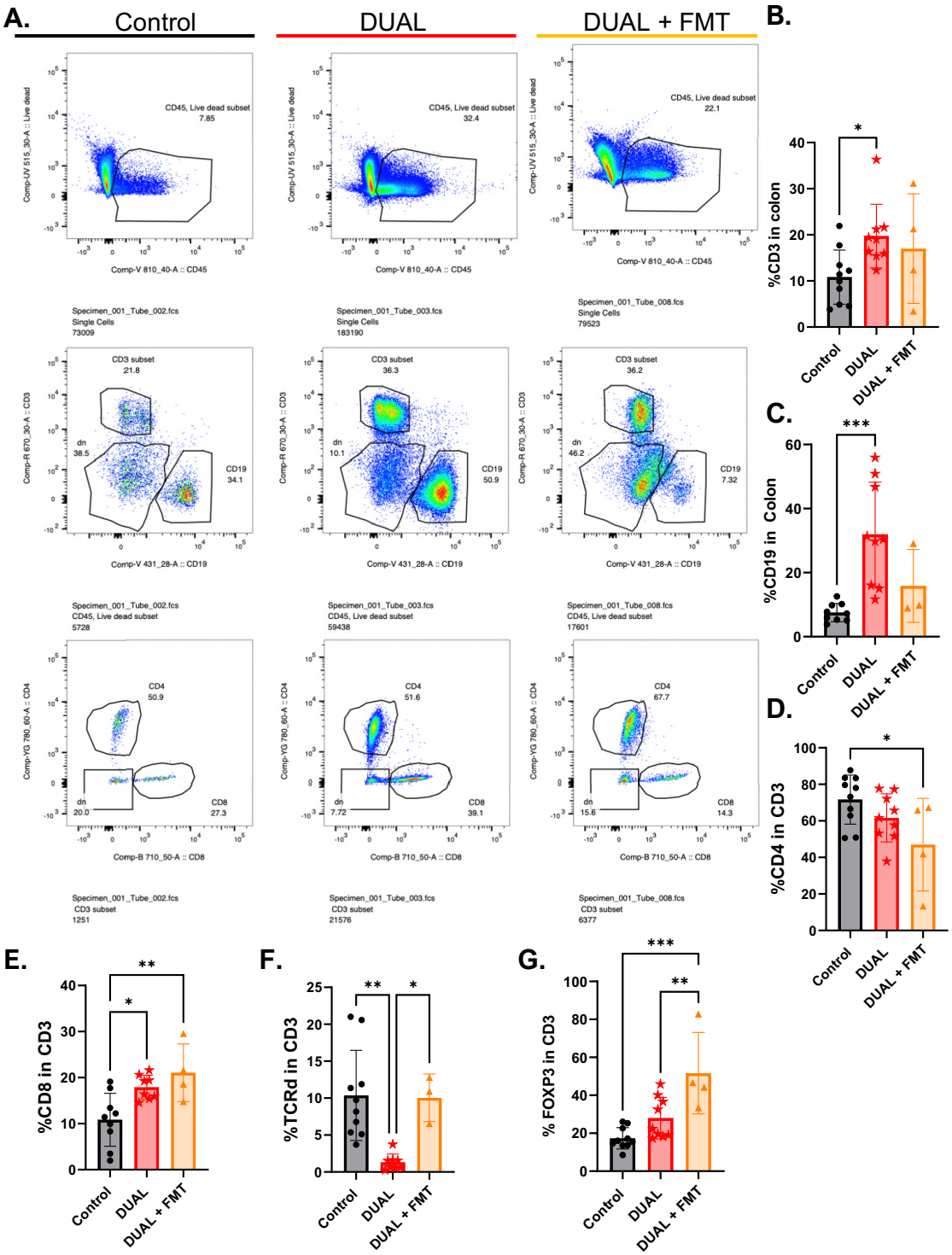

Fig. 120. A. Flow cytometry dot plots in colon. (N = 4-9). **B.** %CD3 in CD45 in colon. **C.** %CD19 in CD45 in colon. **D.** %CD4 in CD3. **E.** %CD8 in CD3. **F.** %TCRd in CD3. **G.** %FOXP3 in CD3. Significant differences are denoted as follows: p<0.05: *; p<0.01: **; p<0.001: ***.

Finally, we decided to investigate if FMT in 23 weeks DUAL feeding could have any beneficial effects on the gut barrier and, consequently, improve gut permeability. MUC2 IF staining revealed no significant difference after FMT in comparison to DUAL-fed mice **(Fig. 121A-B).**

At the TJs level, we found a slight but significant increase in the levels of ZO-1 expression after FMT **(Fig. 121C-D)**. Consequently, analysis of the intestinal permeability by FITC Dextran revealed no difference between DUAL and DUAL+FMT mice **(Fig. 121E).**

The attempt to modify the microbiome using FMT for long-term DUAL feeding exhibiting CLD did not produce remarkable improvements in either the liver or the intestine. As a result, the liver continued to exhibit signs of steatohepatitis and fibrosis, while the gut permeability remained elevated DUAL + FMT animals.

7.34. DUAL WITHDRAWAL AFTER LONG-TERM DUAL FEEDING SLIGHTLY AMELIORED LIVER PHYSIOLOGY

As a final step, we decided to evaluate if DUAL withdrawal could have any beneficial effect on advanced CLD induced by long term DUAL feeding. 10-week-old C57BL/6J male mice were fed with DUAL diet. After 23 weeks of DUAL feeding, treatment was replaced by normal filtered water and regular chow diet for 21 more days as described in **material and methods section 6.2.3.6. DUAL withdrawal (Fig. 25).**

When we evaluated hepatic steatosis and some genes related to lipid metabolism, such as *Cd36* and *Pparγ,* a significant reduction was observed compared to DUAL animals **(Fig. 122A, B)**. However, the levels remained significantly different contrasted to controls.

In terms of hepatic inflammation, we observed a depletion in the expression of *Tnfα and Tlr2* compared to DUAL animals; nevertheless, levels of both genes remained increased in comparison to the control group **(Fig. 122C-E)**. The levels of *Tlr4* after DUAL withdrawal were significantly reduced and reached the control levels.

At last, the hepatic expression of the fibrosis related gene *CollagenI* was slightly decreased after DUAL withdrawal **(Fig. 122F).**

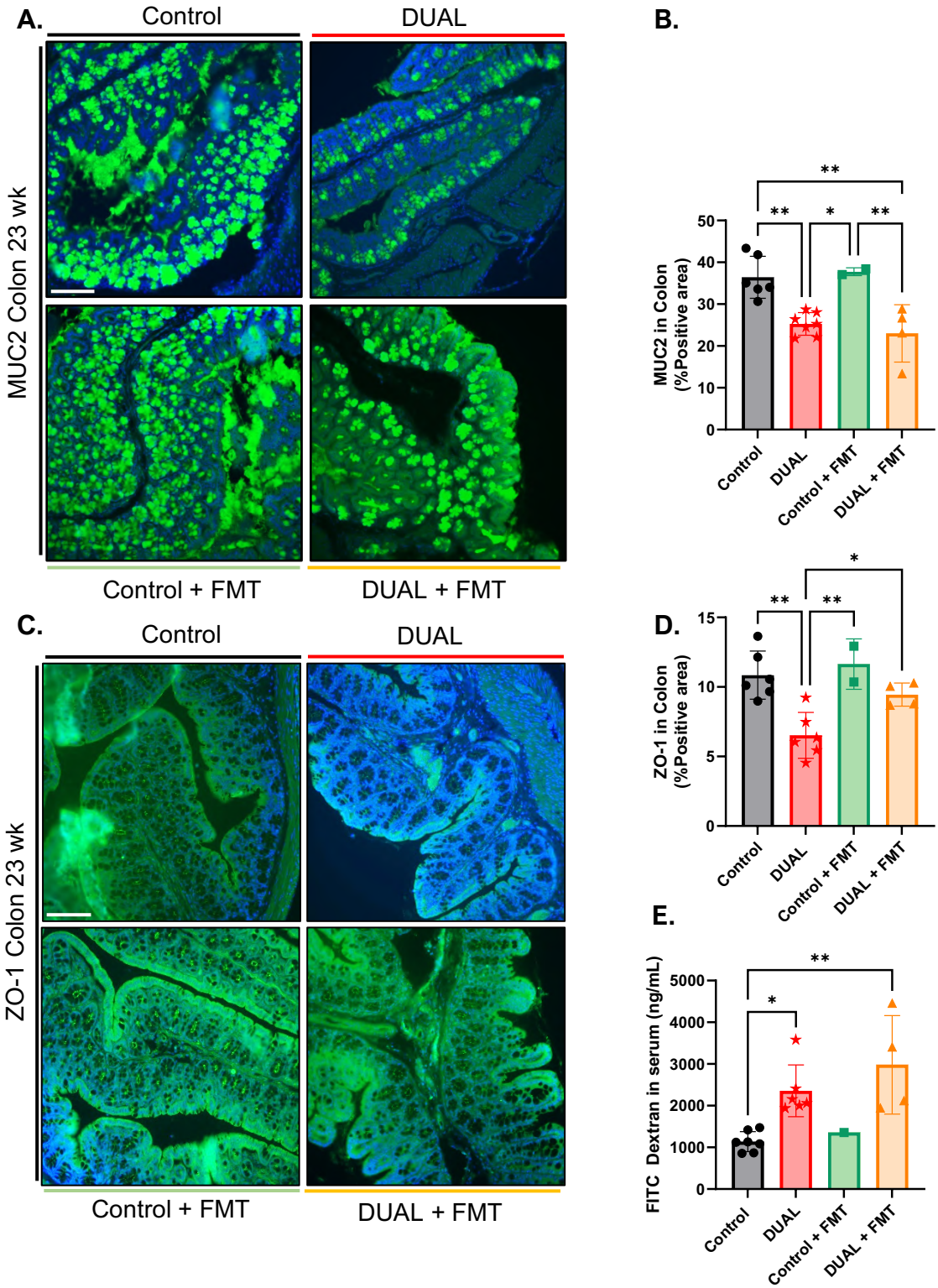

Fig. 121. A. MUC2 IF staining in colon, representative pictures. **B.** Quantification of positive MUC2 stained area (%) using ImageJ software. (N = 2-7). **C.** ZO-1 IF staining in colon. Scale = 100 µm. **D.** Quantification of positive ZO-1-stained area (%) using ImageJ software. (N = 2-6). **E.** FITC dextran concentration in serum (ng/mL). (N = 2-6). Significant differences are denoted as follows: p<0.05: *; p<0.01: **.

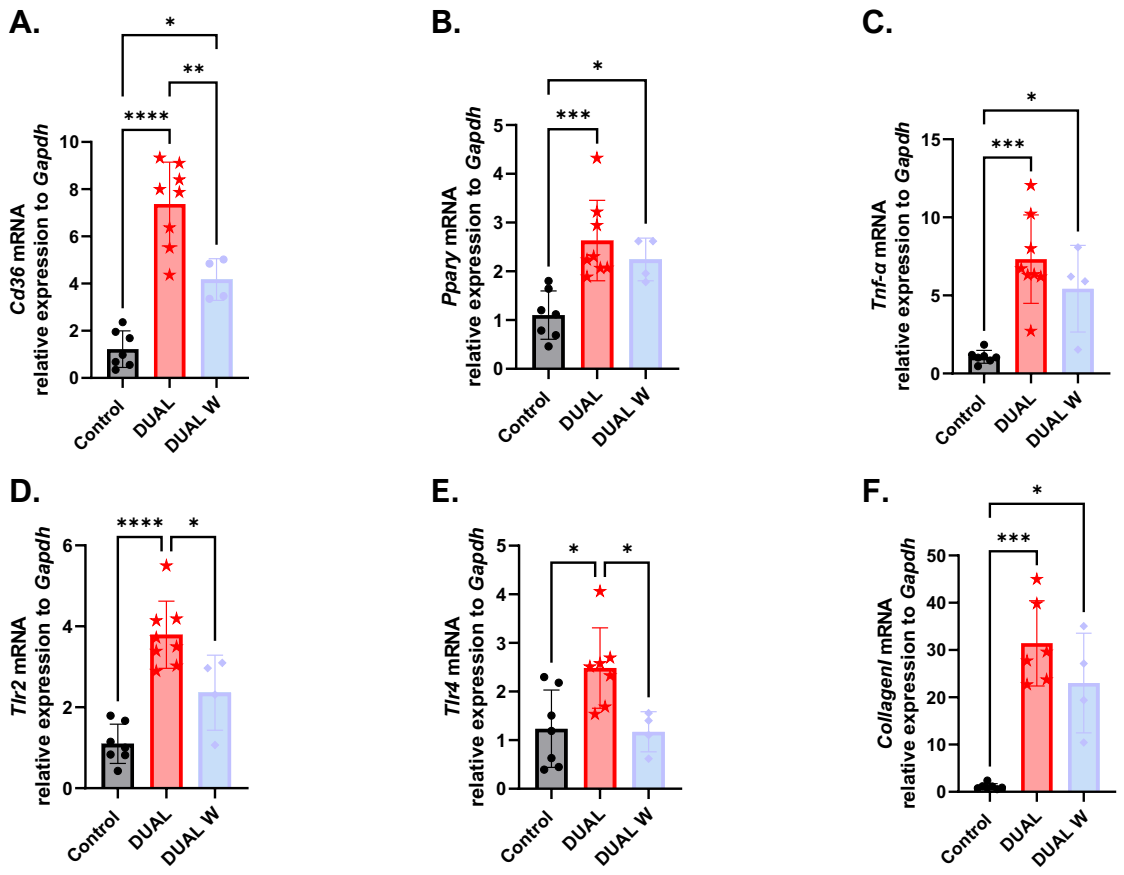

Fig. 122. A-F. *Cd36, Ppary, Tlr2, Tlr4, CollagenI* mRNA relative expression to *Gapdh* was determined in liver tissue by RT-qPCR (N = 4-8). Significant differences are denoted as follows: p<0.05: *; p<0.001: ***; p<0.0001: ****.

Thus, although DUAL W looked a putative therapeutical option, beneficial effects resulted insufficient in cases of advanced CLD.

Discussion

8. DISCUSSION

Approximately 2 billion people worldwide consume alcohol, and among them, up to 75 million individuals are diagnosed with alcohol use disorders and face high risk of developing ALD (227). Furthermore, modern societies have adopted unhealthy fast food habits that significantly contribute to weight gain and the subsequent development of NAFLD (228). Recent data suggest that between 30-70% of the population is overweight (229). As a result, it is highly probable that some individuals experience an overlap between poor dietary habits, patterns of alcohol consumption, and high caloric intake. Additionally, it is common for individuals to combine high-calorie meals with moderate and regular alcohol consumption (46).

Notably, the hepatotoxicity (liver-damaging effects) of alcohol is doubled for patients with a BMI exceeding 35 kg/m^2 (227). Recent epidemiological and experimental evidence has emphasized the perilous synergistic relationship between alcohol, obesity, and MS in the progression of CLD (230, 231, 232). Research indicates that one of these factors often takes precedence while the other contributes as a cofactor for morbidity and mortality (197).

Hence, a new animal model that faithfully reproduces all the extrahepatic and intrahepatic features of dual etiology CLD would help to understand the synergistic effect of alcohol and MS.

In our study, we developed a physiological experimental model in mice that mimics human dietary habits by combining WD (high- fat, fructose and cholesterol) and alcohol administration.

While some hybrid models have been proposed previously (233, 234), most of them have certain limitations and fail to fully replicate all the physiological, metabolic, histological and clinical characteristics of human steatohepatitis, including hepatic inflammation and advanced fibrosis (144, 235). This is primarily due to the inherent aversion mice have towards alcohol, resulting in mice consuming much less alcohol when it is provided in their drinking water. Consequently, the mice only experience moderate steatosis but not significant liver damage (236).

In our DUAL model, alcohol flavor was masked by adding 6.75% D-glucose into the EtOH drinking water.

To induce steatohepatitis, we used a WD consisting of 40% fat, 22% fructose, and 2% cholesterol. The inclusion of glucose in the drinking water enhanced the absorption of fructose from the diet. Meanwhile, fructose facilitated glucose uptake and storage in the liver. This combination led to a more pronounced detrimental effect (237).

An important aspect of our model was the incorporation of D-glucose in the water, which helped overcome the mice's aversion to alcohol. By sweetening the water, we masked the taste of alcohol, resulting in increased alcohol consumption. DUAL animals consumed 32.2 g/kg of alcohol per day, surpassing the threshold that has been established to consider ALD and high risk of alcohol-related cirrhosis in humans (25 g/kg/day) (238). Furthermore, the consumption of WD augmented alcohol intake. Previous studies have suggested a positive correlation between ethanol and fat, wherein each nutrient stimulates the consumption of the other. This synergistic vicious cycle can significantly increase calorie intake (178).

Consequently, upon initiating the DUAL diet, the mice began to experience body weight gain and developed obesity, as indicated by an increase in the BMI. After 23 weeks, the DUAL group was 19% heavier compared to the control group. It is worth noting that abdominal obesity is a predominant risk factor for MS (181). Alongside obesity, the DUAL animals also developed dyslipidemia and hyperglycemia, three significant medical conditions associated with MS (239). However, it is important to highlight that impaired fasting glycemia in the DUAL mice did not coincide with glucose intolerance or IR. In fact, the area under the curve during the ITT was significantly lower in the DUAL diet- treated animals compared to the controls. Nevertheless, interpreting this as enhanced insulin action would be an erroneous explanation of the results. We believe that the DUAL mice exhibited a defect in the counter-regulatory response to insulin, particularly in terms of gluconeogenesis (240).

Another significant characteristic of DUAL-induced obesity is the notable damage observed in WAT. The hypertrophic adipocytes undergo inflammatory changes and crown like structures surrounding necrotic adipocytes were identified.

Adipocyte death and subsequent inflammation contributed to increased lipolysis, lipid flux to the liver and production of pro-inflammatory cytokines that play a substantial role in the progression of the disease (179, 197).

Hepatic steatosis induced by the DUAL diet was rapidly developed. Within a relatively short period of feeding, there was a significant influx of FFAs into the liver confirmed by *Cd36* upregulation.

The metabolomic analysis helped us to understand the fate of lipids in the liver. The concentrations of MUFA (products SCD-1 enzyme) were significantly elevated in DUAL mice. It is well known that MUFA are preferentially incorporated into TG and thus play a significant role in TG synthesis and intrahepatic lipid deposition (241). However, not only TG, but also high DG content was accumulated in DUAL livers which has been previously reported in association with hepatic IR and lipid metabolism imbalance (17, 242).

Deficiency in the lipid export was identified by a diminution of PC content. The decreased PC level has been described in both ALD and NAFLD as an important contributor to TG accumulation in the hepatic parenchyma (108). The lipidomic study in DUAL liver revealed low PC (22:6)/PC and PC(20:4)/PE(20:4) ratios, which indicates a reduced activity of PEMT - an essential enzyme for VLDL assembly.

Moreover, due to insufficient β-oxidation, lipid accumulation became significant and continued to increase gradually over time. As a result, DUAL mice exhibited remarkable micro and macrovesicular steatosis, accompanied by hepatocyte ballooning.

Conjugated and unconjugated cholesterol accumulation was also identified in DUAL livers. Cholesterol esters (a non-toxic path to store cholesterol) were depleted in DUAL livers whereas FC, known to be highly cytotoxic, was augmented (243, 244). Besides, as a result of poor VLDL secretion, cholesterol export was disrupted, contributing to its accumulation.

The excessive accumulation of lipids in adipose tissue and liver is the result of elevated intestinal nutrient absorption of energy-dense foods (rich in lipids and sugars) (187). The DUAL mice exhibited an enhanced ability to absorb fat in the intestine, which prompted obesity and hepatic lipid accumulation.

BAs are the central player in intestinal lipid absorption: they not only emulsify dietary fats, but also function as important signaling molecules that regulate metabolism by modulating nuclear and membrane receptors (245). Consequently, disruptions in the BA cycle have been observed in many CLD (246).

FXR is the most important nuclear receptor for maintaining BA homeostasis. It is predominantly found in the small intestine and liver. Under normal conditions BAs act as endogenous ligands that activate FXR signaling, which in turn, suppresses their own synthesis (247). However, under a disease state, FXR signaling in the liver can be altered or diminished, leading to various consequences that were examined in detail in our DUAL mouse model.

FXR depletion in the small intestine and subsequently liver resulted in a reduced expression of BSEP, the export pump from hepatocytes to bile canaliculi. However, no pathological accumulation of BAs was detected in DUAL livers, indicating that the bile synthesis remained unaffected, and the export rated was not hindered by the feeding.

FXR signaling in the intestine acts as a negative regulator of ASBT (245). Thus, FXR downregulation detected in DUAL animals lead to ASBT activation, which contributed to the internalization of BAs into the enterocytes. *Ost-α* and *Ost-β* expression remained unchanged, ensuring bile salt flow to the bloodstream. Deficient transportation of BA into hepatocytes carried by NTCP finally resulted in increased serum BA concentrations.

The moderate increase in BAs in serum can have detrimental effects on lipid, glucose, and energy metabolism (248, 249). BAs are recognized as metabolic integrators of lipid and glucose metabolism and energy expenditure within the enterohepatic circulation. Some studies have linked altered BA plasma levels to obesity and IR. Moreover, BAs modulate TG production by inhibiting hepatic fatty acid and TG biosynthesis through the BAs-FXR-SHP-Srebp1c pathway, and stimulate fatty acid oxidation *via* the BAs-FXR-PPARα pathway (248). However, the retention of BAs in the serum, along with FXR depletion, had the opposite effect in DUAL livers: increased TG production and reduced lipid oxidation.

Altogether, the elevated lipid accumulation in the liver disrupted metabolic regulation, leading to oxidative stress, triggering cell death, inflammation, and the infiltration of immune cells into the liver tissue.

The contribution of immune cells to the development of NAFLD has been mainly explored in human and multiple mouse models, and it is highly consistent with immune cell infiltration landscape in DUAL livers.

Significant alterations have been described in the myeloid compartment, with a notable increase in monocytes and monocyte-derived cells (250). Similarly, in our DUAL model, monocytes were rapidly recruited to the liver, where they can differentiate into pro-inflammatory macrophages or lead to monocyte-derived KCs (251).

Early-NASH predominantly exhibits neutrophil accumulation and increases in innate-like T cells, such as NKT cells, in both mice and humans (250). Dendritic cell (DC) activation has been described to promote liver inflammation potentially by activating $CD8^+$ T cells and contributing to hepatic injury during NASH. Additionally, B cells, in particular IgA+ plasma cells, also contribute to NASH by promoting liver inflammation, injury, and fibrosis. Moreover, IgA+ plasma cells can drive the progression to HCC through their immunosuppressive effects by inducing $CD8^+$ T cells exhaustion (250). Consistently, in DUAL livers, we detected significantly increased populations of $CD3^+/CD8^+$ T-lymphocytes.

In addition, the loss of $CD4^+$ T cells, found in DUAL animals, has been linked to cytotoxic effects mediated by fatty acids. The loss of $CD4^+$ T cells restricts their antitumor potential and favors the progression from NASH to HCC (250).

Furthermore, the upregulation of TNF-α and NF-κβ in DUAL animals closely mirrors the pathogenesis of human-like steatohepatitis and correlates with disease progression towards advanced fibrosis (252).

DUAL mice exhibited similarities to human disease, not only in the initiation of steatohepatitis, but also in the progression towards fibrosis, cirrhosis, and tumorigenesis.

Immune cells such as TNF-α-producing cells contributed to the activation of HSCs and stimulated the production of collagen fibers and the deposition of ECM in the liver, thereby promoting fibrogenesis (196). DUAL diet-fed mice developed

steatohepatitis as early as 10 weeks, and after 23 weeks of feeding, they progress to a more fibrotic stage, particularly affecting the portal and bridging areas of the liver.

Following one year of being on the DUAL diet, the animals displayed significant accumulation of collagen and the development of cirrhotic micronodules.

The DUAL diet described in this study also served as an effective promoter of liver tumorigenesis induced by DEN in mice. Remarkably, preneoplastic nodules develop within a relatively short period of 26 weeks following DEN injection when combined with DUAL diet. This finding highlights the significance of identifying individuals with excessive alcohol consumption and MS, as they face a higher risk of liver-related cancer.

In the second part of the study, we aimed to characterize the gut-liver axis in the preclinical DUAL model.

Over the past ten years, there has been an intriguing discovery that various liver diseases, including NASH, ASH, cirrhosis, and HCC are either systemic than solely liver related conditions (28, 253). Latest discoveries of the gut-liver communication pathways have provided valuable insights into the fundamental mechanisms underlying both ALD and NAFLD (108).

The activation of *Tlr2/4/9* in the liver of DUAL mice, prompted the idea that, in addition to the direct hepatotoxic effects of alcohol and WD, the compromised intestinal barrier and an abnormal microbiome might potentially contribute to the pathogenesis (254, 255).

Thus, we decided to characterize changes induced by DUAL diet in the gut. High plasticity of the intestine leads to the easy adaption in response to nutrients and external factors (256). However, aging, stress conditions and certain pathological factors impact the structural integrity of the gut (151, 257).

We revealed that DUAL feeding resulted in remarkable macroscopical and microscopical alterations in the murine intestine. In mice fed with DUAL diet for 23 weeks, we detected the reduction of the total gut length, colon length and structural crypts deterioration manifested by a decrease in the depth. In fact, such

shortening is one of the biological markers in the assessment of colonic inflammation (199).

The comprehensive analysis of H&E in the colon also revealed the presence of multiple GALT. Innate and adaptative hematopoietic immune cells form the anatomical basis for a beneficial mutualistic relation with commensal microbiota, contribute to host defense and immune homeostasis. Studies in mice have demonstrated a key role of GALT in the induction of local immune responses and protection against mucosal pathogens (69, 258, 259).

GALT containing high T- and B- cell populations increased in DUAL animals. Moreover, underlying inflammation was confirmed by the increase of proinflammatory cytokines (as TNF-α), and by the presence of active T and B cells, revealed by flow cytometry in DUAL colon. Previous epidemiological studies indicate that high fat diets and obesity contribute to chronic intestinal inflammation, that can definitely be boosted by alcohol intake and its metabolites, inducing gut damage (49, 260).

The DUAL-induced inflammatory environment within the intestinal lamina propria, rich in the pro-inflammatory cytokine TNF-α, increases IEC shedding and compromises barrier integrity further fueling more inflammation and cell death (261). DUAL animals exhibited high levels of cell death in colon that were not only present in the upper part of the crypt, but were extended to the basal area, suggesting extended damage towards the stem cell.

Actively proliferating colonic stem cells are located at the very bottom of the crypts and fuel the self-renewal of the epithelium (204). Fully differentiated enterocytes cover the flat surface of the colon and are continuously replaced by new generations of cells that exit the crypt pockets. In different types of inflammatory conditions, the loss of IECs from the surface exceeds the rate of epithelial generation in the crypt. Importantly, DUAL damage in gut induced by DUAL diet triggered no compensatory proliferation and resulted in villus shortening (villus atrophy), gap formation in the epithelium and permeability defects (262). Altogether, these events created a positive feedback loop further increasing inflammatory response and epithelial damage (263).

The detailed analysis of the gut barrier integrity in DUAL mice revealed the significant disruption at the level of the mucus layer and TJs. Previous *in vitro* studies, have shown that pro-inflammatory cytokines such as TNF-α, induce TJs barrier loss by the phosphorylation of myosin regulatory light chain (MLC), a common intermediate in the pathophysiologic regulation of this barrier, reducing transepithelial resistance and consequently increasing gut permeability (68, 264). In addition, the loss of the integrity of the GVB in the DUAL mice reported a feature of uncontrolled translocation of substances across the endothelial cells (265). Consistently, DUAL animals reported increased bidirectional intestinal permeability evaluated by FITC-dextran experiment and the identification of albumin in feces.

From a “leaky” gut, bacteria and bacterial antigens can access the MNLs that provide the systemic firewall for dissemination of the intestinal products (265, 266). Although gut barrier impairment did not induce bacteriemia and no bacteria were detected in the liver, the MNLs in DUAL animals were enlarged suggesting an underlying inflammation.

Chronic alcohol and high fat diet exposure increase circulating concentrations of LPS and other PAMP molecules that subsequently were recognized by TLRs and initiate the systemic and hepatic immune responses (197). Additionally, an increased level of LPS in the bloodstream is linked to metabolic disorders and chronic illnesses that course with chronic inflammation as obesity, CLD, or IBD (267).

Notably, the immune response triggered by LPS can vary depending on the specific microbial species it originates from (267). Thus, we performed an analysis of 16s rRNA gene sequences from stool and found significant microbial dysbiosis in DUAL animals in comparison to controls. Dysbiosis can be categorized into three different types: 1) Loss of beneficial organisms, 2) Excessive growth of potentially harmful organisms, and 3) Loss of overall microbial diversity (268). All these pathological alterations have been found in DUAL-fed animals.

DUAL microbiome analysis revealed a decrease in the commensal bacteria *Muribaculaceae*, which has been described in some studies to play a vital role in

modulating energy metabolism in mice and its abundance is related to resistance to obesity (269).

Moreover, we showed the abundance of *Blautia* in DUAL mice. Previously, *Blautia* a genus of *Lachnospiraceae* family has been identified to increase in human patients with NAFLD and decrease after NAFLD treatment in rodents (270, 271, 272).

An increase in *Bacteroides* was another major feature exhibited by our DUAL animals that coincided with the cohort of dual etiology CLD patients. Interestingly, it had been previously described in NAFLD humans and mice (273). Published literature suggests several mechanisms that may explain why increased *Bacteroides* abundance in the gut promotes fatty liver and steatohepatitis. *Bacteroides* abundance displays strong positive correlations with the fecal content of deoxycholic acid, D-pinitol, choline, raffinose and stachyose (the two last contain glucose and fructose). Conversely, negative correlations between fecal *Bacteroides* and fecal SCFAs and amino acids have been reported. Most of these compounds influence the pathogenesis of NASH and have been found in DUAL mice (273).

We also observed that increases in fecal *Bacteroides* abundance were paralleled by decreases in *Prevotella*. This finding is consistent with evidence that Bacteroides and *Prevotella* are competitors. Dietary composition is known to influence the balance between *Bacteroides* and *Prevotella* in the gut: WD rich in fat and sugar favors *Bacteroides* growth. Thus, evidence of increased *Bacteroides* and decreased *Prevotella* in our DUAL mice is in line with previously published information and similarity between diet and human NASH (273).

Finally, DUAL-associated gut microbiota was associated with decreased α-diversity (richness and evenness).

Gut microbiome α-diversity has been linked to human health. Having a wide array of microbes in the gut makes intestinal microbiome more capable and resilient. In contrast, lower levels of diversity is associated with several acute and chronic diseases, including NAFLD and ALD (274, 275).

Bacterial translocation is a key mechanism in cirrhosis-related inflammation, involving imbalances in gut bacteria and impaired intestinal barrier. Selective

intestinal decontamination (SID) is a treatment that uses oral ABX to inhibit intestinal gram-negative flora while preserving the remaining flora. It was initially used to prevent bacterial infections in cirrhotic patients (276). In our study we used a cocktail of non-absorbable and low absorbable ABX as proof of concept that the dysbiotic microbiota of DUAL animals was completely implicated in the development of the disease.

The cocktail of ABX either in the water or by gavage improved liver physiology in terms of steatosis, inflammation, liver injury and fibrosis. Depletion of bacteria ameliorated lipid accumulation by increasing the levels of lipid oxidation though CPT-1c. Moreover, LPS, one of the main triggers of hepatic inflammation, is significantly reduced as a consequence of the depletion of Gram-negative bacteria. Several studies (277, 278) have reported that LPS is associated with reduced CPT1 levels in the liver and its consequent decrease in lipid oxidation and hepatic steatosis. Thus, ABX administration and the subsequent decrease in LPS would alleviate hepatic steatosis (277, 278).

Furthermore, decreased LPS in the bloodstream, reduced the activation of TLR4, decreasing the levels of inflammation and consequently the progression of hepatic fibrosis by HSCs (279).

Our result suggested that the depletion of the unbalanced DUAL microbiota (mainly composed of Gram-negative and harmful bacteria) had a significant positive effect on CLD development.

However, bacteria exert symbiotic functions with the host related to metabolism, maintaining immune homeostasis, and a healthy gut barrier (280). Germ-free mice report deficient immune system and altered lipid, cholesterol, xenobiotic/toxin, and BA metabolism (281, 282). Thus, ABX use needs to be limited for bacterial infections although in our DUAL model served as a validation of the role of microbiome in CLD development.

Microbiome modulation was proposed as a novel therapeutical approach for CLD (283). Although nutritional and habit intervention are the main recommendations for ALD and NAFLD, dietary adherence has been reported to be complicated (284). Currently, it is known that the beneficial effect observed in clinical trials can be translated into “real-life” only in the presence of good adherence to the

prescribed therapy (285). Thus, we decided to modify the microbiota in DUAL mice in parallel to continuing feeding.

The first therapeutical approach for microbiome modulation was the supplementation of probiotics. The study design included a placebo group. Some clinical trials reported that the supplementation of probiotics can alleviate liver steatosis, improve serum transaminases and inflammation. However, there are some contradictions in this regard (286, 287, 288).

Surprisingly, probiotics supplemented to DUAL animals did not exhibit any significant benefit. Thus, we postulate that the supplementation of probiotics with certain types of beneficial bacteria did not induce any substantial changes in gut microbiome able to reverse CLD pathophysiology. Our results show that DUAL gut is mainly colonized by Gram-negative bacteria with a decrease in commensal bacteria. We think that commensal probiotic bacteria confront severe difficulties in colonization of the DUAL gut. The microbiota footprint within the gastrointestinal tract, even in situations of dysbiosis, maintains its own homeostasis, and undergoes intricate adaptations to impede pathogen adhesion and proliferation. These adaptations include nutrient competition, competitive metabolic interactions and niche exclusion. Hence, our hypothesis suggests that the gut microenvironment becomes inhospitable for probiotics, impeding their viability within the DUAL colon (289).

Therefore, a second therapeutical approach was proposed. We hypothesized that fecal transplantation of the complete microbiome from a “healthy” donor might have a higher opportunity for restoration of decimated DUAL microbiota.

FMT has been already proposed as a treatment for NAFLD. Animal studies report that autologous or orthologous FMT from lean healthy donors potentiate loss of body weight and adiposity, have beneficial effects on MS, improve gut permeability and decreased steatosis and inflammation in the liver of recipients (222, 290, 291).

Our results showed that FMT after short-term DUAL feeding did not lead to any significant changes in terms of obesity (BMI and WAT deposition). However, mild improvements in the liver were observed: liver injury, steatosis, hepatic inflammation and fibrosis were partially reduced.

Although no changes in gut morphology were identified, altered gut barrier was ameliorated at the level of the mucus layer and TJs. As a result, the increased gut permeability was reduced after FMT.

Recently published randomized trials proposed that FMT from a thin and healthy donor given to patients with NAFLD may improve obesity features, liver physiology and intestinal permeability (292). Clinical trials with FMT in NAFLD patients reported effects on intestinal microbiota composition that was associated with beneficial changes in liver transaminases, total cholesterol and intestinal permeability (292, 293). Nevertheless, FMT effect on IR and systemic MS are still controversial between studies (292, 294). Moreover, FMT has also been proposed to treat severe ASH in order to increase life expectancy after liver transplant and to decrease inflammation (134).

Our results in DUAL animals are highly comparable to the published clinical trials: FMT induces mild beneficial effects on liver, although the extrahepatic changes were not improved. Most notable intestinal changes suggested that the donor microbiota was able to colonize the DUAL gut and partially recovers dysbiosis induced by the diet. However, to confirm microbiome compositional changes induced by FMT, further 16s rRNA analysis of bacteria needs to be performed in future experiments.

Altogether, the beneficial effects of microbiome modulation for DUAL mice are limited. Still, the dietary and lifestyle changes are the recommendable cornerstone of treatment for CLD patients (alcoholic and non-alcoholic etiology) (295).

As a next step, we compared how efficient simple lifestyle modifications were in comparison to microbiome modulating methods in DUAL mice.

Thus, after 10 weeks of DUAL feeding, the diet was replaced with chow diet and tap water for 21 days. DUAL W strongly reduced hepatomegaly and hepatic steatosis. Diet W diminished lipid uptake and increased hepatic oxidation, resulting in lower levels of lipid accumulation in the liver, processes that are known to play an important role in NASH (296). However, the changes observed in hepatic and intestinal injury and inflammation were not so robust (297).

Importantly, DUAL W induced major extrahepatic effects related to obesity features. Lower lipid volume coming from chow diet resulted in the restoration of lipid metabolism in the liver and subsequently linked to decreased hepatic injury, liver inflammation as well as fibrosis. Moreover, recent evidence suggests that microbiome is dynamic and changes on dietary patterns might result in different gut microbial composition and activity, which can contribute to the improvement of obesity and liver related diseases. Some studies have indicated that, as early as two days after the commencement of a dietary intervention, the microbiota exhibited responsive behavior and underwent alterations in composition. Furthermore, a healthy dietary pattern associated with specific microbiome profiles demonstrated protective effects against the onset of diabetes in obese individuals (298). Therefore, we hypothesized that DUAL W induced beneficial changes in microbiota. Nevertheless, 16s rRNA microbiome analysis has to be performed in the future.

Altogether, after detailed comparison of all the therapeutic methods used in the current study - DUAL W was the most effective strategy for early stage of CLD DUAL etiology **Table 11.**

Table 11. Comparison between all therapeutic options related to microbiome modulation and DUAL withdrawal for early CLD induced by short-term DUAL feeding (10wk).

Therapeutic option early CLD induced by short-term DUAL feeding (10wk)	ABX	PROBIOTICS	FMT	DUAL W
EXTRAHEPATIC FEATURES				
Body weight				
Fat deposition				
Cholesterol				
LIVER PATOPHYSIOLOGY				
Hepatomegaly				
Hepatic steatosis				
Liver damage				
Hepatic inflammation				
TLR expression				
Fibrosis				
GUT PHENOTYPE				
Gut phenotype				
Gut permeability				

No beneficial effect — Minor changes — Mild changes — Control level

However, under advanced CLD state (23 weeks DUAL feeding) microbiome modulation by FMT did not exhibit any beneficial effect in terms of obesity and hepatic mass. Minor changes in intrahepatic lipid accumulation were not sufficient to improve liver inflammation and fibrosis. No positive changes were observed in the gut. In addition, levels on effector immune cells in the intestine remained mostly unchanged after FMT. In addition, gut permeability remained increased.

Altogether, microbiome modulation failed to improve advanced liver and gut phenotypes induced by long term DUAL feeding. We suggest that gut environment under chronic inflammatory conditions and DUAL feeding are antagonistic for the colonization by "healthy" new bacteria.

Surprisingly, even DUAL W applied to the advanced DUAL animals (after 23 weeks of feeding) resulted in only marginal positive effects on the liver, mainly related to steatosis and fibrosis. This observation explains the difficulties associated with reversing advanced liver damage in patients with CLD **(Table 12).**

Table 12. Comparison between microbiome modulation (FMT) vs. DUAL withdrawal as therapeutic options for advanced CLD induced by long-term DUAL feeding (23wk).

Therapeutic option advanced CLD induced by long-term DUAL feeding (23wk)	FMT	DUAL W
Hepatic steatosis		
Liver inflammation		
TLR expression		
Fibrosis		

No beneficial effect | Minor changes | Mild changes | Control level

Based on our study, we conclude that microbiome modulation is a feasible option for the treatment of early stages of CLD. However, the refusal of dietary modification and persistent alcohol consumption might impede bacterial colonization and survival (298). Therefore, the synergistic modulation of microbiome by FMT, together with dietary intervention, could be used in combination for a more efficient early stage CLD treatment. Furthermore, the combination of both therapeutical approaches could be evaluated in future studies for an advanced stage CLD treatment.

Conclusions

9. CONCLUSIONS

- The DUAL model is a suitable model to study CLD thus it mimics all extrahepatic and intrahepatic features as it occurs in humans.

- DUAL mice exhibited strong damage in gut, increased gut permeability and induced GUT dysbiosis characterized by increase of Gram-negative bacteria and simultaneous decrease of commensal bacteria.

- Dysbiosis found in DUAL animals was comparable to results in dual etiology CLD patients.

- Microbiome depletion, by ABX, proved that dysbiosis is a target player in CLD pathophysiology in terms of steatosis, inflammation, and fibrosis, therefore microbiome could be used as a therapeutic target.

- The use of probiotics in an early stage CLD model (10 weeks feeding) to target the microbiome, parallel to DUAL diet feeding, has no significant beneficial effect on the liver.

- The use of FMT in an early stage CLD (10 weeks feeding) to target the microbiome, parallel to DUAL diet feeding, had mild beneficial effects on the liver.

- The best therapeutic option for short term DUAL feeding was DUAL withdrawal for 21 days.

- The use of FMT in advanced CLD (23 weeks feeding) to target the microbiome parallel to DUAL feeding had no beneficial effect on the liver.

- Microbiome intervention maintaining a DUAL diet suggests that “healthy bacteria” cannot survive in gut environment induced by DUAL diet and,

consequently, there is no final microbiota population that can exert a beneficial effect on the disease.

References

10. REFERENCES

1. Abdel-Misih SR, Bloomston M. Liver anatomy. Surg Clin North Am. 2010;90(4):643-53.

2. Si-Tayeb K, Lemaigre FP, Duncan SA. Organogenesis and development of the liver. Dev Cell. 2010;18(2):175-89.

3. Chapter 3 - Assessment of hepatic function: Implications for the surgical patient. In: William RJ, editor. Blumgart's Surgery of the Liver, Biliary Tract and Pancreas, 2-Volume Set (Sixth Edition). Sixth Edition ed. Philadelphia: Elsevier; 2017. p. 60-5.e2.

4. Eipel C, Abshagen K, Vollmar B. Regulation of hepatic blood flow: the hepatic arterial buffer response revisited. World J Gastroenterol. 2010;16(48):6046-57.

5. Braet F, Wisse E. Structural and functional aspects of liver sinusoidal endothelial cell fenestrae: a review. Comp Hepatol. 2002;1(1):1.

6. Boyer JL. Bile formation and secretion. Compr Physiol. 2013;3(3):1035-78.

7. Kalra A, Yetiskul E, Wehrle CJ, Tuma F. Physiology, Liver. StatPearls. Treasure Island (FL)2023.

8. Ishibashi H, Nakamura M, Komori A, Migita K, Shimoda S. Liver architecture, cell function, and disease. Semin Immunopathol. 2009;31(3):399-409.

9. Rappaport AM, Borowy ZJ, Lougheed WM, Lotto WN. Subdivision of hexagonal liver lobules into a structural and functional unit; role in hepatic physiology and pathology. Anat Rec. 1954;119(1):11-33.

10. Cunningham RP, Porat-Shliom N. Liver Zonation - Revisiting Old Questions With New Technologies. Front Physiol. 2021;12:732929.

11. Gracia-Sancho J, Caparros E, Fernandez-Iglesias A, Frances R. Role of liver sinusoidal endothelial cells in liver diseases. Nat Rev Gastroenterol Hepatol. 2021;18(6):411-31.

12. Ramos-Tovar E, Muriel P. Molecular Mechanisms That Link Oxidative Stress, Inflammation, and Fibrosis in the Liver. Antioxidants (Basel). 2020;9(12).

13. Sanz-García C, Fernández-Iglesias A, Gracia-Sancho J, Arráez-Aybar LA, Nevzorova YA, Cubero FJ. The Space of Disse: The Liver Hub in Health and Disease. Livers. 2021;1(1):3-26.
14. Fausto N, Campbell JS. The role of hepatocytes and oval cells in liver regeneration and repopulation. Mech Dev. 2003;120(1):117-30.
15. Nguyen P, Leray V, Diez M, Serisier S, Le Bloc'h J, Siliart B, et al. Liver lipid metabolism. J Anim Physiol Anim Nutr (Berl). 2008;92(3):272-83.
16. Petersen MC, Shulman GI. Roles of Diacylglycerols and Ceramides in Hepatic Insulin Resistance. Trends Pharmacol Sci. 2017;38(7):649-65.
17. Neuschwander-Tetri BA. Nontriglyceride hepatic lipotoxicity: the new paradigm for the pathogenesis of NASH. Curr Gastroenterol Rep. 2010;12(1):49-56.
18. Sanders FW, Griffin JL. De novo lipogenesis in the liver in health and disease: more than just a shunting yard for glucose. Biol Rev Camb Philos Soc. 2016;91(2):452-68.
19. Duwaerts CC, Maher JJ. Macronutrients and the Adipose-Liver Axis in Obesity and Fatty Liver. Cell Mol Gastroenterol Hepatol. 2019;7(4):749-61.
20. Kim KH. Regulation of mammalian acetyl-coenzyme A carboxylase. Annu Rev Nutr. 1997;17:77-99.
21. Dorn C, Riener MO, Kirovski G, Saugspier M, Steib K, Weiss TS, et al. Expression of fatty acid synthase in nonalcoholic fatty liver disease. Int J Clin Exp Pathol. 2010;3(5):505-14.
22. Moslehi A, Hamidi-Zad Z. Role of SREBPs in Liver Diseases: A Mini-review. J Clin Transl Hepatol. 2018;6(3):332-8.
23. Alves-Bezerra M, Cohen DE. Triglyceride Metabolism in the Liver. Compr Physiol. 2017;8(1):1-8.
24. Selen ES, Choi J, Wolfgang MJ. Discordant hepatic fatty acid oxidation and triglyceride hydrolysis leads to liver disease. JCI Insight. 2021;6(2).
25. Hall D, Poussin C, Velagapudi VR, Empsen C, Joffraud M, Beckmann JS, et al. Peroxisomal and microsomal lipid pathways associated with resistance to hepatic steatosis and reduced pro-inflammatory state. J Biol Chem. 2010;285(40):31011-23.

26. Powell EE, Wong VW, Rinella M. Non-alcoholic fatty liver disease. Lancet. 2021;397(10290):2212-24.

27. Guo X, Yin X, Liu Z, Wang J. Non-Alcoholic Fatty Liver Disease (NAFLD) Pathogenesis and Natural Products for Prevention and Treatment. Int J Mol Sci. 2022;23(24).

28. Osna NA, Donohue TM, Jr., Kharbanda KK. Alcoholic Liver Disease: Pathogenesis and Current Management. Alcohol Res. 2017;38(2):147-61.

29. Lieber CS. Alcoholic liver disease: new insights in pathogenesis lead to new treatments. J Hepatol. 2000;32(1 Suppl):113-28.

30. Hyun J, Han J, Lee C, Yoon M, Jung Y. Pathophysiological Aspects of Alcohol Metabolism in the Liver. Int J Mol Sci. 2021;22(11).

31. Zakhari S. Overview: how is alcohol metabolized by the body? Alcohol Res Health. 2006;29(4):245-54.

32. Park SH, Lee YS, Sim J, Seo S, Seo W. Alcoholic liver disease: a new insight into the pathogenesis of liver disease. Arch Pharm Res. 2022;45(7):447-59.

33. Donohue TM, Jr. Alcohol-induced steatosis in liver cells. World J Gastroenterol. 2007;13(37):4974-8.

34. Jeon S, Carr R. Alcohol effects on hepatic lipid metabolism. J Lipid Res. 2020;61(4):470-9.

35. Gao B, Bataller R. Alcoholic liver disease: pathogenesis and new therapeutic targets. Gastroenterology. 2011;141(5):1572-85.

36. Wattacheril J, Chalasani N. Nonalcoholic fatty liver disease (NAFLD): is it really a serious condition? Hepatology. 2012;56(4):1580-4.

37. Musso G, Cassader M, Paschetta E, Gambino R. Bioactive Lipid Species and Metabolic Pathways in Progression and Resolution of Nonalcoholic Steatohepatitis. Gastroenterology. 2018;155(2):282-302 e8.

38. Geng Y, Faber KN, de Meijer VE, Blokzijl H, Moshage H. How does hepatic lipid accumulation lead to lipotoxicity in non-alcoholic fatty liver disease? Hepatol Int. 2021;15(1):21-35.

39. Chu WM. Tumor necrosis factor. Cancer Lett. 2013;328(2):222-5.

40. Moayedfard Z, Sani F, Alizadeh A, Bagheri Lankarani K, Zarei M, Azarpira N. The role of the immune system in the pathogenesis of NAFLD and potential therapeutic impacts of mesenchymal stem cell-derived extracellular vesicles. Stem Cell Res Ther. 2022;13(1):242.

41. Hirsova P, Gores GJ. Death Receptor-Mediated Cell Death and Proinflammatory Signaling in Nonalcoholic Steatohepatitis. Cell Mol Gastroenterol Hepatol. 2015;1(1):17-27.

42. Tsuchida T, Friedman SL. Mechanisms of hepatic stellate cell activation. Nat Rev Gastroenterol Hepatol. 2017;14(7):397-411.

43. Heyens LJM, Busschots D, Koek GH, Robaeys G, Francque S. Liver Fibrosis in Non-alcoholic Fatty Liver Disease: From Liver Biopsy to Non-invasive Biomarkers in Diagnosis and Treatment. Front Med (Lausanne). 2021;8:615978.

44. Matsuda M, Seki E. Hepatic Stellate Cell-Macrophage Crosstalk in Liver Fibrosis and Carcinogenesis. Semin Liver Dis. 2020;40(3):307-20.

45. Roehlen N, Crouchet E, Baumert TF. Liver Fibrosis: Mechanistic Concepts and Therapeutic Perspectives. Cells. 2020;9(4).

46. Mahli A, Hellerbrand C. Alcohol and Obesity: A Dangerous Association for Fatty Liver Disease. Dig Dis. 2016;34 Suppl 1:32-9.

47. Purohit V, Russo D, Coates PM. Role of fatty liver, dietary fatty acid supplements, and obesity in the progression of alcoholic liver disease: introduction and summary of the symposium. Alcohol. 2004;34(1):3-8.

48. Longo M, Zatterale F, Naderi J, Parrillo L, Formisano P, Raciti GA, et al. Adipose Tissue Dysfunction as Determinant of Obesity-Associated Metabolic Complications. Int J Mol Sci. 2019;20(9).

49. Bishehsari F, Magno E, Swanson G, Desai V, Voigt RM, Forsyth CB, et al. Alcohol and Gut-Derived Inflammation. Alcohol Res. 2017;38(2):163-71.

50. Hussain MM. Intestinal lipid absorption and lipoprotein formation. Curr Opin Lipidol. 2014;25(3):200-6.

51. Zhang M, Yang XJ. Effects of a high fat diet on intestinal microbiota and gastrointestinal diseases. World J Gastroenterol. 2016;22(40):8905-9.

52. Plaza-Diaz J, Solis-Urra P, Rodriguez-Rodriguez F, Olivares-Arancibia J, Navarro-Oliveros M, Abadia-Molina F, et al. The Gut Barrier, Intestinal Microbiota,

and Liver Disease: Molecular Mechanisms and Strategies to Manage. Int J Mol Sci. 2020;21(21).

53. Nicoletti A, Ponziani FR, Biolato M, Valenza V, Marrone G, Sganga G, et al. Intestinal permeability in the pathogenesis of liver damage: From non-alcoholic fatty liver disease to liver transplantation. World J Gastroenterol. 2019;25(33):4814-34.

54. Proszkowiec-Weglarz M. Gastrointestinal anatomy and physiology. In: Colin G. Scanes SD, editor. Sturkie's Avian Physiology (Seventh Edition): Academic Press; 2022. p. 485-527.

55. Mowat AM, Agace WW. Regional specialization within the intestinal immune system. Nat Rev Immunol. 2014;14(10):667-85.

56. Shaker A, Rubin DC. Intestinal stem cells and epithelial-mesenchymal interactions in the crypt and stem cell niche. Transl Res. 2010;156(3):180-7.

57. Vancamelbeke M, Vermeire S. The intestinal barrier: a fundamental role in health and disease. Expert Rev Gastroenterol Hepatol. 2017;11(9):821-34.

58. Pelaseyed T, Bergstrom JH, Gustafsson JK, Ermund A, Birchenough GM, Schutte A, et al. The mucus and mucins of the goblet cells and enterocytes provide the first defense line of the gastrointestinal tract and interact with the immune system. Immunol Rev. 2014;260(1):8-20.

59. Johansson ME, Phillipson M, Petersson J, Velcich A, Holm L, Hansson GC. The inner of the two Muc2 mucin-dependent mucus layers in colon is devoid of bacteria. Proc Natl Acad Sci U S A. 2008;105(39):15064-9.

60. Vanuytsel T, Tack J, Farre R. The Role of Intestinal Permeability in Gastrointestinal Disorders and Current Methods of Evaluation. Front Nutr. 2021;8:717925.

61. Chelakkot C, Ghim J, Ryu SH. Mechanisms regulating intestinal barrier integrity and its pathological implications. Exp Mol Med. 2018;50(8):1-9.

62. Itoh M, Furuse M, Morita K, Kubota K, Saitou M, Tsukita S. Direct binding of three tight junction-associated MAGUKs, ZO-1, ZO-2, and ZO-3, with the COOH termini of claudins. J Cell Biol. 1999;147(6):1351-63.

63. Otani T, Nguyen TP, Tokuda S, Sugihara K, Sugawara T, Furuse K, et al. Claudins and JAM-A coordinately regulate tight junction formation and epithelial polarity. J Cell Biol. 2019;218(10):3372-96.

64. Otani T, Furuse M. Tight Junction Structure and Function Revisited. Trends Cell Biol. 2020;30(10):805-17.

65. Di Tommaso N, Santopaolo F, Gasbarrini A, Ponziani FR. The Gut-Vascular Barrier as a New Protagonist in Intestinal and Extraintestinal Diseases. Int J Mol Sci. 2023;24(2).

66. Brescia P, Rescigno M. The gut vascular barrier: a new player in the gut-liver-brain axis. Trends Mol Med. 2021;27(9):844-55.

67. Takiishi T, Fenero CIM, Camara NOS. Intestinal barrier and gut microbiota: Shaping our immune responses throughout life. Tissue Barriers. 2017;5(4):e1373208.

68. Buckley A, Turner JR. Cell Biology of Tight Junction Barrier Regulation and Mucosal Disease. Cold Spring Harb Perspect Biol. 2018;10(1).

69. Morbe UM, Jorgensen PB, Fenton TM, von Burg N, Riis LB, Spencer J, et al. Human gut-associated lymphoid tissues (GALT); diversity, structure, and function. Mucosal Immunol. 2021;14(4):793-802.

70. Yatsunenko T, Rey FE, Manary MJ, Trehan I, Dominguez-Bello MG, Contreras M, et al. Human gut microbiome viewed across age and geography. Nature. 2012;486(7402):222-7.

71. Ghosh S, Whitley CS, Haribabu B, Jala VR. Regulation of Intestinal Barrier Function by Microbial Metabolites. Cell Mol Gastroenterol Hepatol. 2021;11(5):1463-82.

72. Sender R, Fuchs S, Milo R. Revised Estimates for the Number of Human and Bacteria Cells in the Body. PLoS Biol. 2016;14(8):e1002533.

73. Thursby E, Juge N. Introduction to the human gut microbiota. Biochem J. 2017;474(11):1823-36.

74. Clemente JC, Ursell LK, Parfrey LW, Knight R. The impact of the gut microbiota on human health: an integrative view. Cell. 2012;148(6):1258-70.

75. Zheng D, Liwinski T, Elinav E. Interaction between microbiota and immunity in health and disease. Cell Res. 2020;30(6):492-506.

76. Caballero-Flores G, Pickard JM, Nunez G. Microbiota-mediated colonization resistance: mechanisms and regulation. Nat Rev Microbiol. 2022.

77. Adak A, Khan MR. An insight into gut microbiota and its functionalities. Cell Mol Life Sci. 2019;76(3):473-93.

78. Rinninella E, Raoul P, Cintoni M, Franceschi F, Miggiano GAD, Gasbarrini A, et al. What is the Healthy Gut Microbiota Composition? A Changing Ecosystem across Age, Environment, Diet, and Diseases. Microorganisms. 2019;7(1).

79. Rowland I, Gibson G, Heinken A, Scott K, Swann J, Thiele I, et al. Gut microbiota functions: metabolism of nutrients and other food components. Eur J Nutr. 2018;57(1):1-24.

80. Rinninella E, Cintoni M, Raoul P, Lopetuso LR, Scaldaferri F, Pulcini G, et al. Food Components and Dietary Habits: Keys for a Healthy Gut Microbiota Composition. Nutrients. 2019;11(10).

81. Oliphant K, Allen-Vercoe E. Macronutrient metabolism by the human gut microbiome: major fermentation by-products and their impact on host health. Microbiome. 2019;7(1):91.

82. Hou K, Wu ZX, Chen XY, Wang JQ, Zhang D, Xiao C, et al. Microbiota in health and diseases. Signal Transduct Target Ther. 2022;7(1):135.

83. Wechsler ME, Munitz A, Ackerman SJ, Drake MG, Jackson DJ, Wardlaw AJ, et al. Eosinophils in Health and Disease: A State-of-the-Art Review. Mayo Clin Proc. 2021;96(10):2694-707.

84. Gasaly N, de Vos P, Hermoso MA. Impact of Bacterial Metabolites on Gut Barrier Function and Host Immunity: A Focus on Bacterial Metabolism and Its Relevance for Intestinal Inflammation. Front Immunol. 2021;12:658354.

85. Sharma R, Schumacher U, Ronaasen V, Coates M. Rat intestinal mucosal responses to a microbial flora and different diets. Gut. 1995;36(2):209-14.

86. Petersson J, Schreiber O, Hansson GC, Gendler SJ, Velcich A, Lundberg JO, et al. Importance and regulation of the colonic mucus barrier in a mouse model of colitis. Am J Physiol Gastrointest Liver Physiol. 2011;300(2):G327-33.

87. Herath M, Hosie S, Bornstein JC, Franks AE, Hill-Yardin EL. The Role of the Gastrointestinal Mucus System in Intestinal Homeostasis: Implications for Neurological Disorders. Front Cell Infect Microbiol. 2020;10:248.

88. Makki K, Deehan EC, Walter J, Backhed F. The Impact of Dietary Fiber on Gut Microbiota in Host Health and Disease. Cell Host Microbe. 2018;23(6):705-15.

89. Cornick S, Tawiah A, Chadee K. Roles and regulation of the mucus barrier in the gut. Tissue Barriers. 2015;3(1-2):e982426.

90. Vinolo MA, Rodrigues HG, Hatanaka E, Sato FT, Sampaio SC, Curi R. Suppressive effect of short-chain fatty acids on production of proinflammatory mediators by neutrophils. J Nutr Biochem. 2011;22(9):849-55.

91. Miao W, Wu X, Wang K, Wang W, Wang Y, Li Z, et al. Sodium Butyrate Promotes Reassembly of Tight Junctions in Caco-2 Monolayers Involving Inhibition of MLCK/MLC2 Pathway and Phosphorylation of PKCbeta2. Int J Mol Sci. 2016;17(10).

92. Cunningham KE, Turner JR. Myosin light chain kinase: pulling the strings of epithelial tight junction function. Ann N Y Acad Sci. 2012;1258(1):34-42.

93. Ruff WE, Greiling TM, Kriegel MA. Host-microbiota interactions in immune-mediated diseases. Nat Rev Microbiol. 2020;18(9):521-38.

94. Wiest R, Lawson M, Geuking M. Pathological bacterial translocation in liver cirrhosis. J Hepatol. 2014;60(1):197-209.

95. Ray A, Cot M, Puzo G, Gilleron M, Nigou J. Bacterial cell wall macroamphiphiles: pathogen-/microbe-associated molecular patterns detected by mammalian innate immune system. Biochimie. 2013;95(1):33-42.

96. Kawai T, Akira S. The roles of TLRs, RLRs and NLRs in pathogen recognition. Int Immunol. 2009;21(4):317-37.

97. Kawai T, Akira S. Signaling to NF-kappaB by Toll-like receptors. Trends Mol Med. 2007;13(11):460-9.

98. Volta U, Bonazzi C, Bianchi FB, Baldoni AM, Zoli M, Pisi E. IgA antibodies to dietary antigens in liver cirrhosis. Ric Clin Lab. 1987;17(3):235-42.

99. Schnabl B, Brenner DA. Interactions between the intestinal microbiome and liver diseases. Gastroenterology. 2014;146(6):1513-24.

100. Tilg H, Cani PD, Mayer EA. Gut microbiome and liver diseases. Gut. 2016;65(12):2035-44.

101. Dawson PA. Hepatic bile acid uptake in humans and mice: Multiple pathways and expanding potential role for gut-liver signaling. Hepatology. 2017;66(5):1384-6.

102. Thomas C, Pellicciari R, Pruzanski M, Auwerx J, Schoonjans K. Targeting bile-acid signalling for metabolic diseases. Nat Rev Drug Discov. 2008;7(8):678-93.

103. Schubert K, Olde Damink SWM, von Bergen M, Schaap FG. Interactions between bile salts, gut microbiota, and hepatic innate immunity. Immunol Rev. 2017;279(1):23-35.

104. Seeger C, Mason WS. Sodium-dependent taurocholic cotransporting polypeptide: a candidate receptor for human hepatitis B virus. Gut. 2013;62(8):1093-5.

105. Zollner G, Marschall HU, Wagner M, Trauner M. Role of nuclear receptors in the adaptive response to bile acids and cholestasis: pathogenetic and therapeutic considerations. Mol Pharm. 2006;3(3):231-51.

106. Lindner C, Thomsen I, Wahl B, Ugur M, Sethi MK, Friedrichsen M, et al. Diversification of memory B cells drives the continuous adaptation of secretory antibodies to gut microbiota. Nat Immunol. 2015;16(8):880-8.

107. Eksteen B, Grant AJ, Miles A, Curbishley SM, Lalor PF, Hubscher SG, et al. Hepatic endothelial CCL25 mediates the recruitment of CCR9+ gut-homing lymphocytes to the liver in primary sclerosing cholangitis. J Exp Med. 2004;200(11):1511-7.

108. Tripathi A, Debelius J, Brenner DA, Karin M, Loomba R, Schnabl B, et al. The gut-liver axis and the intersection with the microbiome. Nat Rev Gastroenterol Hepatol. 2018;15(7):397-411.

109. Kiziltas S. Toll-like receptors in pathophysiology of liver diseases. World J Hepatol. 2016;8(32):1354-69.

110. Adachi Y, Moore LE, Bradford BU, Gao W, Thurman RG. Antibiotics prevent liver injury in rats following long-term exposure to ethanol. Gastroenterology. 1995;108(1):218-24.

111. Bauer TM, Schwacha H, Steinbruckner B, Brinkmann FE, Ditzen AK, Aponte JJ, et al. Small intestinal bacterial overgrowth in human cirrhosis is associated with systemic endotoxemia. Am J Gastroenterol. 2002;97(9):2364-70.
112. Kalambokis GN, Tsianos EV. Rifaximin reduces endotoxemia and improves liver function and disease severity in patients with decompensated cirrhosis. Hepatology. 2012;55(2):655-6.
113. Henao-Mejia J, Elinav E, Jin C, Hao L, Mehal WZ, Strowig T, et al. Inflammasome-mediated dysbiosis regulates progression of NAFLD and obesity. Nature. 2012;482(7384):179-85.
114. Dapito DH, Mencin A, Gwak GY, Pradere JP, Jang MK, Mederacke I, et al. Promotion of hepatocellular carcinoma by the intestinal microbiota and TLR4. Cancer Cell. 2012;21(4):504-16.
115. Zhu L, Baker SS, Gill C, Liu W, Alkhouri R, Baker RD, et al. Characterization of gut microbiomes in nonalcoholic steatohepatitis (NASH) patients: a connection between endogenous alcohol and NASH. Hepatology. 2013;57(2):601-9.
116. Giannelli V, Di Gregorio V, Iebba V, Giusto M, Schippa S, Merli M, et al. Microbiota and the gut-liver axis: bacterial translocation, inflammation and infection in cirrhosis. World J Gastroenterol. 2014;20(45):16795-810.
117. Dumas ME, Barton RH, Toye A, Cloarec O, Blancher C, Rothwell A, et al. Metabolic profiling reveals a contribution of gut microbiota to fatty liver phenotype in insulin-resistant mice. Proc Natl Acad Sci U S A. 2006;103(33):12511-6.
118. Jiang W, Wu N, Wang X, Chi Y, Zhang Y, Qiu X, et al. Dysbiosis gut microbiota associated with inflammation and impaired mucosal immune function in intestine of humans with non-alcoholic fatty liver disease. Sci Rep. 2015;5:8096.
119. Asrani SK, Mellinger J, Arab JP, Shah VH. Reducing the Global Burden of Alcohol-Associated Liver Disease: A Blueprint for Action. Hepatology. 2021;73(5):2039-50.
120. Younossi Z, Aggarwal P, Shrestha I, Fernandes J, Johansen P, Augusto M, et al. The burden of non-alcoholic steatohepatitis: A systematic review of health-related quality of life and patient-reported outcomes. JHEP Rep. 2022;4(9):100525.

121. Younossi Z, Henry L. Contribution of Alcoholic and Nonalcoholic Fatty Liver Disease to the Burden of Liver-Related Morbidity and Mortality. Gastroenterology. 2016;150(8):1778-85.

122. Younossi ZM, Blissett D, Blissett R, Henry L, Stepanova M, Younossi Y, et al. The economic and clinical burden of nonalcoholic fatty liver disease in the United States and Europe. Hepatology. 2016;64(5):1577-86.

123. higado AEpeed. EHGNA. Enfermedad de hígado graso no alcohólico: un estudio integral. Casal FG, editor. Madrid: Libroacadémico, S.L.; 2021. 200 p.

124. Singh S, Osna NA, Kharbanda KK. Treatment options for alcoholic and non-alcoholic fatty liver disease: A review. World J Gastroenterol. 2017;23(36):6549-70.

125. Guo W, Ge X, Lu J, Xu X, Gao J, Wang Q, et al. Diet and Risk of Non-Alcoholic Fatty Liver Disease, Cirrhosis, and Liver Cancer: A Large Prospective Cohort Study in UK Biobank. Nutrients. 2022;14(24).

126. Hajdarevic B, Vehabovic I, Catic T, Masic I. The Role of Diet Therapy in the Treatment of Liver Disease. Mater Sociomed. 2020;32(3):200-6.

127. Nobili V, Carter-Kent C, Feldstein AE. The role of lifestyle changes in the management of chronic liver disease. BMC Med. 2011;9:70.

128. Cigrovski Berkovic M, Bilic-Curcic I, Mrzljak A, Cigrovski V. NAFLD and Physical Exercise: Ready, Steady, Go! Front Nutr. 2021;8:734859.

129. Ma Q, Ye J, Shao C, Lin Y, Wu T, Zhong B. Metabolic benefits of changing sedentary lifestyles in nonalcoholic fatty liver disease: a meta-analysis of randomized controlled trials. Ther Adv Endocrinol Metab. 2022;13:20420188221122426.

130. Patel K, Harrison SA, Elkhashab M, Trotter JF, Herring R, Rojter SE, et al. Cilofexor, a Nonsteroidal FXR Agonist, in Patients With Noncirrhotic NASH: A Phase 2 Randomized Controlled Trial. Hepatology. 2020;72(1):58-71.

131. Harrison SA, Bashir MR, Lee KJ, Shim-Lopez J, Lee J, Wagner B, et al. A structurally optimized FXR agonist, MET409, reduced liver fat content over 12 weeks in patients with non-alcoholic steatohepatitis. J Hepatol. 2021;75(1):25-33.

132. Saez-Lara MJ, Robles-Sanchez C, Ruiz-Ojeda FJ, Plaza-Diaz J, Gil A. Effects of Probiotics and Synbiotics on Obesity, Insulin Resistance Syndrome,

Type 2 Diabetes and Non-Alcoholic Fatty Liver Disease: A Review of Human Clinical Trials. Int J Mol Sci. 2016;17(6).

133. Leong KSW, Jayasinghe TN, Wilson BC, Derraik JGB, Albert BB, Chiavaroli V, et al. Effects of Fecal Microbiome Transfer in Adolescents With Obesity: The Gut Bugs Randomized Controlled Trial. JAMA Netw Open. 2020;3(12):e2030415.

134. Xue L, Deng Z, Luo W, He X, Chen Y. Effect of Fecal Microbiota Transplantation on Non-Alcoholic Fatty Liver Disease: A Randomized Clinical Trial. Front Cell Infect Microbiol. 2022;12:759306.

135. Bilal M, Ashraf S, Zhao X. Dietary Component-Induced Inflammation and Its Amelioration by Prebiotics, Probiotics, and Synbiotics. Front Nutr. 2022;9:931458.

136. Fukuda S, Toh H, Hase K, Oshima K, Nakanishi Y, Yoshimura K, et al. Bifidobacteria can protect from enteropathogenic infection through production of acetate. Nature. 2011;469(7331):543-7.

137. Xing W, Gao W, Lv X, Zhao Z, Mao G, Dong X, et al. The effects of supplementation of probiotics, prebiotics, or synbiotics on patients with non-alcoholic fatty liver disease: A meta-analysis of randomized controlled trials. Front Nutr. 2022;9:1024678.

138. Hassouneh R, Bajaj JS. Gut Microbiota Modulation and Fecal Transplantation: An Overview on Innovative Strategies for Hepatic Encephalopathy Treatment. J Clin Med. 2021;10(2).

139. Popa D, Neamtu B, Mihalache M, Boicean A, Banciu A, Banciu DD, et al. Fecal Microbiota Transplant in Severe and Non-Severe Clostridioides difficile Infection. Is There a Role of FMT in Primary Severe CDI? J Clin Med. 2021;10(24).

140. Choudhury J, Sanyal AJ. Clinical aspects of fatty liver disease. Semin Liver Dis. 2004;24(4):349-62.

141. Marroni CA, Fleck AM, Jr., Fernandes SA, Galant LH, Mucenic M, de Mattos Meine MH, et al. Liver transplantation and alcoholic liver disease: History, controversies, and considerations. World J Gastroenterol. 2018;24(26):2785-805.

142. Haldar D, Kern B, Hodson J, Armstrong MJ, Adam R, Berlakovich G, et al. Outcomes of liver transplantation for non-alcoholic steatohepatitis: A European Liver Transplant Registry study. J Hepatol. 2019;71(2):313-22.

143. Habka D, Mann D, Landes R, Soto-Gutierrez A. Future Economics of Liver Transplantation: A 20-Year Cost Modeling Forecast and the Prospect of Bioengineering Autologous Liver Grafts. PLoS One. 2015;10(7):e0131764.

144. Nevzorova YA, Boyer-Diaz Z, Cubero FJ, Gracia-Sancho J. Animal models for liver disease - A practical approach for translational research. J Hepatol. 2020;73(2):423-40.

145. Grice EA, Segre JA. The human microbiome: our second genome. Annu Rev Genomics Hum Genet. 2012;13:151-70.

146. Weiskirchen R, Friedman SL. Hepatic Stellate Cells: Methods and Protocols: Springer US; 2023.

147. Benede-Ubieto R, Estevez-Vazquez O, Guo F, Chen C, Singh Y, Nakaya HI, et al. An Experimental DUAL Model of Advanced Liver Damage. Hepatol Commun. 2021;5(6):1051-68.

148. Rodriguez-Palacios A, Khoretonenko MV, Ilic S. Institutional protocols for the oral administration (gavage) of chemicals and microscopic microbial communities to mice: Analytical consensus. Exp Biol Med (Maywood). 2019;244(6):459-70.

149. Benede-Ubieto R, Estevez-Vazquez O, Ramadori P, Cubero FJ, Nevzorova YA. Guidelines and Considerations for Metabolic Tolerance Tests in Mice. Diabetes Metab Syndr Obes. 2020;13:439-50.

150. Gupta J, Nebreda AR. Analysis of Intestinal Permeability in Mice. Bio-protocol. 2014;4(22):e1289.

151. He D, Wu H, Xiang J, Ruan X, Peng P, Ruan Y, et al. Gut stem cell aging is driven by mTORC1 via a p38 MAPK-p53 pathway. Nat Commun. 2020;11(1):37.

152. Bedossa P, Poitou C, Veyrie N, Bouillot JL, Basdevant A, Paradis V, et al. Histopathological algorithm and scoring system for evaluation of liver lesions in morbidly obese patients. Hepatology. 2012;56(5):1751-9.

153. Mehlem A, Hagberg CE, Muhl L, Eriksson U, Falkevall A. Imaging of neutral lipids by oil red O for analyzing the metabolic status in health and disease. Nat Protoc. 2013;8(6):1149-54.

154. Kraus D, Yang Q, Kahn BB. Lipid Extraction from Mouse Feces. Bio Protoc. 2015;5(1).

155. Livak KJ, Schmittgen TD. Analysis of relative gene expression data using real-time quantitative PCR and the 2(-Delta Delta C(T)) Method. Methods. 2001;25(4):402-8.

156. Ewels PA, Peltzer A, Fillinger S, Patel H, Alneberg J, Wilm A, et al. The nf-core framework for community-curated bioinformatics pipelines. Nat Biotechnol. 2020;38(3):276-8.

157. Di Tommaso P, Chatzou M, Floden EW, Barja PP, Palumbo E, Notredame C. Nextflow enables reproducible computational workflows. Nat Biotechnol. 2017;35(4):316-9.

158. Merkel D. Docker: lightweight Linux containers for consistent development and deployment. Linux Journal. 2014;2014.

159. Dobin A, Davis CA, Schlesinger F, Drenkow J, Zaleski C, Jha S, et al. STAR: ultrafast universal RNA-seq aligner. Bioinformatics. 2013;29(1):15-21.

160. Liao Y, Smyth GK, Shi W. featureCounts: an efficient general purpose program for assigning sequence reads to genomic features. Bioinformatics. 2014;30(7):923-30.

161. Patro R, Duggal G, Love MI, Irizarry RA, Kingsford C. Salmon provides fast and bias-aware quantification of transcript expression. Nat Methods. 2017;14(4):417-9.

162. Love MI, Huber W, Anders S. Moderated estimation of fold change and dispersion for RNA-seq data with DESeq2. Genome Biol. 2014;15(12):550.

163. Barr J, Caballeria J, Martinez-Arranz I, Dominguez-Diez A, Alonso C, Muntane J, et al. Obesity-dependent metabolic signatures associated with nonalcoholic fatty liver disease progression. J Proteome Res. 2012;11(4):2521-32.

164. van der Kloet FM, Bobeldijk I, Verheij ER, Jellema RH. Analytical error reduction using single point calibration for accurate and precise metabolomic phenotyping. J Proteome Res. 2009;8(11):5132-41.

165. Martinez-Arranz I, Mayo R, Perez-Cormenzana M, Minchole I, Salazar L, Alonso C, et al. Enhancing metabolomics research through data mining. J Proteomics. 2015;127(Pt B):275-88.

166. Godon JJ, Zumstein E, Dabert P, Habouzit F, Moletta R. Molecular microbial diversity of an anaerobic digestor as determined by small-subunit rDNA sequence analysis. Appl Environ Microbiol. 1997;63(7):2802-13.

167. Lagkouvardos I, Klaring K, Heinzmann SS, Platz S, Scholz B, Engel KH, et al. Gut metabolites and bacterial community networks during a pilot intervention study with flaxseeds in healthy adult men. Mol Nutr Food Res. 2015;59(8):1614-28.

168. Berry D, Ben Mahfoudh K, Wagner M, Loy A. Barcoded primers used in multiplex amplicon pyrosequencing bias amplification. Appl Environ Microbiol. 2011;77(21):7846-9.

169. Klindworth A, Pruesse E, Schweer T, Peplies J, Quast C, Horn M, et al. Evaluation of general 16S ribosomal RNA gene PCR primers for classical and next-generation sequencing-based diversity studies. Nucleic Acids Res. 2013;41(1):e1.

170. Lagkouvardos I, Joseph D, Kapfhammer M, Giritli S, Horn M, Haller D, et al. IMNGS: A comprehensive open resource of processed 16S rRNA microbial profiles for ecology and diversity studies. Sci Rep. 2016;6:33721.

171. Edgar RC. UPARSE: highly accurate OTU sequences from microbial amplicon reads. Nat Methods. 2013;10(10):996-8.

172. Edgar RC. Search and clustering orders of magnitude faster than BLAST. Bioinformatics. 2010;26(19):2460-1.

173. Pruesse E, Peplies J, Glockner FO. SINA: accurate high-throughput multiple sequence alignment of ribosomal RNA genes. Bioinformatics. 2012;28(14):1823-9.

174. Lagkouvardos I, Fischer S, Kumar N, Clavel T. Rhea: a transparent and modular R pipeline for microbial profiling based on 16S rRNA gene amplicons. PeerJ. 2017;5:e2836.

175. Chen J, Bittinger K, Charlson ES, Hoffmann C, Lewis J, Wu GD, et al. Associating microbiome composition with environmental covariates using generalized UniFrac distances. Bioinformatics. 2012;28(16):2106-13.

176. Jost L. Partitioning diversity into independent alpha and beta components. Ecology. 2007;88(10):2427-39.

177. Yoon SH, Ha SM, Kwon S, Lim J, Kim Y, Seo H, et al. Introducing EzBioCloud: a taxonomically united database of 16S rRNA gene sequences and whole-genome assemblies. Int J Syst Evol Microbiol. 2017;67(5):1613-7.
178. Barson JR, Karatayev O, Chang GQ, Johnson DF, Bocarsly ME, Hoebel BG, et al. Positive relationship between dietary fat, ethanol intake, triglycerides, and hypothalamic peptides: counteraction by lipid-lowering drugs. Alcohol. 2009;43(6):433-41.
179. Parker R, Kim SJ, Gao B. Alcohol, adipose tissue and liver disease: mechanistic links and clinical considerations. Nat Rev Gastroenterol Hepatol. 2018;15(1):50-9.
180. Divoux A, Tordjman J, Lacasa D, Veyrie N, Hugol D, Aissat A, et al. Fibrosis in human adipose tissue: composition, distribution, and link with lipid metabolism and fat mass loss. Diabetes. 2010;59(11):2817-25.
181. Paschos P, Paletas K. Non alcoholic fatty liver disease and metabolic syndrome. Hippokratia. 2009;13(1):9-19.
182. Boyle M, Masson S, Anstee QM. The bidirectional impacts of alcohol consumption and the metabolic syndrome: Cofactors for progressive fatty liver disease. J Hepatol. 2018;68(2):251-67.
183. Clapper JR, Hendricks MD, Gu G, Wittmer C, Dolman CS, Herich J, et al. Diet-induced mouse model of fatty liver disease and nonalcoholic steatohepatitis reflecting clinical disease progression and methods of assessment. Am J Physiol Gastrointest Liver Physiol. 2013;305(7):G483-95.
184. Noga AA, Zhao Y, Vance DE. An unexpected requirement for phosphatidylethanolamine N-methyltransferase in the secretion of very low density lipoproteins. J Biol Chem. 2002;277(44):42358-65.
185. Yao PM, Tabas I. Free cholesterol loading of macrophages induces apoptosis involving the fas pathway. J Biol Chem. 2000;275(31):23807-13.
186. Arguello G, Balboa E, Arrese M, Zanlungo S. Recent insights on the role of cholesterol in non-alcoholic fatty liver disease. Biochim Biophys Acta. 2015;1852(9):1765-78.

187. Wit M, Trujillo-Viera J, Strohmeyer A, Klingenspor M, Hankir M, Sumara G. When fat meets the gut-focus on intestinal lipid handling in metabolic health and disease. EMBO Mol Med. 2022;14(5):e14742.

188. Yoshitsugu R, Kikuchi K, Iwaya H, Fujii N, Hori S, Lee DG, et al. Alteration of Bile Acid Metabolism by a High-Fat Diet Is Associated with Plasma Transaminase Activities and Glucose Intolerance in Rats. J Nutr Sci Vitaminol (Tokyo). 2019;65(1):45-51.

189. Farooqui N, Elhence A, Shalimar. A Current Understanding of Bile Acids in Chronic Liver Disease. J Clin Exp Hepatol. 2022;12(1):155-73.

190. Gottlieb A, Canbay A. Why Bile Acids Are So Important in Non-Alcoholic Fatty Liver Disease (NAFLD) Progression. Cells. 2019;8(11).

191. Dawson PA, Lan T, Rao A. Bile acid transporters. J Lipid Res. 2009;50(12):2340-57.

192. Poupon R. Liver alkaline phosphatase: a missing link between choleresis and biliary inflammation. Hepatology. 2015;61(6):2080-90.

193. Stofan M, Guo GL. Bile Acids and FXR: Novel Targets for Liver Diseases. Front Med (Lausanne). 2020;7:544.

194. Mantena SK, King AL, Andringa KK, Eccleston HB, Bailey SM. Mitochondrial dysfunction and oxidative stress in the pathogenesis of alcohol- and obesity-induced fatty liver diseases. Free Radic Biol Med. 2008;44(7):1259-72.

195. Wang K. Molecular mechanisms of hepatic apoptosis. Cell Death Dis. 2014;5(1):e996.

196. Yang YM, Seki E. TNFalpha in liver fibrosis. Curr Pathobiol Rep. 2015;3(4):253-61.

197. Ntandja Wandji LC, Gnemmi V, Mathurin P, Louvet A. Combined alcoholic and non-alcoholic steatohepatitis. JHEP Rep. 2020;2(3):100101.

198. Meroni M, Longo M, Dongiovanni P. Alcohol or Gut Microbiota: Who Is the Guilty? Int J Mol Sci. 2019;20(18).

199. Chassaing B, Aitken JD, Malleshappa M, Vijay-Kumar M. Dextran sulfate sodium (DSS)-induced colitis in mice. Curr Protoc Immunol. 2014;104:15 25 1-15 25 14.

200. Fan Y, Bergmann A. Apoptosis-induced compensatory proliferation. The Cell is dead. Long live the Cell! Trends Cell Biol. 2008;18(10):467-73.
201. Bouskra D, Brezillon C, Berard M, Werts C, Varona R, Boneca IG, et al. Lymphoid tissue genesis induced by commensals through NOD1 regulates intestinal homeostasis. Nature. 2008;456(7221):507-10.
202. Baptista AP, Olivier BJ, Goverse G, Greuter M, Knippenberg M, Kusser K, et al. Colonic patch and colonic SILT development are independent and differentially regulated events. Mucosal Immunol. 2013;6(3):511-21.
203. Nielsen MM, Witherden DA, Havran WL. gammadelta T cells in homeostasis and host defence of epithelial barrier tissues. Nat Rev Immunol. 2017;17(12):733-45.
204. Snippert HJ. Colonic Crypts: Safe Haven from Microbial Products. Cell. 2016;165(7):1564-6.
205. Kuo WT, Odenwald MA, Turner JR, Zuo L. Tight junction proteins occludin and ZO-1 as regulators of epithelial proliferation and survival. Ann N Y Acad Sci. 2022;1514(1):21-33.
206. Mouries J, Brescia P, Silvestri A, Spadoni I, Sorribas M, Wiest R, et al. Microbiota-driven gut vascular barrier disruption is a prerequisite for non-alcoholic steatohepatitis development. J Hepatol. 2019;71(6):1216-28.
207. Zhao Y, Zhao J. PV1: Gatekeeper of Endothelial Permeability. Am J Respir Cell Mol Biol. 2020;63(4):413-4.
208. Wang L, Llorente C, Hartmann P, Yang AM, Chen P, Schnabl B. Methods to determine intestinal permeability and bacterial translocation during liver disease. J Immunol Methods. 2015;421:44-53.
209. Tsiaoussis GI, Assimakopoulos SF, Tsamandas AC, Triantos CK, Thomopoulos KC. Intestinal barrier dysfunction in cirrhosis: Current concepts in pathophysiology and clinical implications. World J Hepatol. 2015;7(17):2058-68.
210. Aguirre Valadez JM, Rivera-Espinosa L, Mendez-Guerrero O, Chavez-Pacheco JL, Garcia Juarez I, Torre A. Intestinal permeability in a patient with liver cirrhosis. Ther Clin Risk Manag. 2016;12:1729-48.

211. Xie Y, Tu B, Xu Z, Zhang X, Bi J, Zhao M, et al. Bacterial distributions and prognosis of bloodstream infections in patients with liver cirrhosis. Sci Rep. 2017;7(1):11482.

212. Candelli M, Franza L, Pignataro G, Ojetti V, Covino M, Piccioni A, et al. Interaction between Lipopolysaccharide and Gut Microbiota in Inflammatory Bowel Diseases. Int J Mol Sci. 2021;22(12).

213. Schwabe RF, Seki E, Brenner DA. Toll-like receptor signaling in the liver. Gastroenterology. 2006;130(6):1886-900.

214. Singh RK, Chang HW, Yan D, Lee KM, Ucmak D, Wong K, et al. Influence of diet on the gut microbiome and implications for human health. J Transl Med. 2017;15(1):73.

215. Llado Fernandez S, Vetrovsky T, Baldrian P. The concept of operational taxonomic units revisited: genomes of bacteria that are regarded as closely related are often highly dissimilar. Folia Microbiol (Praha). 2019;64(1):19-23.

216. Guohong L, Qingxi Z, Hongyun W. Characteristics of intestinal bacteria with fatty liver diseases and cirrhosis. Ann Hepatol. 2019;18(6):796-803.

217. Behary J, Amorim N, Jiang XT, Raposo A, Gong L, McGovern E, et al. Gut microbiota impact on the peripheral immune response in non-alcoholic fatty liver disease related hepatocellular carcinoma. Nat Commun. 2021;12(1):187.

218. Smith BJ, Miller RA, Ericsson AC, Harrison DC, Strong R, Schmidt TM. Changes in the gut microbiome and fermentation products concurrent with enhanced longevity in acarbose-treated mice. BMC Microbiol. 2019;19(1):130.

219. Wang L, Wan YY. The role of gut microbiota in liver disease development and treatment. Liver Res. 2019;3(1):3-18.

220. Durack J, Lynch SV. The gut microbiome: Relationships with disease and opportunities for therapy. J Exp Med. 2019;216(1):20-40.

221. Marechal L, Laviolette M, Rodrigue-Way A, Sow B, Brochu M, Caron V, et al. The CD36-PPARgamma Pathway in Metabolic Disorders. Int J Mol Sci. 2018;19(5).

222. Zhou D, Pan Q, Shen F, Cao HX, Ding WJ, Chen YW, et al. Total fecal microbiota transplantation alleviates high-fat diet-induced steatohepatitis in mice via beneficial regulation of gut microbiota. Sci Rep. 2017;7(1):1529.

223. Bajaj JS, Kassam Z, Fagan A, Gavis EA, Liu E, Cox IJ, et al. Fecal microbiota transplant from a rational stool donor improves hepatic encephalopathy: A randomized clinical trial. Hepatology. 2017;66(6):1727-38.
224. Leoni S, Tovoli F, Napoli L, Serio I, Ferri S, Bolondi L. Current guidelines for the management of non-alcoholic fatty liver disease: A systematic review with comparative analysis. World J Gastroenterol. 2018;24(30):3361-73.
225. Singal AK, Bataller R, Ahn J, Kamath PS, Shah VH. ACG Clinical Guideline: Alcoholic Liver Disease. Am J Gastroenterol. 2018;113(2):175-94.
226. Jacobse J, Li J, Rings E, Samsom JN, Goettel JA. Intestinal Regulatory T Cells as Specialized Tissue-Restricted Immune Cells in Intestinal Immune Homeostasis and Disease. Front Immunol. 2021;12:716499.
227. Pimpin L, Cortez-Pinto H, Negro F, Corbould E, Lazarus JV, Webber L, et al. Burden of liver disease in Europe: Epidemiology and analysis of risk factors to identify prevention policies. J Hepatol. 2018;69(3):718-35.
228. Huh Y, Cho YJ, Nam GE. Recent Epidemiology and Risk Factors of Nonalcoholic Fatty Liver Disease. J Obes Metab Syndr. 2022;31(1):17-27.
229. WHO. Obesity and overweight 2021 [Available from: https://www.who.int/news-room/fact-sheets/detail/obesity-and-overweight.
230. Naveau S, Cassard-Doulcier AM, Njike-Nakseu M, Bouchet-Delbos L, Barri-Ova N, Boujedidi H, et al. Harmful effect of adipose tissue on liver lesions in patients with alcoholic liver disease. J Hepatol. 2010;52(6):895-902.
231. Hart CL, Morrison DS, Batty GD, Mitchell RJ, Davey Smith G. Effect of body mass index and alcohol consumption on liver disease: analysis of data from two prospective cohort studies. BMJ. 2010;340:c1240.
232. Chang Y, Cho YK, Kim Y, Sung E, Ahn J, Jung HS, et al. Nonheavy Drinking and Worsening of Noninvasive Fibrosis Markers in Nonalcoholic Fatty Liver Disease: A Cohort Study. Hepatology. 2019;69(1):64-75.
233. Lazaro R, Wu R, Lee S, Zhu NL, Chen CL, French SW, et al. Osteopontin deficiency does not prevent but promotes alcoholic neutrophilic hepatitis in mice. Hepatology. 2015;61(1):129-40.

234. Gabele E, Dostert K, Dorn C, Patsenker E, Stickel F, Hellerbrand C. A new model of interactive effects of alcohol and high-fat diet on hepatic fibrosis. Alcohol Clin Exp Res. 2011;35(7):1361-7.

235. Nevzorova YA, Weiskirchen R, Liedtke C. Mouse Models for Hepatic Stellate Cell Activation and Liver Fibrosis Initiation. Methods Mol Biol. 2023;2669:177-91.

236. D'Souza El-Guindy NB, Kovacs EJ, De Witte P, Spies C, Littleton JM, de Villiers WJ, et al. Laboratory models available to study alcohol-induced organ damage and immune variations: choosing the appropriate model. Alcohol Clin Exp Res. 2010;34(9):1489-511.

237. Laughlin MR. Normal roles for dietary fructose in carbohydrate metabolism. Nutrients. 2014;6(8):3117-29.

238. Mathurin P, Bataller R. Trends in the management and burden of alcoholic liver disease. J Hepatol. 2015;62(1 Suppl):S38-46.

239. Lonardo A, Ballestri S, Marchesini G, Angulo P, Loria P. Nonalcoholic fatty liver disease: a precursor of the metabolic syndrome. Dig Liver Dis. 2015;47(3):181-90.

240. Ayala JE, Samuel VT, Morton GJ, Obici S, Croniger CM, Shulman GI, et al. Standard operating procedures for describing and performing metabolic tests of glucose homeostasis in mice. Dis Model Mech. 2010;3(9-10):525-34.

241. Malhi H, Gores GJ. Molecular mechanisms of lipotoxicity in nonalcoholic fatty liver disease. Semin Liver Dis. 2008;28(4):360-9.

242. Finck BN, Hall AM. Does Diacylglycerol Accumulation in Fatty Liver Disease Cause Hepatic Insulin Resistance? Biomed Res Int. 2015;2015:104132.

243. Gan LT, Van Rooyen DM, Koina ME, McCuskey RS, Teoh NC, Farrell GC. Hepatocyte free cholesterol lipotoxicity results from JNK1-mediated mitochondrial injury and is HMGB1 and TLR4-dependent. J Hepatol. 2014;61(6):1376-84.

244. Horn CL, Morales AL, Savard C, Farrell GC, Ioannou GN. Role of Cholesterol-Associated Steatohepatitis in the Development of NASH. Hepatol Commun. 2022;6(1):12-35.

245. Ding L, Yang L, Wang Z, Huang W. Bile acid nuclear receptor FXR and digestive system diseases. Acta Pharm Sin B. 2015;5(2):135-44.
246. Chiang JYL, Ferrell JM. Bile Acid Metabolism in Liver Pathobiology. Gene Expr. 2018;18(2):71-87.
247. Zhang F, Xi L, Duan Y, Qin H, Wei M, Wu Y, et al. The ileum-liver Farnesoid X Receptor signaling axis mediates the compensatory mechanism of 17alpha-ethynylestradiol-induced cholestasis via increasing hepatic biosynthesis of chenodeoxycholic acids in rats. Eur J Pharm Sci. 2018;123:404-15.
248. Li R, Andreu-Sanchez S, Kuipers F, Fu J. Gut microbiome and bile acids in obesity-related diseases. Best Pract Res Clin Endocrinol Metab. 2021;35(3):101493.
249. Chavez-Talavera O, Haas J, Grzych G, Tailleux A, Staels B. Bile acid alterations in nonalcoholic fatty liver disease, obesity, insulin resistance and type 2 diabetes: what do the human studies tell? Curr Opin Lipidol. 2019;30(3):244-54.
250. Huby T, Gautier EL. Immune cell-mediated features of non-alcoholic steatohepatitis. Nat Rev Immunol. 2022;22(7):429-43.
251. Shi C, Pamer EG. Monocyte recruitment during infection and inflammation. Nat Rev Immunol. 2011;11(11):762-74.
252. Luedde T, Schwabe RF. NF-kappaB in the liver--linking injury, fibrosis and hepatocellular carcinoma. Nat Rev Gastroenterol Hepatol. 2011;8(2):108-18.
253. Byrne CD, Targher G. NAFLD: a multisystem disease. J Hepatol. 2015;62(1 Suppl):S47-64.
254. Mencin A, Kluwe J, Schwabe RF. Toll-like receptors as targets in chronic liver diseases. Gut. 2009;58(5):704-20.
255. Albillos A, de Gottardi A, Rescigno M. The gut-liver axis in liver disease: Pathophysiological basis for therapy. J Hepatol. 2020;72(3):558-77.
256. Le Gall M, Thenet S, Aguanno D, Jarry AC, Genser L, Ribeiro-Parenti L, et al. Intestinal plasticity in response to nutrition and gastrointestinal surgery. Nutr Rev. 2019;77(3):129-43.
257. Gulhane M, Murray L, Lourie R, Tong H, Sheng YH, Wang R, et al. High Fat Diets Induce Colonic Epithelial Cell Stress and Inflammation that is Reversed by IL-22. Sci Rep. 2016;6:28990.

258. Pearson C, Uhlig HH, Powrie F. Lymphoid microenvironments and innate lymphoid cells in the gut. Trends Immunol. 2012;33(6):289-96.

259. Nagler-Anderson C. Man the barrier! Strategic defences in the intestinal mucosa. Nat Rev Immunol. 2001;1(1):59-67.

260. Basson AR, Chen C, Sagl F, Trotter A, Bederman I, Gomez-Nguyen A, et al. Regulation of Intestinal Inflammation by Dietary Fats. Front Immunol. 2020;11:604989.

261. Blander JM. Death in the intestinal epithelium-basic biology and implications for inflammatory bowel disease. FEBS J. 2016;283(14):2720-30.

262. Williams JM, Duckworth CA, Watson AJ, Frey MR, Miguel JC, Burkitt MD, et al. A mouse model of pathological small intestinal epithelial cell apoptosis and shedding induced by systemic administration of lipopolysaccharide. Dis Model Mech. 2013;6(6):1388-99.

263. Subramanian S, Geng H, Tan XD. Cell death of intestinal epithelial cells in intestinal diseases. Sheng Li Xue Bao. 2020;72(3):308-24.

264. Zolotarevsky Y, Hecht G, Koutsouris A, Gonzalez DE, Quan C, Tom J, et al. A membrane-permeant peptide that inhibits MLC kinase restores barrier function in in vitro models of intestinal disease. Gastroenterology. 2002;123(1):163-72.

265. Spadoni I, Zagato E, Bertocchi A, Paolinelli R, Hot E, Di Sabatino A, et al. A gut-vascular barrier controls the systemic dissemination of bacteria. Science. 2015;350(6262):830-4.

266. Macpherson AJ, Smith K. Mesenteric lymph nodes at the center of immune anatomy. J Exp Med. 2006;203(3):497-500.

267. Mohr AE, Crawford M, Jasbi P, Fessler S, Sweazea KL. Lipopolysaccharide and the gut microbiota: considering structural variation. FEBS Lett. 2022;596(7):849-75.

268. DeGruttola AK, Low D, Mizoguchi A, Mizoguchi E. Current Understanding of Dysbiosis in Disease in Human and Animal Models. Inflamm Bowel Dis. 2016;22(5):1137-50.

269. Wang B, Kong Q, Li X, Zhao J, Zhang H, Chen W, et al. A High-Fat Diet Increases Gut Microbiota Biodiversity and Energy Expenditure Due to Nutrient Difference. Nutrients. 2020;12(10).

270. Yang M, Qi X, Li N, Kaifi JT, Chen S, Wheeler AA, et al. Western diet contributes to the pathogenesis of non-alcoholic steatohepatitis in male mice via remodeling gut microbiota and increasing production of 2-oleoylglycerol. Nat Commun. 2023;14(1):228.
271. Shen F, Zheng RD, Sun XQ, Ding WJ, Wang XY, Fan JG. Gut microbiota dysbiosis in patients with non-alcoholic fatty liver disease. Hepatobiliary Pancreat Dis Int. 2017;16(4):375-81.
272. Tang W, Yao X, Xia F, Yang M, Chen Z, Zhou B, et al. Modulation of the Gut Microbiota in Rats by Hugan Qingzhi Tablets during the Treatment of High-Fat-Diet-Induced Nonalcoholic Fatty Liver Disease. Oxid Med Cell Longev. 2018;2018:7261619.
273. Boursier J, Mueller O, Barret M, Machado M, Fizanne L, Araujo-Perez F, et al. The severity of nonalcoholic fatty liver disease is associated with gut dysbiosis and shift in the metabolic function of the gut microbiota. Hepatology. 2016;63(3):764-75.
274. Lozupone CA, Stombaugh JI, Gordon JI, Jansson JK, Knight R. Diversity, stability and resilience of the human gut microbiota. Nature. 2012;489(7415):220-30.
275. Manor O, Dai CL, Kornilov SA, Smith B, Price ND, Lovejoy JC, et al. Health and disease markers correlate with gut microbiome composition across thousands of people. Nat Commun. 2020;11(1):5206.
276. Garcia-Tsao G. Prophylactic Antibiotics in Cirrhosis: Are They Promoting or Preventing Infections? Clin Liver Dis (Hoboken). 2019;14(3):98-102.
277. Maitra U, Chang S, Singh N, Li L. Molecular mechanism underlying the suppression of lipid oxidation during endotoxemia. Mol Immunol. 2009;47(2-3):420-5.
278. Miller AM, Wang H, Bertola A, Park O, Horiguchi N, Ki SH, et al. Inflammation-associated interleukin-6/signal transducer and activator of transcription 3 activation ameliorates alcoholic and nonalcoholic fatty liver diseases in interleukin-10-deficient mice. Hepatology. 2011;54(3):846-56.

279. An L, Wirth U, Koch D, Schirren M, Drefs M, Koliogiannis D, et al. The Role of Gut-Derived Lipopolysaccharides and the Intestinal Barrier in Fatty Liver Diseases. J Gastrointest Surg. 2022;26(3):671-83.

280. Malard F, Dore J, Gaugler B, Mohty M. Introduction to host microbiome symbiosis in health and disease. Mucosal Immunol. 2021;14(3):547-54.

281. Round JL, Mazmanian SK. The gut microbiota shapes intestinal immune responses during health and disease. Nat Rev Immunol. 2009;9(5):313-23.

282. Just S, Mondot S, Ecker J, Wegner K, Rath E, Gau L, et al. The gut microbiota drives the impact of bile acids and fat source in diet on mouse metabolism. Microbiome. 2018;6(1):134.

283. Bajaj JS, Ng SC, Schnabl B. Promises of microbiome-based therapies. J Hepatol. 2022;76(6):1379-91.

284. Anderson JW, Konz EC, Frederich RC, Wood CL. Long-term weight-loss maintenance: a meta-analysis of US studies. Am J Clin Nutr. 2001;74(5):579-84.

285. Baratta F, Angelico F, Del Ben M. Challenges in Improving Adherence to Diet and Drug Treatment in Hypercholesterolemia Patients. International Journal of Environmental Research and Public Health. 2023;20(10):5878.

286. Liu L, Li P, Liu Y, Zhang Y. Efficacy of Probiotics and Synbiotics in Patients with Nonalcoholic Fatty Liver Disease: A Meta-Analysis. Dig Dis Sci. 2019;64(12):3402-12.

287. Zhou X, Wang J, Zhou S, Liao J, Ye Z, Mao L. Efficacy of probiotics on nonalcoholic fatty liver disease: A meta-analysis. Medicine (Baltimore). 2023;102(4):e32734.

288. Derosa G, Guasti L, D'Angelo A, Martinotti C, Valentino MC, Di Matteo S, et al. Probiotic Therapy With VSL#3((R)) in Patients With NAFLD: A Randomized Clinical Trial. Front Nutr. 2022;9:846873.

289. Khan I, Bai Y, Zha L, Ullah N, Ullah H, Shah SRH, et al. Mechanism of the Gut Microbiota Colonization Resistance and Enteric Pathogen Infection. Front Cell Infect Microbiol. 2021;11:716299.

290. Perez-Matute P, Iniguez M, de Toro M, Recio-Fernandez E, Oteo JA. Autologous fecal transplantation from a lean state potentiates caloric restriction effects on body weight and adiposity in obese mice. Sci Rep. 2020;10(1):9388.

291. Lai ZL, Tseng CH, Ho HJ, Cheung CKY, Lin JY, Chen YJ, et al. Fecal microbiota transplantation confers beneficial metabolic effects of diet and exercise on diet-induced obese mice. Sci Rep. 2018;8(1):15625.
292. Craven L, Rahman A, Nair Parvathy S, Beaton M, Silverman J, Qumosani K, et al. Allogenic Fecal Microbiota Transplantation in Patients With Nonalcoholic Fatty Liver Disease Improves Abnormal Small Intestinal Permeability: A Randomized Control Trial. Am J Gastroenterol. 2020;115(7):1055-65.
293. Witjes JJ, Smits LP, Pekmez CT, Prodan A, Meijnikman AS, Troelstra MA, et al. Donor Fecal Microbiota Transplantation Alters Gut Microbiota and Metabolites in Obese Individuals With Steatohepatitis. Hepatol Commun. 2020;4(11):1578-90.
294. Vrieze A, Van Nood E, Holleman F, Salojarvi J, Kootte RS, Bartelsman JF, et al. Transfer of intestinal microbiota from lean donors increases insulin sensitivity in individuals with metabolic syndrome. Gastroenterology. 2012;143(4):913-6 e7.
295. van der Windt DJ, Sud V, Zhang H, Tsung A, Huang H. The Effects of Physical Exercise on Fatty Liver Disease. Gene Expr. 2018;18(2):89-101.
296. Ipsen DH, Lykkesfeldt J, Tveden-Nyborg P. Molecular mechanisms of hepatic lipid accumulation in non-alcoholic fatty liver disease. Cell Mol Life Sci. 2018;75(18):3313-27.
297. Estevez-Vazquez O, Benede-Ubieto R, Guo F, Gomez-Santos B, Aspichueta P, Reissing J, et al. Fat: Quality, or Quantity? What Matters Most for the Progression of Metabolic Associated Fatty Liver Disease (MAFLD). Biomedicines. 2021;9(10).
298. Kim B, Choi HN, Yim JE. Effect of Diet on the Gut Microbiota Associated with Obesity. J Obes Metab Syndr. 2019;28(4):216-24.

Apendix

11. APENDIX

11.1. PUBLICATIONS

1. Ramadori P, Woitok MM, Estévez-Vázquez O, **Benedé-Ubieto R,** Leal-Lassalle H, Lamas-Paz A, Guo F, Fabre J, Otto J, Verwaayen A, Reissing J, Bruns T, Erschfeld S, Haas U, Paffen D, Nelson LJ, Vaquero J, Bañares R, Trautwein C, Cubero FJ, Liedtke C, Nevzorova YA. Lack of Cyclin E1 in hepatocytes aggravates ethanol-induced liver injury and hepatic steatosis in experimental murine model of acute and chronic alcohol-associated liver disease. Biochim Biophysica Acta Mol Basis Dis. 2023 Apr;1869(4):166646. doi: 10.1016/j.bbadis.2023.166646. Epub 2023 Feb 1. PMID: 36736843. (IF 6.633, Q1).

2. Goikoetxea-Usandizaga, Naroa; Bravo, Miren; Egia-Mendikute, Leire; Abecia, Leticia; Serrano-Maciá, Marina; Urdinguio, Rocío G.; Clos-García, Marc; Rodríguez-Agudo, Rubén; Araujo-Legido, Raquel; López-Bermudo, Lucía; Delgado, Teresa C.; Lachiondo-Ortega, Sofía; González-Recio, Irene; Gil-Pitarch, Clàudia; Peña-Cearra, Ainize; Simón, Jorge; **Benedé-Ubieto, Raquel;** Ariño, Silvia; Herranz, Jose M.; Azkargorta, Mikel; Salazar-Bermeo, Julio; Martí, Nuria; Varela-Rey, Marta; Falcón-Pérez, Juan M.; Lorenzo, Óscar; Nogueiras, Rubén; Elortza, Félix; Nevzorova, Yulia A.; Cubero, Francisco J.; Saura, Domingo; Martínez-Cruz, Luis Alfonso; Sabio, Guadalupe; Palazón, Asís; Sancho-Bru, Pau; Elguezabal, Natalia; Fraga, Mario F.; Ávila, Matías A.; Bataller, Ramón; Marín, José J.G.; Martín, Franz; Martínez-Chantar, María Luz. The outcome of boosting mitochondrial activity in alcohol-associated liver disease is organ-dependent. Hepatology ():10.1097/HEP.0000000000000303, February 9, 2023. (IF 17.298, Q1).

3. Lamas-Paz, A; Moran, L; Estevez-Vazquez, O; **Benedé-Ubieto, R**; Salinas, B; Sydor, S; Vilchez-Vargas, R; Moreno, L; Gomez del Moral, M; Bechmann, LP; Martinez-Naves, E; Vaquero, J; Banares, R; Nevzorova, YA; Cubero, FJ. Blood and fecal extracellular vesicles (EVS) as biomarkers of injury in the gut-liver axis during alcohol-induced liver disease. Alcoholism- Clinical and experimental reserarch 2022, 46: 81-82. (IF 3.928, Q2) [Proceeding].

4. Guo, F.; Estévez-Vázquez, O.*; **Benedé-Ubieto, R.*;** Maya-Miles, D.; Zheng, K.; Gallego-Durán, R.; Rojas, Á.; Ampuero, J.; Romero-Gómez, M.; Philip, K.; Egbuniwe, I.U.; Chen, C.; Simon, J.; Delgado, T.C.; Martínez-Chantar, M.L.; Sun, J.; Reissing, J.; Bruns, T.; Lamas-Paz, A.; Moral, M.G.d.; Woitok, M.M.; Vaquero, J.; Regueiro, J.R.; Liedtke, C.; Trautwein, C.; Bañares, R.; Cubero, F.J.; Nevzorova, Y.A. A Shortcut from Metabolic-Associated Fatty Liver Disease (MAFLD) to Hepatocellular Carcinoma (HCC): c-MYC a Promising Target for Preventative Strategies and Individualized Therapy. Cancers 2022, 14, 192. https://doi.org/10.3390/cancers14010192. (IF 6.639, Q1)

5. Estévez-Vázquez, O.; **Benedé-Ubieto, R.;*** Guo, F.; Gómez-Santos, B.; Aspichueta, P.; Reissing, J.; Bruns, T.; Sanz-García, C.; Sydor, S.; Bechmann, L.P.; Maranillo, E.; Sañudo, J.R.; Vázquez, M.T.; Lamas-Paz, A.; Morán, L.; Mazariegos, M.S.; Ciudin, A.; Pericàs, J.M.; Peligros, M.I.; Vaquero, J.; Martínez-Naves, E.; Liedtke, C.; Regueiro, J.R.; Trautwein, C.; Bañares, R.; Cubero, F.J.; Nevzorova, Y.A. Fat: Quality, or Quantity? What Matters Most for the Progression of Metabolic Associated Fatty Liver Disease (MAFLD). Biomedicines 2021, 9, 1289. https://doi.org/10.3390/biomedicines9101289. (IF 6.08, Q1)

6. **Benedé-Ubieto, R.,*** Estévez-Vázquez, O., Guo, F., Chen, C., Singh, Y., Nakaya, H.I., Gómez del Moral, M., Lamas-Paz, A., Morán, L., López-Alcántara, N., Reissing, J., Bruns, T., Avila, M.A., Santamaría, E., Mazariegos, M.S., Woitok, M.M., Haas, U., Zheng, K., Juárez, I., Martín-Villa, J.M., Asensio, I., Vaquero, J., Peligros, M.I., Argemi, J., Bataller, R., Ampuero, J., Romero Gómez, M., Trautwein, C., Liedtke, C., Bañares, R., Cubero, F.J. and Nevzorova, Y.A. (2021), An Experimental DUAL Model of Advanced Liver Damage. Hepatol Commun, 5: 1051-1068. https://doi.org/10.1002/hep4.1698. (IF 5.073, Q1)

7. **Benedé-Ubieto R,** Estévez-Vázquez O, Flores-Perojo V, Macías-Rodríguez RU, Ruiz-Margáin A, Martínez-Naves E, Regueiro JR, Ávila MA, Trautwein C, Bañares R, Bosch J, Cubero FJ, Nevzorova YA. Abnormal Liver Function Test in Patients Infected with Coronavirus (SARS-CoV-2): A Retrospective Single-Center Study from Spain. J Clin Med. 2021 Mar 3;10(5):1039. doi: 10.3390/jcm10051039. PMID: 33802486; PMCID: PMC7959465. (IF 4.241, Q1)

8. **Benedé-Ubieto, R.*,** Guo, F., Estévez-Vázquez, O., Woitok, MM., Zheng, K., Asensio, I., Juárez Martín-Delgado, I., Martín-Villa, JM., Vaquero, J., Bañares, R., Liedtke, C., Cubero, FJ., Nevzorova, Y.A. (2020). Shedding the light on BASH: a novel experimental model of advanced liver damage. Journal of Hepatology, 73(01): S190. DOI: 10.1016/S0168-8278(20)30887-4. (IF 20.582, Q1). [Proceeding].

9. Guo, F., Zheng, K., **Benedé-Ubieto, R.*,** Woitok, MM., Estévez-Vázquez, O., Kaye, P., Liedtke, C., Cubero, FJ., Nevzorova, YA. (2020). A shortcut from non-alcoholic fatty liver disease to HCC: c-Myc, a promising theranostic target. Journal of Hepatology, 73(01): S661-S662. DOI: 10.1016/S0168-8278(20)31785-2. (IF 20.582, Q1).

10. **Benedé-Ubieto, R.*,** Estévez-Vázquez, O., Ramadori, P., Cubero, F. J., & Nevzorova, Y. A. (2020). Guidelines and Considerations for Metabolic Tolerance Tests in Mice. Diabetes, metabolic syndrome, and obesity: targets and therapy, 13, 439–450. DOI: 10.2147/DMSO.S234665 (IF 2.842; Q3).

11. Guo, F., Zheng, K., **Benedé-Ubieto, R*.,** Cubero, FJ., Nevzorova, YA. The Lieber-DeCarli Diet-A Flagship Model for Experimental Alcoholic Liver Disease. (2018). Alcohol Clin Exp Res, 42 (10): 1828 – 1840. DOI: 10.1111/acer.13840. (IF 5.3, Q1).

12. **Benedé-Ubieto, R*.,** Guo, F., Estévez-Vázquez, O., Woitok, MM., Zheng, K., Asensio, I., Juárez Martín-Delgado, I., Martín-Villa, JM., Vaquero, J., Bañares, R., Liedtke, C., Cubero, FJ., Nevzorova, YA. (2020). Shedding light on BASH: A novel experimental model of advanced liver damage. Zeitschrift für Gastroenterologie, 58(01): 5 – 5. DOI: 10.1055/s-0039-3402111. [Proceeding].

13. **Benedé-Ubieto, R*.,** Estévez-Vázquez, O., Morán, L., López-Alcántara, N., Guo, F., Chaobo, CH., Macias-Rodriguez, RU., Ruíz-Margaín, A., Zheng, K., Ramadori, P., Cubero, FJ., Nevzorova, YA. (2019). Cumulative effects of western diet and alcohol abuse: A novel model of ASH/NASH derived liver injury. Hepatology; 70 (1) Suppl: 829a. DOI: 0.1002/hep.30941. (IF 14.679, Q1) [Proceeding].

14. **Benedé-Ubieto, R*;** Estévez-Vázquez, O., Morán, L., López-Alcántara, N., Guo, F., Chaobo, CH., Macias-Rodriguez, RU., Ruíz-Margaín, A., Zheng, K., Ramadori, P., Cubero, FJ., Nevzorova, YA. Cumulative effects of western diet and alcohol abuse: A novel model of ASH/NASH derived liver injury. (2019). Journal of Hepatology, 70 (1): e274. DOI: 10.1016/S0618-8278(19)30521-3. (IF 20.582, Q1) [Proceeding].

15. Guo, F., Zheng, K., **Benedé-Ubieto, R*.,** Estévez-Vázquez, O., Ramadori, P., Woitok, MM., Chen, C., Trautwein, C., Liedtke, C., Cubero, FJ., Nevzorova, YA. c-MYC overexpression in hepatocytes is associated with spontaneous development of non-alcoholic steatohepatitis (NASH) in mice. (2019). Zeitschrift für Gastroenterologie, 57(01):44 – 44. DOI: 10.1055/s-0038-1677162. [Proceeding].

11.2. CONFERENCES

1. **48º Congreso anual de la Asociación Española para el Estudio del Hígado (AEEH).** "Unveiling the Gut-Liver Axis crosstalk in DUAL etiology". **Raquel Benedé-Ubieto,** Olga Estévez-Vázquez, Salvador Iborra, Ana Redondo-Urzainqui, Matías A. Avila, José María Herranz, Alexander Tyakht, Viktoria Odintsova, Beatriz Gómez-Santos, Patricia Aspichueta, Johanna Reissing, Oluwatomi Ibidapo-Obe, Tony Bruns, Marina S. Mazariegos, Héctor Leal, Javier Vaquero, Christian Trautwein, Christian Liedtke, Rafael Bañares, Francisco Javier Cubero, Yulia A. Nevzorova. (Madrid, España). (15-17/03/2023) Poster.
2. **48º Congreso anual de la Asociación Española para el Estudio del Hígado (AEEH).** "The beneficial effects of the diet withdrawal and physical exercise on steatohepatitis of dual etiology". Olga Estévez-Vázquez, **Raquel Benedé-Ubieto,** Héctor Leal-Lassalle, Jeanne Fabre, Johanna Reissing, Marina Mazariegos León, Carlos Sanz Garcia, Tony Bruns, Javier Vaquero, Rafael Bañares, Francisco Javier Cubero, Yulia A. Nevzorova. (Madrid, España). (15-17/03/2023) Poster.
3. **CA-17112: Prospective european drug-induced liver injury network closing meeting, WGs meeting, 8th CG & 5th MC Meeting. COST.** (Prague,

Czechia). Action member. (9-10/03/2023).

4. **Joint Meeting of ISBRA and ESBRA 2nd World Congress on Alcohol and Alcoholism**. "Blood and fecal extracellular vesicles (EVS) as biomarkers of injury in the gut liver axis during alcohol induced liver disease". A Lamas Paz, L Moran, O Estevez Vazquez, **R Benede Ubieto,** B Salinas, S Sydor, R Vilchez Vargas, L Moreno, M Gomez del Moral, LP Bechmann, E Martinez Naves, J Vaquero, R Banares, YA Nevzorova, FJ Cubero. Krakow, Poland. Dates: (17/10/2022 - 20/10/2022).
5. **EMBO workshop, Energy balance in metabolic disorders (2022).** "Unveiling the Gut-Liver Axis crosstalk in DUAL etiology". **Benedé-Ubieto, R**; Estévez- Vázquez, O; Iborra, S; Redondo- Urzainqui, A; Avila, MA; Herranz, JM; Tyakht, AV; Odintsova, VE; Gómez-Santos, B; Aspichueta, P; Reissing, J; Bruns, T; Mazariegos, MS; Vaquero, J; Trautwein, C; Liedtke, C; Bañares, R; Cubero, FJ; Nevzorova, YA. (Malaga, Spain). (10/2022). Poster + Flash talk.
6. **EMBO workshop, Energy balance in metabolic disorders (2022).** "A novel role for CDKN1A in metabolic- associated fatty liver disease (MAFLD)". Lamas-Paz, A; Jorquera-Olave, G; Morán, L; Estévez- Vázquez, O; **Benedé-Ubieto, R;** Vaquero, J; Bañares, R; Sanz- García, C; Martinez-Naves, E; Cardoso Delgado, T; Martinez- Chantar, M; Puigserver, P; Nevzorova, YA; Cubero, FJ. Poster. (Malaga, Spain). (10/2022). Poster.
7. **47 Congreso Anual de la Asociación Española para el Estudio del Hígado (2022).** "Papel de p21/CDKN1A en la progresión de la enfermedad del hígado graso no alcohólico (EHGNA/NASH)". Lamas-Paz, A; Guo, FF; Hao, F; Estévez Vázquez, O; **Benedé-Ubieto, R**; Vázquez-Ogando, E; Blázquez López, E; Asensio, I; Vaquero, J; Bañares, R; Sanz-García, C; Martínez-Naves, E; C. Delgado, T; Martínez Chantar, M; Puigserver, P; Nevzorova, YA; Cubero, FJ. (Madrid, Spain). (25-27/07/2022). Oral communication.
8. **47 Congreso Anual de la Asociación Española para el Estudio del Hígado (2022).** "A short-term diet withdrawal ameliorates steatohepatitis in DUAL-fed mice". Estévez-Vázquez, O; **Benedé-Ubieto, R**; Reissing, J; Bruns, T; Vaquero, J; Liedtke, C; Trautwein, C; Bañares, R; Cubero, FJ; Nevzorova, YA. (Madrid, Spain). (25-27/07/2022). Poster.

9. **GASL Annual Meeting 2022.** “Gender- related differences in response to DUAL diet in murine model of steatohepatitis”. **Benedé Ubieto, R**; Estévez-Vázquez, O; Dumartin, M; Reissing, J; Bruns, T; Vaquero, J; Liedtke, C; Trautwein, C; Bañares, R; Cubero, FJ; Nevzorova, YA. (27-28/01/2022). Z Gastroenterol 2022; 60(01): e26 DOI: 10.1055/s-0041-1740733. Poster prize. (Hamburg (Mainz), Germany) (Online). (27-28/01/2022). Poster.
10. **Falk Symposium Pathophysiology and Clinical Management of Alcoholic liver disease.** “Gender- related differences in response to DUAL diet in murine model of steatohepatitis”. **Benedé Ubieto, R**; Estévez-Vázquez, O; Dumartin, M; Reissing, J; Bruns, T; Vaquero, J; Liedtke, C; Trautwein, C; Bañares, R; Cubero, FJ; Nevzorova, YA. (Hamburg (Mainz), Germany) (Online). (27-28/01/2022). Poster.
11. **Falk Symposium Pathophysiology and Clinical Management of Alcoholic liver disease.** “A short-term diet withdrawal ameliorates steatohepatitis in DUAL-fed mice”. Estévez-Vázquez, O; **Benedé-Ubieto, R**; Reissing, J; Bruns, T; Vaquero, J; Liedtke, C; Trautwein, C; Bañares, R; Cubero, FJ; Nevzorova, YA. (Hamburg (Mainz), Germany) (Online). (27-28/01/2022). Poster.
12. **Tercera reunión de hepatología traslacional.** “Fat: quality, or quantity? What matters most for the progression of Metabolic Associated Fatty Liver Disease (MAFLD)”. Estévez-Vázquez, O; **Benedé-Ubieto, R;** Guo, FF; Gómez-Santos, B; Aspichueta, P; Reissing, J; Bruns, T; Sanz-García, C; Sydor, S; Bechmann, LP; Maranillo, E; Sañudo, JR; Vázquez, T; Lamas-Paz, A; Morán, L; Mazariegos, MS; Ciudin, A; Vaquero, J; Martínez-Naves, E; Liedtke, C; Regueiro, JR; Trautwein, C; Bañares, R; Cubero, FJ; Nevzorova YA. (Alicante, Spain). (22-23/10/2022). Poster.
13. **Tercera reunión de hepatología traslacional.** “Gender- related differences in response to DUAL diet in murine model of steatohepatitis”. **Benedé Ubieto, R;** Estévez-Vázquez, O; Dumartin, M; Reissing, J; Bruns, T; Vaquero, J; Liedtke, C; Trautwein, C; Bañares, R; Cubero, FJ; Nevzorova, YA. (Alicante, Spain). (22-23/10/2022). Poster.
14. **International workshop on liver and gut fibrosis.** “A novel hybrid murine model of BASH with rapid progression to advanced fibrosis”. **Benedé Ubieto,**

R; Estévez-Vázquez, O; Guo, FF; Woitok, MM; Zheng, K; Asensio, A; Juárez Martín-Delgado, I; Martín-Villa, JM; Peligros, I; Vaquero, J; Bañares, R; Liedtke, C; Cubero, FJ; Nevzorova, YA. (Valencia, Spain). (7-8/10/2022). Oral communication.

15. **International workshop on liver and gut fibrosis.** "Gender- related differences in response to DUAL diet in murine model of steatohepatitis". **Benedé Ubieto, R**; Estévez-Vázquez, O; Dumartin, M; Reissing, J; Bruns, T; Vaquero, J; Liedtke, C; Trautwein, C; Bañares, R; Cubero, FJ; Nevzorova, YA. (Valencia, Spain). (7-8/10/2022). Poster.
16. **Liver Cancer Summit 2021. (EASL).** "The combination of alcohol and metabolic syndrome is a fast track to hepatic tumorigenesis". **Benedé-Ubieto R;** Chen C; Estévez-Vázquez O; Guo F; Lamas-Paz A; Morán L; Reißing J; Bruns T; Zheng K; Peligros MI; Vaquero J; Trautwein C; Liedtke C; Bañares R; Cubero FJ; Nevzorova YA. (5 – 6/02/2021). Poster.
17. **DILC 2020 (Digital International Liver Congress) (EASL).** "Shedding light on BASH: A novel experimental model of advanced liver damage". **Benedé-Ubieto R**; Guo F; Estévez-Vázquez O; Woitok MM; Zheng K; Asensio I; Juárez Martín-Delgado I; Martín-Villa JM; Vaquero J; Bañares R; Liedtke C; Cubero FJ; Nevzorova YA. (27 – 29/08/2020). Poster.
18. **GASL 2020 (German Association for the Study of the Liver).** "Shedding light on BASH: A novel experimental model of advanced liver damage". **Benedé-Ubieto R**; Guo F; EstévezVázquez O; Woitok MM; Zheng K; Asensio I; Juárez Martín-Delgado I; Martín-Villa JM; Vaquero J; Bañares R; Liedtke C; Cubero FJ; Nevzorova YA. (Mainz, Germany). (14 – 15/02/2020). Poster.
19. **AASLD 2019 (American Association for the Study of the Liver). "**Cumulative effects of western diet and alcohol abuse: a novel experimental mouse model of ASH/NASH-derived liver injury". **Benedé-Ubieto R;** Estévez-Vázquez O; Morán L; López-Alcántara N; Guo F; Chaobo CHEN; Macias-Rodriguez RU; Ruíz-Margaín A; Zheng K; Ramadori P; Cubero FJ; Nevzorova YA. (Boston, USA). (08/11/2019-12/09/2019). Poster.
20. **NAFLD SUMMIT 2019. (EASL).** "The genetic background strongly influences the development of steatohepatitis and metabolic syndrome in a novel

experimental model of dual ASH/NASH". **Benedé-Ubieto R,** Estévez-Vázquez O, Guo F, Zheng K, Woitok MM, Asensio I, Vaquero J, Rafael Bañares, Cubero FJ, Nevzorova YA. (Sevilla, Spain). (26/09/2019 – 18/09/2019). Poster.

21. **NAFLD SUMMIT 2019. (EASL).** "Differential effects of palmitic acid on the development of NASH and related metabolic disorders". Estévez Vázquez O, Guo F, **Benedé-Ubieto R,** Chaobo Chen, Vaquero J, Bañares R, Cubero FJ, Nevzorova YA. (Sevilla, Spain). (26/09/2019 – 18/09/2019). Poster.
22. **Paris NASH Meeting.** "Differential effects of palmitic acid on the development of NASH and related metabolic disorders". Estévez-Vázquez O, **Benedé-Ubieto R,** Guo F, Lamas-Paz A, Vaquero J, Bañares R, Cubero FJ, Nevzorova YA. (Paris, France). (11/07/2019 – 12/07/2019). Poster.
23. **The International Liver Congress (ILC) 2019. (EASL).** "Cumulative effects of western diet and alcohol abuse: A novel model of ASH/NASH derived liver injury". **Benedé-Ubieto R;** Estévez- Vázquez O; Morán L; López-Alcántara N; Guo F; Chaobo CHEN; Macias-Rodriguez RU; Ruíz-Margaín A; Zheng K; Ramadori P; Cubero FJ; Nevzorova YA. (Vienna, Austria). (10/04/2019 - 14/04/2019). Poster.
24. **German Association for the Study of the Liver GASL annual meeting 2019**. "c-MYC overexpression in hepatocytes is associated with spontaneous development of non-alcoholic steatohepatitis (NASH) in mice". Guo F, Zheng K, **Benedé-Ubieto R,** Estévez-Vázquez O, Woitok MM, Ramadori P, Chaobo CHEN, Trautwein C, Liedtke C, Cubero FJ, Nevzorova YA. (Heidelberg, Germany). (22/02/2019 – 23/02/2019). Poster.
25. **Asociación española para el estudio del hígado (AEEH) congress 2019.** "Effects of Western Diet and Palmitic Acid in the development of Non-Alcoholic Fatty Liver Disease (NAFLD) and related metabolic disorders". Estévez-Vázquez O, Guo F, **Benedé-Ubieto R,** Chaobo CHEN, Vaquero J, Bañares R, Cubero FJ, Nevzorova YA. (Madrid, Spain). (20/02/2019 – 22/02/2019). Oral poster.
26. **8th European Club for Liver Cell Biology.** "C-MYC overexpression in hepatocytes is associated with spontaneous development of non-alcoholic steatohepatitis (NASH) in mice". Guo F, Zheng K, **Benedé-Ubieto R,** Ramadori

P, Chaobo CHEN, Trautwein C, Liedtke C, Cubero FJ, Nevzorova YA. (Bonn, Germany). (4/10/2018 – 6/10/2019). Poster.

27. **NAFLD SUMMIT 2018. (EASL).** "Cumulative effects of western diet and alcohol abuse: A novel model of ASH/NASHderived liver injury". **Benedé-Ubieto R;** Guo F; Zheng K; Ramadori P; Cubero FJ; Nevzorova YA. (Geneve, Switzerland). (20/09/2018 – 22/09/2018). Poster.
28. **NAFLD SUMMIT 2018. (EASL).** "C-MYC overexpression in hepatocytes is responsible for the spontaneous development of murine non-alcoholic steatohepatitis". Poster. Guo F, Zheng K, Benedé- Ubieto R, Ramadori P, Chaobo CHEN, Morán L, Trautwein C, Liedtke C, Cubero FJ, Nevzorova YA. (Geneve, Switzerland). (20/09/2018 – 22/09/2018). Poster.

11.3. TRAINING COURSES

1. **Basic Science School: Microbiome in chronic liver disease. (EASL).** London, UK, (27-29/09/2023).
2. **Curso de manejo de FACSCelestaTM** (Laboratorio de Aplicaciones). BD.Madrid, Spain. (17/01/2023).
3. **Flow cytometry induction course: fundamentals, applications, data analysis and data presentation.** 7,5 h. (28-29/11/2022). Flow cytometry unit of the Spanish National Cancer Research Centre (CNIO).
4. **Segunda escuela de Investigación CIBEREHD. "Ómicas en el estudio de las enfermedades hepáticas y digestivas".** Bilbao, Spain. (5-6/10/2023).
5. **Función de Eutanasia de los Animales: Función B.** Animalaria Formación y Gestión S.L.
6. **Función de Realización de los Procedimientos: Función C.** Animalaria Formación y Gestión S.L.

11.4. MEMBERSHIP OF SCIENTIFIC SOCIETIES

1. Member of the European Association for the Study of the Liver (EASL).

11.5. MOST RELEVANT HONORS AND AWARDS

1. Beca Aprendizaje Nuevas Tecnologías (2021) – AEEH.
2. Erasmus + UCM – Uniklinik RWTH Aachen (January 2020 – April 2020).
3. Predoctoral UCM-Santander Fellowship (2019-2024).